# A STUDY OF FLEXIBLE SUPERCAPACITORS: DESIGN, MANUFACTURE AND TESTING

A thesis submitted for the degree of
Doctor of Philosophy

by

**Ruirong Zhang**

College of Engineering, Design and Physical Sciences
Brunel University London
Uxbridge, UB8 3PH
United Kingdom

June 2016

Supervision: Dr Yanmeng Xu and Professor David Harrison

# Abstract

Supercapacitors have attracted great attention because of their high power density, long life cycle and high efficiency. They can be generally classified into two types: electrical double-layer capacitors (EDLCs) and pseudocapacitors. Compared with pseudocapacitors, EDLCs have a very fast charge/discharge rate, higher power density, higher coulombic efficiency and longer cycle life. Recently, in order to meet the requirements of portable and wearable electronics, supercapacitor development is moving towards flexible and stretchable solutions. This thesis presents the design, fabrication, performance testing and optimisation of flexible strip and fibre EDLCs.

In this research, a sandwich structured strip EDLC was designed and manufactured. Experimental design was utilised to optimise the operation parameters of the EDLC in order to improve its capacity for energy storage. The flexibility of the strip EDLCs was studied extensively by mechanical tests under static and dynamic loading conditions, and the correlation between the electrochemical performance of the EDLCs and the mechanical testing process was investigated. Novel coaxial fibre EDLCs have also been studied and developed in this study. Fibre supercapacitors showed a good flexibility and weavability. The activated carbon produced by ball-milling method with optimum specific capacitance was mixed with commercial ink to produce active material to optimise the electrochemical performance of fibre EDLCs.

The flexible EDLCs were applied into different appliances to demonstrate the stability of performance and the usability of EDLCs developed in this study. The electrical current and potential range can be altered by connecting multiple strip or fibre EDLCs in parallel or in series to meet the power and energy requirements. It has been proved that the flexible EDLCs developed have a great potential to be used as energy storage devices for smart electronics. This thesis makes original contributions to knowledge, including using an advanced test method to study the electrochemical performance of flexible supercapacitors under static and dynamic mechanical testing, investigation of the effect of key parameters in the manufacturing process on the performance of strip supercapacitors using experimental design method to optimise the supercapacitors' performance, and optimisation of the performance of fibre supercapacitors by improving the structure and using a new active material with higher specific capacitance.

# Acknowledgements

I would like to express my deepest appreciation to my supervisors Dr Yanmeng Xu and Professor David Harrison for their continuous encouragement, great support, invaluable guidance and understanding throughout the whole period of my PhD study in Brunel University London. I appreciated the opportunity to pursue my PhD in this flexible energy storage subject provided by Dr Yanmeng Xu and Professor David Harrison. Dr Yanmeng Xu is very kind and patient, he spent his time to discuss the problems occurred in experiments, data analysis and paper writing and gave me a lot of suggestions and support to overcome the difficulties during my PhD study. Professor David Harrison is very responsible and helpful, I respect his work. Without their support and help, the improvement could not be achieved. I would like to thank my supervisors for their guidance on writing scientific papers including this PhD thesis.

I also would like to thank Professor John Fyson for his support and help in my study. He is very kind and helpful. His professional suggestions and comments are very important to improve our experiment and scientific papers. I wish to thank my colleagues Mr Anan Tanwilaisiri and Mr Milad Areir. It's my pleasure to work with a group of brilliant and helpful people. I also appreciated the colleagues outside Brunel University London who worked with me together for the Project Powerweave.

I would like to thank my friends who have supported me especially: Ms Su Guo, Dr Miqing Li, Ms Leilei Zhang and Dr Feng Yan for their support and encourage, Dr Bo Jiang for his help with image analysis knowledge, Dr Thomas Maltby, Dr Xixi Dong, Mr Wei Guan and Mr Andrews Offei Nyanteh for their help.

I would like to express my warmest thanks to my parents, my husband, my sister, my brothers and parents in laws. My parents always support me and respect my choice; they give me love and support unconditionally. My husband always supports and encourages me, he is so kind, patient and lovely, and inspires me to pursue my dream. My sister and brothers always support me and share their experiences to me. My parents in laws are also supporting and caring me.

Finally, I would like to thank the department of Design, Brunel University London.

# Publication List

1. **Ruirong Zhang**, Yanmeng Xu, David Harrison, John Fyson and Darren Southee. Experimental Design to Optimise Electrical Performance of Strip Supercapacitors. International Journal of Electrochemical Science. 1 (2016) 675-684.
2. **Ruirong Zhang**, Yanmeng Xu, David Harrison, John Fyson and Darren Southee. A Study of the Electrochemical Performance of Strip Supercapacitors under Bending Conditions. International Journal of Electrochemical Science. (2016) In Press
3. **Ruirong Zhang**, Yanmeng Xu, David Harrison, John Fyson, Fulian Qiu, Darren Southee. Flexible strip supercapacitors for future energy storage. International Journal of Automation and Computing, 12 (2015) 43-49.
4. **Ruirong Zhang**, Yanmeng Xu, David Harrison, John Fyson, Darren Southee, Anan Tanwilaisiri. A study of the performance of the combination of energy storage fibres. IEEE Proceedings of the 21th International Conference on Automation & Computing, 2015.
5. **Ruirong Zhang**, Yanmeng Xu, David Harrison, John Fyson, Darren Southee, Anan Tanwilaisiri. Fabrication and characterisation of energy storage fibres. IEEE Proceedings of the 20th International Conference on Automation & Computing, (2014) 228-230.
6. **Ruirong Zhang**, Yanmeng Xu, David Harrison, John Fyson, Fulian Qiu, Darren Southee. A study of flexible supercapacitors for future energy storage. IEEE Proceedings of 19th International Conference on Automation and Computing (2013) 1-4.
7. **Ruirong Zhang**, Yanmeng Xu, David Harrison, John Fyson, Darren Southee, Anan Tanwilaisiri. Fabrication and characterization of smart fabric using energy storage fibres. Systems Science & Control Engineering, 3 (2015) 391-396.
8. Anan Tanwilaisiri, Yanmeng Xu, David Harrison, John Fyson, **Ruirong Zhang**. Techniques of 3D Printing and Ink-Jet Printing. International Conference on Intelligent Materials and Manufacturing Engineering, (2015) 37.

# Lists of Figures

## Lists of Tables

# Nomenclature

A list of symbols is given with a brief description and units used

| Symbol | Definition and Units |
|---|---|
| $A$ | Surface area of each electrode ($m^2$ $g^{-1}$) |
| $C$ | Capacitance (F) |
| $C_L$ | Specific capacitance per unit length (mF $cm^{-1}$) |
| $D$ | Distance between the two electrodes (mm) |
| $E$ | Energy (J) |
| $L$ | Length of the fibre supercapacitors (cm) |
| $P$ | Power (W) |
| $Q$ | Stored charge (C) |
| $Q_{total}$ | Supercapacitor's charge at maximum voltage (C) |
| $V$ | Voltage (V) |
| $\Delta V$ | Voltage of the discharge (V) |
| $\varepsilon_0$ | Dielectric constant of free space (F $m^{-1}$) |
| $\varepsilon_r$ | Dielectric constant |
| $\Delta I$ | Total current ($\lvert I_1 - I_2 \rvert$) difference on the CV curve (A) |

| | |
|---|---|
| I | Discharge current (A) |
| Cs | Specific capacitance of the electrode (F) |
| M | Average mass of activated carbon (g) |
| $X_i$ | Coded value |
| $x_i$ | Corresponding actual value |
| $x_i^0$ | Actual value at the centre point |
| $\Delta x_i$ | Step change of the actual values |

| **Abbreviation** | **Description** |
|---|---|
| AC/ACFs | Activated carbon/Activated carbon films |
| CC | Cotton cloth |
| CMC | Carboxymethyl cellulose |
| CNTs | Carbon nanotubes |
| CTR | Charge transfer resistance |
| CV | Cyclic voltammetry |
| EDS | Energy dispersive spectroscopy |
| EDLCs | Electrical double-layer capacitors |
| EIS | Electrochemical impedance spectroscopy |
| ESR | Equivalent series resistance |
| HECs | Hybrid electrochemical capacitors |

| | |
|---|---|
| GCD | Galvanostatic charge-discharge |
| GAS | Graphene aerogels |
| LED | Light-emitting diode |
| MF | Melamine-formaldehyde |
| MSC | Micro-supercapacitors |
| NEC | Nippon Electric Company |
| PANI | Polyaniline |
| PEDOT | Poly(3,4-ethylenedioxythiophene) |
| PEO-PMMA | Poly(ethylene oxide)-grafted poly(methyl)-methacrylate |
| PF | Phenol-furfural |
| PC | Propylene carbonate |
| PG | Porous graphene |
| PPy | Polypyrrole |
| PRI | Pinnacle Research Institute |
| PVA | Polyvinyl alcohol |
| PVDF | Poly(vinylidene fluoride) |
| P(VDF-HFP) | Poly (vinylidene fluoride-co-hexafluoropropylene) |
| RF | Resorcinol-formaldehyde |
| SWCNT | Single-walled carbon nanotube |
| SEM | Scanning electron microscopy |

| | |
|---|---|
| SOHIO | Standard Oil Company, Cleveland, Ohio |
| XRD | X-ray diffraction |

# Table of Contents

# Chapter 1. Introduction

## 1.1. Background

Most of the current energy supply is based on fossil fuels resources. However, their reserves are limited and will be depleted in a near future. Meanwhile, the environmental pollution caused by the consumption of fossil-fuels becomes worse with the consumption of fossil-fuels increasing. There is a high requirement to use energy effectively and to develop renewable and clean energy sources to enable sustainable development. The fast-growing market of portable electronics and electric vehicles stimulates the development of environmental friendly energy storage devices with high energy and power density, such as batteries and supercapacitors.

Supercapacitors, also named electrochemical capacitors and ultracapacitors, as energy storage devices with a high power capability, excellent reversibility (90–95% or higher), and a long cycle life (>$10^5$ cycles) have been studied over the past few decades [1][2]. Categorised by the working mechanism, supercapacitors can be generally classified into two types: (1) electrical double-layer capacitors (EDLCs), in which capacitance arises from the charge separation at the electrode/electrolyte interface, such as carbon based supercapacitors and (2) pseudocapacitors, in which capacitance arises from reversible faradic reactions occurring at the electrode surface, such as transition metal oxide based supercapacitors.

Figure 1.1 shows the Ragone plot of typical energy storage and conversion devices, in which, their specific energy and specific power are presented [1]. It is found that batteries and fuel cells have a low power density whereas conventional capacitors have a high power density (more than $10^6$ W/kg), with a low energy density. Supercapacitors also have a larger energy density than conventional capacitors. The reason is that conventional supercapacitors store charge on low surface area plates, but supercapacitors store charge in an electric double layer set up by ions at the interface between a high-surface-area carbon electrode and an electrolyte [1][3].

Compared to batteries, supercapacitors can deliver hundreds to many thousands of times more than the power of a similar sized battery [3]. In addition, the charge is stored in EDLCs by an electrostatic way which is very fast and highly reversible. The charge is stored in pseudocapacitors by highly reversible redox reactions in addition to the electric double-layer storage, and this gives supercapacitors a much longer cycle life than batteries. However, the charge is stored by redox reactions of the active masses in batteries which need longer time for charging/and discharging and also limit cycle life of batteries. In a word, supercapacitors occupy an important position in terms of the energy density as well as power density, and can fill in the gap between batteries and conventional capacitors as shown in Figure 1.1 [1].

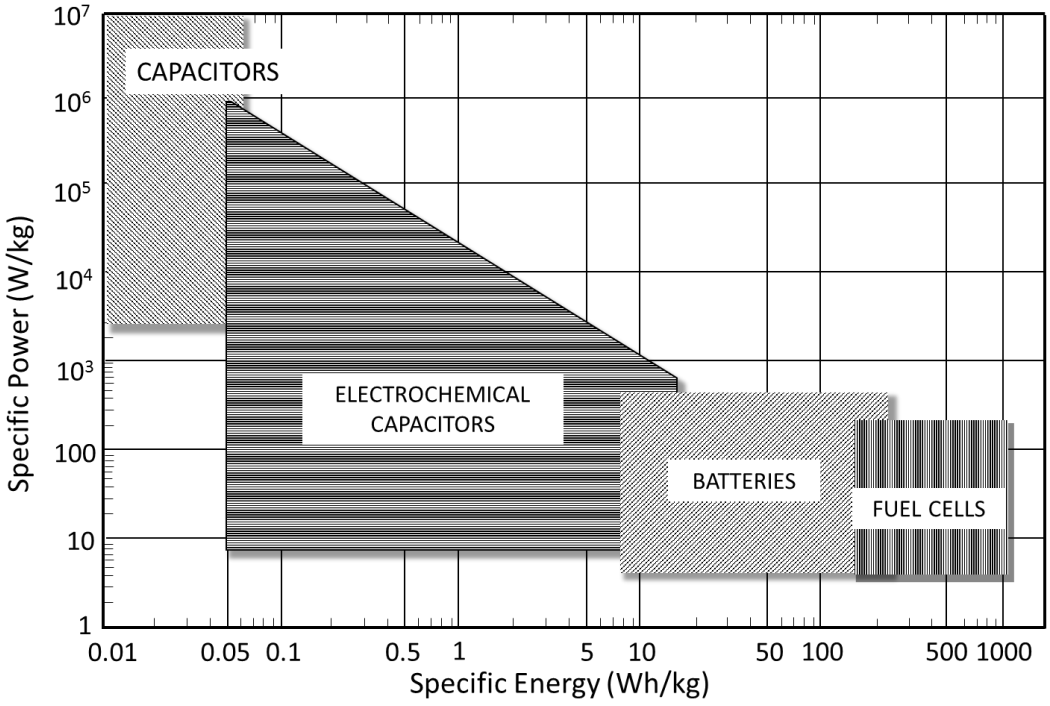


Figure 1.1 Ragone plot for various energy storage and conversion devices. The indicated areas are rough guide lines [1].

Based on typical properties, supercapacitors are widely used in the following ways: firstly, the largest proportion of commercial supercapacitors are used in consumer electronics, in which they mainly serve as backup sources for memories, system boards, clocks and microcomputers; secondly, supercapacitors are used as the main power source, such as

power source for toys, fail-safe positioning devices and starter applications; thirdly, supercapacitors are used as alternative power sources, such as an application for solar watch and solar lanterns, road marking lanterns and traffic warning signals. Supercapacitors are also used as a short time energy storage device in electric vehicles, hybrid electric vehicles, fuel cell vehicles and industrial equipment, such as emergency power supplies in hospitals or factories, airport buses, railway systems and for seaport rubber-tired gantry cranes [1][3].

## 1.2. Objective of this thesis work

Recently, in order to meet requires of portable and wearable electronics, supercapacitor development is moving towards flexible and stretchable solutions. However, many existing commercial supercapacitors are too rigid and heavy for the intended uses. It is a challenge to develop flexible supercapacitors which are compatible with flexible/wearable electronics [4][5]. That led to the research question: is it possible to develop flexible and weavable supercapacitors? This main research question can be divided into three questions: how to design flexible supercapacitors? how to manufacture flexible supercapacitors? how to characterise their flexibility and electrochemical performance?

This thesis work is aimed at the design and manufacture of environment friendly, low cost and flexible supercapacitors. Thin strip shaped and fibre shaped supercapacitors were fabricated, characterised and optimised. The major objectives of this thesis are as follows:

- To design the shape and structure of flexible supercapacitors following conventional working mechanism of supercapacitors.
- To manufacture flexible supercapacitors using low cost materials.
- To characterise the electrochemical performance and the flexibility of the supercapacitors manufactured.
- To study the electrochemical performance of flexible supercapacitors under mechanical testing conditions
- To investigate the effects of the main operation factors of the structure on the performance of flexible supercapacitors.

- To improve and optimise the electrochemical performance and the manufacture process of flexible supercapacitors.

## 1.3. Thesis structure

Beginning from an introduction of the research background of this thesis project in Chapter 1, Chapter 2 presents a literature review of previous studies of the working principle, electrode materials, types and applications of supercapacitors, as well as the development trends of the supercapacitors. The current progress on the flexible supercapacitors is also reviewed in Chapter 2. Chapter 3 describes the materials and reagents, as well as the experimental methods in this thesis work. Chapter 4 presents the design, fabrication and characterisation of strip supercapacitors. The electrochemical performance of this kind of strip supercapacitor was studied under bending, mechanical tensile stretching and pressure conditions. In Chapter 5, the effects of key practical factors including the binder content, the thickness of the active layer and the concentration of the electrolyte on the electrochemical performance of strip supercapacitors are shown. These results could be very important for flexible strip supercapacitor design, and optimisation of the performance. Chapter 6 presents the design, fabrication and characterisation of coaxial fibre supercapacitors. The structure of fibre supercapacitors and preparation methods are further improved in order to produce long stable fibre supercapacitors. The flexibility of this kind of fibre supercapacitor is also studied in Chapter 6. Chapter 7 discusses the effect of the ball-milling time on the specific capacitance of milled activated carbon. The optimum milled activated carbon is used as the active layer coating material to improve the electrochemical performance of the fibre supercapacitors. Finally, the main conclusions of the study and suggestions for future work are outlined in Chapter 8 and Chapter 9.

# Chapter 2. Literature Review

## 2.1. Historical background

Supercapacitors, also named electrochemical capacitors and ultracapacitors, have been studied over the past few decades [1]. They provide an energy storage technology with high power density, long cycling life and high reversibility. In 1853, the concept of the double-layer capacitance was first described by Hermann von Helmholtz. However, it was not until 1957, that the first patent on double-layer capacitance structure was granted to Becker at General Electric Corporation, in which porous carbon with high specific surface area was used as electrode material for an electrochemical capacitor for the first time [6]. In 1962, an energy storage device using porous carbon as an electrode material was patented by the Standard Oil Company, Cleveland, Ohio (SOHIO) and in this patent. It was acknowledged that "the double-layer at the interface behaves like a capacitor of relatively high specific capacity" [7]. SOHIO also patented another disc-shaped capacitor with a carbon paste soaked in an electrolyte in 1970 [8]. In 1971, this double-layer capacitor technology was licensed to the Nippon Electric Company (NEC) by SOHIO, and NEC successfully manufactured the first commercially double-layer capacitor with the name of "supercapacitor" [9]. From that time on, the industrialization period of the supercapacitor had started with the development of key technologies. These included improving the electrode materials, electrolyte and the manufacturing process. A kind of supercapacitor named "Gold capacitor", used for memory backup applications, was developed by Panasonic in 1978. The Pinnacle Research Institute (PRI) developed the first high power double-layer capacitors named "PRI Ultracapacitors" by incorporating metal-oxide in the electrode in 1982. In late 70's and 80's, Conway et. al. made a great contribution to the supercapacitor research, using $RuO_2$ as the electrode material which showed a high specific capacitance and a low internal resistance [10][11]. The US Department of Energy developed a study in hybrid electric vehicles, in which, the Ultracapacitor Development Program was developed by Maxwell Laboratories in 1992.

Recently, supercapacitors are manufactured by a number of companies around the world, and widely used. In Japan and America, Panasonic, NEC, Epcos, ELNA, Cooper and

AVX have developed a variety of electric double-layer capacitor (EDLC) components. In addition, Evans and Maxwell produce integrated modules with voltage balancing circuitry. ESMA in Russia offers different kinds of EDLC modules for applications in power quality improvement and electric vehicles. Currently, commercial supercapacitors are widely used as power sources for communication devices, digital cameras, mobile phones, electric hybrid vehicles, electric tools, pulse laser techniques, uninterruptible power supplies for computers, standby power for random access memory devices and storage of the energy generated by solar cells [12][13].

## 2.2. Principle of conventional capacitors and supercapacitors

As is known, the supercapacitor has a greater capacity than conventional capacitor. The description of the working mechanisms for the conventional capacitors and supercapacitors are as follows.

### 2.2.1. Principle of conventional capacitors

As shown in Figure 2.1, the conventional capacitor has two conducting electrodes and in order to prevent electrical contact between them, an insulating dielectric material called a separator is interposed. Opposite charges accumulate on the surface of each electrode when a voltage is applied between the two electrodes. The charges can be kept separate by the dielectric. That is the way in which a capacitor stores energy [14].

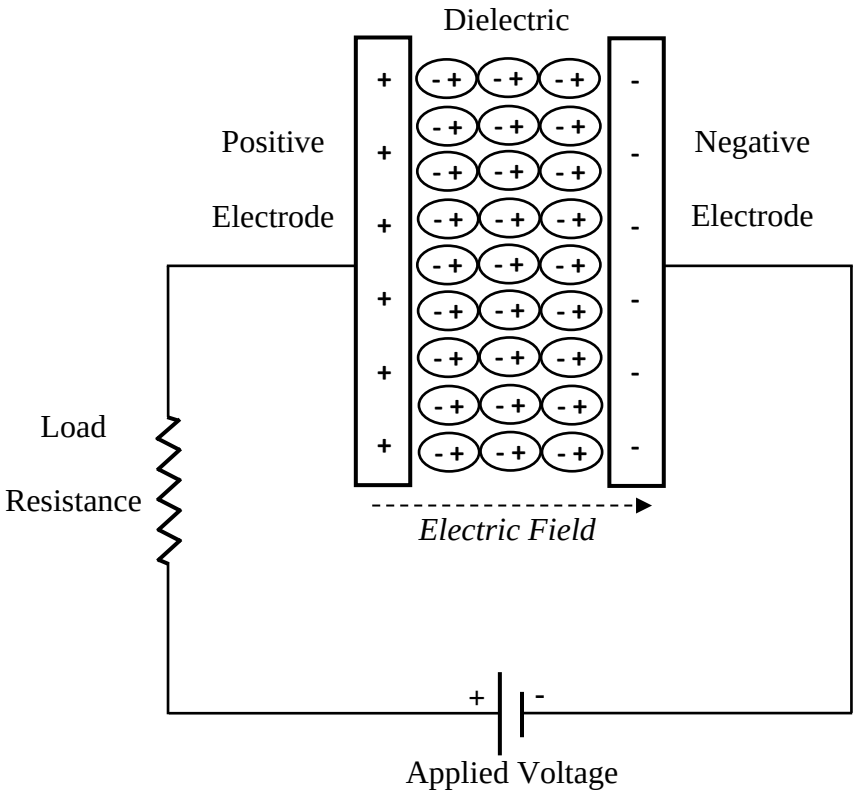


Figure 2.1 Schematic of a conventional capacitor.

Capacitance *C* (F) is defined as the ratio of stored charge *Q* (C) to the applied voltage *V (V)*:

$$C = \frac{Q}{V} \tag{2.1}$$

For a conventional capacitor, *C* can be calculated by equation:

$$C = \varepsilon_0 \varepsilon_r \frac{A}{D} \tag{2.2}$$

Where *A* is the surface area of each electrode ($m^2$ $g^{-1}$), *D* is the distance between the two electrodes (m), $\varepsilon_0$ is the dielectric constant of free space (F $m^{-1}$), and $\varepsilon_r$ is the dielectric constant of the insulating material between the two electrodes.

Energy density and power density are two primary characteristics of a capacitor. The energy *E* of a capacitor is directly calculated as follows:

$$E = \frac{1}{2}CV^2 \quad (2.3)$$

The power *P* is the energy expended per unit time. As shown in Figure 2.1, capacitors are generally described as a circuit in series with an external resistance *R* in order to determine *P* for a capacitor.

The internal resistance, named as the equivalent series resistance (ESR), is usually measured as an aggregate. So the internal components of the capacitor, such as electrodes, current collectors and dielectric materials, all contribute to the ESR. The discharge current is determined by these resistances. When matched impedance ($R = ESR$) is measured, the maximum power $P_{max}$ for a capacitor [2][15][16] can be calculated by:

$$P_{max} = \frac{V^2}{4 \times ESR} \quad (2.4)$$

This equation shows how the ESR can affect the maximum power of a capacitor. For a capacitor, the energy or power density can be calculated as a quantity per unit mass or per unit volume. Conventional capacitors have relatively high power densities, but relatively low energy densities when compared to electrochemical batteries and to fuel cells as shown in Figure 1.1. In other words, a battery can store more energy than a capacitor, but it cannot deliver it very quickly, so its power density is low. Capacitors, on the other hand, store relatively less energy per unit mass or volume, but electrical energy stored can be discharged rapidly to produce a large power, so their power density is usually high.

### 2.2.2. Principle of supercapacitors

Generally, the basic principle for conventional capacitors is also true for supercapacitors. As shown in Figure 2.1 and Figure 2.2, schematics of supercapacitors and conventional capacitors are similar. Supercapacitors consist of two conducting electrodes separated by an insulating dielectric material. The difference between them is that electrodes for supercapacitors normally have much higher surface areas than those for conventional capacitors, and an electrolyte solution in a separator between them. Therefore, the capacitance and energy calculated from Equations (2.2) and (2.3) increases dramatically over that of the conventional capacitors because of the much higher surface area A and smaller distance *D* between two electrodes.

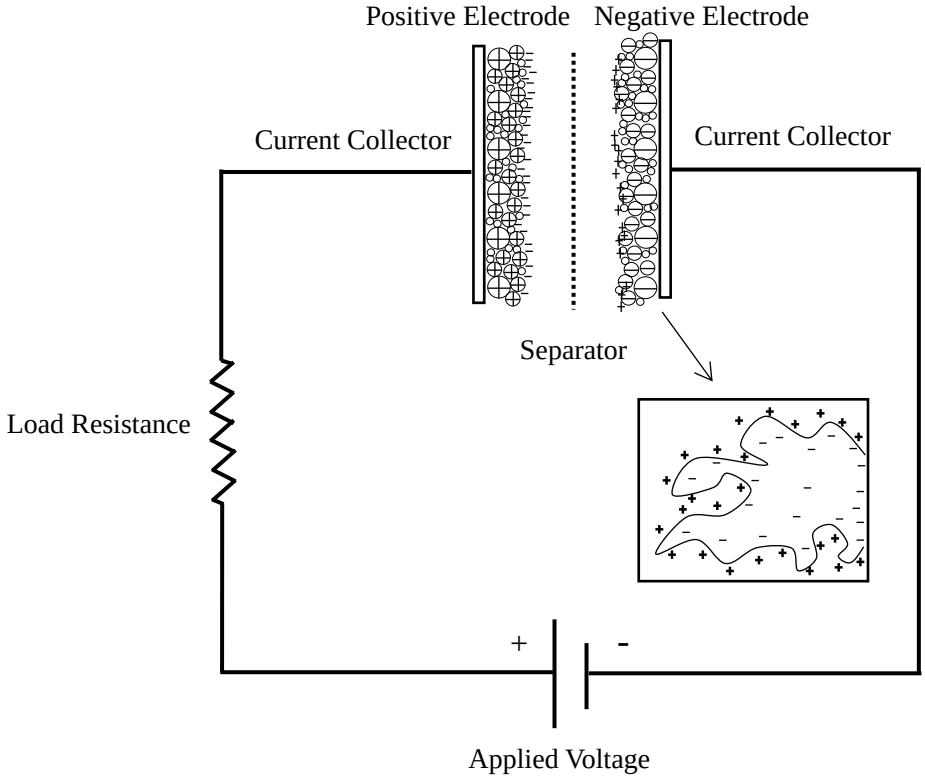


Figure 2.2 Schematic of an electrochemical double-layer capacitor.

## 2.3. Types of supercapacitors

Based on the working mechanism, supercapacitors could be divided into three main classes: electrochemical double-layer capacitors (EDLCs), pseudocapacitors and hybrid capacitors (See Figure 2.3). All the supercapacitors can be characterised by unique mechanisms for storing charge, which are electrostatic storage, reversible Faradaic redox and a combination of the two. For pseudocapacitors, there are Faradaic processes which consist of oxidation-reduction reactions [17][18][19][20][21]. The energy is stored in pseudocapacitors by a chemical mechanism, such as in transition metal oxide based supercapacitors. In contrast, a non-Faradaic mechanism occurs in EDLCs, in which, the charges are kept separately at the electrode/electrolyte interface by physical processes which do not include the making or breaking process of chemical bonds. Examples of these are carbon based supercapacitors [17][18][22][23][24][25][26] [27]. The third type is the hybrid capacitor, the energy storage process is a combination of the Faradaic and

non-Faradic, such as carbon and transition metal oxide materials composite supercapacitors.

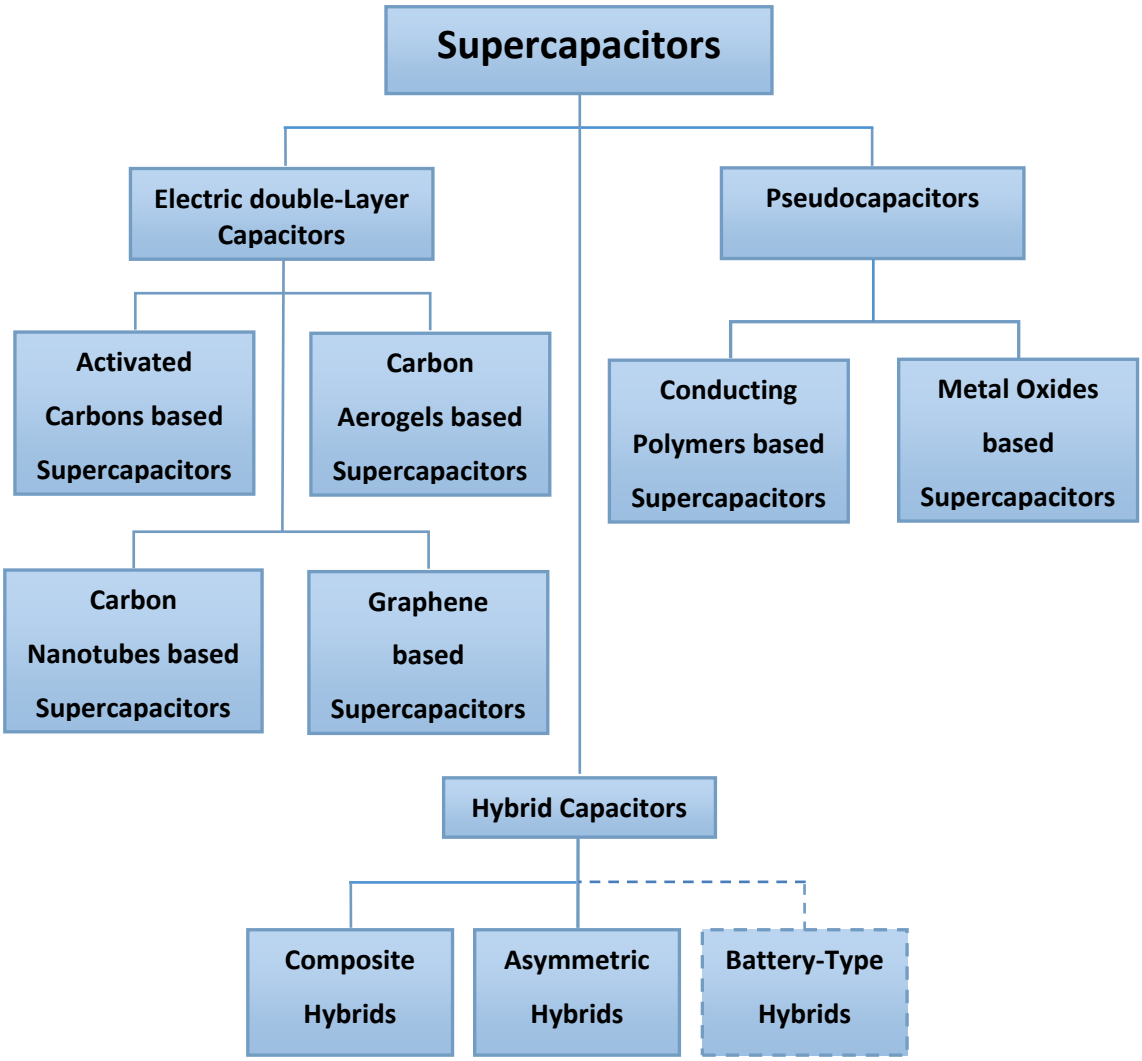


Figure 2.3 Types of supercapacitors.

### 2.3.1. Electrical double-layer capacitors

A schematic of typical charged EDLCs is illustrated in Figure 2.4. EDLCs consist of two electrodes, an electrolyte, and a separator. For EDLCs, charging and discharging storage are highly reversible. This results in very high cycling stabilities.

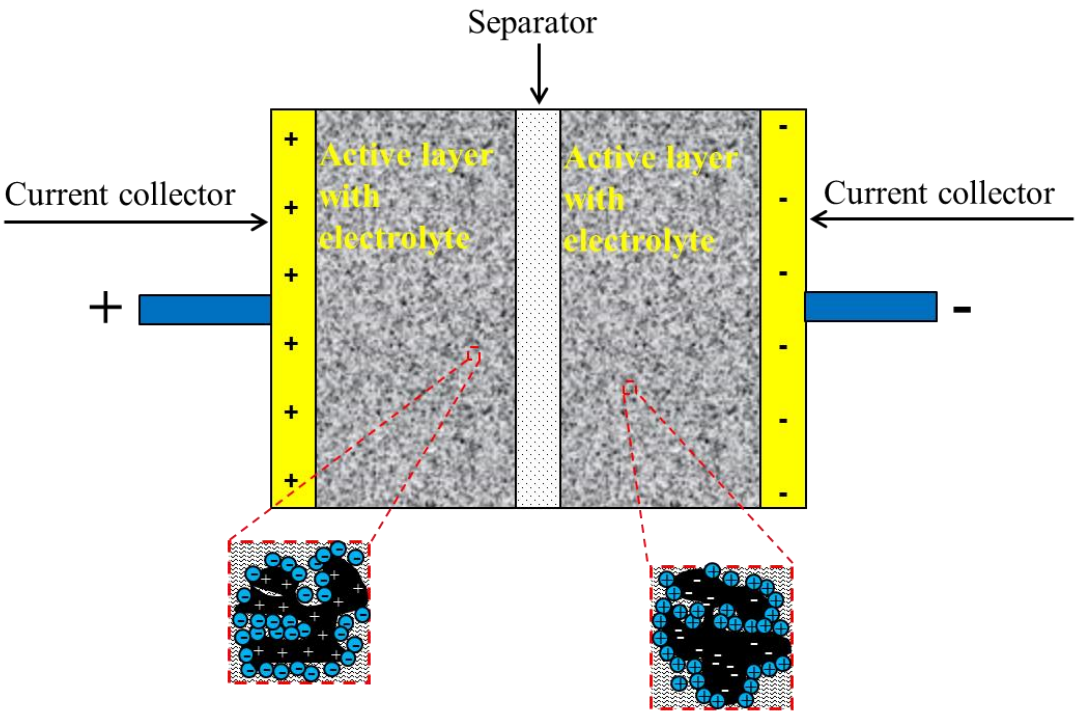


Figure 2.4 Schematic diagram of a typical charged EDLC.

EDLCs store energy by using an electrochemical double-layer of charge. Charges on the electrode surfaces accumulate when a voltage, which is less than that to cause a chemical reaction, is applied. Ions of the electrolyte solution diffuse across the separator and enter the pores of the electrode. Opposite charges accumulate at the interface between the electrode and the electrolyte because of the applied potential. Nevertheless, the recombination of the ions is prevented by careful engineering of the electrodes. Therefore, the two electrodes produce a double-layer of charge.

Porous carbon with high surface area, low cost and high stability has been utilized as electrode material ever since development of the electrochemical capacitor began. Recently, different kinds of carbon materials are widely used to store charge in EDLC electrodes, such as activated carbons (ACs), carbon aerogels, carbon nanotubes and graphene.

### 2.3.1.1. Activated carbon based supercapacitors

Among the different carbon materials, ACs are especially attractive as electrodes for capacitors due to their high specific surface area, good adsorption property and low cost. AC is derived from carbon-rich precursors by carbonization and activation in an inert atmosphere with subsequent selective oxidation in $CO_2$, water vapour or KOH to increase the specific surface area and pore volume (Figure 2.5) [28][29]. This surface area is mainly contributed to a complex interconnected network of internal pores. The pores are classified into three classes: micropores ($d < 2$ nm), mesopores ($2 \text{ nm} < d < 50$ nm) and macropores ($d > 50$ nm) [30]. The surface area of the porous carbon material can be measured by an important analytical technique named Brunaver, Emmett and Teller (BET) method, in which the specific surface area of a material is determined by physical adsorption of a gas on the surface of the solid and by calculating the amount of adsorbate gas corresponding to a monomolecular layer on the surface. Theoretically, the higher the specific surface area of an AC, the higher the specific capacitance should be expected because the carbon surface provides a large interface for the formation of the double layer capacitance. For example, Lota and his colleagues [31] developed a simple method with KOH at 850 ℃ to re-activate a commercial AC. The effective areas of the re-activated materials were increased dramatically compared with commercial ACs. As such, the corresponding specific capacitance of the re-activated carbon increased to three times higher than that of the raw AC.

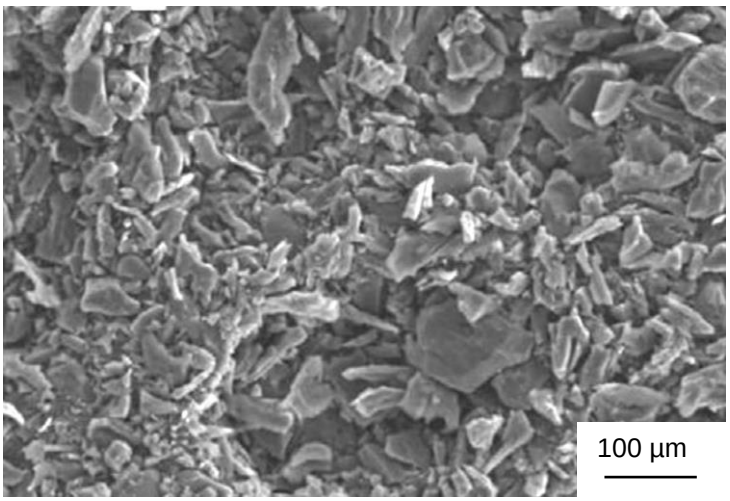


Figure 2.5 SEM of AC synthesized by heat treatment with KOH activation [29].

Practically, the situation is more complicated, there was no linear relationship between the specific surface area and the capacitance [32][33][34]. Besides the specific surface area, the pore sizes distribution is also very important. It affects the electrolyte ions diffusion. Gryglewicz et al. [35] studied effect of pore size distribution of coal-based AC on double layer capacitance. As shown in Figure 2.6, the ACs with a BET surface area up to 1000 $m^2$ $g^{-1}$ and the mesopore content of 46.3-86.9%, the higher specific capacitance was obtained when the BET surface area increased. For the ACs with a surface area over 1000 $m^2g^{-1}$, no linear relationship was found. Because highly developed surface area of ACs was along with a lower mesopore fraction. The double layer capacitance depends not only on the surface area but also on the pore size distribution. It was found that ACs with high surface area and the mesopore between 20% and 50% were more appropriate for active electrode material in the EDLCs. Because of the large sulfate ion size, larger micropores and small mesopores (2-5 nm) are most suitable with this acidic electrolyte.

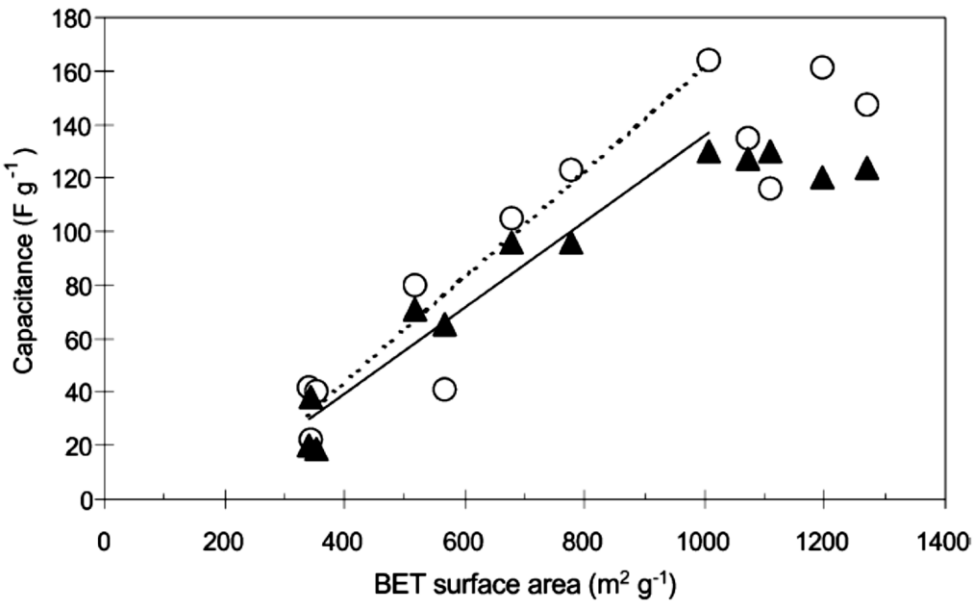


Figure 2.6 Specific capacitance in acidic and alkaline electrolytes as a function of BET surface area for AC ((○) 1 mol/L $H_2SO_4$; (▲) 6 mol/L KOH) [35].

Apart from the specific surface area and pore size distribution, the surface functionality would also influence the performance of EDLCs. Teng et al. proved the capacitance was enhanced when the surface was functionalized in aqueous acid [36][37]. Qu [26] studied

the influences of AC structure and surface groups on the performance of a supercapacitor. It was found that the higher percentage of edge orientation favoured the stronger bonding of surface functional groups. These surface functional groups would influence the wettability of the electrodes and contribute to the capacitance of supercapacitors.

In general, ACs which showed good performance in supercapacitors should have these characteristics: (a) a high specific surface area, (b) a microtexture well adapted to allow good electrolyte accessibility into the inner surface of the electrode, (c) a low resistivity, and (d) an appropriate surface functionality [32][35].

#### 2.3.1.2. Carbon aerogels and xerogel based supercapacitors

Carbon aerogel, because of its versatile properties such as high surface area (400-1000 $m^2$ $g^{-1}$), fine pore size, high porosity and outstanding electrical conductivity, is considered as a promising material for supercapacitors [38][39][40][41]. The excellent properties of carbon aerogels are due to the three-dimensional mesoporous network of carbon nanoparticles. Generally, carbon aerogels are produced by pyrolysis of organic aerogels based on resorcinol and formaldehyde (RF) via a sol-gel process [42]. The microtexture of aerogels, especially the particle size and the pore distribution can be determined by different synthesis parameters, such as selection of the reaction conditions, activation procedure, the pyrolysis temperature and the presence of selected dopants [42][43][44].

Mayer et al. [45] developed a carbon aerogel by a carbonisation of RF resin via a sol-gel route. It was the first time to use the carbon aerogel as electrode material for supercapacitors. This carbon aerogel showed high surface areas per unit volume (100-700 $m^2$ $cm^{-3}$, as measured by BET analysis) with bulk densities of 0.3 to 1.0 g $cm^{-3}$. The typical morphology permitted energy stored to be released rapidly. This resulted in a high power density. The porosity and surface area of these carbon aerogel can be controlled by the sol-gel process. Lin et al. [46] further developed the carbon aerogel sol-gel synthesis procedure to produce high surface area carbon xerogels with a controlled pore structure. They studied the effect of synthesis pH on the surface area, pore size distribution, nanostructure and the pore volume of carbon xerogels, and found that carbon xerogels prepared at a lower pH had a higher surface area and pore volume, as well as a larger pore size distribution. The reason is that the acid-catalysed condensation reaction rate could be

increased at lower pH. Carbon aerogel derived from a modified RF method without supercritical drying step was activated under $CO_2$ flow and further modified with a surfactant by Fang et al. [47]. It was found that the specific surface area of carbon aerogel increased dramatically after activation, therefore, specific capacitance increased considerably. The internal resistance of the capacitors decreased and the specific capacitance increased. Chang et al. [48] further studied the effect of the $CO_2$ activation time on the surface and porous structure of carbon aerogel. As shown in Figure 2.7, a three-dimensional interconnected network structure was maintained after activation, and the surface of carbon skeleton was etched dramatically by $CO_2$. Large amount of micropores and mesopores were into carbon aerogels by $CO_2$ activation, which resulted in a specific surface area increase. Higher specific surface area could be achieved with longer activation time. Therefore, the corresponding specific capacitance increased significally.

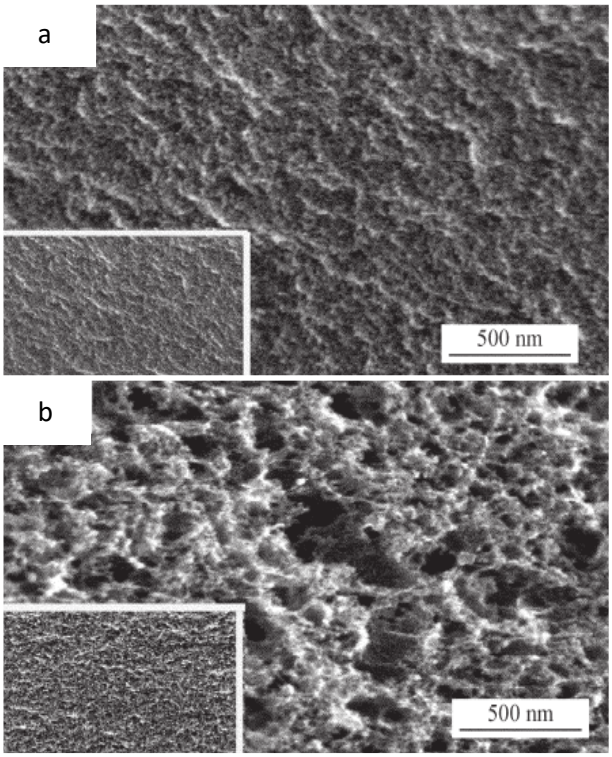


Figure 2.7 SEM of carbon aerogel (a) and activated carbon aerogel with the $CO_2$ activation for 10 h (b) [48].

Microporous carbon xerogels were synthesised by Zubizarreta et al. in reference [49]. They further studied the effect of the initial pH, the drying method and using methanol as a solvent in the synthesis process on the textural properties of carbon gel. It was found that an initial pH of 7 and multimode microwave drying method was an easy way to produce homogeneous microporous carbon gels.

### 2.3.1.3. Carbon nanotube based supercapacitors

Carbon nanotubes (CNTs) have been used as an EDLC electrode material because of their unique properties, such as high electric conductivity, large pore size, chemical stability, as well as a reasonable specific surface area. There are two main types of carbon nanotubes: (1) single-walled nanotubes (SWNTs) which consist of a single graphite sheet seamlessly wrapped into a cylindrical tube (Figure 2.8a) and multiwalled nanotubes (MWNTs) which comprise an array of such nanotubes that are concentrically nested like rings of a tree trunk (Figure 2.8b) [50]. SWNTs and MWNTs are usually produced by carbon-arc discharge, laser ablation of carbon, or chemical vapour deposition [51].

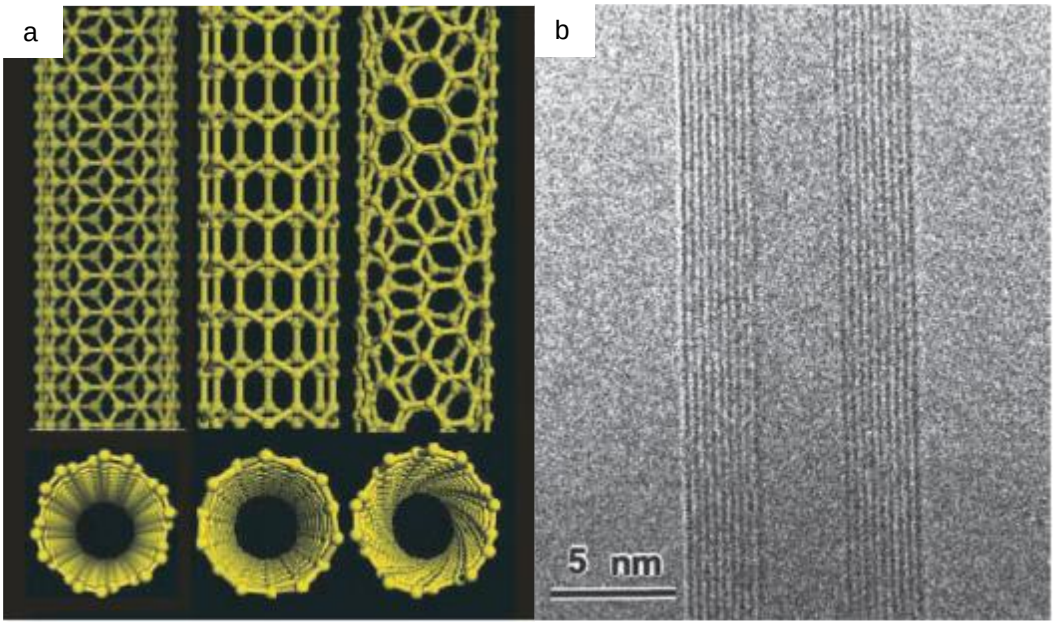


Figure 2.8 (a) Schematic illustrations of the three typical structures of SWNTs; (b) Transmission electron microscope (TEM) image of a MWNT containing a concentrically nested array of nine SWNTs [50].

Normally, CNTs when used as electrode material have an open and accessible network of mesopores. The mesopores are interconnected so that almost all the available surface area is used, resulting in a continuous charge distribution after charging. Also, the electrolyte ions can get access into the mesoporous network more easily, which results in a lower ESR of carbon nanotube electrodes. In order to further reduce the ESR, some new fabrication techniques have been used for the carbon nanotube electrodes preparation process. For instance, carbon nanotubes can be grown directly onto the current collectors, or subjected to heat-treatment. Chen et al. [52] produced carbon nanotube electrodes by growing carbon nanotubes directly onto graphite foil. This method simplified the electrode fabrication process, and further minimized the contact resistance. The specific capacitance maximum recorded was 115.7 F/g in 1.0 M $H_2SO_4$ when the potential scan rate is 100 mV/s.

Generally, the specific surface area of CNTs is lower than that of AC used as electrode materials. Researchers have developed some strategies to enhance the surface area to improve the capacitance of CNTs. In reference [53], in order to improve surface area, a series of the carbon nanotubes were activated by KOH, then the effects of CNTs KOH-activation on the electrochemical performance of EDLCs were studied. The results showed that the capacitance of CNTs was improved after KOH activation, and the specific capacitance of the activated CNTs was proportional to their specific surface area because the pores were large enough for ion transfer. However, the rate performance of the activated CNTs was less than raw CNTs. Therefore, the KOH activation still needs optimizing to improve both the capacitance and rate performance.

Although some good progresses were made on the CNTs based supercapacitors, such as the power capabilities could be above 8 kW $kg^{-1}$, their specific energies were generally lower compared with the values achieved from many conventional high specific surface area carbons. In addition, the high cost also limits their utilization in the energy storage device [54].

#### 2.3.1.4. Graphene or graphene oxide based supercapacitors

Graphene is an allotrope of carbon with the form of a two-dimensional and atomic-scale hexagonal lattice. It is the basic construction unit of all the graphitic carbons, such as

fullerenes, CNTs and graphite [55]. Since graphene was discovered in 2004, it has received rapidly growing attention. Because of its unique structure, graphene has some remarkable properties, such as a high surface area, high electrical conductivity, great flexibility and excellent mechanical properties. These unique properties make graphene a good material for energy storage in supercapacitors [56][57]. Graphene sheets could be synthesised by different methods, such as mechanical cleavage of graphite [58] chemical exfoliation of graphite [59], unzipping carbon nanotubes [60], epitaxial growth on SiC surface [61] and chemical vapour deposition [62]. Among these synthesis methods, mechanical exfoliation could produce highest quality graphene, and chemical method could improve the productivity of the graphene. Figure 2.9 illustrates schematically the chemical method to synthesise graphene [59]. Firstly, graphite oxide was made from graphite using the Hummers method [63] or the modified Hummers method [64]. Graphene oxide could be produced by exfoliation of graphite oxide using simple sonication [65]. Then the graphene was obtained via chemical reduction of graphene oxide using a reducing agent. Based on the above chemical method, Gao et al. [66] further developed a two-step reduction process to produce graphene. Graphite oxide obtained by oxidation of graphite powder according the modified Hummers method, was deoxygenated with sodium borohydride ($NaBH_4$) and dehydrated with concentrated sulfuric acid. This two-step reduction strategy yielded nearly pure graphene which was highly conductive and has very few functional groups.

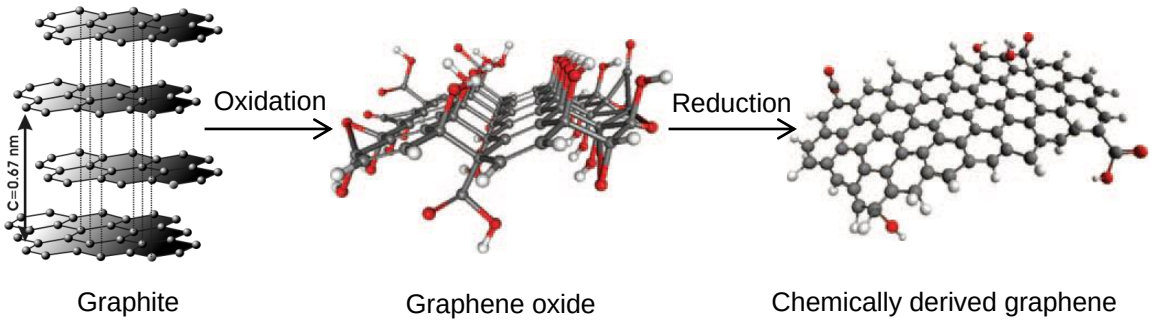


Figure 2.9 Schematic of the synthesis of chemically derived graphene [59].

In reference [67], graphenes were made by three different methods: exfoliation of graphitic oxide, heating nanodiamond and decomposition of camphor. The results showed

samples prepared by the first two methods exhibited high specific capacitance in $H_2SO_4$ electrolyte. The value could reach 117 F/g, which was comparable to that obtained using ACs as electrode materials in an aqueous electrolyte. Stoller et al. [68] produced supercapacitors using a chemically modified graphene. The specific capacitances were 135 F/g in aqueous electrolyte and 99 F/g in organic electrolyte. In addition, this material also showed consistently good performance at a wide range of scan rates because of the high electrical conductivity. Although there is continuous reporting of the study of graphene for energy storage, real applications have yet to be realized. The main reason is that it is still difficult to produce high-quality graphene by a reliable and scalable approach [56].

Graphene oxide is an intermediate in the chemical synthesis method of oxidation-exfoliation-reduction of graphite. As a single sheet of graphite oxide, graphene oxide has some oxygen functional groups on its basal planes and edges [69], which are beneficial to additional pseudocapacitance in supercapacitance. Although the surface area of graphene oxide is less than that of graphene, graphene oxide exhibited a higher capacitance with the value of up to 189 F $g^{-1}$ probably because of oxygen-containing functional groups on the surface. Compared to graphene, graphene oxide also showed a good rate of charge loss and cycle durability [70]. Because of the good performance and low cost, graphene oxide is considered a better choice than graphene as the electrode material in supercapacitors [70].

### 2.3.2. Pseudocapacitors

EDLCs store charge electrostatically, while pseudocapacitors store charge by the reversible redox reactions at the surface of active materials. Metal oxides and conducting polymers have been mainly used as electrode materials to store charges in pseudocapacitors [71][72]. A higher specific capacitance and energy density can be achieved in pseudocapacitors due to these Faradaic processes in redox-active materials compared with EDLCs.

#### 2.3.2.1. Metal oxide based supercapacitors

Metal oxides, such as $RuO_2$, $TiO_2$, CuO and $MnO_2$, have been used as electrode materials for pseudocapacitors due to their high conductivity [2][1][73][74]. As an electrode

material, ruthenium oxide ($RuO_2$) has been widely studied because of remarkable high specific capacitance, good electrical conductivity and high thermal stability. In the $RuO_2$ based supercapacitors, there are a series of redox reactions during the charge/discharge process. The oxidation states can change among $Ru^{4+,}$ $Ru^{3+}$ and $Ru^{2+}$ during the process, as shown in the following results in the pseudocapacitance which mainly contributes to capacitance [75]:

$$RuO_2 + xH^+ + xe^- \leftrightarrow Ru_{2-x}(OH)_x$$

In which, $0 \leq x \leq 2$. It has been reported that the specific capacitance is more than 700 F/g [76][77]. Hu et al. [78] developed a kind of supercapacitor using a nanotubular arrayed architecture of hydrous $RuO_2$ as electrode material, which showed an ultrahigh specific capacitance of 1300 F/g. It was found that in the hydrous form, the capacitance of $RuO_2$ exceeded that of carbon-based and conducting polymer materials. Furthermore, the ESR of hydrous ruthenium oxide was lower than that of other electrode materials. However, Ru-based supercapacitors are expensive which limits their application. Less expensive metal oxides have been studied using electrode materials, such as $MnO_2$ [79], $SnO_2$ [80], $V_2O_5$ [81] and $Fe_3O_4$ [82]. Among them, manganese oxide has been considered as a strong candidate [83] because of its nontoxicity, low cost and high abundance of raw materials [84]. Lee and his co-workers [85] initially reported that supercapacitors using amorphous $MnO_2{\cdot}nH_2O$ as electrodes materials in a mild 2 M KCl aqueous electrolyte exhibited an ideal specific capacitance of 200 F/g in 1999. Three years later, Hong and colleagues [86] developed a supercapacitor which consisted of amorphous manganese oxide as a cathode and AC as an anode. The supercapacitor showed ideal capacitor behaviour in neutral KCl aqueous electrolyte with an extended working window of 2 V, twice that of symmetric aqueous supercapacitors. Devaraj et al. synthesized nanometre scale particles of $MnO_2$ by a microemulsion method [87]. The specific capacitance of the supercapacitor using $MnO_2$ nanoparticles as the electrode material was about 297 F/g, which was greater than that of the normal sized $MnO_2$ particles. His following work [88] further studied the effect of the particle size and pore size on the performance. This provided a method to improve the electrochemical performance of $MnO_2$ particle by controlling the particle size and porous structure.

### 2.3.2.2. Conducting polymer based supercapacitors

Another common electrode material is a conducting polymer which has a relatively high capacitance, high conductivity and a relatively low ESR compared to carbon-based electrode materials, plus the cost is relatively cheaper than metal oxides. The conductivity of conducting polymers is rendered by a conjugated bond system along the polymer backbone [89].

As shown in Figure 2.10, the energy storage mechanism of conducting-polymer-based supercapacitors is different from that of the EDLCs. In general, the EDLCs store energy by an electrostatic method. The fast sorption and desorption of the ions on the inter surface between the porous carbon materials and electrolyte result in high power capabilities, but a low specific energy [90]. Conducting polymers store charge by a redox reaction and thereby can increase the energy stored and reduce self-discharge. However, the power capabilities of these materials are relatively low because of the slow diffusion of ions within the electrode. Particularly, the conducting polymers can be *p*-doped with anions during oxidation and n-doped with cations when being reduced. These two charging processes can be demonstrated by the simplified equations as follows:

$$Cp \rightarrow Cp^{n+}(A^{-})_n + ne^{-} \qquad \text{(p-doping)}$$

$$Cp + ne^{-} \rightarrow (C^{+})_n Cp^{n-} \qquad \text{(n-doping)}$$

In the discharging processes, the reverse reactions will occur following the reverse of the above equations.

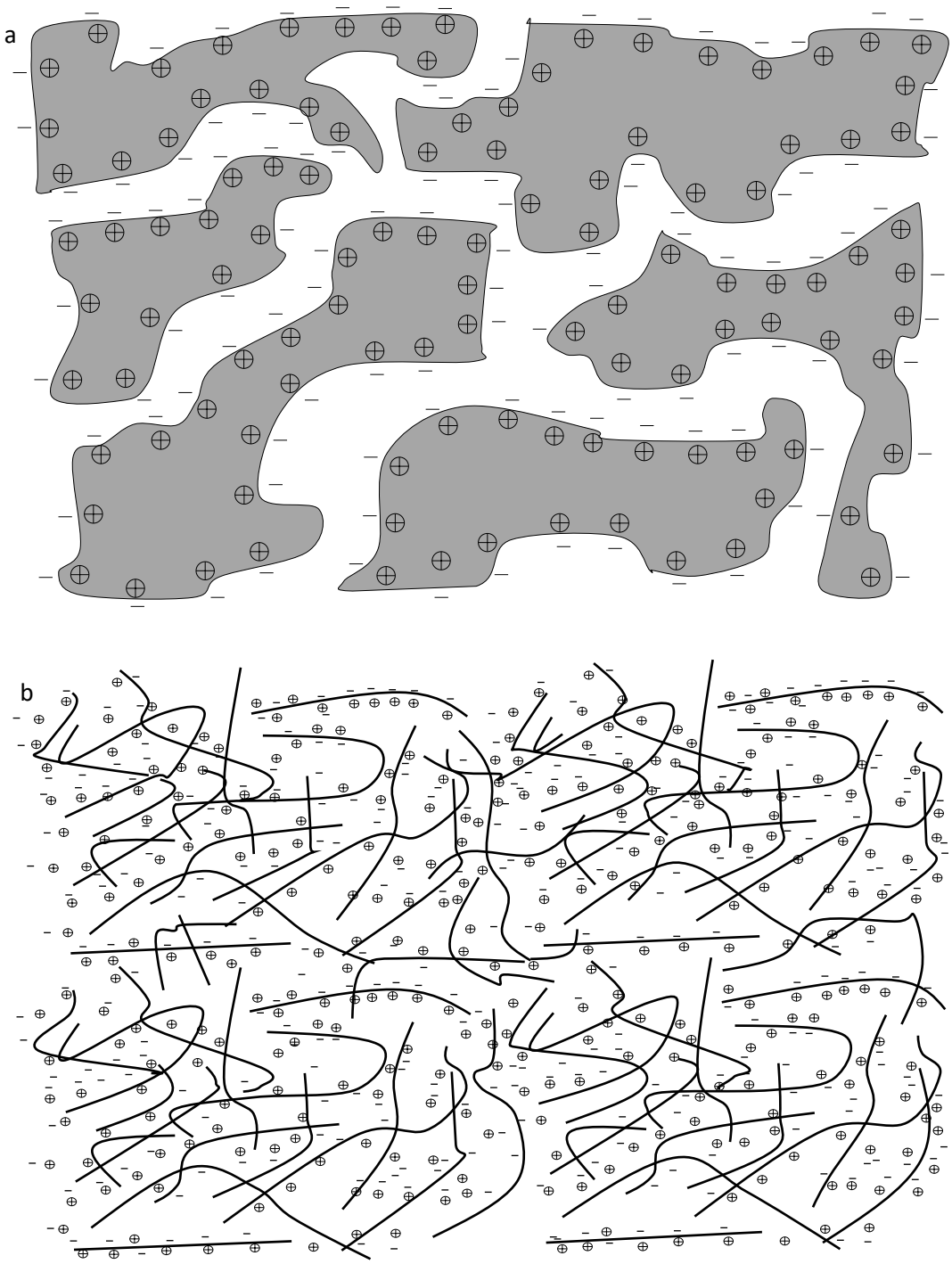


Figure 2.10 Comparison of charging of (a) double-layer capacitor (carbon) and (b) pseudo-capacitor (conducting polymer) [89].

The common conducting polymers in supercapacitor applications are polyaniline (PANI), polypyrrole (PPy), poly(3,4-ethylenedioxythiophene) (PEDOT), and their corresponding

derivatives [91][92]. Take polyaniline for an example, it can have a high doping level and high electroactivity and show a high specific capacitance of 400-500 F/g in an acidic medium [93]. Polyaniline requires a proton to be exchanged during charge or discharge; therefore an acidic solution or a protic ionic liquid is used in the pseudocapacitors using polyaniline materials.

### 2.3.3. Hybrid supercapacitors

Hybrid electrochemical capacitors which consist of a double-layer carbon material and a pseudocapacitance material have attracted significant attentions [18]. The capacitance of hybrid supercapacitors consists of double layer capacitance stored by porous carbon materials and the pseudocapacitance stored by the metal oxide or conducting polymer [14]. Hybrid supercapacitors are designed to combine the advantage of the EDLCs and the pseudocapacitors meanwhile overcoming most of their disadvantages.

Hybrid supercapacitors are classified into three different types by electrode configuration: asymmetric hybrids, composite hybrids and battery-type hybrids. Asymmetric hybrids consist of an EDLC electrode and pseudocapacitor electrode [94][95][96]. For example in 2001, Arbizzani and co-workers [94] developed a new hybrid supercapacitor using a p-doped polymer as the positive electrode and AC as the negative electrode. This hybrid supercapacitor showed good specific power and significantly higher specific energy by utilizing both faradaic and non-faradaic processes to store energy. Asymmetric hybrid supercapacitors have a better cycling stability than comparable pseudocapacitors. They can achieve higher energy and power densities than comparable EDLCs.

Composite hybrid supercapacitors are different from the asymmetric hybrids and use the composite materials to integrate carbon materials with either metal oxides or conducting polymer materials as electrode materials [97]. Porous carbon materials can provide a high surface area backbone to enhance the contact between the metal oxides or conducting polymer materials and the electrolyte. The metal oxides or conducting polymer materials can further increase the capacitance by faradaic reactions.

The third type is battery-type hybrids which have two different electrodes: one is a supercapacitor electrode, the other one is battery electrode [98][99][100]. As shown in Figure 1.1, the batteries showed higher energy densities than supercapacitors, while the

power densities of supercapacitors were higher than those of batteries. The battery-type hybrids have a big potential to fill the gap between the normal supercapacitors and batteries if they can combine the higher energy density of batteries and specific power, short charge time, cycle life as well as reversibility of supercapacitors.

### 2.3.4. Comparison of the performance of different materials based supercapacitors

Figure 2.11 shows the capacitive performance for carbon and pseudocapacitor materials [101]. It was found that metal oxides or conducting polymers showed higher specific capacitances compared with carbon materials. Because the metal oxides or conducting polymers store electrochemical charge using highly reversible surface redox reactions, which is quite different from the electrostatic energy storage process in carbon materials, these fast and reversible surface processes have dramatically increased the charge storage performance. However, pseudocapacitors usually lack stability during cycling because of unwanted redox reactions in charge/discharge process. For example, amorphous hydrous $RuO_2$ prepared by sol-gel methods exhibited a high specific capacitance of 720 F $g^{-1}$ [102]. The high capacitance was obtained because hydrous surface layers enable facile transport of electrons and protons. It was found that the capacitance decreased dramatically at higher rates due to proton depletion and over-saturation in the electrolyte during the charge-discharge cycling process [103]. In order to improve the rate performance, many studies have attempted to combine small particles of hydrous $RuO_2$ with carbon materials, such as with ACs [104][105] and carbon black [106]. The rate capability of such hydrous $RuO_2$ composites certainly improved. However, the high-cost of $RuO_2$ still limits its application.

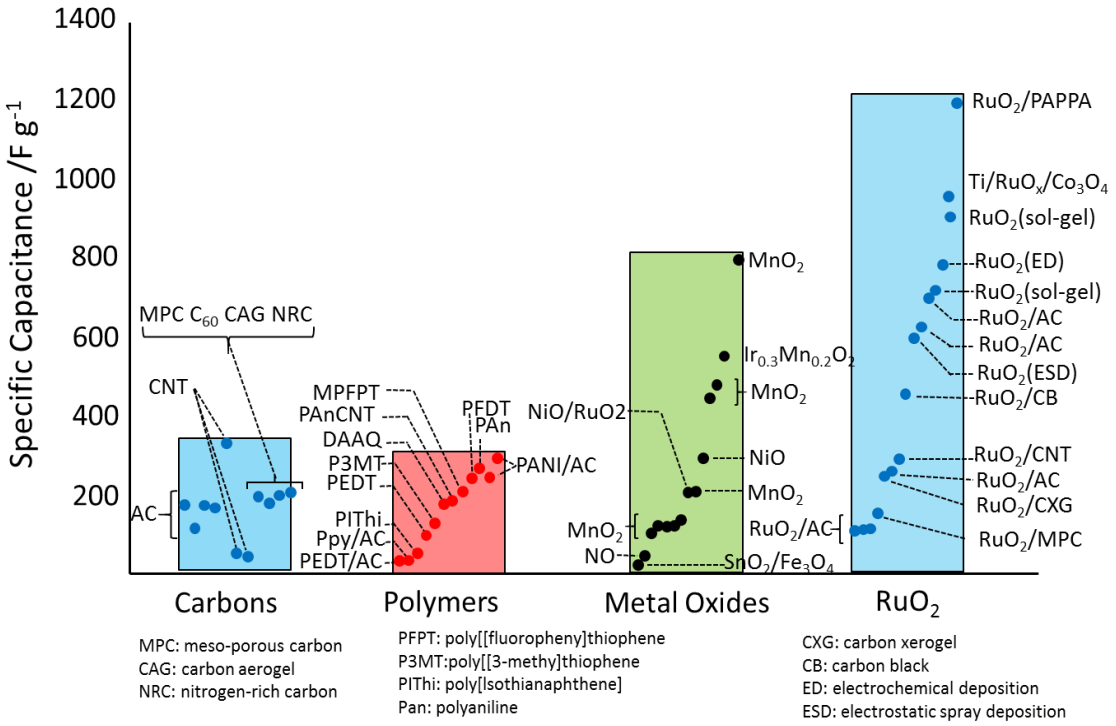


Figure 2.11 The performance for carbon and pseudocapacitor electrodes [101].

## 2.4. Flexible supercapacitors

A supercapacitor, is an energy storage device, with a particularly high power density, long life cycle, high reversibility, is environmental friendly and can be made safely [18][107], has a great potential in consumer electronics and large-sized energy storage applications, such as in communications devices, hybrid electrical vehicles, aviation and power industries. Future developments of supercapacitors are moving toward thinner, lighter and cheaper solutions, as many existing supercapacitors are still too bulky and heavy for their intended applications. There is currently a strong need for the development of lightweight, low-cost, environmental friendly and flexible energy storage devices [108][109][110]. Recently, particular attention has being given to flexible supercapacitors. There are some reports on the flexible/stretchable supercapacitors [109][111][112][113][114][115]. Recent progress on flexible supercapacitors is reviewed in this part of the chapter. The flexible electrodes, electrolyte and the structure of flexible supercapacitors are shown in this part.

### 2.4.1. Flexible electrodes

Flexible supercapacitors have been intensely studied as flexible/wearable power sources for next generation all-in-one portable and wearable electronics. Carbon materials are typically used as electrode activated materials in an EDLC, while metal oxides and conducting polymers are usually used for electrode materials in pseudocapacitors [84][116]. Flexible electrodes can be roughly divided into three types: carbon flexible electrodes, metal oxides or/and conducting polymers flexible electrodes and carbon composite electrodes. Carbon flexible electrodes are composed of only carbon networks made from one or more carbon shapes, and metal oxides or/and conducting polymers electrodes are made from metal oxides or conducting polymers or the mixing of metal oxides and conducting polymers, whereas carbon composite electrodes are composites of carbon networks with various pseudocapacitor materials [117].

#### 2.4.1.1. Carbon flexible electrodes

Carbon materials with high surface area such as AC [118], CNTs [119], carbon aerogels [120] and graphene [121] are usually used as the active materials for flexible EDLCs [5]. In reference [118], continuous, visibly defect-free, lithographically patterned activated carbon films (ACFs) are described and used to produce EDLC devices. The synthesized thin carbon film electrodes showed a high capacitance in excess of 510 F/g (>390 F/cm3) at a slow scan rate of 1 mV/s and in excess of 325 F/g (>250 F/cm3) at an ultrahigh current density of 45000 mA/g by GCD tests. In particular, after 10000 GCD cycles, this EDLC also showed no significant change and therefore good stability. Jost et al. [111] developed flexible textile for energy storage using AC (YP17) as the active material of electrodes. A high gravimetric and areal capacitance was achieved, of 85 F/g and 0.43 $F/cm^2$ on cotton lawn and polyester microfibre, respectively.

CNTs, especially single-walled carbon nanotube (SWCNT), have intrinsically excellent properties as active materials. Kang et al. [122] developed novel all-solid-state flexible supercapacitors using CNTs, regular office paper, and an ionic-liquid-based silica gel electrolyte. As a solid-state flexible supercapacitor, this supercapacitor demonstrated high electrochemical performance, excellent stability and high flexibility. The specific capacitance of the CNT electrode supercapacitors was 135 F/g at a current density of 2

A/g. the maximum power and energy density were 164 kW/kg and 41 Wh/kg, respectively. Kaempgen et al. [123] fabricated thin film supercapacitors using printable materials to make flexible devices on plastic. The electrodes were made from sprayed networks of SWCNTs used as both electrodes and charge collectors. The SWCNTs formed an entangled random network on a flexible plastic substrate (polyethylene terephthalate, PET) as shown in Figure 2.12. This SWCNT network film printed on PET was demonstrated as an easy-fabrication supercapacitor as shown in Figure 2.12, which showed high energy and power densities (6 Wh/kg for both electrolytes and 23 and 70 kW/kg for aqueous gel electrolyte and organic electrolyte, respectively) which was comparable to performance in other SWCNT-based supercapacitor devices made by different methods.

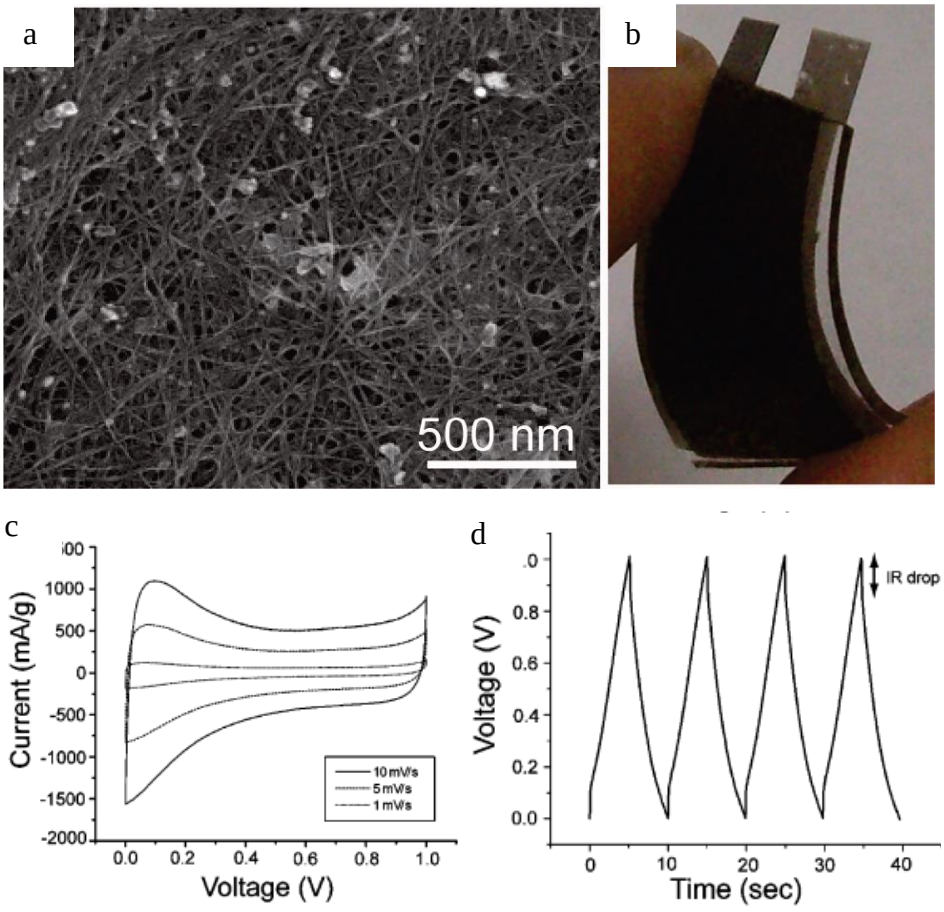


Figure 2.12 (a) SEM image of as-deposited SWCNT networks; (b) Thin film supercapacitor using sprayed SWCNT films on PET as electrodes and a gel electrolyte as both electrolyte and separator [123].

As electrode active materials, graphene-based materials have excellent mechanical and electrical properties as well as a high surface area [43][124][125]. Kady et al. [126] used a standard LightScribe DVD optical drive to make graphene through the direct laser reduction of graphite oxide films. The robust laser-scribed graphene (LSG) films, which could be used directly as supercapacitors electrodes without binders or current collectors, showed high electrical conductivity and high specific surface area. The LSG supercapacitors could be bent without degrading performance. Liu et al. [127] prepared flexible graphene sheets (GNSs)-cotton cloth (CC) composite fabric using a simple "brush-coating and drying" process. A flexible supercapacitor was made using this GNSs-CC composite fabric as the electrode material and pure CC as the separator. This supercapacitor showed the specific capacitance of 81.7 F/g in aqueous electrolyte, and also exhibited satisfactory capacitance in ionic-liquid/organic electrolyte. Moreover, the modification or a composite of graphene and other graphene derivatives may be good for all-solid-state flexible supercapacitor electrodes. Graphene aerogels (GAs) is a new class of ultra-light and porous carbon materials with high surface-area-to-volume ratios. Wu [128] used a simplified all-solid-state supercapacitor based on three-dimensional nitrogen and boron co-doped monolithic graphene aerogels. This device had an electrode-separator-electrolyte integrated structure, in which graphene aerogels were used as additive/binder-free electrodes and polyvinyl alcohol (PVA)/$H_2SO_4$ gel served as solid-state electrolyte. This thin device showed high specific capacitance (about 65 F/g), enhanced energy density (about 8.65 Wh/kg) or a power density.

The macroscopic porous morphology of carbon cloth is favourable for the ion diffusion and electron transport. Wang et al. [129] successfully manufactured a highly porous graphene on carbon cloth (PG/CC) though an electrophoretic deposition process. When this PG/CC was used as electrodes for flexible all-solid-state supercapacitors, the specific capacitance was 79.19 F/g, which was much higher than that of regular graphene on the carbon cloth (32.35 F/g). The excellent mechanical stability and flexibility of PG on carbon cloth ensured the device had good flexibility. The resultant flexible SCs showed high specific capacitance, good cycling stability, and enhanced energy density and power density (1.64 Wh/kg and 0.67 kW/kg).

### 2.4.1.2. Metal oxides or/and conducting polymers electrodes

Among the transition metal oxides, $RuO_x$ and $MnO_x$ are mainly used in flexible solid-state supercapacitors. As an electrode material, $RuO_x$ has wide potential window, good thermal stability, metallic type conductivity, highly reversible redox reactions, remarkably high specific capacitance, long cycle life, and high rate capability [130]. A solution-based binder-free synthetic approach was used to produce $RuO_2$ thin films for all-solid-state supercapacitors. All-solid-state thin film supercapacitors were fabricated by a simple process using two slightly separated nanocrystalline $RuO_2$ thin films which were well solidified in the $H_2SO_4$-PVA gel electrolyte. The $RuO_2$ nanostructures showed a high specific capacitance of 234 F/g. This device still showed good stability after 1000 cycles. Because their flexibility and high safety, all-solid-state thin film supercapacitors are considered as competitive candidates in flexible electronics [131].

Another widely used material is $MnO_x$, which is often considered as the promising transition metal oxide for pseudocapacitors due to its high theoretical specific capacitance (1100–1300 F/g), low cost, environmental friendly and abundant resources [132][133]. Yang et al. [134] developed a new kind of worm-like amorphous $MnO_2$ nanowires (NWs) on textiles for high performance flexible supercapacitors. The flexible solid-state symmetric SCs assembled with worm-like $MnO_2$ electrodes exhibited a high energy density of 6.3 Wh/kg. Manganese oxides with other valence states also exhibited potential applications in solid-state SCs. Two slightly separated stacked of nanosheet-like $Mn_3O_4$ electrodes well solidified in a PVA/$H_2SO_4$ gel electrolyte were assembled to form a solid-state supercapacitor [135]. This integrated device showed a high specific capacitance of 127 F/g for these electrode materials with good power and energy density. The flexible and solid-state $Mn_3O_4$ supercapacitor brought new design opportunities of device configuration for future energy-storage devices.

In comparison, conducting polymers used as capacitors materials in redox pseudocapacitors are much cheaper than $RuO_2$ and can generate a comparably large specific capacitance. Conducting polymers can be positively or negatively charged with ion insertion in the polymer matrix to balance the injected charge.

Yuan et al. fabricated all-solid-state PANI-based flexible SCs on paper substrates as effective energy storage units for storing electric energy [136]. A 40 μm thick PVA/$H_3PO_4$ membrane was used as the electrolyte. The all-solid-state supercapacitor showed a power density of around 3 W/$cm^3$ at an energy density of around 0.01 Wh/$cm^3$. PPy often shows greater mass density and better degree of flexibility than most other conducting polymers. It can transport ions and electrons, such as in $MnO_2$/PPy/$MnO_2$ triple-walled nanotube arrays [137]. To further enhance the response of ions and electrons in PPy, an interesting nanocomposite structure of PPy/gold was designed [138]. Considering the entire supercapacitor including both of the PVA/$HClO_4$ gel electrolyte and PPy/nanoporous gold electrodes, the volumetric power and energy of the flexible SC device was estimated to be 56.7 W/$cm^3$ and 2.8 mWh/$cm^3$, respectively. PPy-coated paper made via a "soak and polymerization" method was highly conductive and could be used as electrodes to assemble flexible solid-state supercapacitors [139]. For most of the polymer supercapacitor systems, their CV curves exhibit one maximum or several maxima. This behaviour is in contrast to that of carbon based supercapacitors, whose CV curve approximates an ideal rectangular shape [15]. Polymer can combine with metal oxides materials for achieving better electrochemical performance, such as $Fe_2O_3$/PANI [140], $MnO_2$/PANI[141] and PPy/PANI [142]. In reference [132], Jaidev et al. prepared a novel binary hybrid nanocomposite based on polyaniline (PANI) and α-$MnO_2$ nanotubes (MNTs) by in situ polymerization. A symmetrical supercapacitor was fabricated using this hybrid nanocomposite as the electrode active material and 1.0 M $H_2SO_4$ as electrolyte, the nanocomposite showed maximum specific capacitance of 626 F/g and corresponding energy density of 17.8 W h/kg at a specific current density of 2 A/g in the potential range 0-0.7 V.

#### 2.4.1.3. Carbon composite electrodes

Generally, the specific capacitance values of single carbon electrodes are small. Because the pseudocapacitive materials involve a fast and highly reversible faradic reaction for energy storage, flexible electrodes with higher specific capacitance can be manufactured by coating the pseudocapacitive materials onto the carbon infrastructure. Recently, much effort has been devoted to fabric carbon composite materials made by coating various polymer materials or metal oxides onto carbon materials. Metal oxides can be coated onto carbon networks through electrodeposition [143][144][145] or in situ growth methods

[146] [147][148], whereas carbon/polymer composite electrodes can be prepared by electropolymerization [149][150][151], and chemical polymerization [149][152][153] [154]. For example, Chen et al. [145] synthesised hierarchically a porous structure composite of manganese dioxide ($MnO_2$) nanosheets on flexible carbon cloth though an anodic electrodeposition technique. These porous $MnO_2$/carbon composite electrodes were assembled into highly flexible supercapacitors, which showed a high specific capacitance of 425 F/g and good crack resistance owing to its efficient release of bending stress. Yuan et al. [143] manufactured a highly flexible solid-state supercapacitor with an energy density of 4.8 Wh/kg at a power density of 14 kW/kg ($PVA/H_3PO_4$ gel electrolyte), in which carbon nanoparticles/$MnO_2$ nanorod electrodes were made via an electrochemical deposition process.

PANI are the most commonly used polymeric pseudocapacitor electrode materials, and can be electropolymerizated on carbon networks (such as CC, SWNT paper, and graphene paper) to make composite materials with good electrochemical performance. Horng et al. [151] used a simple and convenient route to directly fabricate polyaniline nanowires (PANI-NWs) onto the surface of carbon cloth by an electrochemical method. Then PANI-NWs/carbon cloth electrodes were assembled into flexible supercapacitors which showed a high capacitance (1079 F/g and 1.8 F/cm$^2$ for mass and area-normalized capacitance) and a high energy density (100.9 Wh/kg at a power density of 12.1 kW/kg).

Meng et al. [152] demonstrated a novel kind of ultrathin all-solid-state supercapacitor with two PANI/CNT nano-composite electrodes which were separated by a $PVA/H_2SO_4$ gel electrolyte (Figure 2.13). In this reference, the PANI was polymerized to form a uniform coating on the freestanding CNT networks made of randomly entangled individual CNTs and CNT bundles by the in situ chemical solution method. The thickness of this flexible all-solid-state supercapacitor device was about 113 μm, which was comparable to commercial standard A4 print paper. This ultrathin supercapacitor showed super flexibility and good electrochemical performance: and under its highly twisted state, this ultrathin supercapacitor also showed a high specific capacitance of 350 F/g for electrode materials. This device had good cycle stability after 1000 cycles and a leakage current was only as small as 17.2 μA. Three supercapacitor units (each size ~0.65 cm × 5.0 cm) in series were charged at 2.5 V for 15 min. This rolled-up 15 cm long paper-like device could light the LED very well for almost 30 min. Yao et al. [155] introduced a

simple and low-cost method to fabricate graphite/PANI hybrid composite electrodes on paper for flexible solid-state supercapacitors. In this, the PANI nanowire networks were synthesized by oxidation of aniline through a conventional three-electrode system. The hybrid electrodes showed a low sheet resistance of 32.3 Ω $sq^{-1}$ and a high areal capacitance of 355.6 mF $cm^{-2}$ at a current density of 0.5 mA $cm^{-2}$. The paper-based symmetric supercapacitor exhibited a volume capacitance of 3.55 F $cm^{-3}$ at a current density of 4.57 mA $cm^{-3}$, and an energy density of about 0.32 mWh $cm^{-3}$ at a power density of 0.054 W $cm^{-3}$ normalized to the whole volume of the solid-state device.

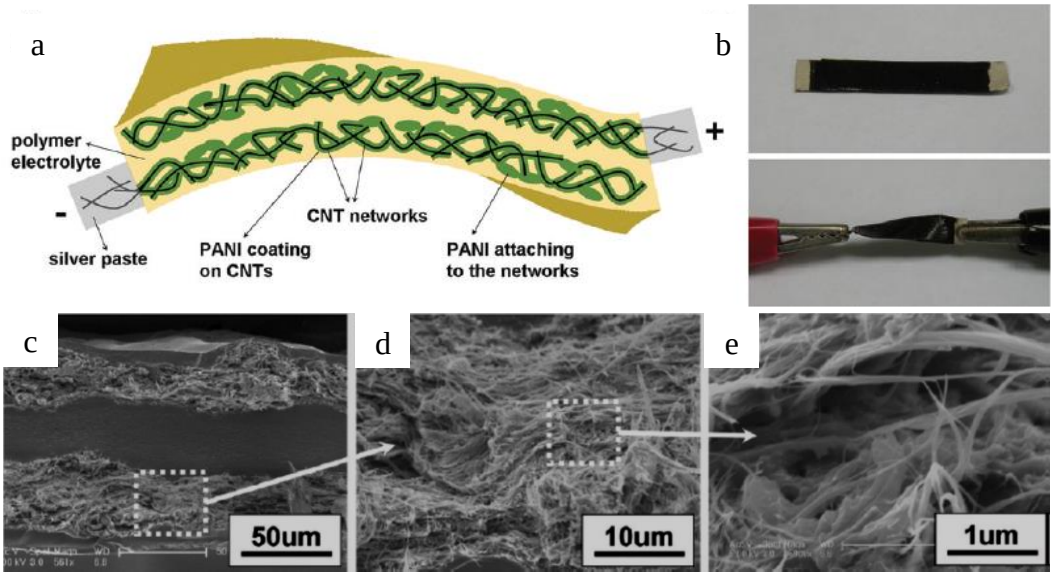


Figure 2.13 (a) Schematic illustration of the PANI/CNT nanocomposite electrodes well solidified in the polymer gel electrolyte; (b) the all-solid-state device (size ~0.5 cm × 2.0 cm) under normal condition (top) and its highly flexible (twisting) state under electrochemical measurements (bottom); (c) SEM cross-section of the ultrathin all-solid-state device and (d,e) SEM of PANI coating CNT networks were under different magnifications [152].

### 2.4.2. Flexible electrolyte

The electrolyte is another important component of the flexible supercapacitor in addition to the electrodes. There are two types of electrolytes commonly used in flexible

supercapacitors. The first type is liquid electrolyte. Generally, liquid electrolytes are aqueous or organic solutions. Aqueous electrolytes contain acid (e. g. $H_2SO_4$ or $H_3PO_4$ aqueous solution), neutral salt (e. g., $KNO_3$, LiCl, $Na_2SO_4$, or $Li_2SO_4$ aqueous solution), or alkaline (e. g., LiOH, NaOH aqueous solution) [103[151][156][153]. Organic electrolytes normally are the mixtures of a salt dissolved in an organic solvent [157] [158]. The voltage window of the organic electrolytes is usually in the range of 2.4-4 V, which is much higher than that of aqueous electrolytes (below 1 V). Such as in reference [158], the organic electrolyte was prepared by dissolving the tetraethylammonium tetrafluoroborate in propylene carbonate. Liquid electrolytes are used widely in supercapacitors.

The other important type is the solid-state electrolyte. The gel agents used commonly in a gel electrolyte are PVA, poly(vinylidene fluoride) (PVDF), and poly (vinylidene fluoride-co-hexafluoropropylene) (P(VDF-HFP) [159]. For instance, $H_3PO_4$/PVA [119][125], KOH/PVA [160], BMIM+BF4-(1-butyl-3-methylimidazolium tetrafluoroborate) ionic liquid/PVDF [161], aqueous $Ca(NO_3)_2$-$SiO_2$ [162], 1-butyl-3-methylimidazolium chloride ([BMIM][Cl]) ionic liquid-cellulose [110]. The gel electrolyte was used as the electrolyte and separator, and showed good flexibility when it was dried. For example, Niu et al. [125] developed all-solid-state flexible ultrathin micro-supercapacitors using PVA/$H_3PO_4$ as the gel electrolyte. This PVA gel electrolyte was beneficial for the flexibility of an ultrathin micro-structure. It was easily prepared as follows: PVA powder was dissolved in de-ionized water at about 90 ℃ with constant stirring, until the solution became transparent. After cooling the solution down, concentrated $H_3PO_4$ was added. This mixing solution was thoroughly stirred until a clear solution was obtained. This method is widely used to prepare PVA matrix gel electrolyte [119][125] [131][135]. Yang et al. [119] developed a kind of fibre-shaped supercapacitor which showed a high stretchability because the $H_3PO_4$/PVA gel electrolyte as well as the rubber fibre substrate were stretchable.

It was discovered that the ionic conductivity of the electrolyte was improved when the mediators were added into the gel electrolyte. For example, Yu et al. [163] used PVA/KOH–KI as a gel electrolyte in quasi-solid-state supercapacitors, and found that the introduction of KI increased the ionic conductivity of electrolyte, resulting in the increase of the pseudocapacitance of the AC electrode (increasing by 74.28%) compared to the

PVA/KOH system at the same current density. Another example is Nafion, which is usually used as a membrane and effective ionomer. Choi et al. manufactured an all-solid-state flexible supercapacitor using Nafion-functionalized reduced graphene oxide (rGO) thin films as the electrodes and solvent-cast Nafion membranes as electrolyte and separator. The all-solid-state supercapacitors showed a 2-fold increase in specific capacitance, high charging discharge rate capability and good durability performance under cycles of bending and relaxing. This proved that a Nafion based electrolyte also has a high flexibility [164].

In order to enlarge the working window of the flexible supercapacitors, non-aqueous gel electrolytes were developed. They consist of either plasticized polymer complexes with electrolytic salts or polar polymer matrices swollen with organic electrolyte solutions. As an example, Matsuda et al. prepared a polymeric gel electrolyte composed of poly(ethylene oxide)-grafted poly(methyl)-methacrylate (PEO-PMMA) swollen with an organic solution which was the complex of propylene carbonate (PC) and tetraethylammonium tetrafluoroborate ($TEABF_4$) [165]. When this non-aqueous gel electrolyte was used in an EDLC, the maximum capacitance was 0.57 $F/cm^2$, which was comparable to that of usual liquid-type EDLCs. Ionic liquids are considered excellent non-aqueous electrolytes in supercapacitors, because of their wide electrochemical potential window and good ionic conductivity. Ionic liquids solid-state gel electrolyte is another important non-aqueous gel electrolyte [166]. Due to the organic electrolyte and ionic liquid can operate under much higher potential windows, the voltage window can reach 2.7–3.7 V [167].

### 2.4.3. The shape of the flexible supercapacitor

The electrode materials and electrolyte used for flexible supercapacitors have been summarised in the above sections. In this section, the shapes of the flexible supercapacitors are also reviewed. Two main shapes of flexible supercapacitors reported in the references are fibre-like and sheet-like supercapacitors.

#### 2.4.3.1. Fibre-shaped supercapacitors

Fibre-shaped supercapacitors are attractive as power sources for miniaturized electronic devices, especially for wearable and portable electronics. There are two main structures of

the fibre-shaped supercapacitors: (1) double-fibre shaped supercapacitors with two fibre electrodes; (2) coaxial fibre-shaped supercapacitors.

The first type is the double-fibre shaped supercapacitor which consists of two fibre electrodes. These two fibre supercapacitors are placed in parallel or twisted together, a gel electrolyte or an insert fibre was used as the separator [168][169][170][171]. For example, Fu et al. [114] designed a novel and efficient flexible fibre supercapacitor which consisted of two fibre electrodes, a helical spacer wire, and an electrolyte. A schematic diagram of the fibre-shaped supercapacitor is shown in Figure 2.9. The helical spacer wire enabled the efficient separation of the two fibre electrodes. The fibre electrode was composed of a conductive fibrous substrate and electrochemically active materials. As shown in Figure 2.14, plastic fibre coated Au film by magnetron sputtering was used as the core fibre of one electrode. Commercial pen ink was deposited on the surface of the plastic fibre with Au coating film. It was found that the pen ink layer was uniform and complete, and composed of nanoparticles 20 nm in size which bond together to form a porous morphology (Figure 2.14). Two fibre electrodes separated with a spacer wire were placed parallel and packaged into a flexible plastic tube filled with gel electrolyte ($PVA/H_2SO_4$) to make a fibre supercapacitor. The photograph of a flexible fibre supercapacitor packaged using plastic tube was shown in Figure 2.14d, it can be wrapped around a 7.5 mm-diameter glass rod, which displays the excellent flexibility. Commercial pen ink was employed as the active material for the first time, giving good electrochemical capacitance performance, with a real capacitance of 11.9-19.5 mF $cm^{-2}$, an energy density of $1.76\times10^{-6}$-$2.7\times10^{-6}$ Wh $cm^{-2}$, and a power density of up to 9.07 mW $cm^{-2}$

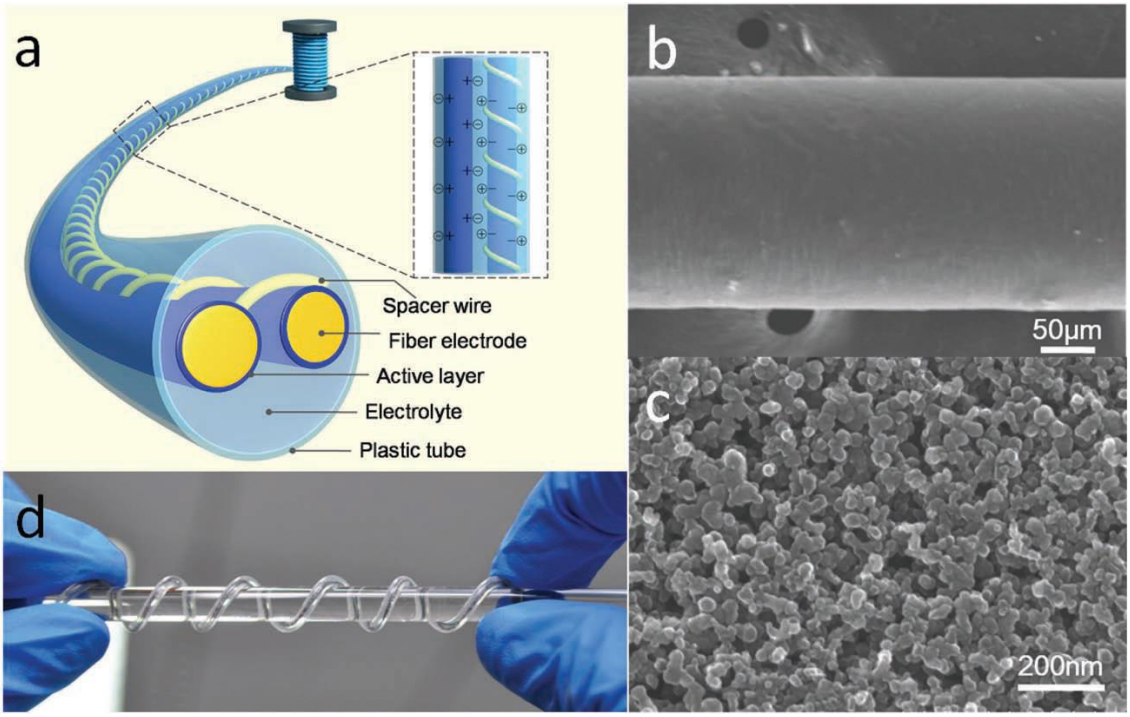


Figure 2.14 (a) Schematic diagram of the fibre supercapacitor; (b) SEM of the plastic fibre electrode coated with pen ink film; (c) SEM of ink nanoparticles at high magnification; (d) A flexible fibre supercapacitor packaged using plastic tube was wrapped around a 7.5 mm-diameter glass rod [94].

The other type is coaxial fibre supercapacitor which is usually fabricated with coaxially arranged electrodes [113][115][119][172][173]. Different from the structure of double fibre supercapacitors in which electrodes are placed in parallel or twisted, the coaxial fibre supercapacitors show a core-sheath structure consisting the inner electrode, electrolyte, separator and outer electrode. As shown in Figure 2.15, Smithyman and Liang developed a flexible coaxial fibre supercapacitor using carbon nanotube network as the electrode materials. This coaxial fibre supercapacitor showed a good flexibility (Figure 2.10d), the specific capacitance was 0.77 F/cm$^3$ and 0.74 F/cm$^3$ for the straight and wound configurations, respectively.

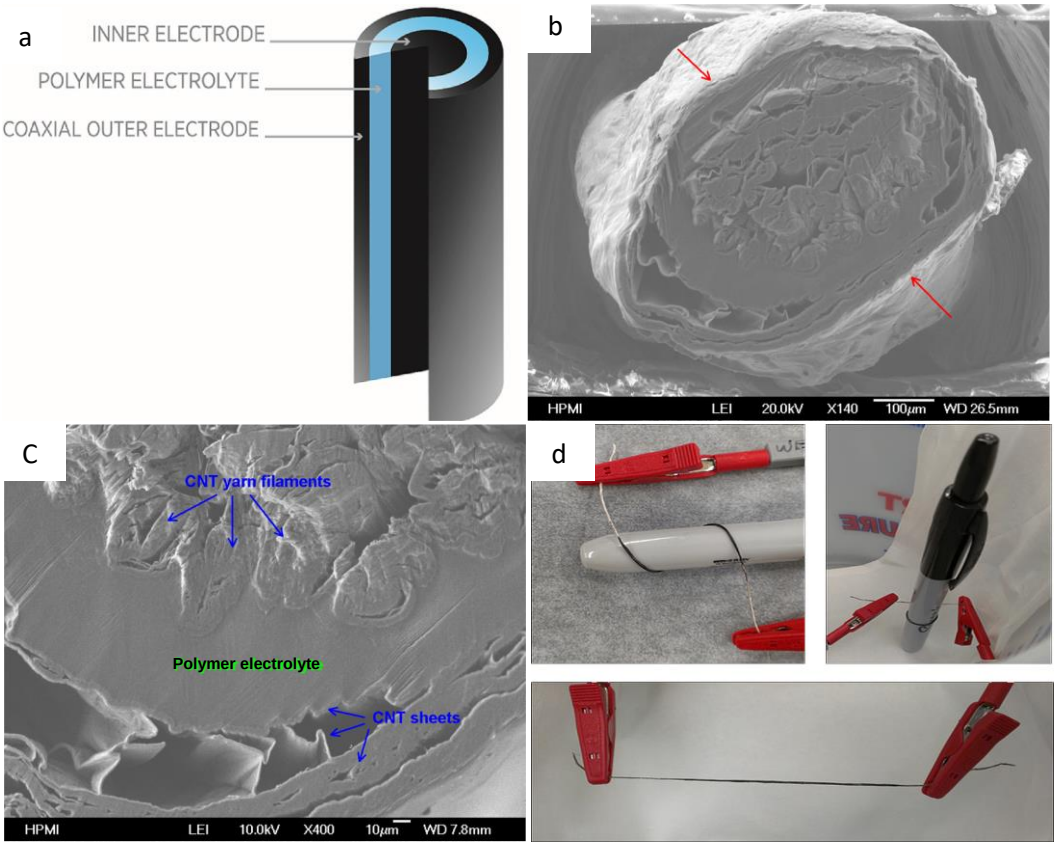


Figure 2.15 (a) Schematic of the coaxial electrode design for flexible fibre electrochemical; (b) SEM of the fibre supercapacitor's cross-section showing deformation caused by cutting with lab shears at room temperature; (c) SEM of different layers of fibre supercapacitor; (d) A fibre supercapacitor in the straight and wound testing configurations [173].

### 2.4.3.2. Sheet-like supercapacitors

Different from the fibre shaped supercapacitor, the thin sheet shaped supercapacitor usually shows sandwich structure in which the two electrode sheets were separated by a separator [111][136][143][151][174][175][176][177][178]. As shown in Figure 2.16a, a flexible sheet shaped supercapacitor with a typical sandwich structure was designed and manufactured using PANI/SWNT/cloth composite as active electrode material. Two flexible electrodes with the same area were separated by glass fibre paper, and then

encapsulated by flexible polyethylene terephthalate film. Because the SWCNT/cloth has a sheet resistance of 60 Ω $sq^{-1}$, the extra current collector is unnecessary in this sheet shaped supercapacitor. Two flexible supercapacitors assembled by two symmetric PANI/SWCNT/cloth composite electrodes were connected in series. After being charged in several seconds using AA batteries with the potential of 3 V, two supercapacitors in series can light a red LED for several minutes. When they were bent to an angle smaller than 90°, there was not noticeably an effect on their performance (Figure 2.16b).

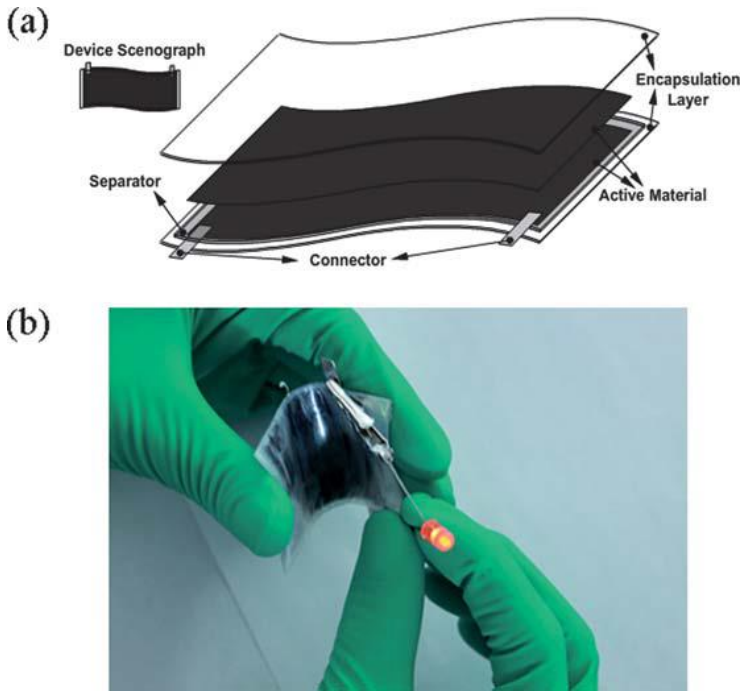


Figure 2.16 (a) Schematic of a flexible sheet shaped supercapacitor device with a sandwich structure; (b) the supercapacitor can light a red LED for several minutes [178].

Shi and his colleagues [179] developed a simple, low cost and efficient flexible sandwich supercapacitor. The electrodes were made by using stainless steel mesh coated by pen ink as electrodes. The devices showed good capacitance performance, such as high specific capacitance (107.8 F/g), high energy density (10.25 Wh/kg), power density (11.36 kW/kg) and an ultra-long cycle lifetime. Moreover, the mesh-based supercapacitors showed much better flexibility compared to plate-type ones, with stable electrochemical performance after several flexings. The stable and robust ink film on mesh electrode made it fully compatible for conventional carbon material modification in fabricating pseudocapacitors. The use of mesh and pen ink dramatically reduced the fabrication cost of light weight and

highly flexible characteristics. The dip-coating method used was simple and easily operated making it suitable for large-scale flexible and wearable energy storage devices.

## 2.5. Typical applications

Supercapacitors can deliver higher power than batteries and store large amount of energy than conventional capacitors. As well as other properties, such as a fast charge/discharge rate and a long cycle life, supercapacitors can be used for the following typical applications.

### 2.5.1. Consumer electronic products

#### 2.5.1.1. Backup power sources

Most of the consumer supercapacitors are used as backup sources for memories, microcomputers, clocks, and system boards [1][13]. In these applications, the primary power source will normally supply the load. The supercapacitors can supply the power for the load in the case of power outages caused by the disconnection or turn-off of primary power source, a system voltage drop caused by switching-in of other heavy loads, or contact problems due to shocks or vibration. For example, supercapacitors served as backup power sources for the TV-channel setting, clock time and recording time. In car audio system and taxi meter, supercapacitors were used as the backup of radio station memory or taxi fare programmes when the car battery is disconnect.

#### 2.5.1.2. Main power sources

Supercapacitors deliver one or several large current pulses of a short duration (ms~s). They can be used as main power sources for some typical applications. For instance, in car toys, there is a supercapacitor which can be recharged from a battery or mains-powered charger in the “rechargeable motors” [1]. This supercapacitor can be charged fast and then supply the power for the acceleration of the toy. When a supercapacitor is used as the main power source, it can be charged by a power supply of low power rating.

#### 2.5.1.3. Alternate power sources

Based on different conditions, supercapacitors were also used as the alternate power sources in the following applications. In the day time the electric load is supplied by solar cells, meanwhile, the supercapacitor is also charged by the solar cell. During the night the power is supplied by the supercapacitor. Such as solar watch, the supercapacitor charged by solar cell can power the watch for several days [1]. Some road marking lanterns and traffic warning signals are also powered by the combination of solar cell and supercapacitor system which is a reliable system with a long lifetime that does not need maintenance.

### 2.5.2. Vehicles applications

In electric vehicles and hybrid electric vehicles, supercapacitors can serve as a short-time energy storage device with high power capability and store the energy obtained from regenerative braking. This energy can be used in the next acceleration process. The use of supercapacitors in this case can reduce the size of primary power source, such as batteries or internal combustion engine [1].

For land-based vehicles, such as buses, delivery vans and cars, a combination of a battery and a supercapacitor can provide a reliable energy supplier system for engine starting, electric power steering, preheating of catalysts, actuators and distributed power system. The similar combination can also be used in aircrafts and ships. Supercapacitors can also be used in transportation vehicles, such as carriers in hospitals and factories, people movers on fairs and wheelchairs. They will rapidly be recharged at the stops where goods or people get on or off board. The reuse of braking energy will save the costs.

### 2.5.3. Industrial process

Some industrial processes, such as chemical process, textile industry process and pharmaceutical process, are very sensitive to interruptions and disturbances of the mains voltage. Once the interruption of the power supply occurred, it will result in expensive loss of production. Supercapacitors can provide a better ration of energy and reliable system to power for those applications.

## 2.6. Research gaps and literature review summary

Previous studies of the working principle, electrode materials, types and applications of supercapacitors were summarised in this chapter. The future developments of supercapacitors are moving towards flexible supercapacitors. The flexible supercapacitor research has become a relatively new field of scientific interest. Current works in this field were also reviewed. Most of the work in this field focused on how to improve the performance by developing new active materials or how to design the novel shape of the flexible supercapacitors.

The gaps identified to be investigated through this research are as follows:

- Previous test methods of supercapacitor flexibility have been relatively simple. In this thesis work, a mechanical testing method will be applied, and combined with the electrochemical performance testing method to study the flexibility and the electrochemical performance under static and dynamic mechanical testing process.
- Previous studies of operation parameters in the design and manufacture of flexible supercapacitor are very limited, although very important for the performance of flexible supercapacitors. In this work, I will investigate the effect of the main operation factors on the performance of flexible supercapacitors using an experimental design method. This will provide a novel way to optimise the performance of supercapacitors by controlling the practical parameters.
- Previously, little work has been done on the optimising the performance of AC by ball-milling method for flexible supercapacitors. In this thesis work, the effect of the ball-milling time on the specific capacitance of AC milled will be investigated, and the milled AC with optimum performance will be used as the active electrode material for the flexible supercapacitors to improve its performance.

It is believed that the progresses in this study of flexible supercapacitors will contribute to some unfilled gaps in knowledge of this new field, and enable the further development of highly flexible energy storage device and accelerate related technology of smart energy sources.

# Chapter 3. Experimental Materials and Measurement Method

In this chapter, the general materials, experimental techniques and instrument details used in this thesis are described. The specific experimental procedures are presented in the experimental section of each chapter.

## 3.1. Reagents and apparatus

### 3.1.1. Chemical and reagents

AC powder (AR grade, 1375 μΩ·cm) was obtained from Sigma-Aldrich. AISI 316L (Fe/Cr18/Ni10/Mo3) foil (Temper annealed) with the thickness of 0.05 mm was purchased from Advent Research Materials Company. Sodium carboxymethyl cellulose ($C_{28}H_{30}Na_8O_{27}$, MW: 250,000) was purchased from Sigma-Aldrich. Tetrabutylammonium tetrafluoroborate ($C_{16}H_{36}BF_4N$, 99%) was also obtained from Sigma-Aldrich. Propylene carbonate ($C_4H_6O_3$, 99.7%) was obtained from Sigma-Aldrich. Phosphoric acid ($H_3PO_4$, dry) and phosphoric acid solution (≥85%, ACS grade) were also purchased from Sigma-Aldrich. Ethanol (≥99.8%, ACS grade) and Acetone (≥99.8%, AR grade) were both purchased from Sigma-Aldrich. Polyvinyl alcohol (PVA, MW 146,000-186,000, >99% hydrolysed) was purchased from Sigma-Aldrich. Postlip filter papers (d=127 mm, the thickness is 130 ± 1 μm) were manufactured by Evans Adlard & Company limited. Copper wires (50 μm and 100 μm in diameter) were obtained from Advent Research Materials. Commercial carbon-based Chinese ink (named Li Tinggui) was purchased from an art shop. Silver paint was purchased from RS Components Ltd, the volume resistivity is 0.001 Ω·cm when fully hardened. All the materials above were used without further purification.

### 3.1.2. Apparatus

The general equipment for materials preparation and electrochemical performance measurement is as follows: Hot Plate & Magnetic stirrer (model, JENWAY 1000) was manufactured by Bibby Scientific Limited. The oven was manufactured by BINDER GmbH Company (Germany). Ultrosonicator (DAWE) was manufactured by DAWE

Instruments Limited. The dip-coating machine was self-designed and self-made.

## 3.2. Physical characterisation and instrumentation

The main characterization techniques and instrumentation employed are shown in this section. The physical characterization of the materials used was studied by optical microscopy, SEM and x-ray diffraction (XRD).

### 3.2.1. Optical microscopy

A Zeiss Optical Microscope was utilized for microstructural observations. The images were taken using an AxioCam MRC digital camera. Some optical images for the cross-section of a fibre supercapacitor were obtained using optical microscopy.

### 3.2.2. Scanning electron microscopy

SEM is a type of electron microscope, which can provide information on surface morphology, elemental composition and electronic structure. The SEM uses a condensed, accelerated electron beam to focus onto a specimen. The electron beam hits the specimen and produces secondary and backscattered electrons. Secondary electrons are emitted from the sample and collected to create an area map of the secondary emissions. Since the intensity of secondary emission is very dependent on local morphology, the area map is a magnified image of the sample. In this thesis work, SEM images were measured on a Zeiss scanning electron microscope (Model SUPRA 35 VP), which was operated at an acceleration voltage of 15 kV. Before measurement, the samples were stuck onto a double-face conducting tape mounted on a metal stud.

### 3.2.3. X-ray diffraction

X-ray diffraction (XRD) is a useful method to study the structure of materials. X-ray is an electromagnetic radiation which has a wavelength in the range from 0.01 to 10 nm. XRD takes advantages of the coherent scattering of x-rays by polycrystalline materials to obtain a wide range of structural information of phases. A series of lattice planes result in a XRD spectrum, which further confirms a given compound. Resultant samples in the thesis were also identified by using XRD on a Shimadzu XRD-6000 diffractometer (Cu Kα radiation,

λ=0.15418 nm) with a scanning speed of 8.00 (deg/min).

## 3.3. Evaluation of electrochemical properties

The electrochemical performance of the EDLCs developed was studied by cyclic voltammetry (CV), a galvanostatic charge-discharge test (GCD) and electrochemical impedance spectroscopy, using a VersaSTAT 3 electrochemical workstation (see Figure 3.1). The Versastat was set up in two electrode mode and as a potentiostat or galvanostat as required. The software to control the Versastat was as supplied (VersaStudio v2.20.4631) and loaded onto a Samsung laptop running Windows 7.

The electrical capacitance of the supercapacitors can be calculated from the CV or GCD testing results. All the testings were performed at room temperature (20 ± 4 °C). It is proved that there was a minor temperature effect on electrochemical performance of EDLCs using organic or water based electrolyte in this room temperature range [180]


Figure 3.1 A VersaSTAT 3 electrochemical workstation.

### 3.3.1. Cyclic voltammetry test

When a voltage is applied to an EDLC, opposite charges accumulate on the surfaces of

the electrodes. The electrodes are separated by a separator to prevent short-circuits and thus an electric potential is produced between the two electrodes to achieve the function of energy storage [1] [14]. Capacitance (C) is defined as the ratio of stored charge (Q) to the applied voltage (V):

$$\mathrm{C} = \mathrm{dQ}/\mathrm{dV} \tag{3.1}$$

The performance of the strip shaped supercapacitors is measured by using standard CV and galvanostatic charge-discharge methods.

A CV test is carried out by applying a positive (charging) voltage sweep, $\mathrm{dV}/\mathrm{dt}$, (scan rate) in a specific voltage range and then reversing (discharging) the voltage sweep polarity immediately after the maximum voltage is achieved whilst measuring the current flow. As shown in Figure 3.2 [181], the electrochemical behaviour of a strip shaped supercapacitor is evaluated based on the corresponding current response against the applied voltage. From the figure 3.2, the capacitance, C1, can be calculated by the equation:

$$C1 = \frac{Q_{total}/2}{\Delta V} \tag{3.2}$$

where $Q_{total}$ is the supercapacitor's charge in coulombs at maximum voltage, which is measured by the CV system used. $\Delta V$ is the voltage between the device's terminals in volts (V).

The capacitance, *C2*, can also be calculated from the difference in the current at a point, usually the centre, of the potential increasing and decreasing curves.

$$C2 = \frac{\Delta I/2}{dV/dt} = \frac{|\mathrm{I_1}-\mathrm{I_2}|/2}{dV/dt} \tag{3.3}$$

where $\Delta I$ is the total current ($|I_1\text{-}I_2|$) difference on the CV curve; *dV/dt* is the voltage scan rate (V/s) [1] [14].

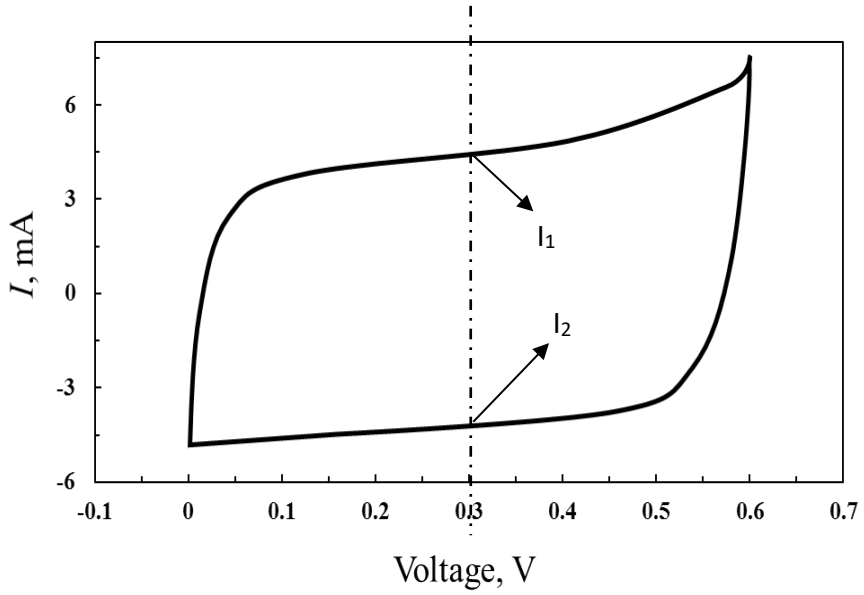


Figure 3.2 A typical CV curve of a supercapacitor recorded at the scan rate of 5 mV/s [181].

### 3.3.2. Galvanostatic charge-discharge test

A galvanostatic charge-discharge (GCD) test is the most preferred DC test performed on supercapacitors for performance evaluation such as charge capacity and life span. The measurement consists of two steps: (1) charging a supercapacitor at a constant current, and (2) discharging at a fixed current over a specific voltage range or charge-discharge time (see Figure 3.3) [181]. The capacitance C3 can be directly calculated by the following equation:

$$C3 = \frac{\mathrm{I}\times\Delta t}{\Delta V} \tag{3.4}$$

where $I$ is the discharge current in amperes (A); $\Delta V$ is the voltage of the discharge (V) [1] [14].

The specific capacitance can be calculated as follows:

$$C_s = \frac{2C}{m} \tag{3.5}$$

Where *Cs* is the specific capacitance of the electrode, *C* is the capacitance calculated from equation (3.1), m is the average mass of activated carbon in each electrode.

*C1*, *C2* and *C3* defined in equations (3.2), (3.3) and (3.4) above are the three different approaches to the capacitance of a supercapacitor. They were used to measure the capacitance for each sample in this study.

The operating voltage range is determined by the electrolyte used in the supercapacitor [1][182]. The rated voltage includes a safety margin against the electrolyte's breakdown voltage, a point at which the electrolyte decomposes or chemical reactions occur. Standard supercapacitors with an aqueous electrolyte normally are specified with a rated voltage of 1.0 V, and the working voltage of supercapacitors with organic solvents is often about 2.5 V [1][182]. In this study, the electrolyte used for strip supercapacitor is organic (tetrabutylammonium tetrafluoroborate ($C_{16}H_{36}BF_4N$) in propylene carbonate ($C_4H_6O_3$)). The working voltage used for this kind of electrolyte is about 2.4 V with a safety margin. The electrolyte for the fibre supercapacitor is $H_3PO_4$/PVA gel electrolyte. The working voltage used for this kind of water-based electrolyte is 0.8 V.

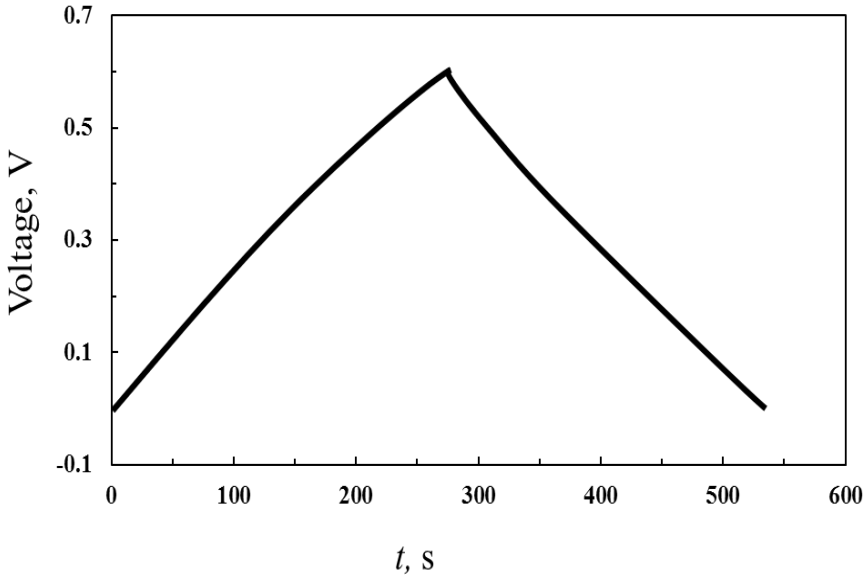


Figure 3.3 A typical GCD curve of a supercapacitor recorded at the current of 2 mA [181].

### 3.3.3. Electrochemical impedance spectroscopy

Electrochemical impedance spectroscopy (EIS) is a very effective method to study in-depth the electrochemical performance of supercapacitors. EIS functions by applying a small alternating current (AC) potential over a wide range of frequencies to an electrochemical sample system and measuring the resulting changes in current caused by the impedance of the sample as a function of frequency. As shown in Figure 3.4, Nyquist plot shows the relationship of imaginary transfer function (Zim) to real transfer function (Zre) and correlates with the system stability. At high frequencies, equivalent series resistance (ESR) value of the supercapacitor was obtained from the intercept of the Nyquist plots with the real axis (R1). ESR value is mainly determined by the electrolyte resistance and contact resistance of the active material/current collector interface. The next intercept (R2) indicates the charge transfer resistance (Rct) which is calculated by the difference between two intercepts (Rct=R2-R1). In other words, the value of the Rct is displayed as the diameter of the semicircle portion of the Nyquist plot in the high frequency range, which is dominantly affected by the electron transfer process. At intermediate frequencies, the inclined line suggests some ion diffusion behaviour of the electrolyte inside the composite electrode. At lower frequency, the straight tail is mainly affected by diffusion process [183] [184].

In this thesis, all the EIS measurements are performed at room temperature using the VersaSTAT 3 electrochemical workstation. The frequency range spanned from high frequencies 100 kHz down to 0.01 Hz.

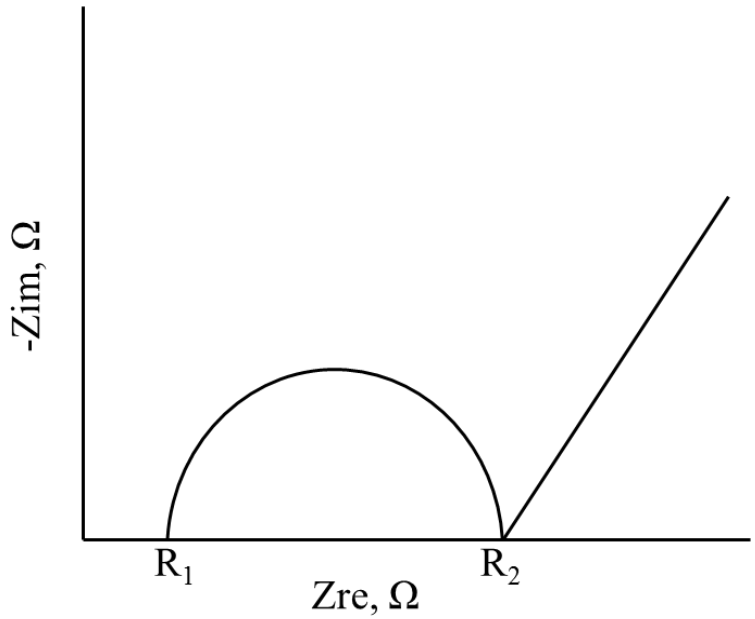


Figure 3.4 Schematic Nyquist impedance plots of a supercapacitor [184].

# Chapter 4. Design and Fabrication of Flexible Strip Supercapacitors

## 4.1. Introduction

Future developments of supercapacitors are moving toward thinner, lighter and cheaper devices, however, many existing supercapacitors are still too bulky and rigid for their intended applications. In this chapter, flexible strip supercapacitors were designed and fabricated using low-cost material by a simple method. The electrochemical performance of strip shaped supercapacitors using AC as the electrode material was investigated. The flexibility of this kind of strip supercapacitors was also studied under bending and mechanical stretching conditions.

## 4.2. Experimental methods

### 4.2.1. A typical structure of an EDLC

In Chapter 2, Figure 2.4 shows the structure and working mechanism of EDLCs. The supercapacitors consist of two electrodes, a separator and electrolyte. The two electrodes, usually made of activated carbon, provide a high surface area, separated by a layer that is ionically-conducting but electronically insulating. The energy is stored by the accumulation of charges at the boundary layer between the electrode and electrolyte.

### 4.2.2. Manufacturing of EDLCs

#### 4.2.2.1. Materials

**(1) Current collector**

AISI 316L stainless steel has improved pitting corrosion resistance with an addition of molybdenum and has excellent resistance to sulphates, phosphates and other salts. Due to its good corrosion resistance, low cost and good conductivity, it is a good choice to use as current collectors for supercapacitors. In this chapter, AISI 316L (Fe/Cr18/Ni10/Mo3)

foil with the thickness of 0.05 mm is used as the current collector.

**(2) Electrode material**

The active materials of the electrodes were prepared by mixing AC with binder (carboxymethyl cellulose, CMC). The morphology of the porous electrode was studied by Zeiss Supera 35 SEM.

Figure 4.1a shows the SEM image of AC particles. It can be seen that the size of the AC particles is not equal, i.e., they are polydisperse and range from hundreds of nanometres to tens of microns. Based on the SEM photo, image analysis software, (Nano Measurer) was used to measure the size of AC particles. After the analysis of the data, the size distribution of the AC particles was obtained and shown in Figure 4.1b. The average size of the AC particles is about 39 μm. Figure 4.1c shows the structure in the SEM photo of the electrode activated materials. Figure 4.1d shows a magnified particle surface shown in Figure 4.1c. A typical porous structure of AC materials can be observed. The diameter of holes on the porous particle is about 100 nm. This microstructure of the AC material will allow the accessibility of electrolyte to the inner surface of the carbon electrode. The porous structure also provides a large surface area for electrical charges to be stored and is beneficial for the specific capacitance value of EDLCs.

**(3) Electrolyte**

The electrolyte used was a solution of propylene carbonate ($C_4H_6O_3$, 99.7%) containing a certain molar of tetrabutylammonium tetrafluoroborate ($C_{16}H_{36}BF_4N$, 99%) obtained from Sigma-Aldrich Company.

**(4) Separator**

Filter paper (Postlip filter paper, d=127 mm, the thickness is 130 ± 1 μm) was used as a separator of a supercapacitor.

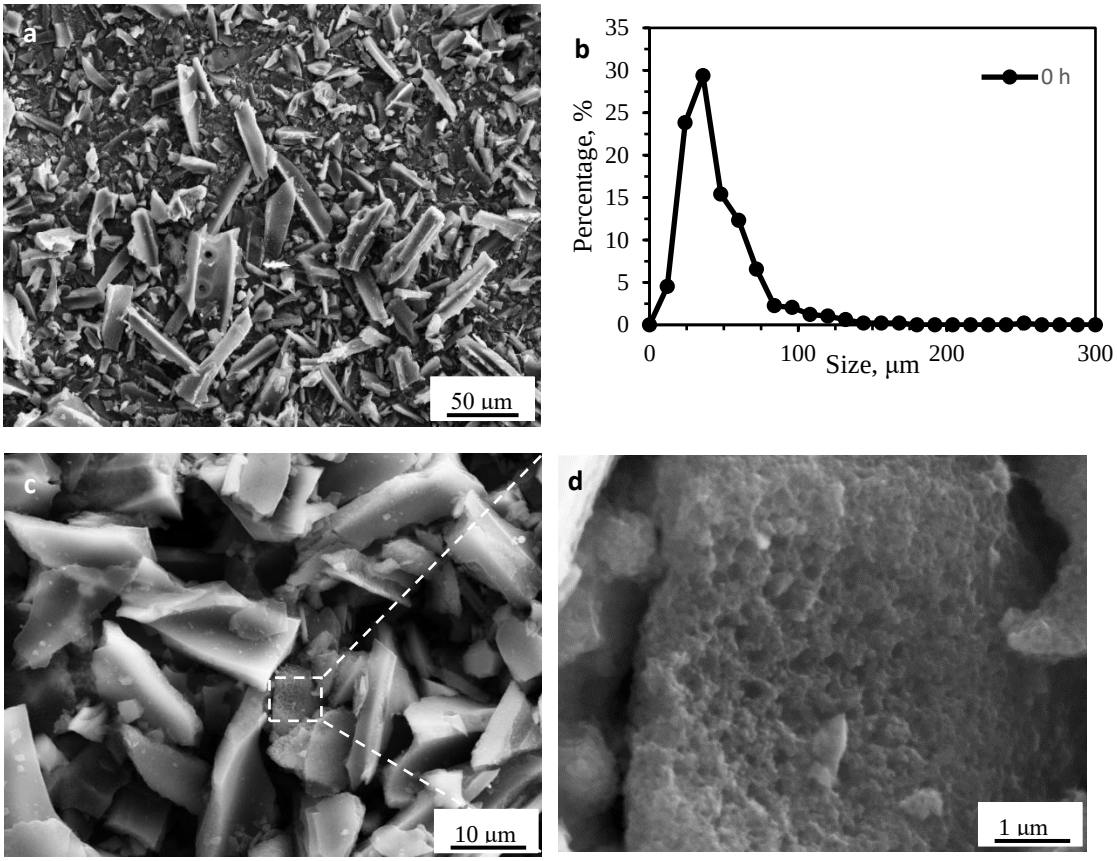


Figure 4.1 (a) SEM image of AC particles; (b) the particle size distribution of the AC; (c) surface of AC materials, and (d) porous structure of an AC particle.

#### 4.2.2.2. Manufacturing of the strip supercapacitor

Figure 4.2 shows the detailed steps of manufacturing the strip supercapacitors. The electrodes consist of a grade AISI 316L stainless steel strip as the current collector coated with active materials. The active materials of the electrodes are prepared by mixing AC with binder (CMC). The AC slurry is made as the following steps: CMC was added into the water/ethanol (1:1) solvent at room temperature with magnetic stirring overnight which gave a 5% of CMC binder solution. AC was then added to the CMC binder solution with magnetic stirring for 8 h to obtain a homogeneous slurry with 5% binder content (based on the total weight of solids). The stainless steel strip was cleaned with acetone. The thickness of the coated slurry was controlled by using a slot in plastic sheet adhered to a surface with double sided tape. The slurry was coated on the exposed surface of the stainless steel strip using a sharp blade. The electrodes were dried after being

coated with the slurry at room temperature overnight, and consequently at 100 °C for 2 h.

The electrolyte was dropped on the surface of the coated active materials on the stainless steel strip. These electrodes with the electrolyte wetted were put in a vacuum desiccator at room temperature for 0.5 h to allow the electrolyte to fully access the porous structures of the AC material. Meanwhile, the filter paper used as a separator was also fully wetted with the electrolyte. Finally, two electrodes separated by the separator were folded together to make a sandwich, which was then sealed together to avoid the loss of electrolyte using a WHSmith A4 laminator to make a complete strip.

### 4.2.3. Testing and characterisation of the electrochemical properties

The electrochemical performance of the EDLCs developed was studied by CV, GCD and EIS test, using a VersaSTAT 3 electrochemical workstation. The electrical capacitance of the supercapacitors can be calculated by the CV or GCD test results. The impedance properties can be analysed by EIS. The details of the characterisation methods and capacitance measurement methods are described in Section 3.3 of Chapter 3.

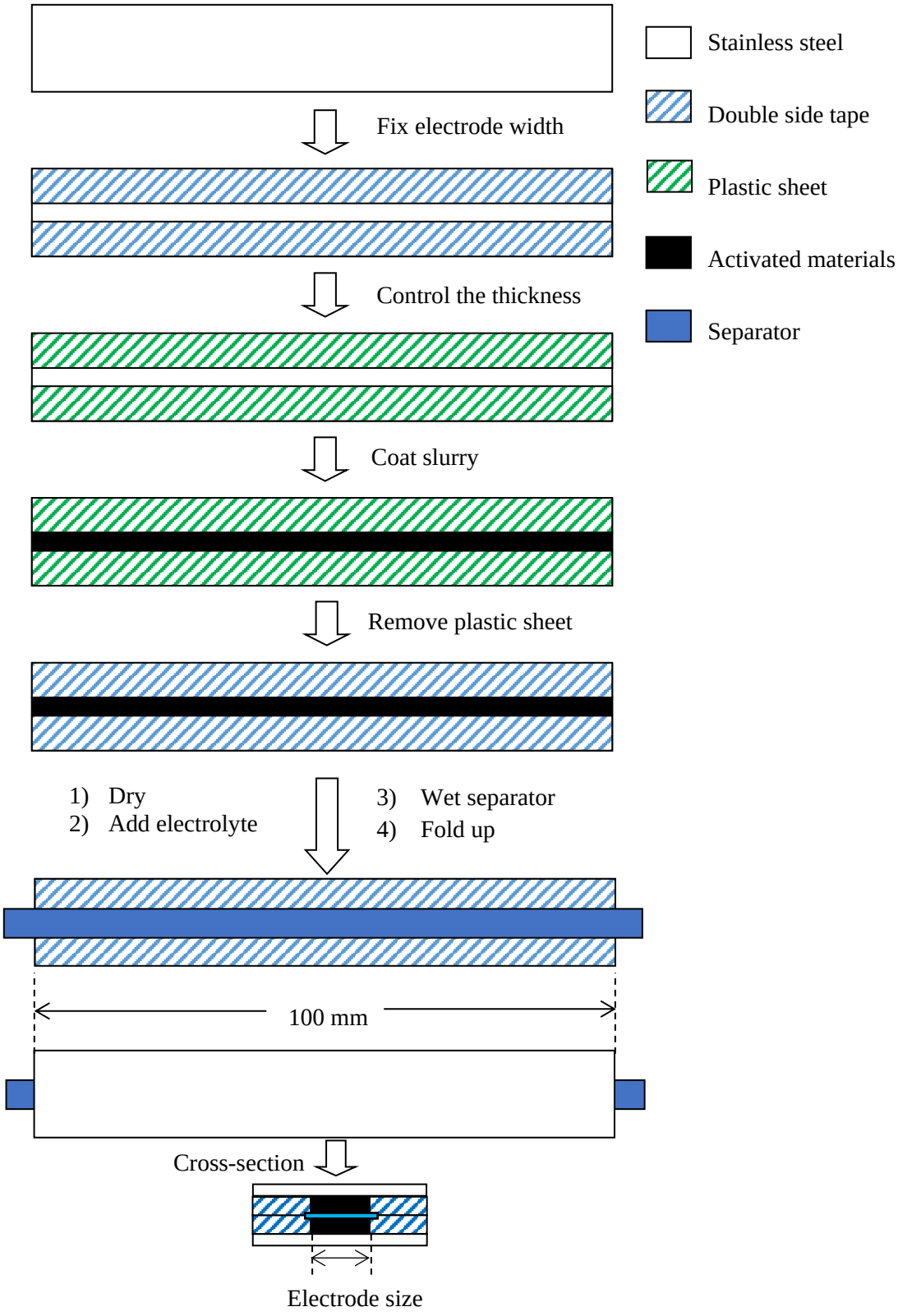


Figure 4.2 Schematic diagram (top view) showing the manufacturing steps for a strip supercapacitor.

## 4.3. Results and discussion

### 4.3.1. Capacitance calculated from the CV curve and GCD curve

#### 4.3.1.1. Effect of scan rates on the capacitance of a strip supercapacitor

CV tests were conducted to characterise the electrochemical performance. All the CV curves were recorded using a two-electrode system with a voltage window from 0 to 2.4 V. Figure 4.3a reveals the CV curves of the supercapacitor at the scan rate from 0.005 V/s to 0.040 V/s. The CV curves are close to a rectangle at the different scan rates of 0.005, 0.010 and 0.020 V/s. This result illustrates a good electrochemical performance of the strip shaped supercapacitors. Different behaviours were found at the highest scan rate of 0.040 V/s. As shown in Figure 4.3b, the capacitances C1 and C2 were calculated by equation (3.2) and (3.3) showing the same trend as the changes of the scan rates: capacitance decreased slightly with the increase of scan rate. For example, when the scan rates rose to 0.010 V/s and 0.020 V/s, the capacitances (C1) dropped to 0.273 F and 0.244 F, respectively. They are almost equal to 80.7% and 72.2% of that measured at 0.005 V/s. Even at the scan rate of 0.040 V/s, the capacitance is still 0.192 F. The slight capacitance decay at higher scan rates implies a good rate performance of the AC. The reason of capacitance reduction with the increased scan rate is attributing to the progressively less efficient diffusion of ions at the higher scan rates [185]. At the lower scan rates, the ions from electrolyte that diffused from the electrolyte have ample time to gain access and penetrate deep into the available inner porous structures easily, resulting in a high capacitance. However, at higher scan rates, efficient infiltration of ions into the inner porous structure is progressively reduced, leading to a reduction in capacitance.

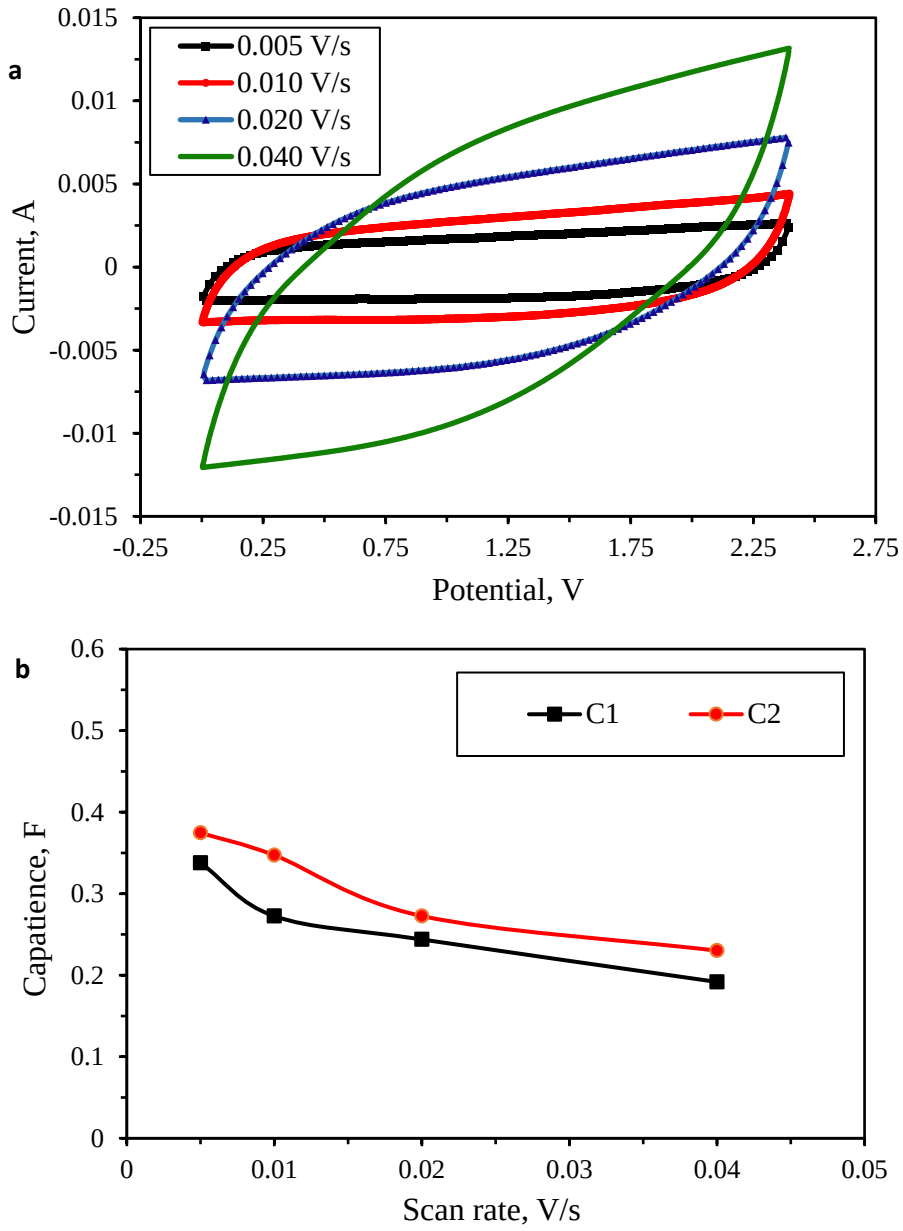


Figure 4.3 (a) CV curves of a strip supercapacitor at different scan rates ranging from 0.005 to 0.040 V/s; (b) the relationship between the capacitance and scan rates.

#### 4.3.1.2. Effect of charging/discharging current on the capacitance of a strip supercapacitor.

Figure 4.4a shows the GCD curves of a strip supercapacitor recorded at different charge currents of 0.006, 0.008, 0.010, 0.012 and 0.014 A. All the GCD curves are well-defined and symmetric. All of them showed an IR drop that happened at the early stage, and the iR drop of the GCD curve increased as the charging/discharging current increased. It can

be seen that charge and discharge time decreased as the charge current increased (Figure 4.4a and Table 4.1). Figure 4.4b shows the relationship between the capacitance (C3) calculated by equation (3.4) and charging/discharging current. When the charge/discharge current increased from 0.006 to 0.014 A, the capacitance decreased from 0.691 to 0.632 F. The decreasing trend of the capacitance with the increasing charge/discharge current is due to the partial surface of the electrode being inaccessible for ions diffusion at the high charge/discharge current [186]. At the lower charge/discharge current, there was ample time for the ions from electrolyte infiltrating from the electrolyte to the available inner porous structures easily, leading to a high capacitance. However, at higher charge/discharge current, the partial surface of the electrode became inefficient because the time for infiltration of ions into the inner porous structure was progressively reduced, which further resulted in a reduction in capacitance. The capacitance at the charging current 0.014 A was still 91.5 % of that measured at the charging current of 0.006 A. This suggests that the AC used as electrode materials has an excellent porous structure which is easy to get access for the electrolyte used in this study even under higher charge current. In other words, the AC used for the strip supercapacitors has excellent electrical properties.

Table 4.1 Capacitances (C3), IR drop and discharging time based on GCD curves for the sample recorded at different charge/discharge currents.

| Charging/discharging current (i), A | IR drop, V | Discharge time, s | Capacitance, F |
|---|---|---|---|
| 0.006 | 0.642 | 202.25 | 0.691 |
| 0.008 | 0.783 | 135.75 | 0.672 |
| 0.010 | 0.986 | 97 | 0.654 |
| 0.012 | 1.060 | 72 | 0.648 |
| 0.014 | 1.168 | 55.5 | 0.632 |

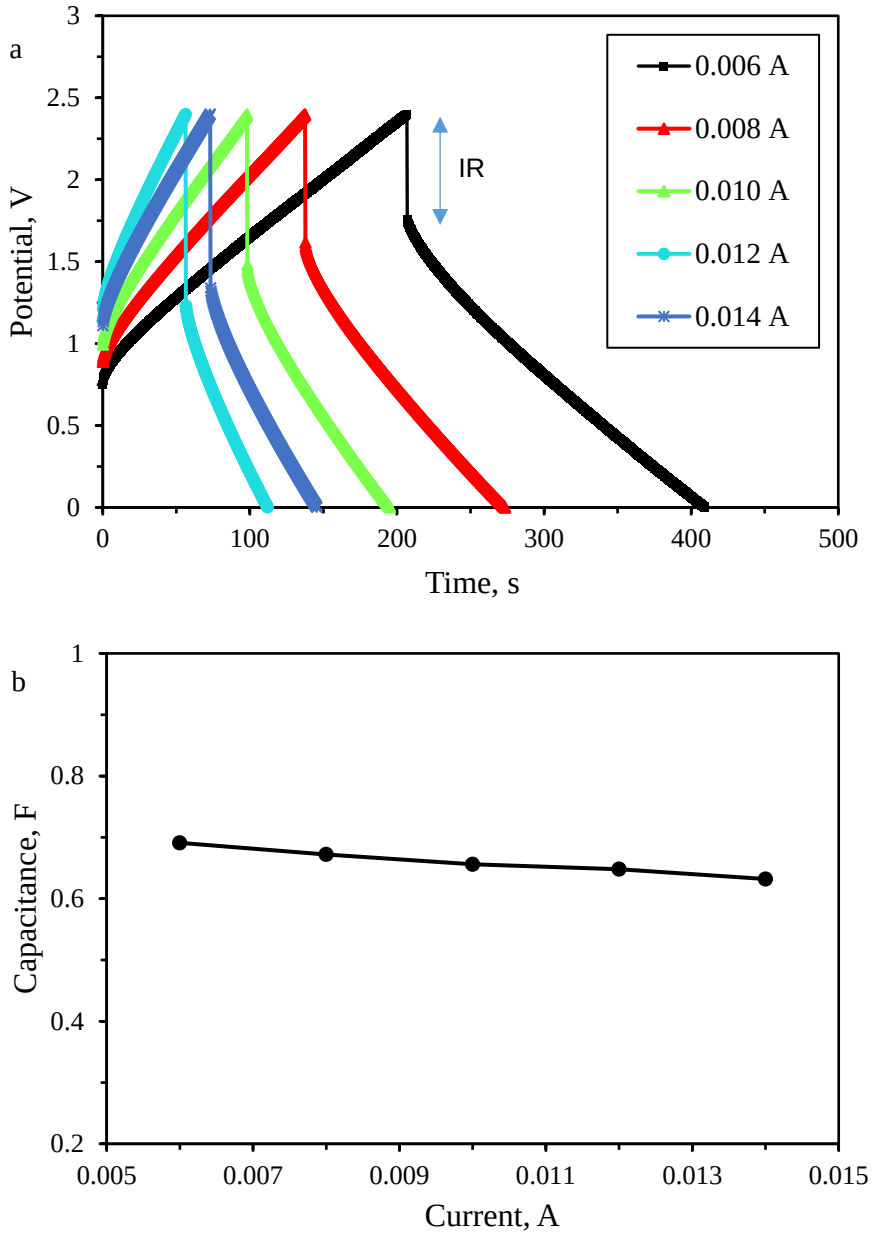


Figure 4.4 (a) GCD curves of a strip supercapacitor at different charging/discharging current of 0.006, 0.008, 0.010, 0.012 and 0.014 A; (b) the relationship between the capacitance (C3) and charging/discharging current.

### 4.3.2. The reproducibility of EDLCs

In order to test the stability of the electrical performance of the EDLCs and the reproducibility, four samples were made under the same conditions. The size of the

electrode is 3 mm ×100 mm and the thickness of the activated materials is 375 μm, the binder content is 5% and the electrolyte concentration is 1.0 mol/L. The EDLCs were characterised using CV and GCD test, and all the results are shown in Figures 4.5a, b and c. It can be found that the shapes of the four CV curves in Figure 4.5a are similar, and the areas of these curves are close, therefore, the capacitances calculated from the CV curves (C1 and C2) are almost the same. As shown in Figure 4.5b, shapes of all the GCD curves are also similar, and there is only slight difference between the charge/discharge times in each curve. That results in the capacitances calculated from the GCD curve (C3) fluctuating around the average value of the capacitance. Figure 4.5c shows the comparison of the capacitance C1, C2 and C3. It is found that the C1 and C3 are close to each other, with the average value of 0.34 and 0.35 F, respectively. These results prove that the manufacturing processes for the strip EDLCs described above have a good reproducibility. Furthermore, it is obvious that there is only a little difference between the two values of C1 and C3 for all the samples, i.e. the values of capacitance based on different tests change slightly. It indicates the capacitance measurement is reliable.

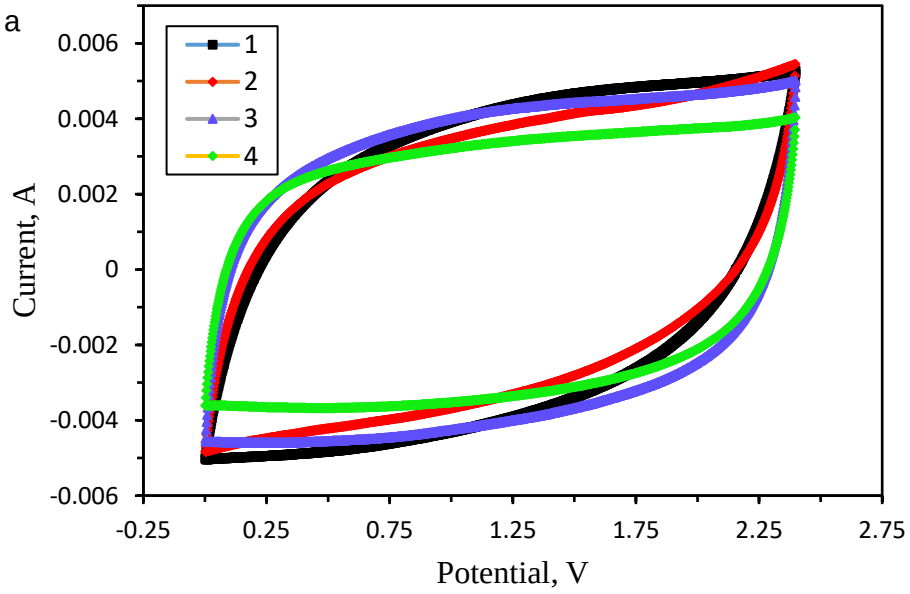

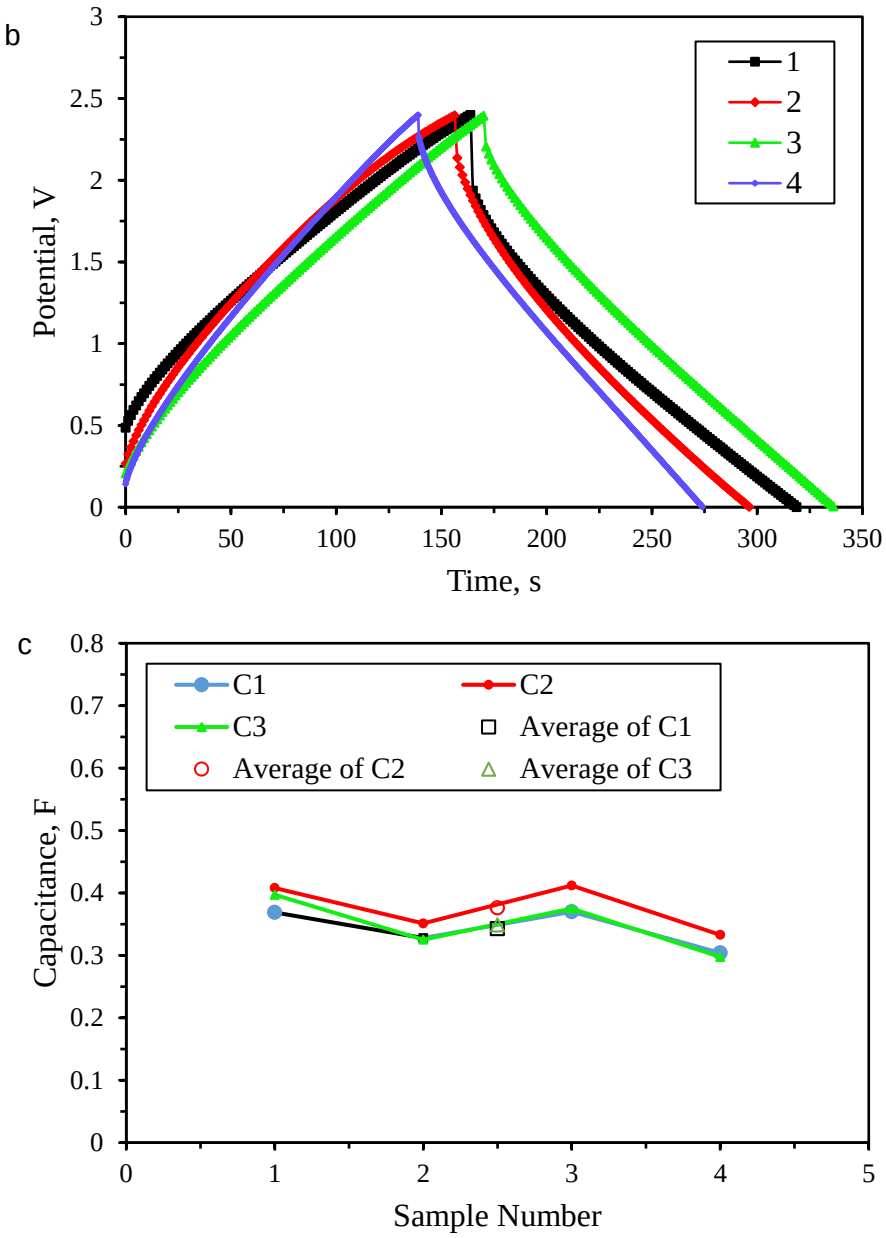


Figure 4.5 (a) CV and (b) GCD curves of four samples with the same conditions, (c) capacitances of these four samples calculated by different methods (CV Curve and GCD curve).

### 4.3.3. Testing the flexibility of strip supercapacitors

#### 4.3.3.1. Effect of the bending angle on the electrochemical performance

A new strip EDLC sample was manufactured by the same method for the bending tests. The conditions of this new EDLC are as follows: the size of the electrode is 5 mm × 100 mm and the thickness of the activated materials is 375 μm, the binder content is 5% (based on the total weight of solids) and the electrolyte concentration is 1.0 mol/L. Figure 4.6a shows the schematic of the bending rig for the tests. The rig consists of two hard plastic plates. The bottom part was fixed horizontally on the table surface, the other moveable part was used to control the bending angle. The bending tests of the supercapacitor were carried out using this bending rig as shown in the insert diagram on bottom right of Figure 4.6b. The bending angle was gradually increased from 0° to 150°. The electrochemical performance of the strip supercapacitor was studied by CV, GCD and EIS measurement while the bending angles were fixed at 0°, 30°, 60°, 90°, 120° and 150°.

**(1) The electrochemical performance characterised by CV test**

Figure 4.6 shows the diagram of the CV curves of the strip supercapacitor sample under different bending angles, at the scan rate of 0.010 V/s. It can be seen that the shapes of the CV curves under the different bending conditions are almost similar. When the bending angle was at 30°, the area of the CV curve became smaller than that of the original sample (when the bending angle was 0°), indicating the corresponding capacitance (C1) decreased. When the bending angle increased to 60°, 90°, 120° and 150°, the area of the CV curves changed only slightly. This indicates there was no significant change for the capacitances of the strip supercapacitor at different bending angles. This was very similar to the finding of the bending experiment for the flexible solid-state supercapacitors based on carbon nanoparticles/$MnO_2$ nanorods hybrid structure reported by Yuan et al. [143].

Table 4.2 shows capacitance for this sample under the different bending angles calculated from the CV curves. All the capacitances (C1) for this sample under different bending angles were calculated by Equation (3.2) based on the CV curves examined. The capacitance of this strip supercapacitor tested at the bending angle of 30° was 0.368 F, which was equivalent to 68.5% of the original capacitance of this strip supercapacitor

capacitance without bending (0.537 F). When the bending angle further increased to 60°, 90°, 120° and 150°, the capacitances changed slightly and fluctuated around 75% of the original capacitance. It suggests that the strip supercapacitor showed a stable performance when the bending angle increased from 30° to 150°. The reason for the capacitance change under the bending conditions could be the resistance increase caused by the contact change of each part (such as electrode, current collector and separator) of the strip supercapacitor.

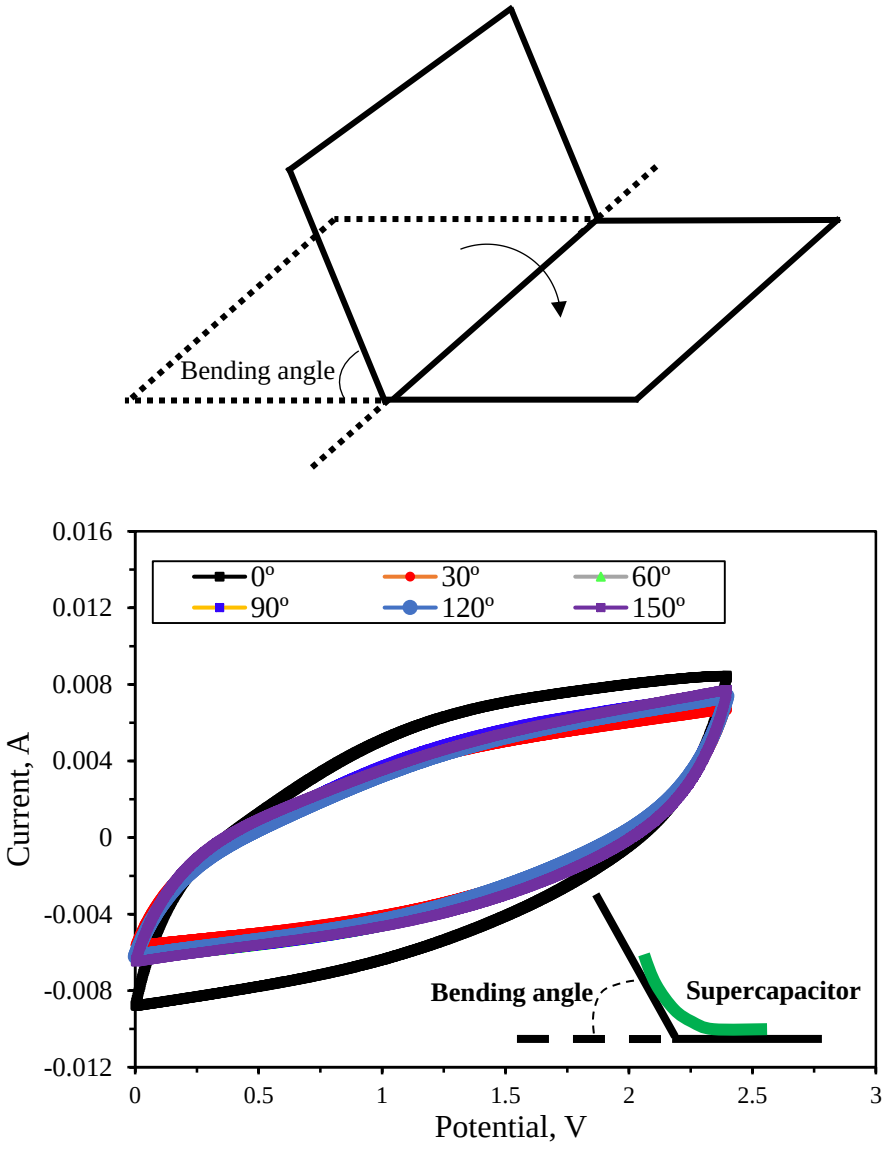


Figure 4.6 (a) Schematic of a simple bending rig; (b) CV curves of a strip supercapacitor at different bending angles from 0-150°, and the insert is a diagram of the sample under the bending condition.

Table 4.2 Capacitances based on the CV curves for the sample under different bending angles.

| Bending angle, ° | Capacitance, F | Percentage, % |
|---|---|---|
| 0 | 0.537 | 100 |
| 30 | 0.368 | 68.5 |
| 60 | 0.408 | 76.0 |
| 90 | 0.416 | 77.4 |
| 120 | 0.391 | 72.8 |
| 150 | 0.411 | 78.5 |

**(2) The electrochemical performance characterised by GCD test**

The GCD curves of this strip supercapacitor under different bending conditions are shown in Figure 4.7. It is apparent that the shapes of the charge/discharge curves recorded at different bending conditions are fairly similar. However, the charge/discharge time decreased significantly when the bending angle increased from 0° to 30°. When the bending angle further increased to 60°, 90°, 120° and 150°, the charging/discharging time increased slightly. The capacitances (C3) calculated by Equation (3.4) based on the GCD curves (Figure 4.7) are shown in Table 4.3. The capacitance decreased dramatically when the original sample was bended with bending angle of 30°. When the bending angle further increased to 60°, 90°, 120° and 150°, the capacitance fluctuated around about 70% of the original capacitance.

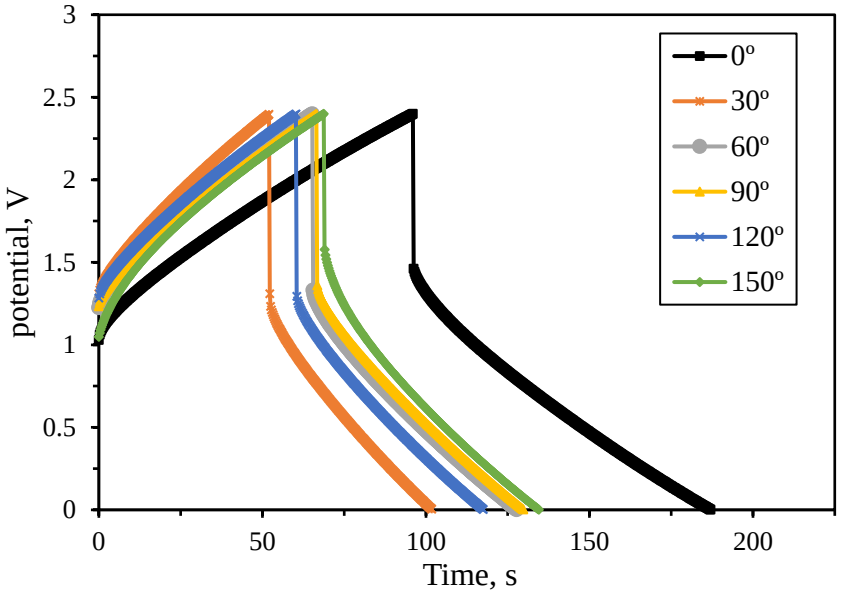


Figure 4.7 GCD curves of a strip supercapacitor at charging current of 0.010 A under different bending angles from 0-150°.

Table 4.3 Capacitances (C3) calculated from the GCD curves for the sample under different bending angles.

| Bending angle,° | C3, F | Percentage, % |
|---|---|---|
| 0 | 0.622 | 100 |
| 30 | 0.379 | 61.0 |
| 60 | 0.468 | 75.3 |
| 90 | 0.464 | 74.7 |
| 120 | 0.441 | 71.0 |
| 150 | 0.416 | 66.8 |

**(3) Comparison of the CV and GCD testing results**

Capacitances C1 and C3 calculated from the CV curves and GCD curves of this strip supercapacitor under different bending conditions are shown in Table 4.4 and Figure 4.8. It can be seen that C1 and C3 have little difference, which had also been proved in the reproducibility tests. They decreased dramatically when the original sample was bended to 30°. When the bending angle further increased to 60°, 90°, 120° and 150°, the capacitance changed slightly. The reason for the capacitance change under the bending

conditions could be a resistance increase caused by the contact changes between each part (such as electrode, current collector and separator) of the strip supercapacitor during the bending process. This will be studied further by the EIS tests later. The results indicate the strip supercapacitor made in this chapter is still functional under bending conditions, and shows a stable electrochemical performance under the bending conditions.

Table 4.4 Capacitances calculated from the GCD curves and that calculated from the CV curves for the sample under different bending angles.

| Bending angle, ° | Capacitance from GCD, F | Capacitance from CV, F |
|---|---|---|
| 0 | 0.622 | 0.537 |
| 30 | 0.379 | 0.368 |
| 60 | 0.468 | 0.408 |
| 90 | 0.464 | 0.416 |
| 120 | 0.441 | 0.391 |
| 150 | 0.416 | 0.411 |

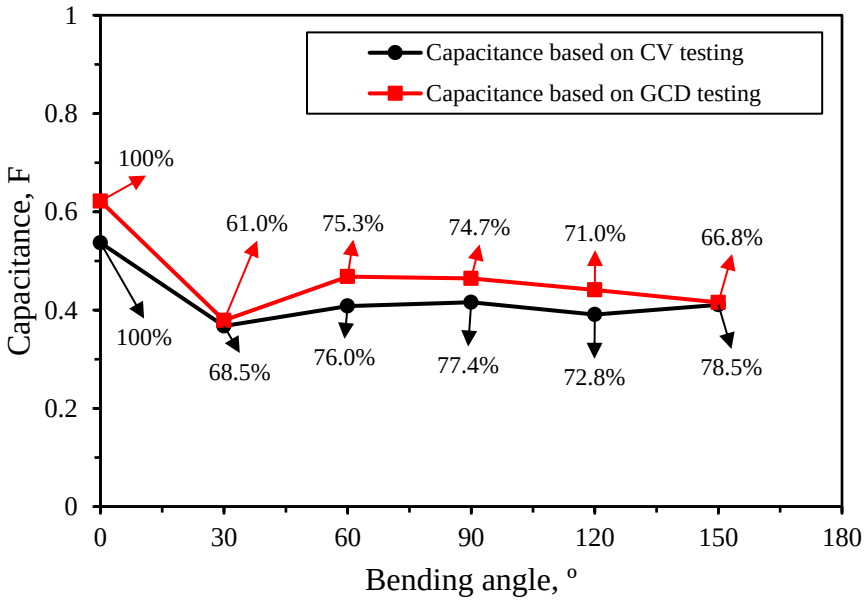


Figure 4.8 Capacitances calculated from CV curves (C1) and GCD curves (C3) of this strip supercapacitor under different bending angles from 0-150°.

**(4) EIS testing and measurement**

In order to find out the reason for the capacitance change for the strip supercapacitor under the bending conditions, EIS was used to further study the electrochemical performance of supercapacitors.

a. Equivalent circuit model

Figure 4.9 shows the Nyquist plot and simulation of the free-standing strip supercapacitor using a 4 mV AC modulation in a frequency range of 100 kHz to 0.01 Hz. The equivalent circuit model (Figure 4.9b) was used for the EIS data simulation using ZView software to get the fitting parameters. In this model, CPE1 and CPE2 are the two constant phase elements, which have the impedance in the form of $Z_{CPE} = \frac{1}{T(j\omega)^P}$ (where $\omega$ is angular frequency, $P$ is a non-dimensional number with the range of 0-1, and $j = \sqrt{-1}$). When $P = 1$, the CPE becomes an ordinary capacitance; When $P = 0$, the CPE impedance becomes independent of frequency and is a plain resistance. The T parameter in above equation is referred to as the magnitude of the CPE [187]. Rs represents the ESR. Rct represents charge transfer resistance (CTR), and is a measure of electric charge transfer through the electrode surface. It is obvious that this equivalent circuit model fits well with the Nyquist plot measured. Therefore, this equivalent circuit model will be applied to all other Nyquit plots measured under other bending conditions.

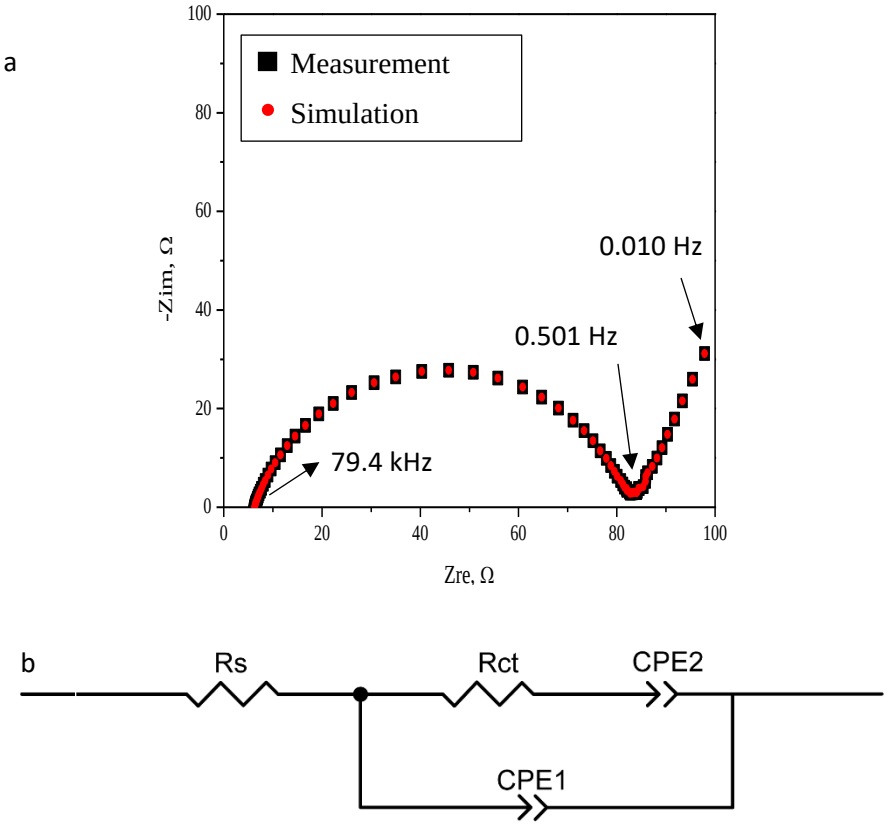


Figure 4.9 (a) Nyquist plot and simulation of the free-standing strip supercapacitor using a 4 mV AC modulation in a frequency range of 100 kHz to 0.01 Hz; (b) equivalent circuit model used to fit the ac impedance data.

b. EIS measurement results and discussion

Figure 4.10 shows the Nyquist plots of the strip supercapacitor under all different bending angles using a 4 mV AC modulation in a frequency range of 100 kHz to 0.01 Hz. All the parameters of the simulation of Nyquists plots are collected in Table 4.5.

At high frequency, the ESR values of the strip supercapacitor under different bending conditions were all below 10 Ω. The resistance values were obtained from the intercept of the Nyquist plots with the real axis. It seems the ESR values of the strip supercapacitor at different bending angles changed slightly. Generally, ESR value is mainly determined by the electrolyte resistance and the contact resistance of the active material/current collector

interface [188][164]. As shown in section 4.2.2.2, the strip supercapacitor was sealed by a laminator to protect the structure and to avoid the electrolyte leaking out. When the strip supercapacitor was under the bending conditions, the organic electrolyte cannot leak out because the whole strip supercapacitor was sealed by laminator. So the electrolyte resistance will not change dramatically due to the total amount of the ions from the electrolyte were kept the same, resulting in only a slight change of the ESR values.

It can be seen from Figure 4.10 that there is a semicircle at high frequencies for all the Nyquist plots of the strip supercapacitor tested at different bending angles. It proves that the equivalent circuit model has not been changed under bending conditions. The semicircle at high frequencies corresponds to the charge transfer limiting process, and the semicircle diameter represents the CTR, as revealed in other research [188] and [164].

It is found that the diameter of the semicircle increased approximately 24 Ω when the bending angle increased from 0° to 30°. It indicates that the CTR increased when the original sample was bent. When the bending angle increased from 30° to 60°, 90° and 120°, the diameter of the semicircle changed only slightly from 101 Ω to 106 Ω, which suggests the CTR changed slightly. It is interesting to see when the bending angle increased from 120° to 150°, the diameter of the semicircle decreased from 106 Ω to 60 Ω unexpectedly, representing the charge transfer resistance decreased about 46 Ω during this process. This might be caused by some parts of the structure distortion of the strip supercapacitor being beneficial to the charge transfer process when the bending angle increased to 150º. However, the general trend is that the CTR increased when the sample was bent.

The transition from the semicircle to the long tail can be seen in Figure 4.10, which is a common phenomenon found in Nyquist plots of supercapacitors and is attributed to the ion diffusion inside the electrode [164]. Compared with the Nyquist plot of the original free-standing sample, the transitions from the semicircle to the long tail of the Nyquist plots for the sample under bending conditions are disordered. It suggests the ion diffusion inside the electrode becomes complex during the bending process. That may be caused by the differences in the dispersion of the ions in the bending region and the straight regions.

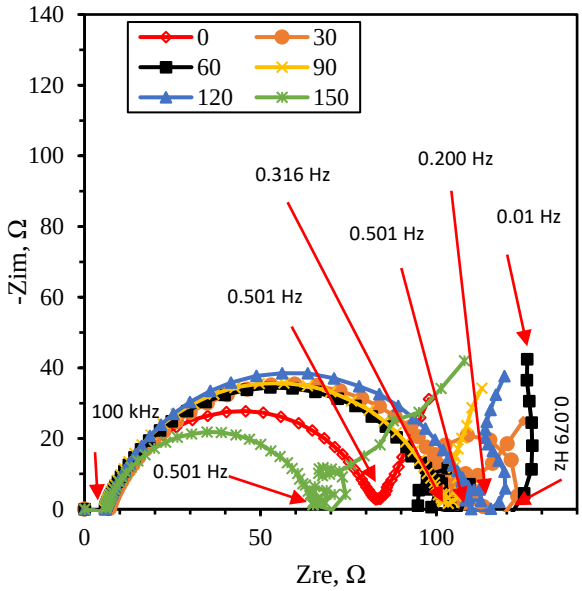


Figure 4.10 Nyquist plots of a strip supercapacitor under different bending conditions using a 4 mV AC modulation for a frequency range between 100 kHz to 0.01 Hz.

Table 4.5 Parameters obtained from simulation of Nyquist plots of a strip supercapacitor under different bending conditions.

| Bending angle, ° | Rs, Ω | Rct, Ω | CPE1-T, $\Omega^{-1}$ $cm^{-2}$ $s^{P}$ | CPE1-P | CPE2-T, $\Omega^{-1}$ $cm^{-2}$ $s^{P}$ | CPE2-P |
|---|---|---|---|---|---|---|
| 0 | 6.2 | 77 | $8.3 \times 10^{-5}$ | 0.8068 | 0.2158 | 0.7066 |
| 30 | 7.0 | 101 | $7.3 \times 10^{-5}$ | 0.7787 | 0.2902 | 0.7114 |
| 60 | 5.8 | 96 | $8.0 \times 10^{-5}$ | 0.7897 | 0.1164 | 0.5704 |
| 90 | 5.7 | 97 | $6.5 \times 10^{-5}$ | 0.8066 | 0.2587 | 0.8136 |
| 120 | 5.9 | 106 | $7.4 \times 10^{-5}$ | 0.7931 | 0.2466 | 0.8558 |
| 150 | 5.9 | 60 | $6.9 \times 10^{-5}$ | 0.8018 | 0.0986 | 0.5677 |

At each bending angle, the Nyquist plot, the CV curve and GCD curve were recorded at the same time. Because it has already been proved that there was little difference between C1 and C3, the capacitances C3 calculated from the GCD curves was used to stand for the capacitance change trend under the bending conditions. C3, as well as ESR and CTR

obtained from the simulation of Nyquist Plots (Figure 4.10) for the sample under different bending angles are shown in Table 4.6 and Figure 4.11. It is noticed that when there was a significant change of the capacitance under the bending condition from 0 to 30°, e.g. the capacitance of the sample decreased from 0.622 to 0.379 F, the values of ESR and CTR changed in an opposite way, i.e. ESR increased from 6.2 to 7.0 Ω and CTR increased from 77 to 101 Ω. The reasons for the changes of the ESR and CTR values are believed to be (1) the increase of ESR caused by the contact change between the active material, the current collector, and the ion diffusion process under bending conditions; (2) the obvious increase of CTR caused by inefficiency charge transfer process under bending conditions. These changes of the resistance will affect the capacitance accordingly. When the bending angle increased from 30° to 150°, the capacitances for the strip at different bending angles fluctuated around 70% of the original capacitance. It proves this strip supercapacitor was flexible and still functional under the bending conditions.

Table 4.6 Capacitances calculated from the GCD curves, ESRs and CTRs collected from the Nyquist Plots for the sample under different bending angles.

| Bending angle, ° | Capacitance from GCD, F | ESR, Ω | CTR, Ω |
|---|---|---|---|
| 0 | 0.622 | 6.2 | 77 |
| 30 | 0.379 | 7.0 | 101 |
| 60 | 0.468 | 5.8 | 96 |
| 90 | 0.464 | 5.7 | 97 |
| 120 | 0.441 | 5.9 | 106 |
| 150 | 0.416 | 5.9 | 60 |

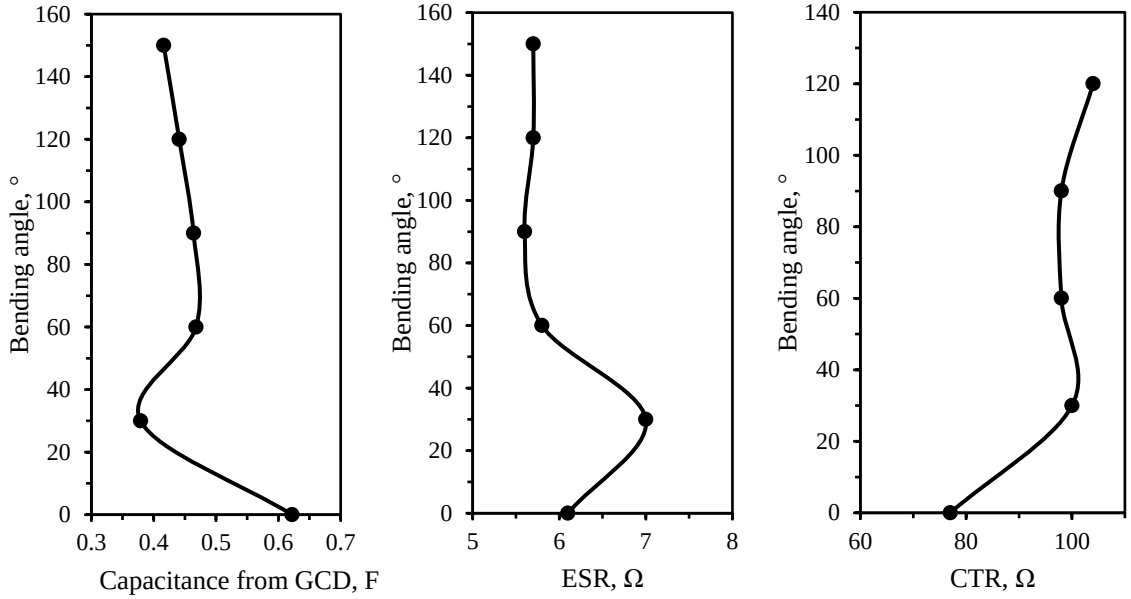


Figure 4.11 Capacitances calculated based on GCD curves and ESRs and CTRs of this strip supercapacitor at different bending angles.

#### 4.3.3.2. Effect of mechanical testing on the electrochemical performance

The aim of this section is to explore the electrochemical performance of the strip supercapacitors under the mechanical tensile conditions. Mechanical tests of the current collector materials (AISI 316L stainless steel strips, Fe/Cr18/Ni10/Mo3) with a thickness about 50 μm were performed with an Instron machine (Model 2580-106/105924) by the crosshead. The testing results revealed mechanical properties of the materials used as strip supercapacitors' current collectors. From this we can find out the important parameters of the materials, such as the maximum load the materials can stand before the breaking point and the extension at the maximum load, and correlate them with the electrochemical performance of the EDLCs under the mechanical testing conditions.

**(1) Mechanical tests of the single layer stainless steel strips with different loading rates**

The single layer of stainless steel strips was first tested. The reason for choosing single layer stainless steel strip material as the first samples to test is to understand the general

features of the material, such as the range of elastic deformation, the maximum tensile load and the maximum tensile extension. Therefore the results from the first sample could build a general impression of property of the stainless steel strip material and help to choose the appropriate parameters in software settings for the next tests. The length between the two grips, where the force was applied, is 80 mm; the width of the strip is 3 mm and the thickness is about 50 μm. The configuration of the loading method and cross-section of the strip is shown in Figure 4.12.

Different loading rates at 5, 10, 20 and 40 N/min were applied to testing the single specimens to investigate the effect of the loading rate on the testing results. Figure 4.13 shows the load-extension curve at the different loading rates. It can be seen that the yield load before the sample was deformed plastically is in the range of 160～188 N; the maximum tensile load before the breaking point is between 175 to 205 N; the tensile extension at the maximum load is between 1.28 to 1.40 mm. These results are shown in Table 4.7. The tensile extension and the tensile strain changed only slightly between runs. The reason is that the stainless steel strip is quite uniform and physical properties are stable. This proved that the loading rates have no apparent influence on the testing results of the stainless steel strip material. Therefore, 40 N/min was chosen as the loading rate for testing the following samples in order to shorten the experiment duration.

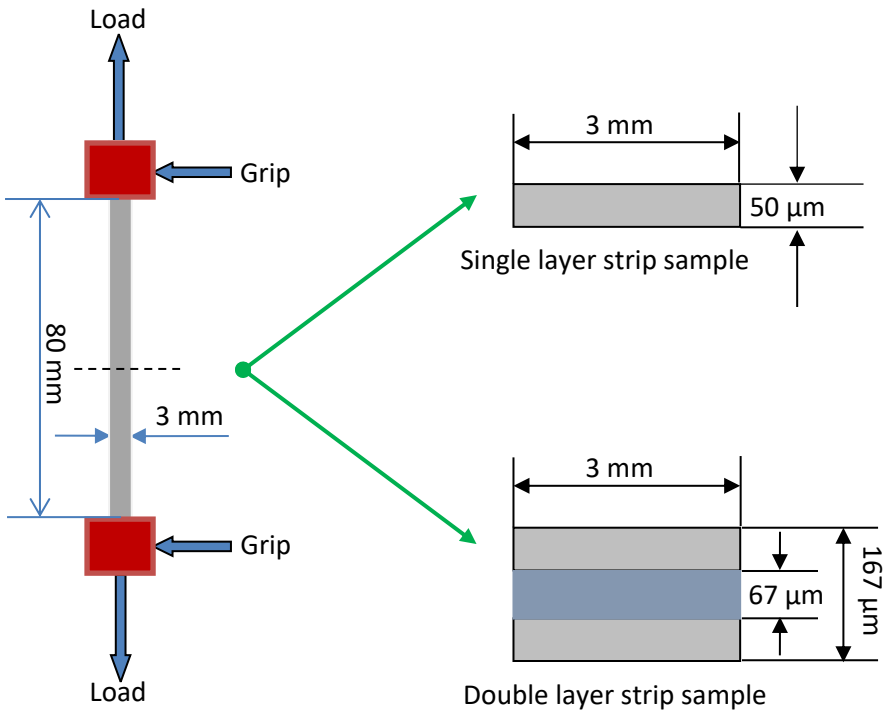


Figure 4.12 Mechanical test methods on the single layer of stainless steel strip sample and double layers of stainless steel strip sample.

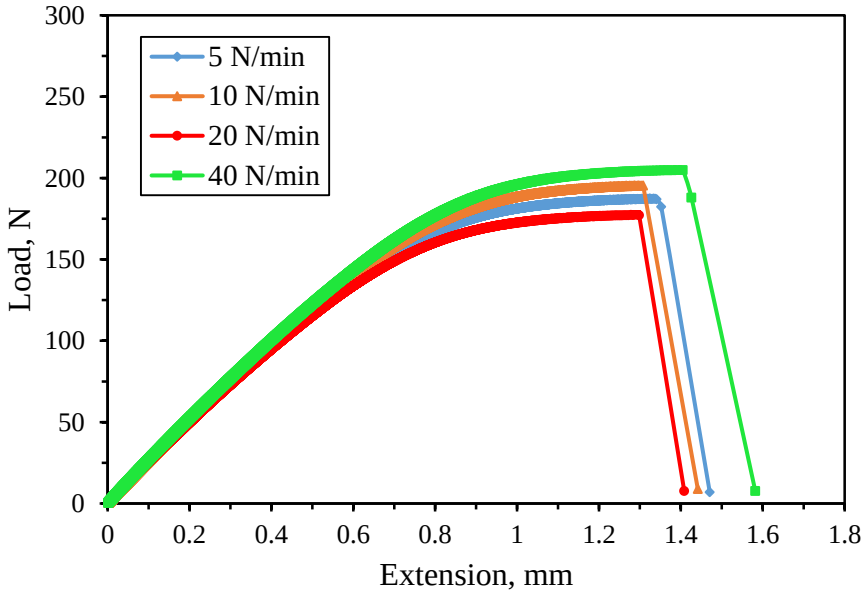


Figure 4.13 The load–extension curves at different loading rates.

Table 4.7 Mechanical testing results of the single layer stainless steel strips at different loading rates.

| Sample No. | Load rate, N/min | Yield load, N | Maximum load, N | Tensile extension at the maximum load, mm | Tensile strain at the maximum load |
|---|---|---|---|---|---|
| 1 | 5 | 170 | 187 | 1.33 | 1.7% |
| 2 | 10 | 180 | 196 | 1.30 | 1.6% |
| 3 | 20 | 160 | 178 | 1.28 | 1.6% |
| 4 | 40 | 188 | 205 | 1.40 | 1.8% |

**(2) Mechanical tests of the double layer stainless steel strip samples**

In order to choose a suitable range of load which the double layered strip supercapacitors can stand, mechanical properties of the double layer stainless steel strips were tested. The double layer stainless steel strips were composed by two single layer strips with a layer of double side tape in the middle, as shown in Figure 4.12. The tensile testing results on the double layer stainless steel strips at the loading rate of 40 N/min are given in Table 4.8 and Figure 4.14. The maximum load of all the specimens is in the range of 341- 428 N, and the average maximum load is 385 N. Meanwhile, the extension of the specimens is in the range of 1.31 ~ 2.10 mm, and the average extension is 1.66 mm, the average tensile strain at maximum load is 2.1%. The average of the yield load and maximum load of the double layer strip samples are 340 and 385 N, separately, which are increased just about 2 times than those of the single layer stainless steel strip sample (188 and 205 N). Although there are differences among the maximum loads obtained, there is minor difference in the elastic range for these samples as shown in Figure 4.13, and it is obvious that the sample was deformed plastically before the yield load. Based on the above experimental results, 0-200 N was chosen as the testing load range in order to obtain the reliable data and not to damage the strip supercapacitors during the test.

Table 4.8 Mechanical testing results of the double layer strips at the loading rate of 40 N/min.

| Sample No. | Yield load, N | Maximum load, N | Tensile extension at maximum load, mm | Tensile strain at maximum load |
|---|---|---|---|---|
| 1 | 306 | 356 | 1.88 | 2.4% |
| 8 | 312 | 373 | 2.10 | 2.6% |
| 9 | 306 | 341 | 2.08 | 2.6% |
| 2 | 354 | 385 | 1.46 | 1.8% |
| 3 | 354 | 389 | 1.37 | 1.7% |
| 4 | 375 | 428 | 1.67 | 2.1% |
| 5 | 370 | 402 | 1.34 | 1.7% |
| 6 | 334 | 389 | 1.75 | 2.2% |
| 7 | 353 | 389 | 1.31 | 1.6% |
| Average | 340 | 383 | 1.66 | 2.1% |

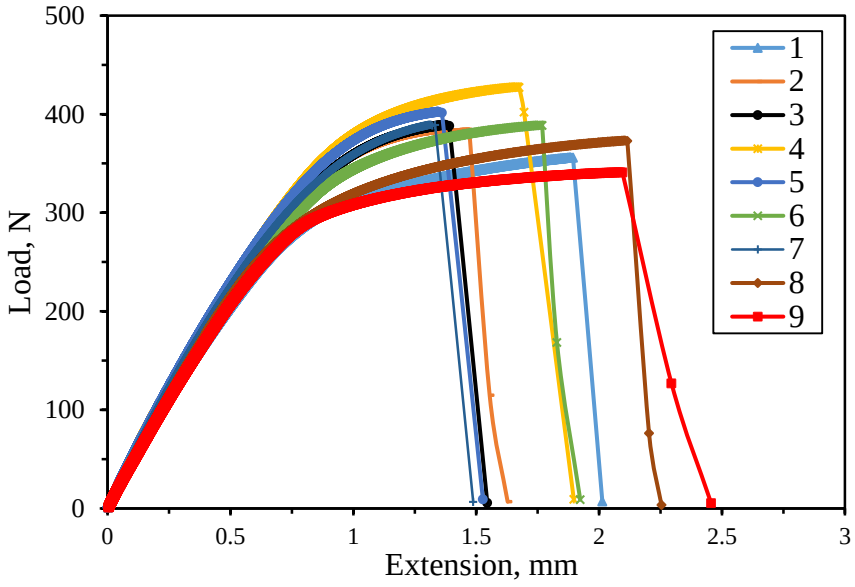


Figure 4.14 The load–extension curves of the double layer strip samples at the loading rate of 40 N/min.

**(3) Effect of the tensile testing condition on the electrochemical performance**

All strip supercapacitors fabricated identically for the mechanical tensile tests have the structure as follows: the thickness of the activated materials was 375 μm, the binder content was 5% (based on the total weight of solids), and the electrolyte concentration was 1.0 mol/L. The electrode size of the samples for the mechanical tensile test was 2 mm × 100 mm.

Mechanical tensile stress tests were performed with an Instron machine (Model 2580-106/105924). The length between the two grips, where the tensile loading was applied, is 80 mm. The configuration of the test is shown in Figure 4.15. A VersaSTAT 3 electrochemical workstation was connected with the sample during the testing process. The CV curves of the sample were recorded using this electrochemical workstation when the sample was stretched at a static loading of 0 N, 100 N, 200 N, and at the dynamic loading process from 0 to 100 N as well as 0 to 200 N. In order to obtain a complete CV curve at the scan rate of 0.020 V/s, the increasing rate of loading was fixed at 25 N/min for the dynamic loading process of 0-100 N, and 50 N/m for the process of 0-200 N.

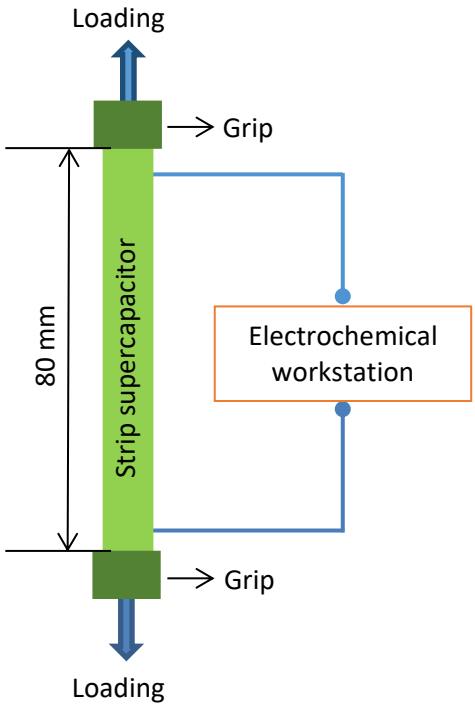


Figure 4.15 Mechanical tensile test methods on the strip EDLC sample.

As shown in Figure 4.16, five CV curves were recorded when the sample was stretched at a static loading of 0 N, 100 N, 200 N, and at the dynamic loading process from 0 to 100 N and 0 to 200 N at the scan rate of 0.020 V/s, respectively. The area of the CV curve for this strip supercapacitor under the static tensile condition of 100 N or 200 N is bigger than the sample without loading. It shows that the capacitance increased when there was a tensile stress of 100 N or 200 N applied to the sample. When the dynamic loading applied from 0 to 100 N at the increasing rate of 25 N/min, the area of the CV curve is quite close to the CV curve of the sample under the static loading of 100 N, which is also bigger than that of the sample without any loading. Similarly, the area of the CV curve for this sample in the dynamic loading process of 0-200 N is close to the CV curve of the sample under the static loading of 200 N, which is also bigger than that of the sample without any loading. All the capacitances for the sample under the different conditions calculated from the CV curves (C1) were listed in Table 4.9. The capacitance and specific capacitance of this sample under the static and dynamic load of 0-100 N are 22% ~ 25% greater than the sample without any tensile stress, whereas 9% ~ 10% greater when the static and dynamic loading were 200 N and 0-200 N, respectively. In addition, it can be seen that the CV curves recorded under the static and dynamic tensile load are quite smooth and complete, which indicates that the strip supercapacitor sample was behaving properly under load and has a stable electrochemical function.

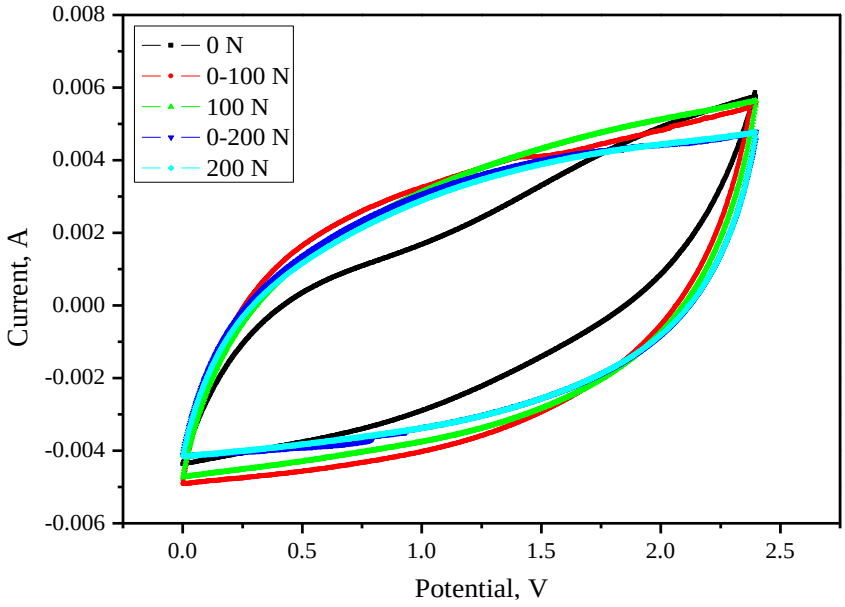


Figure 4.16 CV curves on the static tensile load of 0 N, 100 N, 200 N, and in the dynamic load changing process of 0-100 N and 0-200 N at the scan rate of 0.020 V/s.

Table 4.9 Capacitances and specific capacitances based on the CV curves recorded on the static tensile loading of 0 N, 100 N, 200 N, in the dynamic loading increasing process of 0-100 N and 0-200 N at the scan rate of 0.020 V/s.

| Performance / Condition | Capacitance, F | Specific Capacitance, F/g | Increase, % (compared with original value) |
|---|---|---|---|
| 0 N | 0.135 (original) | 31.3 (original) | 0 |
| 0-100 N (dynamic) | 0.169 | 39.3 | 25 |
| 100 N (static) | 0.165 | 38.3 | 22 |
| 0-200 N (dynamic) | 0.149 | 34.4 | 10 |
| 200 N (static) | 0.147 | 34.0 | 9 |

Figure 4.17 showed the comparison of the capacitances and specific capacitances for the sample under the static tensile stress of 0 N, 100 N and 200 N. It is seen that the capacitance and specific capacitance for this supercapacitor sample with the static loading of 100 N or 200 N is bigger than that of this sample without loading, with an increase of 22% and 9%, respectively. The reason is believed that the cross section of the sample became thinner when the sample was stretched under a tensile load, which resulted in the better contact of each layer in the supercapacitor. It is also noticed that the capacitance for the sample with the loading of 200 N is smaller than that of the sample with 100 N. It is probably because the tensile loading of 200 N results in distortion of the structure reducing the AC porosity of the strip supercapacitor, which has a negative effect on its electrochemical performance.

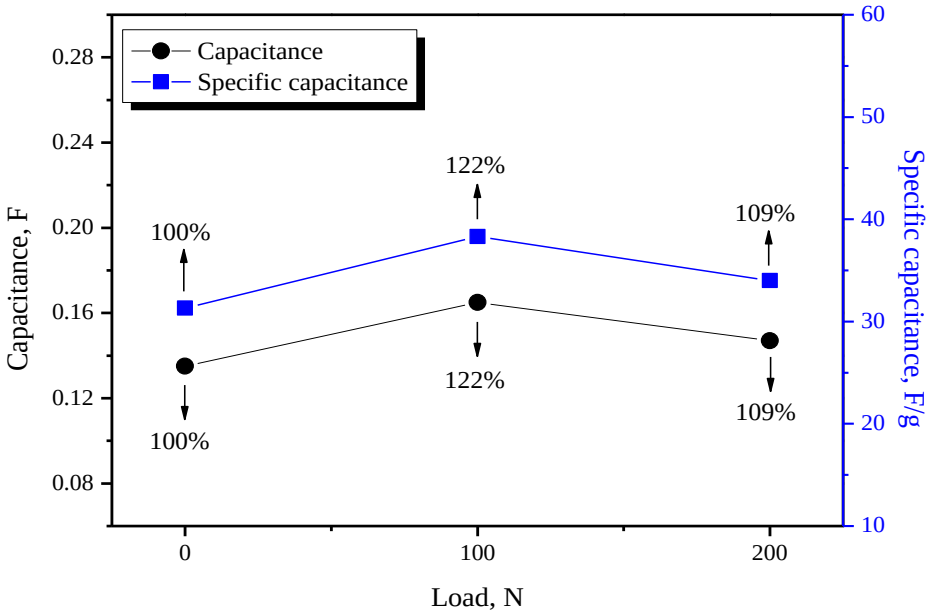


Figure 4.17 Capacitances and specific capacitances obtained from CV curves on the static stretching load of 0 N, 100 N and 200 N at the scan rate of 0.020 V/s.

Further study of the reasons why the capacitance of the capacitors with the loading increased compared to that of the sample without loading was carried out. A series of experiments for the strip supercapacitors under mechanical press condition were also carried out in order to find the correlation between the pressure and the electrochemical performance. Figure 4.18 shows the configuration of the compression tests. Weight plates with different weights (7.2 N and 8.9 N) were put on the surface of the current collector vertically and the electrochemical performances of the sample under the different weights were measured and characterised by electrochemical workstation. The strip supercapacitor used in the mechanical press test has the same thickness of the activated materials (375 μm), binder content (5% of the total weight of solids) and electrolyte concentration (1.0 mol/L) as the sample used in the mechanical tensile testing. Electrode size of the sample for the mechanical compression test was 5 mm × 100 mm in order to fit the experimental rig properly.

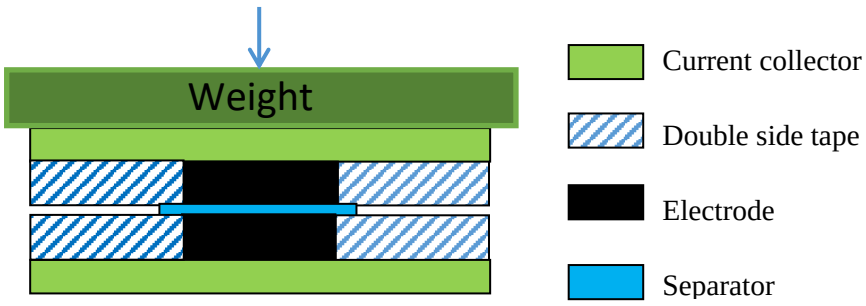


Figure 4.18 Schematic of the Mechanical compression test methods.

It has been proved that the values of the capacitance calculated from CV curve and GCD curve to be very similar, thus in this experiment the GCD test was used to measure the capacitance of the sample. Figure 4.19 shows the GCD curves of the strip supercapacitor sample under different loads. It is obvious that the charge and discharge time extended when the load is added to the original strip sample. It is also found that the IR drop of the GCD curve for the sample with load decreased compared with that for the sample without load. The capacitances based on the GCD curve were calculated by equation (3.4). The capacitance of the strip supercapacitor with the load of 7.2 N is 0.613 F, which increased 4.3 % more than that of the original capacitance for the sample without load (0.588 F). When the load increased slightly from 7.2 to 8.9 N, the capacitance increased from 0.613 to 0.618 F. The capacitance for this sample with the load of 8.9 N increased more than 5.1% than that of the original capacitance for this sample without load (Table 4.10). Because all the strip supercapacitors made were sealed by a laminator, at the same time the double-side tape was used to assemble the structure tightly. So in the stretching experiment, the cross-section will become thinner than the original sample, when the strip supercapacitor is under a load. This result is consistent with the tests when the supercapacitor was under the tensile conditions. Under the compression conditions, the contact of the layers in the supercapacitor became better which may result in a resistance decrease.

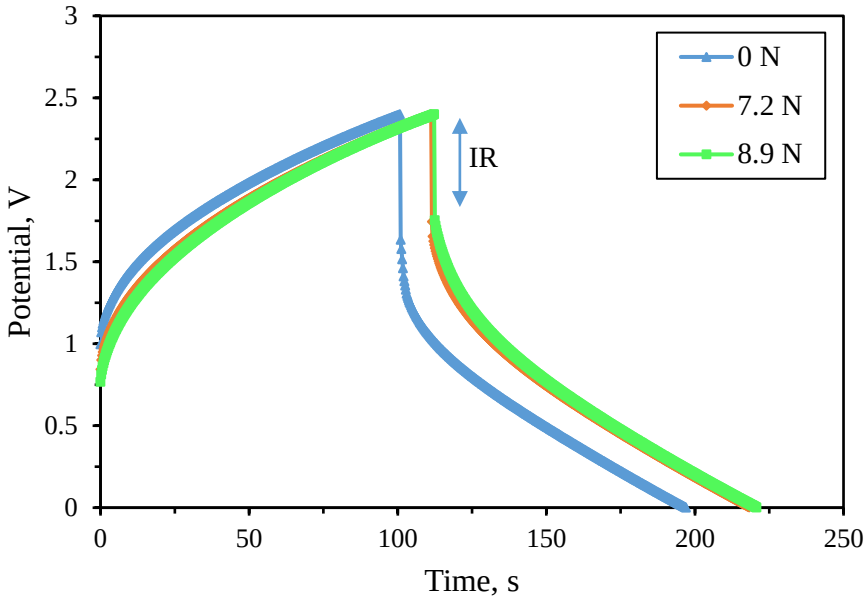


Figure 4.19 GCD curves of a strip supercapacitor at charging current of 0.010 A with different loads on the surface of current collector.

Figure 4.20a shows the Nyquist plots of this strip supercapacitor under different load conditions using a 4 mV AC modulation in a frequency range of 100 kHz to 0.01 Hz. Figure 4.20b shows the equivalent circuit model used for the EIS data simulation, which is similar to the equivalent circuit model shown in Figure 4.10b. In this model, CPE1 and CPE2 are the two constant phase elements, Rs and Rct represent the ESR and charge transfer resistance (CTR), respectively. It is seen that this equivalent circuit model fits well with the Nyquist plots measured. It is beneficial to obtain the ESR and CTR values by simulating the measurement of Nyquist plots using fitting equivalent circuit model (Table 4.11). Capacitance calculated from GCD curves (Figure 4.19), as well as ESR and CTR obtained from the simulation of Nyquist plots (Figure 4.20a).

At high frequency, the ESR values of the strip supercapacitor under different load conditions are 3.9 Ω for 0 N, 4.1 Ω for 7.2 N and 4.1 Ω for 8.9 N, separately. It seems the ESR values of this strip supercapacitor with different loads (0, 7.2 and 8.9 N) changed slightly. Generally, ESR values are mainly determined by the electrolyte resistance and contact resistance at the active material/current collector interface [188][164]. Because this strip supercapacitor was sealed by a laminator which protects the structure and avoids the electrolyte evaporating, in theory, the electrolyte resistance and the contact resistance

at the active material/current collector will not change. If the load is moderate, the organic electrolyte can get access into the effective surface area as usual, so the electrolyte resistance will not change dramatically, which results in the slight change of the ESR values. It is obvious that all the Nyquist plots of this strip supercapacitor with different loads have a similar shape. It shows that the equivalent circuit model is not changed under these load conditions. Moreover, the semicircle at high frequencies corresponds to the charge transfer limiting process, and the semicircle diameter presents the CTR [188][164]. When the load increased from 0 to 7.2 N, the diameter of the semicircle decreased approximately from 112 to 56 Ω, it illustrates the CTR of this strip supercapacitor with the load of 7.2 N decreased about 56 Ω compared to that of this strip supercapacitor without load. Then when the load increased from 7.2 to 8.9 N, the diameter of the semicircle decreased slightly from 56 to 50 Ω. That might be the reason why the capacitance for this kind of strip supercapacitors increased when the load is added.

Table 4.10 Capacitances based on the GCD curves, ESRs and CTRs obtained from the simulation of the Nyquist plots for the sample on the static load of 0 N, 7.2 N and 8.9 N.

| Performance / Condition | Capacitance, F | Increase, % (compared with original value) | ESR, Ω | CTR, Ω |
|---|---|---|---|---|
| 0 N | 0.588 (original) | | 3.9 | 112 |
| 7.2 N | 0.613 | 4.3 | 4.1 | 56 |
| 8.9 N | 0.618 | 5.1 | 4.1 | 50 |

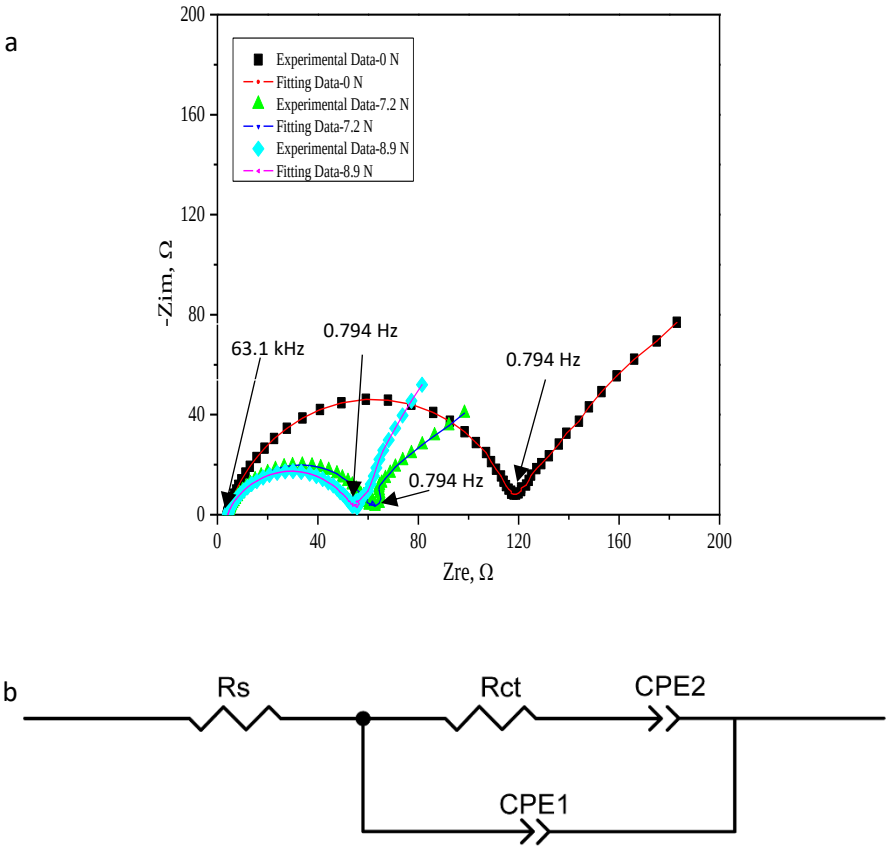


Figure 4.20 (a) Nyquist plots and simulation of the strip supercapacitor with different compressions using a 4 mV AC modulation in a frequency range of 100 kHz to 0.01 Hz; (b) Equivalent circuit model used to fit the ac impedance data.

Table 4.11 Parameters obtained from simulation of Nyquist plots of a strip supercapacitor with different compression.

| Compression, N | Rs, Ω | Rct, Ω | CPE1-T, $\Omega^{-1}$ $cm^{-2}$ $s^{P}$ | CPE1-P | CPE2-T, $\Omega^{-1}$ $cm^{-2}$ $s^{P}$ | CPE2-P |
|---|---|---|---|---|---|---|
| 0 | 3.9 | 112 | $8.1\times10^{-5}$ | 0.8545 | 0.0510 | 0.5943 |
| 7.2 | 4.1 | 56 | $17.1\times10^{-5}$ | 0.7890 | 0.0984 | 0.5941 |
| 8.9 | 4.1 | 50 | $16.8\times10^{-5}$ | 0.7855 | 0.1134 | 0.6965 |

Figure 4.21 shows the effect of the weight on the capacitance of the strip supercapacitors, and Figure 4.22 shows the corresponding ESRs and CTRs of this sample under different

weights. It was clear that the capacitance increases when the weight increases. When the weight increases, although the value of ESR changes slightly, the CTR drops dramatically. This is considered as the reason why the capacitance for this kind of strip supercapacitors increased when the weight is added.

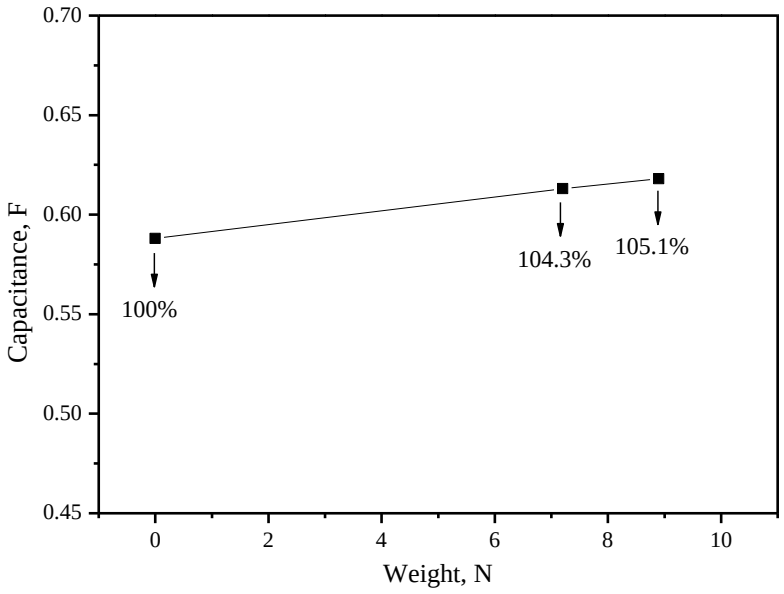


Figure 4.21 Effect of the mechanical press on the capacitance of the strip supercapacitor.

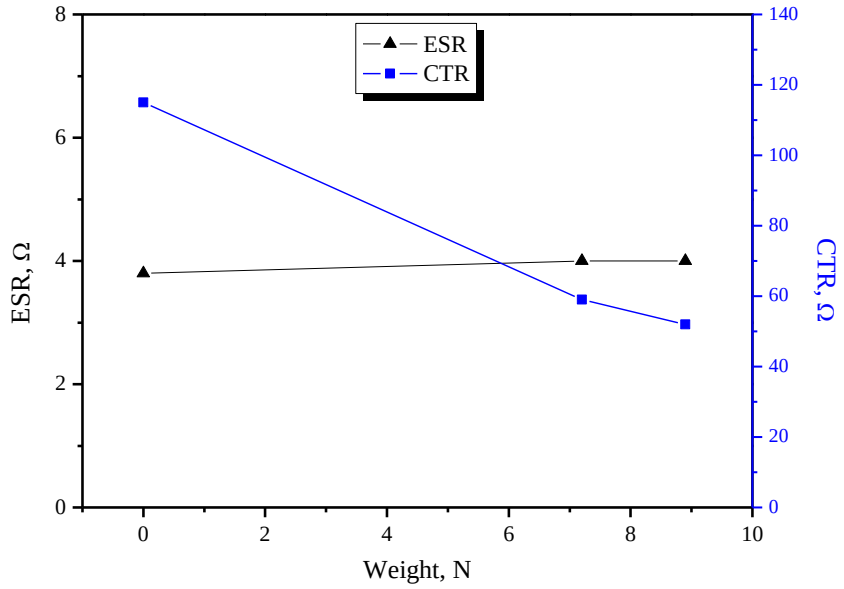


Figure 4.22 ESRs and CTRs for the sample under the static compression load of 0 N, 7.2 N and 8.9 N.

### 4.3.4. Demonstration of the practical usage of flexible strip supercapacitors

The potential applications of the flexible strip supercapacitors have been demonstrated with a portable LED lamp and a smart fan. As shown in Figures 4.23a and b, this charged strip supercapacitor can light up a red LED with the working potential of about 1.6 V. Because the organic solution of propylene carbonate ($C_4H_6O_3$) containing a certain molar of tetrabutylammonium tetrafluoroborate ($C_{16}H_{36}BF_4N$) was used as electrolyte for our strip supercapacitor, the charging potential of this strip supercapacitor used is about 2.4 V. The sample can be fully changed by an energy supplier in about 50 s. This charged strip supercapacitor can light this red LED well for more than 2 mins. The charged strip supercapacitor also could drive a smart fan with the working voltage of 1.8 V well, as shown in Figures 4.23c and d. Although the smart fan could only work for 7 s when the charged strip supercapacitor supplied the energy, it is still a progress for a narrow and thin flexible strip supercapacitor. These demonstrations prove our flexible strip supercapacitor has a big potential to be used for mobile energy supply.

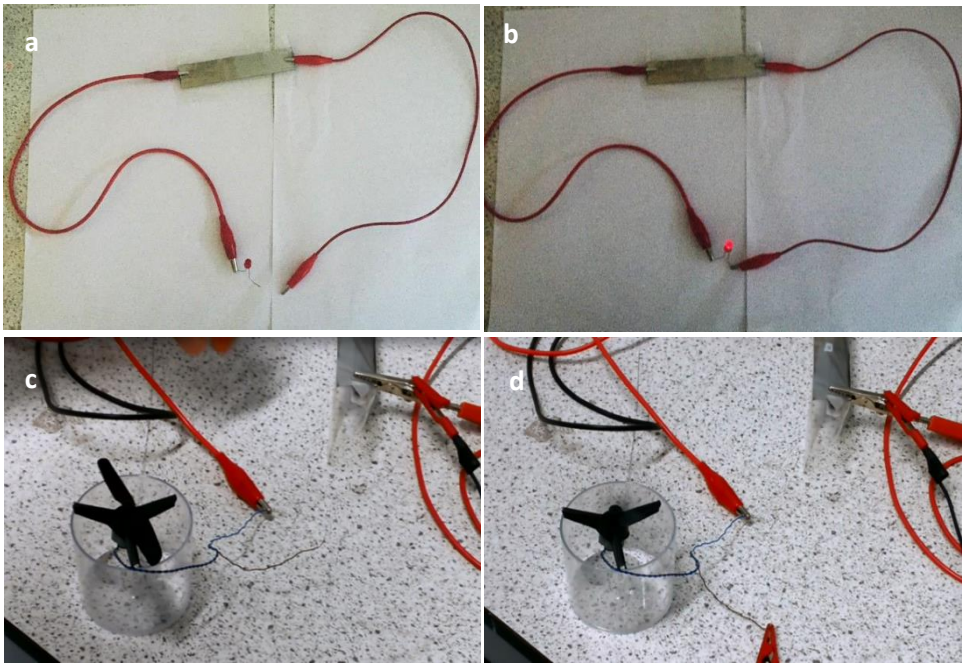


Figure 4.23 (a) Photograph of a red LED and a charged strip supercapacitor in an open circuit; (b) Photograph of a red LED turned on by a charged strip supercapacitor; (c) Photograph of a smart fan and a charged strip supercapacitor in an open circuit; (d) Photograph of a smart fan turned on by a charged strip supercapacitor in an open circuit.

## 4.4. Conclusions

In this chapter, the strip EDLCs were successfully designed, fabricated and characterised. The AC material was porous with an average size of the holes of about 100 nm, which allowed a good accessibility of the electrolyte to the inner surface of porous electrode and further provided a large surface area for electrical charge storage. At the same time, this kind of AC shows a good electrochemical scan rate performance and excellent electrochemical performance under different charging/discharging currents. Furthermore, the preparation process of EDLCs has a good reproducibility. These strip supercapacitors developed are still functional without shorting under bending conditions. At the initial bending at 30° there was significant change of capacitance, however, there was no significant changes found between the bending angles from 30 to 150°. Even at the large bending angle of 150°, the capacitance of the sample is still about 70% of the original capacitance for a free standing sample. Based on the simulation results of Nyquist plots the equivalent circuit model has been developed. The correlation between the capacitance and the ESR and CTR was established and it was found that the increases of the ESR and CTR are the main reason of the capacitance decrease when the strip supercapacitor was bent. The strip supercapacitors under static and dynamic mechanical tensile process work well: the capacitance and specific capacitance for this supercapacitor sample with the static load of 100 N or 200 N is bigger than that of this sample without loading, with an increase of 22% and 9%, respectively. Furthermore, it was found that the capacitance increased when the sample was in the mechanical tensile stress test and press conditions. The reason is believed to be that the mechanical loading is beneficial to the contact of each part in the strip supercapacitor which results in a low CTR. This study also demonstrates that single charged flexible strip supercapacitor could light a red LED well for more than 2 mins or drive a smart fan for 7 s. In a word, these narrow and thin flexible strip supercapacitors have a big potential for use as a mobile energy supply.

# Chapter 5. Manufacture and Optimisation of Strip Supercapacitors

## 5.1. Introduction

In a previous chapter, a kind of flexible strip supercapacitors were discussed that have been designed and manufactured by a blade coating method. The AC material used as the active electrode material is porous and shows good electrochemical scan rate performance. The manufacturing process of the strip supercapacitors has good reproducibility. Strip supercapacitors show a good flexibility during mechanical bending, stretching and compression conditions. In this chapter, the effect of key practical factors including the binder content, the thickness of the active layer and the concentration of the electrolyte on the performance of strip supercapacitors is studied using the JMP™ software ('statistical discovery' software from SAS™). This JMP™ software was a convenient tool to enable easy adjustment of the key experimental parameters of the supercapacitor design to allow the optimisation of the electrical performance as well as to see the key factors and to see if there were any interactions between them. These results could be very important for flexible strip supercapacitors design and optimisation of the performance.

## 5.2. Experimental methods

### 5.2.1. Design and manufacture of strip EDLCs

#### 5.2.1.1. AC electrodes

The electrodes which consist of a 316L stainless steel strip current collector (Fe/Cr18/Ni10/Mo3 with a thickness about 50 μm) coated with active materials were made by the blade coating method, the details being shown in Chapter 4. The AC slurries with different CMC binder content were made as follows: a certain amount of CMC is added into water/ethanol (1:1) solvent at room temperature with magnetic stirring overnight to give a CMC concentration of 5%. Then 0.5 g of the AC were added to the appropriate amount of CMC binder solution (see Table 5.1) with magnetic stirring for 8 h

to get a homogeneous slurry [189] with a certain binder content (based on the total mass of solids).

Table 5.1 Composition of the electrode activated material.

| Binder content /wt-% | 5% Binder solution/g | Solvent/g | AC/g |
|---|---|---|---|
| 1 | 0.101 | 2.769 | 0.5 |
| 2 | 0.204 | 2.766 | 0.5 |
| 5 | 0.526 | 2.444 | 0.5 |
| 7 | 0.753 | 2.217 | 0.5 |
| 8 | 0.870 | 2.100 | 0.5 |

#### 5.2.1.2. Manufacture the strip supercapacitors

The AC slurry was coated on the 3 mm wide exposed surface of the steel strip by blade coating. The thickness of the slurry was controlled by two plastic shim spacers with a 3 mm gap between them. The electrodes were dried in an oven at 100 °C for 2 h before the electrolyte was applied on to them. As shown in Figure 4.2, the two electrodes with electrolyte were separated by the separator to make a sandwich structure which was then sealed together using a laminator filled with plastic laminating pouches to make a complete strip supercapacitor and to make it sealed against loss of electrolyte.

### 5.2.2. Test and characterisation of the electrochemical properties

The electrochemical performance of the EDLCs developed was studied by CV, GCD and EIS, using a VersaSTAT 3 electrochemical workstation. The morphology of the porous electrode was studied by Zeiss Supera 35 SEM. The details of the characterisation methods and capacitance measurement methods are described in Section 3.3.

## 5.3. Optimisation of strip EDLCs using an experimental design method

An experiment is a process or study that results in the collection of data. The results of experiments are not known in advance. Usually, statistical experiments are conducted in situations in which researchers can manipulate the conditions of the experiment and can

control the factors that are relevant to the research objectives and remove those that have no significant effect. Experimental design is the process of planning a study to meet specified objectives in order to decrease the number of experiments. Planning an experiment properly is very important in order to ensure that the right type of data and a sufficient sample size and power are available to answer the research questions of interest as clearly and efficiently as possible. Therefore, it has been widely used in the field of engineering and science [190][191].

### 5.3.1. Factorial design

In any experimental procedure, several experimental variables or factors may influence the result. Factorial design, as an experimental design method, can investigate the influence of experimental variables/factors, and interaction effects on the response or responses. A full factorial design includes all possible combinations of levels of factors in a model [192]. The number of experiments increases when the number of factors increases. Normally, when the combinations of K factors are investigated at two levels, a factorial design will consist of $2^k$ experiments. In order to minimise the risk of missing non-linear relationships in the middle of the intervals, this classical factorial design was developed by considering the centre points in which all factors are set at their mid value and axial points [193]. This improved method is also called central composite design (CCD) method. As shown in Figure 5.1, there are three parts of CCD: the first one is a two level factorial design ($2^k$), where k is the number factors; the second part is the axial points (2k), which establish new extreme levels; the last part of CCD is centre point (m), which repents the middle levels of all the factors. Thus, CCD consists of $2^k+2k+m$ runs. In which, the axial points on the axis of each factor at a distance of $\pm\alpha$ ($\alpha = 2^{k/4}=1.68179$ for k=3) from centre of the cube as studied here.

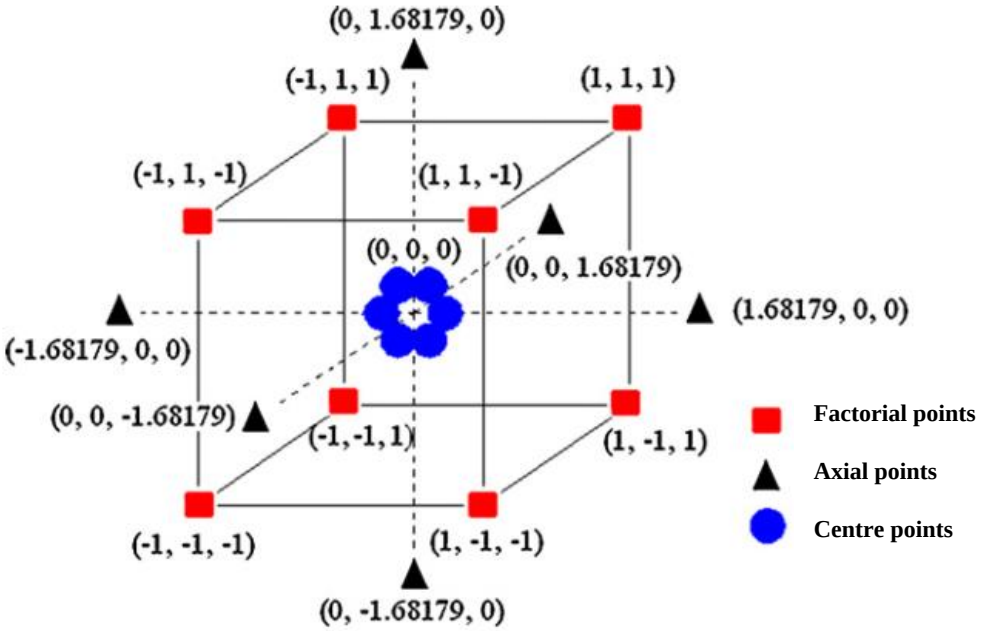


Figure 5.1 Central composite design with three factors and two levels [193].

### 5.3.2. JMP software

A 32 bit version of the JMP software was used for experimental design in this work. The JMP™ software, a tool for the design of experiments, can offer a practical approach for exploring multifactor experimental conditions. Some interacting factors may also be detected and a set of models can be developed to find the optimal conditions for the maximum output performance of the tested specimens. This visual discovery software is a powerful platform which can make data and information visualisation.

### 5.3.3. Experimental conditions

In this study, JMP™ was used to design the experimental conditions of the most expected significant parameters for EDLCs, which included the thickness (μm) of the AC slurry, the electrolyte concentration (molar), and the concentration (wt.%) of the CMC binder (based on the total mass of CMC and AC). In this study, the number of design factors is 3, and the number of centre points recommended in a CCD with three factors is 6, so the number of all the runs in CCD is $2^3+2\times3+6=20$ in this study [194]. The ranges of these

three factors were set at 125 to 625 μm for the AC slurry thickness, 0.5 to 1.5 mol/L for the electrolyte concentration and 1% to 8% for the CMC concentration, which had been determined by a large number of initial experimental studies.

Table 5.2 showed the coded and actual levels of design factors and experimental design conditions. The low, middle and high levels of each factor in the main factorial are coded as -1, 0 and 1, respectively, while the lowest and highest levels of the axial points are coded as -1.682 and 1.682. The relationship between the actual levels and coded levels of factors are determined according to the following equation:

$$X_i = \frac{x_i - x_i^0}{\Delta x_i} \tag{5.1}$$

Where $X_i$ is the coded value, $x_i$ is the corresponding actual value, $x_i^0$ is the actual value at the centre point and $\Delta x_i$ is the step change of the actual values corresponding to coded values unit from 0 to 1. In order to operate with material available (especially the shim) easily, the value of the actual level chosen in this study was the approximation in the model experiments. Because the actual value in the model is difficult to be obtained in our lab. The approximation value used in the experiments is very close to the actual value in the model, the output of experimental design is reliable.

Table 5.2 Variables experimental domain in the optimization of the strip supercapacitors

| Variables | Experimental domain | | | | |
|---|---|---|---|---|---|
| | -1.682 | -1 | 0 | 1 | 1.682 |
| Thickness | 125 | 250 | 375 | 500 | 625 |
| Electrolyte concentration | 0.5 | 0.7 | 1.0 | 1.3 | 1.5 |
| Binder content | 1% | 2% | 5% | 7% | 8% |

## 5.4. Results and discussion

20 EDLCs were fabricated based on the combination of conditions of the three parameters designed by the JMP™ software which were listed in Table 5.3. Furthermore, the correlation between these parameters and the impacts on the electrochemical performance of the EDLCs were studied and analysed using the software.

Table 5.3 Experiment parameters calculated by JMP

| No. | Thickness (μm) | Electrolyte (mol/L) | Binder (wt.%) |
|---|---|---|---|
| 1 | 125 | 1.00 | 5 |
| 2 | 375 | 1.50 | 5 |
| 3 | 375 | 1.00 | 5 |
| 4 | 250 | 1.30 | 7 |
| 5 | 500 | 0.70 | 2 |
| 6 | 250 | 0.70 | 7 |
| 7 | 375 | 1.00 | 5 |
| 8 | 500 | 1.30 | 2 |
| 9 | 250 | 1.30 | 2 |
| 10 | 500 | 0.70 | 7 |
| 11 | 375 | 1.00 | 5 |
| 12 | 250 | 0.70 | 2 |
| 13 | 375 | 1.00 | 1 |
| 14 | 375 | 1.00 | 8 |
| 15 | 625 | 1.00 | 5 |
| 16 | 375 | 1.00 | 5 |
| 17 | 375 | 0.50 | 5 |
| 18 | 375 | 1.00 | 5 |
| 19 | 500 | 1.30 | 7 |
| 20 | 375 | 1.00 | 5 |

### 5.4.1. Characterisation of the AC

Figure 5.2a shows a SEM image of the AC material used in this study. It can be seen that the size of the carbon particles ranges from hundreds of nanometres to tens of microns. Figure 5.2b displays a magnified view of the carbon particle surface, which reveals the typical porous structure of the AC material. The diameter of the pores is about 100 nm. This porous structure will provide a large surface area for electrical charges to be stored.

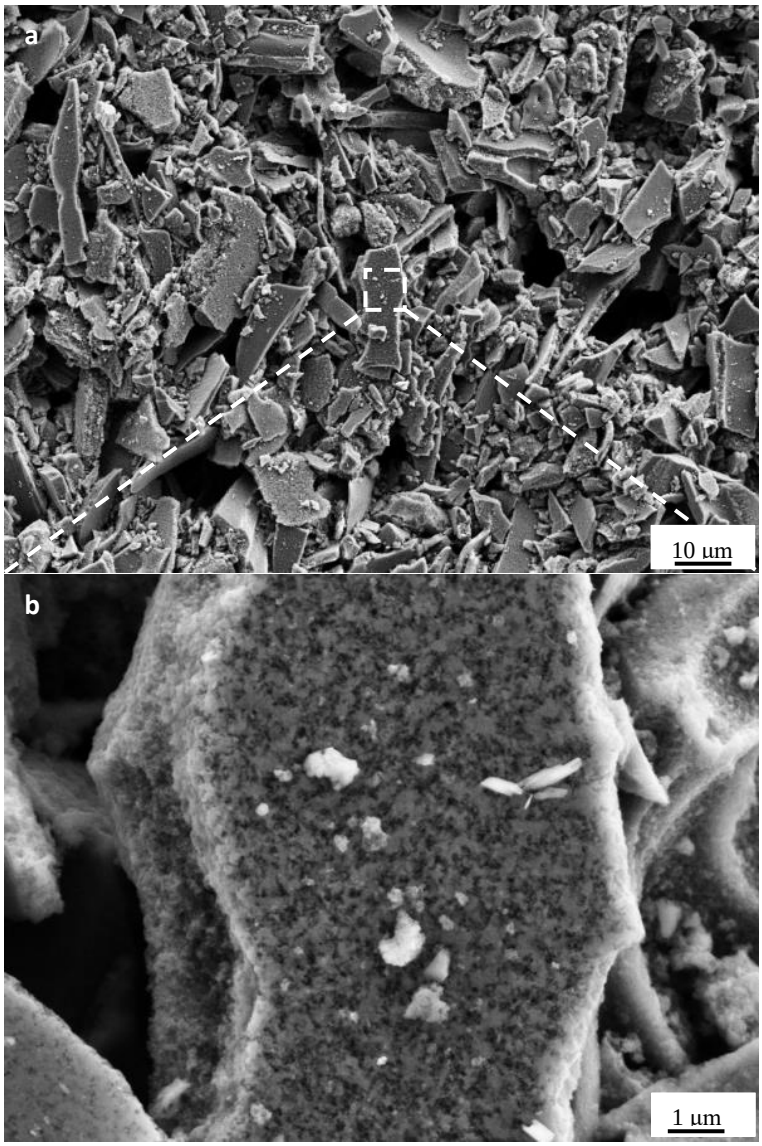


Figure 5.2 (a) SEM images of the AC electrode material; (b) Magnified porous surface of a carbon particle shown in (a).

### 5.4.2. Capacitances of all the strip EDLCs calculated from GCD curves

Based on equation (3.4) and (3.5) in Chapter 3, the capacitances and specific capacitances were calculated from the GCD curves, which are all summarized in Table 5.4. It is found that the highest capacitance with the value of 0.549 F was obtained when the supercapacitor has the thickest electrode (the thickness of the active layer is 625 μm). The highest specific capacitance (73.0 F/g) was obtained for the thinnest supercapacitor with the electrode thickness of 125 μm, however, this supercapacitor showed the smallest capacitance (0.121 F) among total 20 samples. Furthermore, the capacitance of the strip supercapacitor with 1% binder is 0.346 F, which is more than that of strip supercapacitors with highest binder content (8%), same thickness of active layer and electrolyte concentration (0.311 F). All the data are analysed in the following paragraph.

Table 5.4 Capacitances and specific capacitances calculated from GCD curves.

| No. | *Condition | m/g | C3/F | $C_{3m}$/F $g^{-1}$ |
|---|---|---|---|---|
| 1 | 125-1.0-5% | 0.0033 | 0.121 | 73.0 |
| 2 | 375-1.5-5% | 0.0105 | 0.277 | 52.7 |
| 3 | 375-1.0-5% | 0.0133 | 0.254 | 38.2 |
| 4 | 250-1.3-7% | 0.0098 | 0.152 | 31.0 |
| 5 | 500-0.7-2% | 0.0127 | 0.393 | 61.8 |
| 6 | 250-0.7-7% | 0.0079 | 0.235 | 59.4 |
| 7 | 375-1.0-5% | 0.0105 | 0.216 | 41.1 |
| 8 | 500-1.3-2% | 0.0127 | 0.259 | 40.8 |
| 9 | 250-1.3-2% | 0.0113 | 0.205 | 36.3 |
| 10 | 500-0.7-7% | 0.0177 | 0.204 | 23.1 |
| 11 | 375-1.0-5% | 0.0185 | 0.397 | 42.9 |
| 12 | 250-0.7-2% | 0.0118 | 0.317 | 53.8 |
| 13 | 375-1.0-1% | 0.0144 | 0.346 | 48.0 |
| 14 | 375-1.0-8% | 0.0170 | 0.311 | 36.6 |
| 15 | 625-1.0-5% | 0.0238 | 0.549 | 46.1 |
| 16 | 375-1.0-5% | 0.0185 | 0.325 | 35.1 |
| 17 | 375-0.5-5% | 0.0105 | 0.257 | 49.0 |
| 18 | 375-1.0-5% | 0.0157 | 0.373 | 47.5 |
| 19 | 500-1.3-7% | 0.0140 | 0.247 | 35.2 |
| 20 | 375-1.0-5% | 0.0124 | 0.293 | 47.3 |

*condition: thickness of each active layer-electrolyte concentration-binder content.

### 5.4.3. Effect of three main factors on the performance of the flexible strip EDLCs

Based on the capacitances calculated from GCD curves of the strip supercapacitors, the effect of the electrolyte concentration, the thickness of electrode active layer and the binder content on the performance of flexible strip supercapacitors are studied in this section.

#### 5.4.3.1. Effect of the electrolyte concentration

Previous research has indicated that the electrolyte concentration had an obvious effect on capacitance of a supercapacitor [195]. The electrolyte species and concentration are two main factors for electrolyte. In this study, the electrolyte was prepared by dissolving tetrabutylammonium tetrafluoroborate ($C_{16}H_{36}BF_4N$) into propylene carbonate ($C_4H_6O_3$), and this restricts the working voltage used to about 2.4 V with a safety margin against electrolyte decomposition. The range of this organic electrolyte concentration is from 0.5 to 1.5 mol/L for experimental design.

Figure 5.3 shows the effect of the electrolyte concentration on the capacitance of the EDLCs with the thickness of the AC material of 375 μm and the binder content of 5% in the experimental range. The value of capacitance for the strip supercapacitor with the electrolyte concentration of 1.0 mol/L is the average value of capacitance for these six samples with the same condition. It is found that the maximum capacitance of 0.31 F was achieved when the electrolyte concentration was 1.0 mol/L but there was no statistically significant change of the average capacitance from 0.26 F to 0.28 F when the concentration of the electrolyte changed from 0.5 mol/L to 1.5 mol/L. A linear fit was used to analyse these data. From this it is obvious that the fitting line is nearly parallel with the X-axis. This indicates that the electrolyte concentration has little effect on the capacitance of the EDLCs in this range of concentrations. In the reference [195], the result shows that if the electrolyte concentrations are in the range above a particular number, the maximum energy and the capacitance is insensitive to the electrolyte concentration. For our active electrode material and electrolyte type, the range we chose for our experimental design appears to be in the insensitive effect range.

In order to further detect the effect of the electrolyte concentration on the capacitance of the strip supercapacitor, EIS was used. Figure 5.4a showed the Nyquist plots of the strip

supercapacitors with different electrolyte concentrations using a 5 mV AC modulation in a frequency range of 100 kHz to 0.01 Hz. The ESRs and the CTRs obtained from the Figure 5.4b are shown in Table 5.5.

At high frequencies, ESR values of the strip supercapacitor with different electrolyte concentration were all about 12 Ω. The resistance values were obtained from the intercept of the Nyquist plots with the real axis. It seems the ESR values of the strip supercapacitor with different electrolyte concentration changed slightly. This suggests that the electrolyte resistance and the contact resistance of the active material/current collector interface of these three strip supercapacitors with different electrolyte concentrations are similar. It can be seen that there is a semicircle at high frequencies for the Nyquist plots of these strip supercapacitors with different electrolyte concentrations. And the two semicircles of the samples with highest (1.5 mol/L) and lowest (0.5 mol/L) electrolyte concentrations are basically superposed. The semicircle diameter of the Nyquist plot of the sample with the electrolyte concentration of 1.0 mol/L is also very close to that of the sample with the highest and lowest electrolyte concentration. The semicircle at high frequencies corresponds to the charge transfer limiting process, and the semicircle diameter represents the CTR, as revealed in other research [188] and [164]. It indicates that the values of CTRs for the samples are very close. The ESRs and CTRs changed slightly that is believed the reason why the capacitance increased slightly.

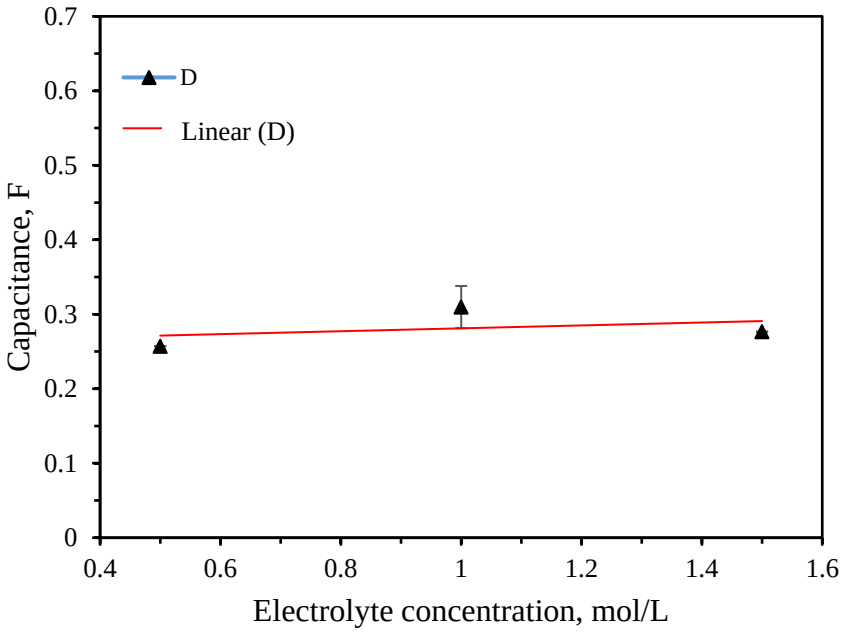


Figure 5.3 Effect of the electrolyte concentration on the capacitance of EDLCs.

a

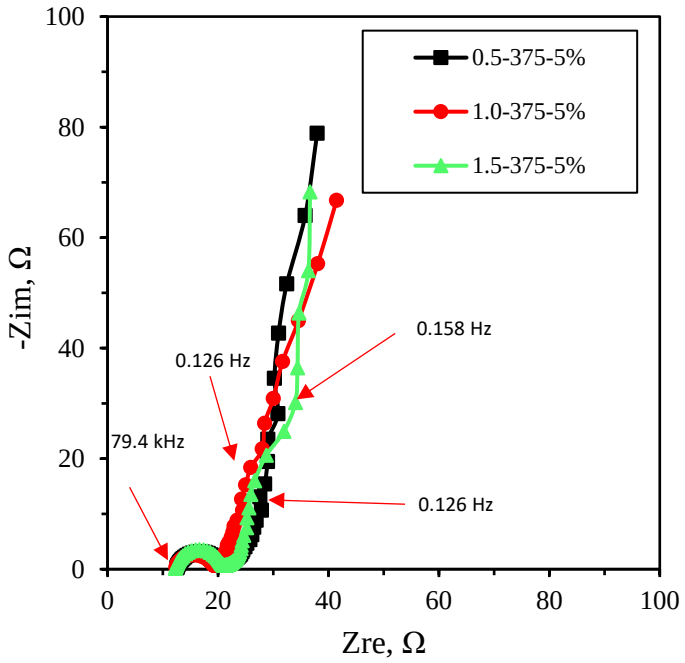

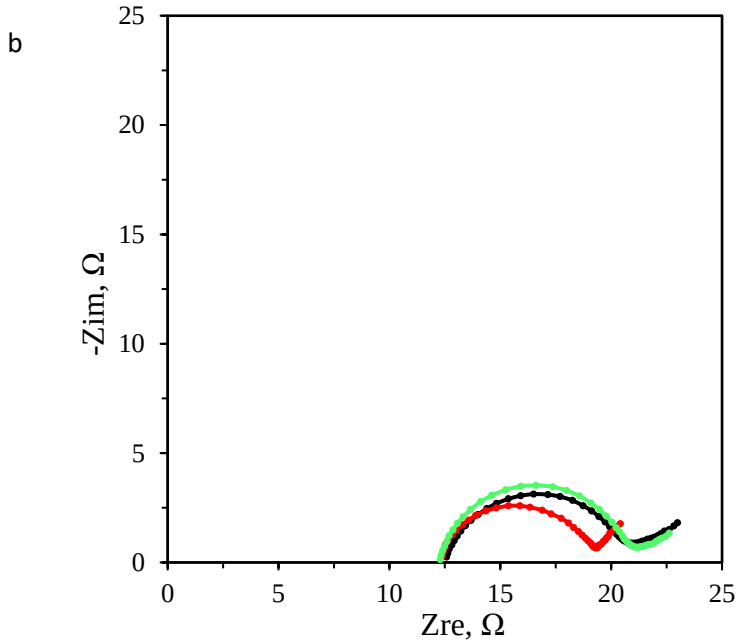


Figure 5.4 (a) Nyquist plots of the strip supercapacitors Nyquist plots of the strip supercapacitors with different electrolyte concentration (0.5 mol/L, 1.0 mol/L and 1.5 mol/L), same active layer thickness (375 µm) and same binder content (5%) using a 5 mV AC modulation for a frequency range between 100 kHz to 0.01 Hz; (b) the enlarged semicircle of the Nyquist plots in above Figure 5.4a.

Table 5.5 ESRs and CTRs obtained from the Nyquist plots of the strip supercapacitors with different electrolyte concentration in Figure 5.4.

| Electrolyte concentration, mol/L | ESR, Ω | CTR, Ω |
|---|---|---|
| 0.5 | 12.6 | 8.4 |
| 1.0 | 12.4 | 6.9 |
| 1.5 | 12.3 | 8.9 |

### 5.4.3.2. Effect of the thickness of the AC material layer

The experimental results also disclosed the relationship between the thickness of the AC material layer and the capacitance. As shown in Figure 5.5, the capacitance for all the EDLCs with the same CMC binder content increased with increases in the thickness of

the AC layer in the range of 125-625 μm. Figure 5.6 shows the mass of the AC material for the electrode with the same CMC binder content increased when the thickness of the active layer increased. For example, when the CMC content was 5%, the thickness of the AC layer increased 3 times from 125 μm to 375 μm, the mass of the AC material increased nearly 4 times from 3.3 mg to 14.7 mg, which further resulted in the increase of capacitance from 0.121 F to 0.299 F. It can be seen that both the mass of the AC materials and the capacitance of the supercapacitor increased as the thickness of the active layer increased. The increase of the AC mass was approximately linearly proportional to the thickness of the AC material layer (Figure 5.6) as expected. It was known when the width and length of active layer was fixed. The volume is linearly related to the thickness of the active layer. Therefore, the mass of AC for the same CMC concentration electrode should theoretically have a linear growth related on the thickness of active layer. The experimental results nearly agreed with the theoretical predicted trend. This suggested that the process of fabrication of strip supercapacitors was reliable. The increase of the capacitance of the supercapacitor may not have been expected to increase proportionally with the increase of the thickness or the mass of the AC material, because the time of electrolyte diffusion processes will be prolonged when the thickness is increased. This might be the main reason for decreasing the specific capacitance when the thickness of the active layer increased (Figure 5.7). Kumagai et al. [196] found the similar phenomenon that thinner electrodes could obtain higher specific capacitance in supercapacitors using AC material AP15 or RP25. A similar result was also presented in the carbon black (BP2000)-based supercapacitors, which is a different material from the supercapacitors fabricated in our work [197].

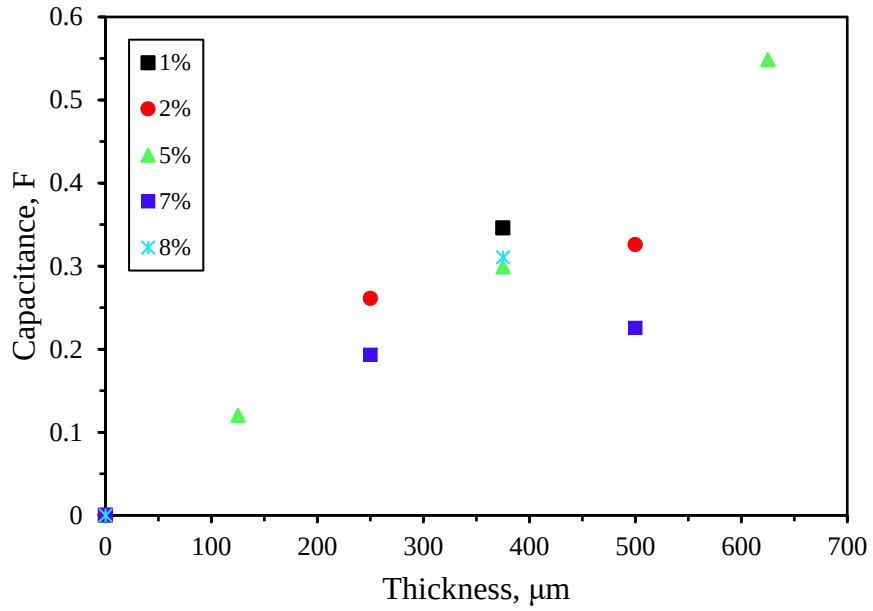


Figure 5.5 Effect of AC electrode layer thickness on the capacitance of EDLCs.

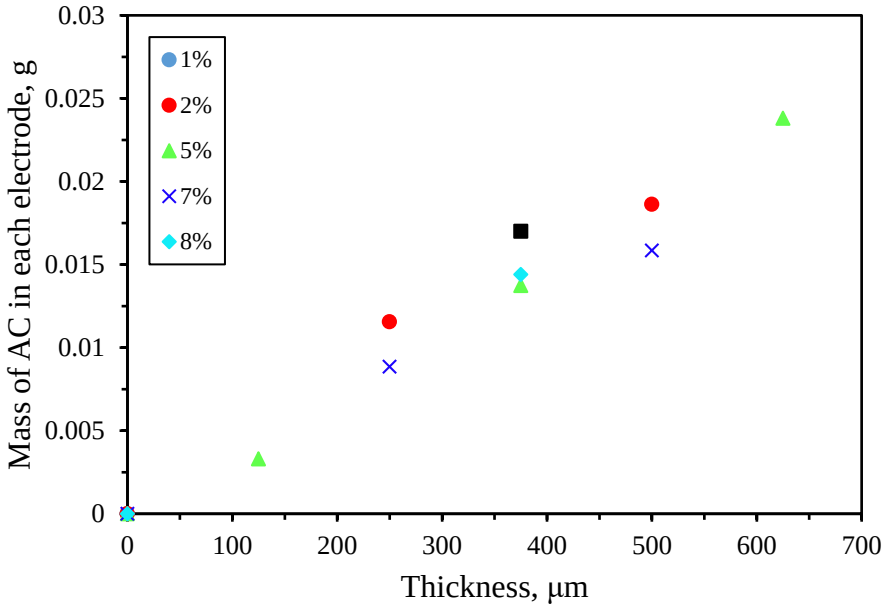


Figure 5.6 The relationship between the mass of AC in each electrode and AC electrode layer thickness.

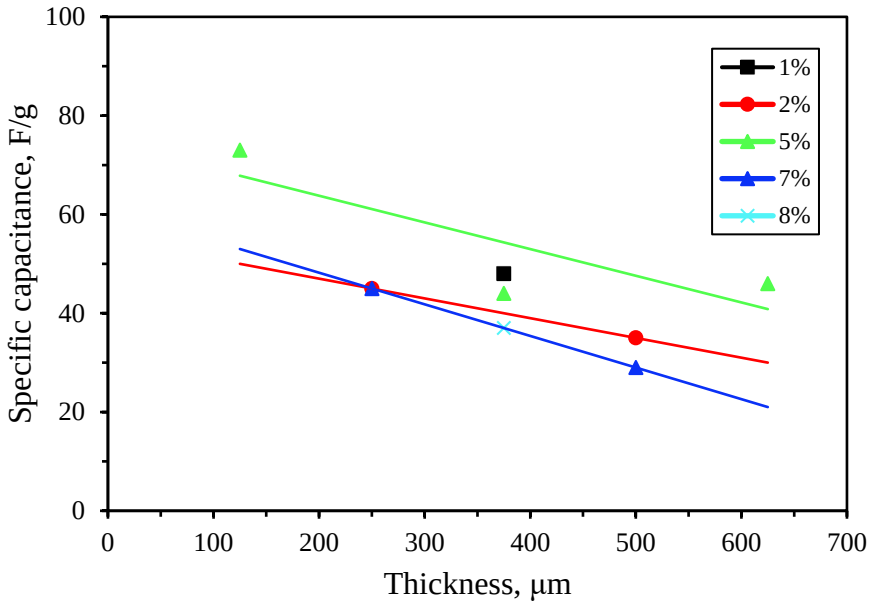


Figure 5.7 Effect of the AC electrode layer thickness on the specific capacitance of EDLCs.

In order to further study the effect of the thickness on the capacitance of the strip supercapacitors, the performance of strip supercapacitors with different active layer thickness (125 μm, 375 μm and 625 μm), same electrolyte concentration (1 mol/L) and same binder content (5%) were studied by GCD and EIS test. Figure 5.8 shows the GCD curves of these three samples recorded at the current of 0.005 A. It is seen that the shapes of the GCD curves are similar, but the discharge time increased when the thickness of the active layer increased, therefore, the corresponding capacitance increased (see Table 5.6).

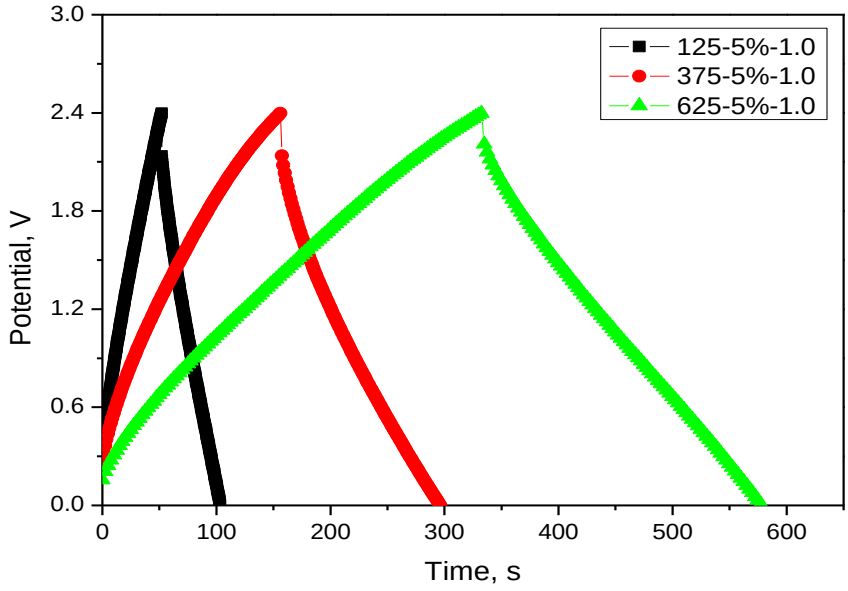


Figure 5.8 GCD curves of strip supercapacitors with different active layer thickness (125 µm, 375 µm and 625 µm), same electrolyte concentration (1.0 mol/L) and same binder content (5%) recorded at the current of 0.005 A.

Figure 5.9 shows the Nyquist plots of the strip supercapacitors with different active layer thicknesses using a 5 mV AC modulation in a frequency range of 100 kHz to 0.01 Hz. The capacitances calculated from Figure 5.8 and the ESRs and CTRs obtained from Figure 5.9 are all shown in Table 5.6.

At high frequency, ESR values are 22.9 Ω for the sample with the thickness of 125 µm, 12.4 Ω for the sample with the thickness of 375 µm and 5.8 Ω for the sample with the thickness of 625 µm, respectively (Figure 5.9 and Table 5.6). It is obvious that the ESR values decrease when the active layer thickness increases. It suggests that the electrolyte resistance and the contact resistance of the active material/current collector interface of these three strip supercapacitors with different active layer thicknesses became smaller. That is believed as the reason for the capacitance increases when the active layer thickness increases.

Values of CTR can be obtained from the semicircle diameters at high frequencies of different Nyquist plots for the samples from Figure 5.9. The CTR Values are 5.9 Ω for the

sample with the thickness of 125 µm, 6.9 Ω for the sample with the thickness of 375 µm and 4.2 Ω for the sample with the thickness of 625 µm, respectively. The CTR values change slightly compared with the variation of ESR values but probably not significantly. Next to the semicircle is the Warburg region, with the phase angle of 45°. This region, also called mass transport region is essentially governed by the diffusion of the charged species within the porous carbon [198]. It is found that the sample with the thickest active layer (625 µm) displays the longest Warburg diffusion region among these three samples. And the thinnest sample with the active layer of 125 µm shows a shortest Warburg diffusion region. In another words, the Warburg diffusion region becomes more prominent when the electrode active layer becomes thicker. The reason is believed that there is a higher porosity available for the transport of ions in the strip supercapacitor with the thicker electrode active layer.

a

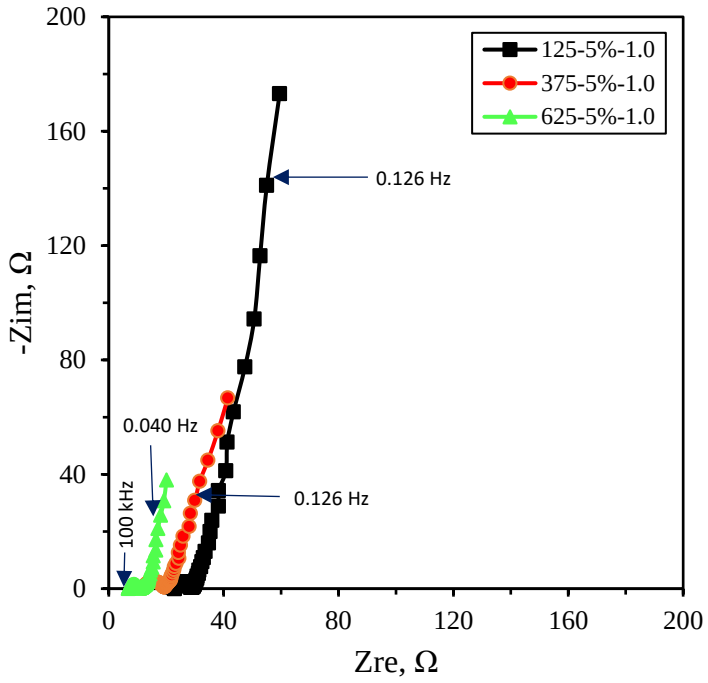

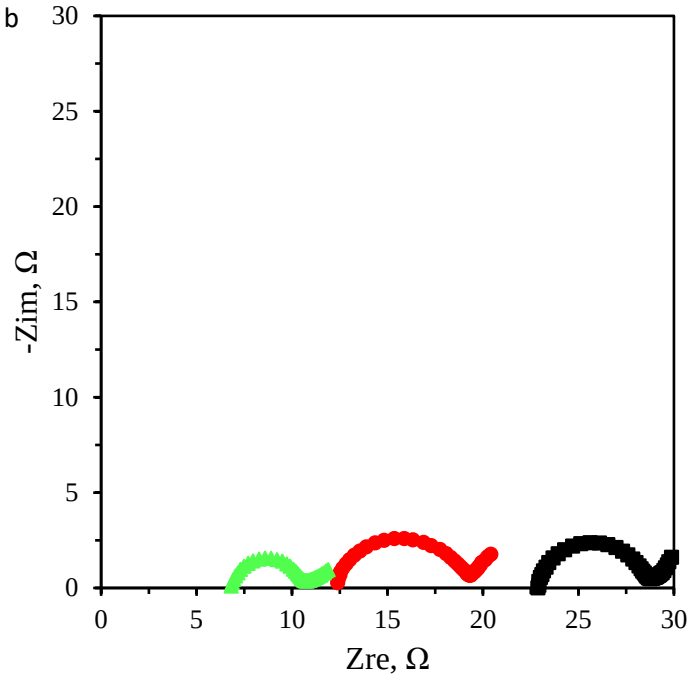


Figure 5.9 (a) Nyquist plots of the strip supercapacitors with different active layer thicknesses (125 µm, 375 µm and 625 µm), same electrolyte concentration (1 mol/L) and same binder content (5%) using a 5 mV AC modulation for a frequency range between 100 kHz to 0.01 Hz, (b) the enlarged semicircles of the Nyquist plots in above Figure 5.9a.

Table 5.6 Capacitances calculated from these GCD curves and other information collected from Figure 5.8 as well as ESRs and CTRs obtained from Figure 5.9.

| Thickness of active layer, µm | $t_{discharge}$, s | Capacitance, F | ESR, Ω | CTR, Ω |
|---|---|---|---|---|
| 125 | 51 | 0.121 | 22.9 | 5.9 |
| 375 | 139 | 0.325 | 12.4 | 6.9 |
| 625 | 223 | 0.549 | 5.8 | 4.2 |

### 5.4.3.3. Effect of the CMC binder content

A binder in the electrode layer can hold the carbon particles together to form a compacted active layer, and help these electrode materials adhere onto the current collector. As an important material which was part of electrode, the binder content was the third main factor studied in this work. Figure 5.10 shows the effect of the binder content on capacitance with different thicknesses of AC slurry. It can be seen that in general the capacitance of the strip EDLCs with the same thickness of active layer decreased when the binder content increased. Take the EDLCs with the active layer thickness of 500 µm for example, when CMC binder content increased from 2% to 7%, the capacitance decreased dramatically from 0.326 F to 0.226 F. This is probably because the increases in concentration of CMC would block more pores or cover the surface of the AC particles resulting in reducing the effective specific surface area for adsorption of the electrolyte. Similar results were present in other carbon based supercapacitors [197][189], in particular, Richner et al. [189] proved that the specific surface area of the active layer certainly decreased when the binder content increased (as measured by the BET method). Consequently, the capacitance of the EDLCs decreased when the content of binder increased.

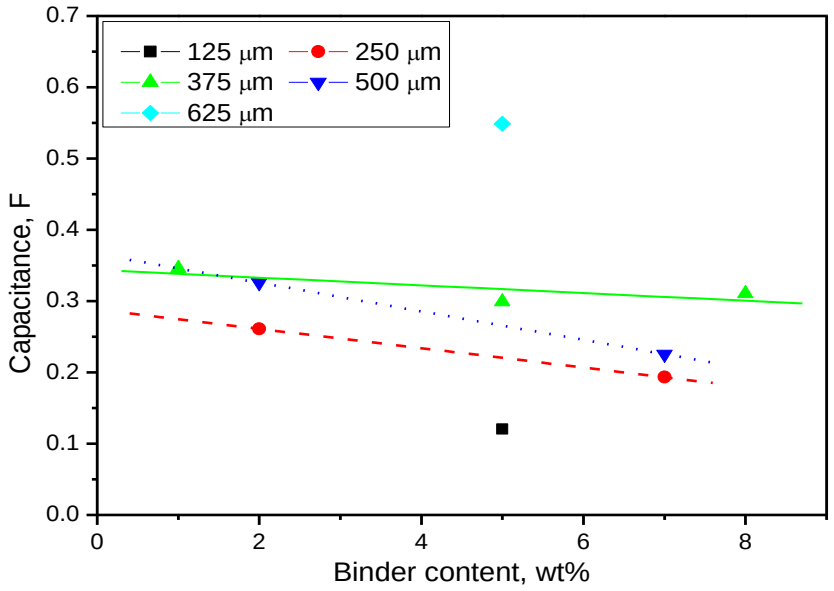


Figure 5.10 Effect of binder content on the capacitance of EDLCs.

The strip supercapacitors with different binder contents (2% and 7%), same electrolyte concentration (1.3 mol/L) and same electrode active layer thickness (250 µm) were used as an example to further detect the effect of the binder content on the capacitance of the strip supercapacitors. The performances of the samples were studied by GCD and EIS test. Figure 5.11 shows the GCD curves of these three samples recorded at the current of 0.005 A. The shapes of these GCD curves are similar. The iR drop decreases when the binder content of the electrode material increases from 2% to 7%. It is seen that the discharge time decreased when the binder content of electrode materials increased, so the corresponding capacitance decreased (Table 5.8).

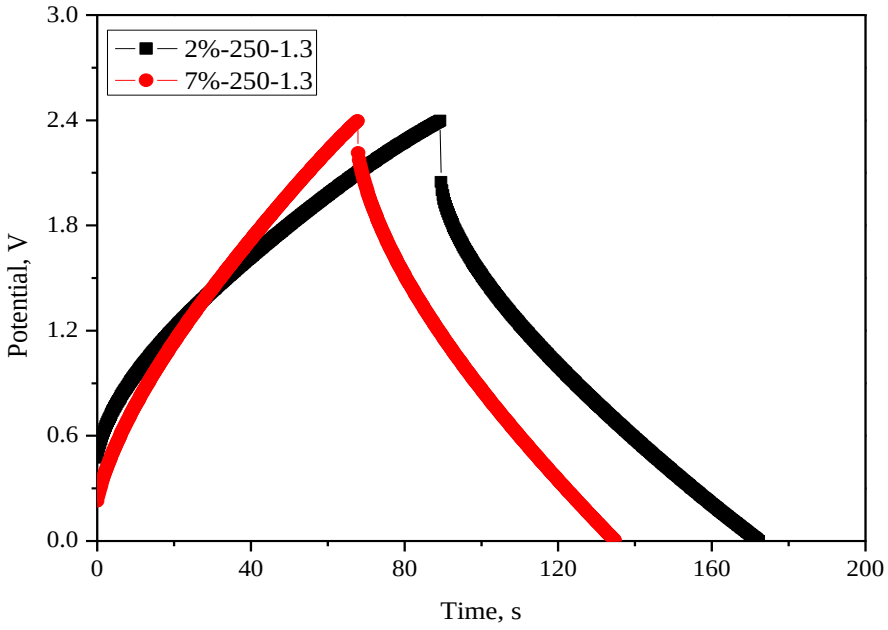


Figure 5.11 GCD curves of strip supercapacitors with with different binder contents (2% and 7%), same electrolyte concentration (1.3 mol/L) and same active layer thickness (250 µm) recorded at the current of 0.005 A.

Figure 5.12 shows the Nyquist plots of the strip supercapacitors with different binder contents using a 5 mV AC modulation in a frequency range of 100 kHz to 0.01 Hz. At high frequency, the ESR values are 13.2 Ω for the sample with the binder content of 2%, 10.9 Ω for the sample with the binder content of 7%, respectively (Figure 5.12 and Table 5.7). It is seen that the ESR values decrease a bit when the binder content increases. The

electrolyte resistance and the contact resistance of the active material/current collector interface of the strip supercapacitor with the binder content of 7% became a bit smaller than the sample with the binder content of 2%. The values of CTR values can be obtained from the semicircle diameters at high frequencies of different Nyquist plots for the samples from Figure 5.12. The CTR values decreased from 15.9 Ω to 8.0 Ω when the binder content of the strip supercapacitor increased from 2% to 7%, respectively. As is known, the main role of a binder inside the electrode layer is to hold carbon particles together forming an electrode porous layer and to let this electrode layer to adhere onto the current collector. When the CMC binder content increases, the connection of the AC particles becomes tight, which results in a good conductivity for electrode. The slurry of the AC is more adhesive, and helps the particle adhere tightly to the stainless steel current collectors. However, the available porous surface area decreases because of the AC content decreases as the binder content increase in the electrode active layer as well as some of the pores becoming blocked. This is believed to be the reason why when the binder content increases, the ESR and CTR values decrease while the capacitance also decreases.

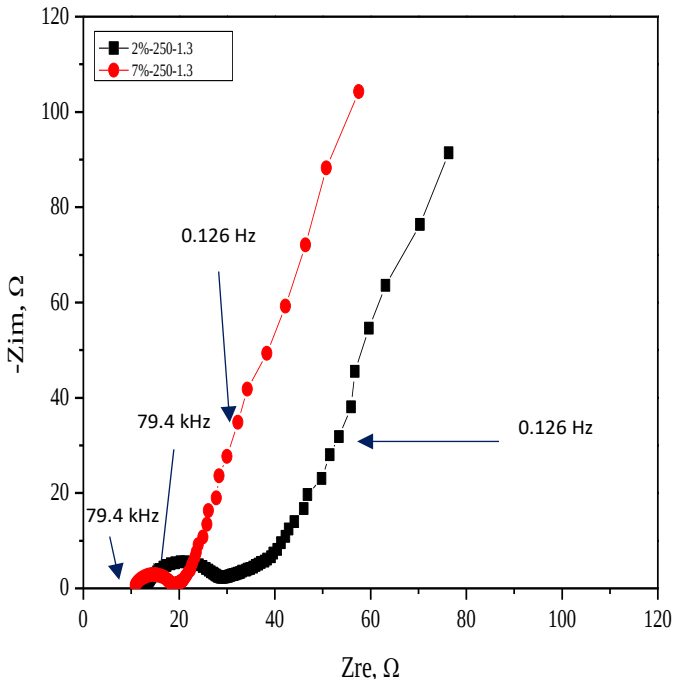


Figure 5.12 Nyquist plots of the strip supercapacitors with different binder contents (2% and 7%), same electrolyte concentration (1.3 mol/L) and same active layer thickness (250 µm) using a 5 mV AC modulation for a frequency range between 100 kHz to 0.01 Hz.

Table 5.7 Capacitances calculated from these GCD curves and other information collected from Figure 5.11 as well as the ESR and CTR obtained from Figure 5.12.

| Binder content, % | $t_{discharge}$, s | Capacitance, F | ESR, Ω | CTR, Ω |
|---|---|---|---|---|
| 2 | 83 | 0.205 | 13.2 | 15.9 |
| 7 | 67 | 0.152 | 10.9 | 8 |

#### 5.4.3.4. Experimental design results

The analysis of results above did not show that there were any interactions (cross-trems) in this experiment, and therefore the factors can be treated independently i.e. there was no synergy or anti-synergy between factors. Considering the factors mentioned above, a best fitting model was obtained by the JMP software for the capacitance of all the corresponding EDLCs with the input experimental design conditions. The result with the best fitting model is displayed as a contour plot in Figure 5.13, where the effect of the electrolyte concentration on the performance was not shown because it had little effect on the capacitance. This result showed a good agreement with the trend as shown in Figure 5.3. It can be seen from Figure 5.5 that the thickness of the active layer played a dominant role in the performance of the EDLCs. In addition, the contour plot also shows that when the content of the binder increased the capacitance of the supercapacitor decreased. These experimental design results were consistent with the experimental results analysed and discussed in Figure 5.3, Figure 5.5 and Figure 5.10.

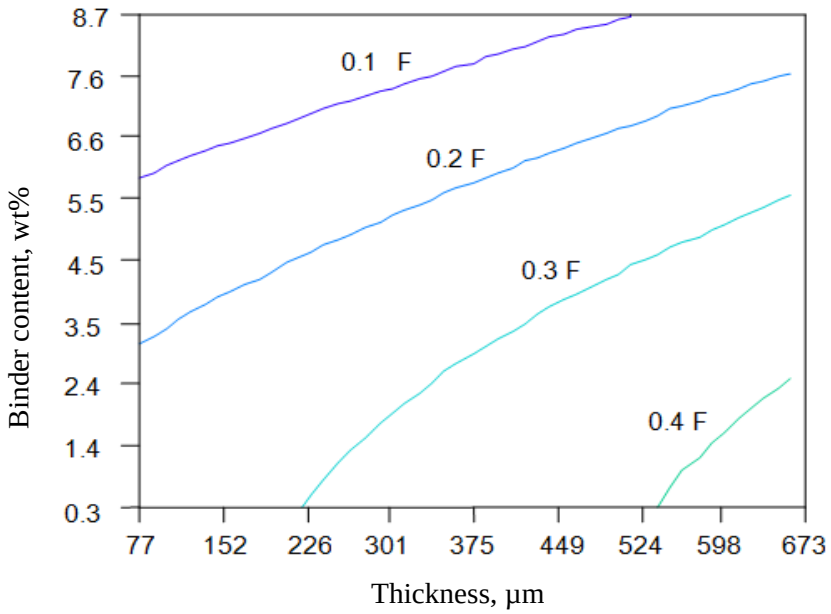


Figure 5.13 Results of JMP optimisation for three parameters (Note the electrolyte concentration was not shown on the graph due to its ignorable effect).

### 5.4.4. Testing the combination of the strip EDLCs in parrallel or series

Different combinations of supercapacitors in series or parallel are useful to obtain a desired operating voltage and energy, so the supercapacitors can be used in a wide range of applications. To exploit the applicability and stability of the combinations of multiple strip supercapacitors, the performance of two strip supercapacitors and their electrical combinations in series and parallel was examined.

Figure 5.14 shows CV curves of two single strip EDLCs (samples **a** and **b**) and their series and parallel combination circuits. The working potential of the two strip EDLCs in parallel is the same as the working potential of the individual single samples, and half of that of samples in series which is extended to 4.8 V. The area of CV curve of the parallel circuits is close to the total area of the two samples **a** and **b**. The area of CV curve of the series circuits would be half of the total area of these two samples. The capacitances calculated from the CV curves are shown in Table 5.8. The capacitance of the parallel circuits is 0.395 F, which is slightly less than the sum of the capacitances (0.407 F) of the two individual samples. The capacitance of series circuits is 0.094 F, which is almost the same as the theoretically expected series capacitance of 0.098 F. These results illustrate

that the electrical properties of the series and parallel combinations of the EDLCs show a good agreement with the theoretical models of series and parallel circuit combinations.

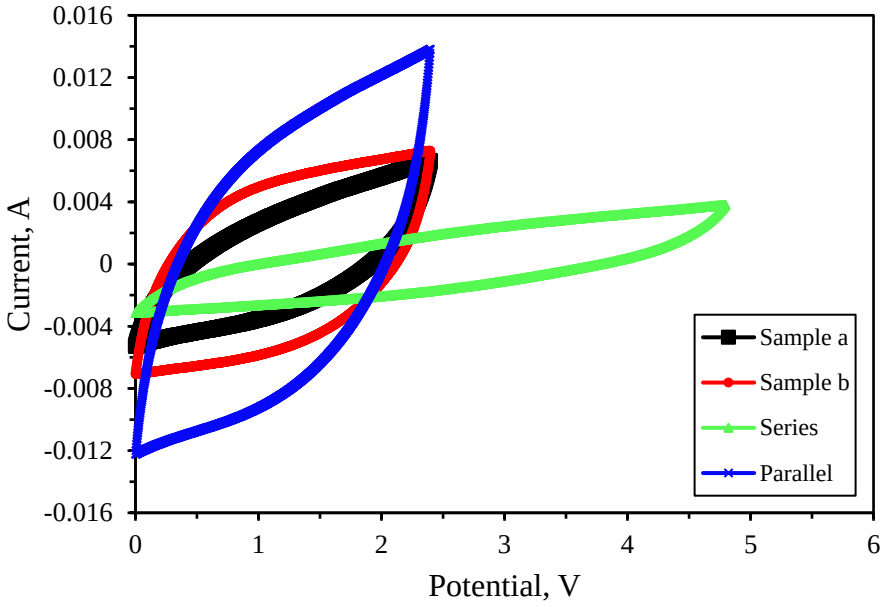


Figure 5.14 CV curves recorded at 20 $mVs^{-1}$ for two single strip supercapacitors and their electrical combinations in series and parallel.

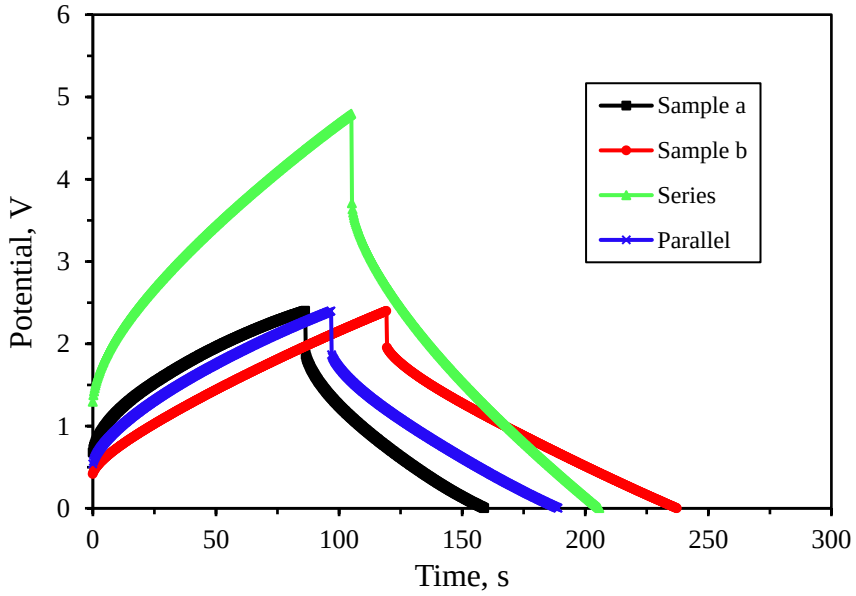


Figure 5.15 GCD curves of the 3rd cycle of each case, for single and series circuit 5 mA is used, and 10 mA for the parallel circuit.

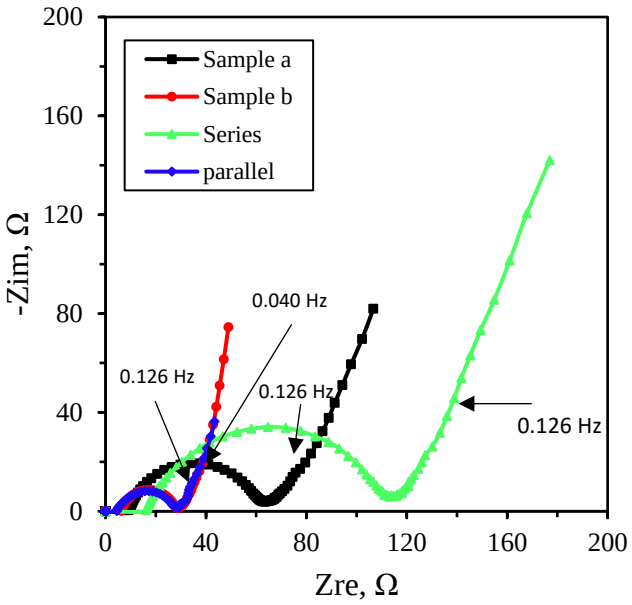


Figure 5.16 Electrochemical performances of two single strip supercapacitors and their electrical combinations in series and parallel using a 4 mV AC modulation for a frequency range of 100 kHz to 0.01 Hz.

Table 5.8 ESRs from Nyquist plots and the capacitances from CV curves and GCD curves with those calculated using theory for series and parallel circuits

| | Capacitance, F (CV) | | Capacitance, F (GCD) | | ESR, Ω | |
|---|---|---|---|---|---|---|
| | exp. | theory | exp. | theory | Exp. | theory |
| Sample a | 0.165 | | 0.194 | | 9.3 | |
| Sample b | 0.242 | | 0.301 | | 6.3 | |
| Series | 0.094 | 0.098 | 0.136 | 0.118 | 15.8 | 15.6 |
| Parallel | 0.395 | 0.407 | 0.493 | 0.495 | 4.3 | 3.8 |

Figure 5.15 shows GCD curves at charge currents of 5 mA for the two individual supercapacitors and the series circuit and of 10 mA for the parallel circuit. The potential window of the parallel circuit is 2.4 V, the same as those of two single strip

supercapacitors, and half of the series circuit. As shown in Table 5.8, capacitances of different cases calculated from the GCD curves show the same trend as those calculated from CV curves. Nyquist plots of the two single samples and the combinations in series or in parallel are shown in Figure 5.16. The shapes of electrochemical impedance curves for the combination circuits are similar to those of the single strip EDLCs. It is observed that there is a sharp increase in the imaginary part of the impedance at the lower frequencies. This trend is consistent with a capacitive behaviour of an electrode. Meanwhile, the semicircular loops shown at high frequencies are probably associated with the porous structure of the AC materials [199]. The high intercept on the real axis is the ESR, as shown in Table 5.8. The capacitance values obtained from the experiments and theoretical calculations for the combinational models of series and parallel resistive and capacitive circuits are also given in Table 5.8. The capacitance of sample **b** is 0.242 F, which is about 1.47 times the sample a's capacitance; it is easily found that the ESR of sample **a** is also about 1.48 times that in sample **b**. For the case of the series circuit, the ESR is 15.8 Ω, which is very close to the sum of the ESRs of the two samples **a** and **b**; the ESR of the parallel circuit is about 4.3 Ω, which is slightly higher than the total theoretical ESR of the parallel circuits of samples **a** and **b**. These results are close to the expected ones for the two different circuits.

The energy (*E*) and power (*P*) of strip supercapacitors can be calculated by [114]

$$E = \frac{1}{2}CV^2 \tag{5.2}$$

$$P = \frac{E}{t_{discharge}} \tag{5.3}$$

where *V* is the operating voltage and *C* is the capacitance of the strip supercapacitors. The capacitance from the GCD curve together with the energy and power based on this capacitance are shown in Figure 5.17. The energies of samples **a** and **b** are 0.559 J and 0.867 J, respectively. The energy of the two strip EDLCs in parallel is 1.420 J, which is very close to the sum of the energies of the two samples (1.426 J), while the energy of the two EDLCs in series has a slightly discrepancy (1.567 J) for this trend. Furthermore, the power of the two EDLCs in series is 0.0156 W, very close to that of these samples in parallel (0.0154 W), which is very close to the sum of sample a's (0.0077 W) and sample b's power (0.0074 W).

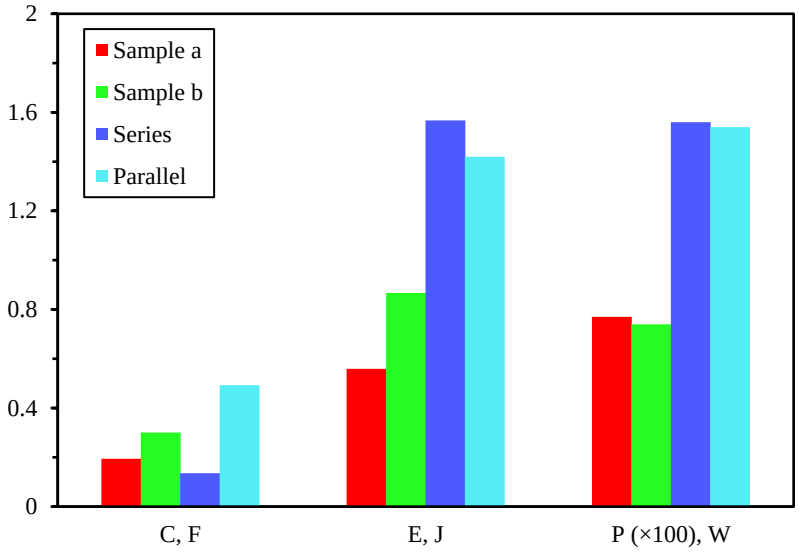


Figure 5.17 The energy, power and capacitance of two single strip supercapacitors and their electrical combinations in series and parallel calculated from GCD curve.

## 5.5. Conclusions

The flexible strip shaped EDLCs (3 mm×100 mm) with different conditions were successfully manufactured and characterized in this study. The relationships between the performance and key factors of the strip EDLCs including the CMC binder concentration, the electrolyte concentration and the thickness of active material layer were presented. The results showed that in the range of 0.5-1.5 mol/L, the electrolyte concentration had little effect on the capacitance; when the thickness of active electrode layer increased from 125 μm to 625 μm, the capacitance increased; and the capacitance decreased when the binder concentration increased from 1% to 8%. These results are very important for flexible strip supercapacitor design and the electrochemical performance improvement. Meanwhile, two sample strip supercapacitors were combined in series and parallel to assess their electrical property as a power supplier. The performance of the series or parallel circuit showed a good agreement with the theoretical models for series and parallel circuit combinations. The strip supercapacitors can be used in various combinations of series or parallel to obtain desired energy or power for different applications.

# Chapter 6. Fabrication and Characterisation of Fibre supercapacitors

## 6.1. Introduction

In Chapter 4 and 5, strip supercapacitors using low-cost materials were developed. These strip supercapacitors show reasonable flexibility: they work well under mechanical bending, stretching and compression conditions. Furthermore, the effect of key practical factors on the performance was studied, and the performance of the strip supercapacitors can be optimised by controlling these practical factors. In order to further improve the weave ability, a coaxial fibre supercapacitor was designed [115][200][201] and manufactured in this chapter. This coaxial fibre structure contains five coated layers: two electrodes layers, two current collector layers and a gel electrolyte. The structure of this coaxial fibre supercapacitor developed was different from either the two fibre electrodes supercapacitor [114] or mesh based supercapacitors [179]. The coaxial fibre was all-solid and had the useful property of being able to be woven to produce different shaped energy storage fabrics.

## 6.2. Experimental methods

### 6.2.1. Materials

Phosphoric acid (dry $H_3PO_4$ powder) and polyvinyl alcohol (PVA, MW 146,000-186,000, > 99% hydrolysed) were purchased from Sigma-Aldrich and used without further purification. Copper wire (50 μm in diameter) obtained from Advent Research Materials was used as the core conductor material. Commercial carbon-based Chinese ink was used as the active coating material. Silver paint (0.001 Ω·cm when fully hardened) was purchased from RS Components Ltd and used as the conducting layer material.

### 6.2.2. Preparation of gel electrolyte

PVA powder was dissolved into deionized water at 80 ℃ under magnetic stirring. When the PVA particles were fully dissolved, the solution became transparent and viscous. Then the $H_3PO_4$/PVA gel electrolyte was made by dissolving 0.8 g $H_3PO_4$ and 1 g PVA in 10 mL deionized water [114].

### 6.2.3. Design of fibre supercapacitors

Based on the working mechanism [1][115], fibre supercapacitors have been designed [201]. As shown in Figure 6.1a, the typical EDLCs consist of the five layers which are two current collectors, two active layers with electrolyte and a separator containing the electrolyte. Following this typical structure of an EDLC, a coaxial single fibre supercapacitor with five layers was designed and manufactured (see Figure 6.1b). The central metal wire and the outer layer of silver paint are current collectors. Two active layers made of Chinese ink are separated by a gel electrolyte layer and serve as electrodes. The energy is stored by the accumulation of electrical charge at the boundary layers between the two electrodes and the electrolyte.

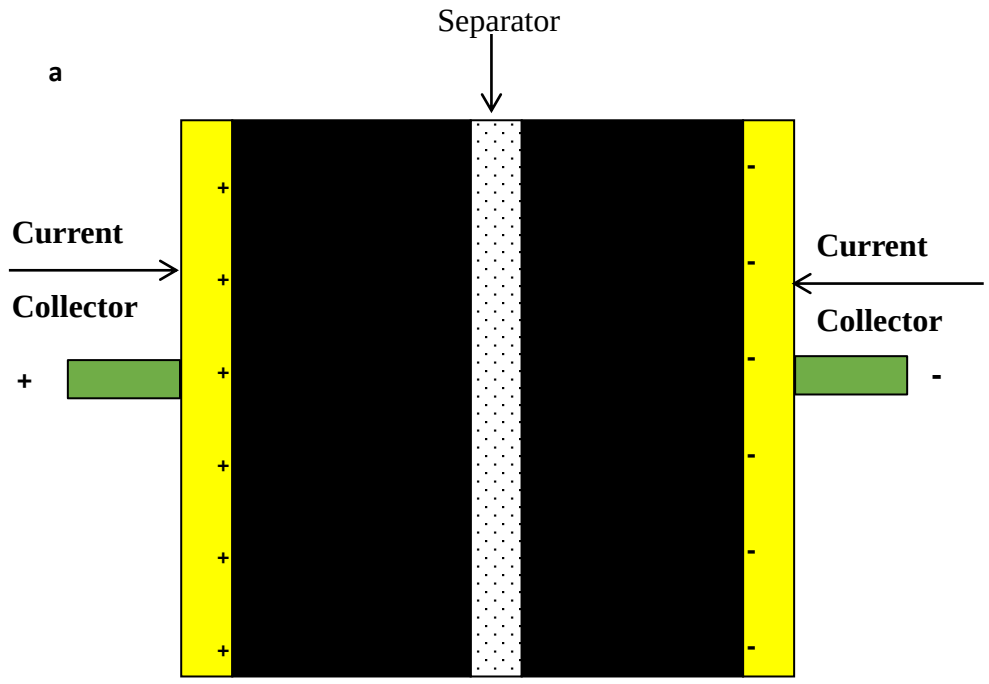

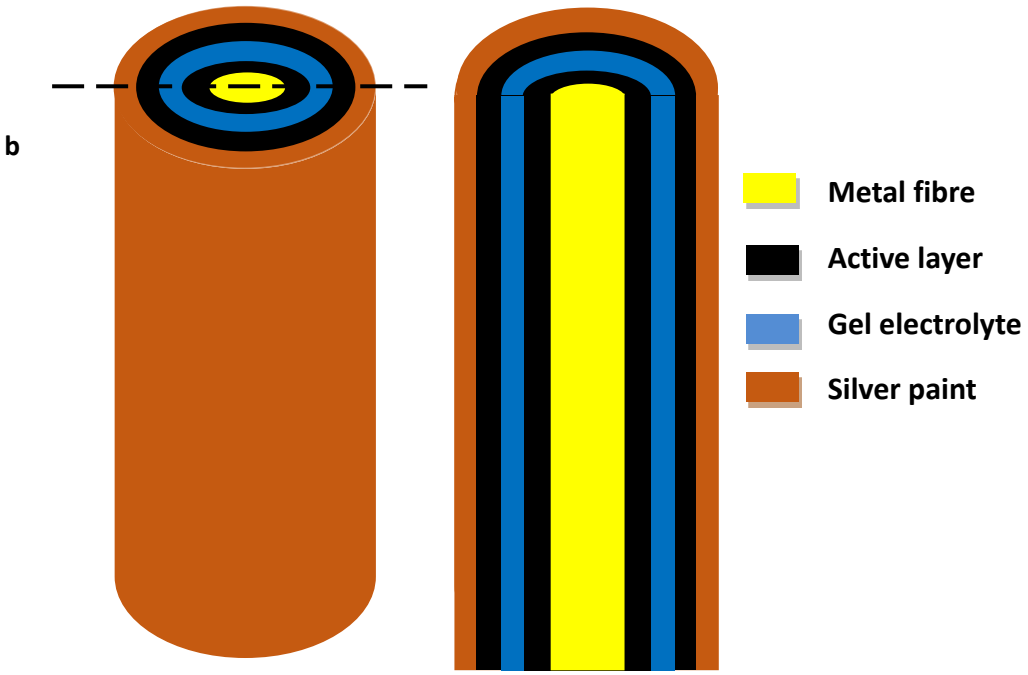


Figure 6.1 (a) Typical structure of an EDLC; (b) 3-D schematic of four coating layers on the metal fibre.

### 6.2.4. Manufacturing method

#### 6.2.4.1. Dip-coating method

Dip coating involves simply immersing a workpiece into a suitable tank containing the coating material, then withdrawing the workpiece with the coating material, and forcing drying or baking the wet coating to achieve the final coating layer [202]. Dip coating is used in many industries for both primer and one-coat finishes, because of its simplicity, low cost, ease of control, good coverage and consistency [202].

Figure 6.2 schematically shows the dip-coating method used to fabricate the fibre supercapacitors. A metal wire was used as a core fibre and a current collector. Firstly, the core fibre was cleaned by ethanol, and then the ink was coated on the surface of this core fibre. After the ink dried, a gel electrolyte ($H_3PO_4$/PVA) was coated as the separator with the $H_3PO_4$ electrolyte. When the unnecessary solvent in this gel electrolyte was evaporated and this gel electrolyte became harder, another ink layer was coated carefully.

When this layer dried, the silver paint was coated as another current collector layer. This five-layer structure for energy storage fibre is fully manufactured by hand with the details following.

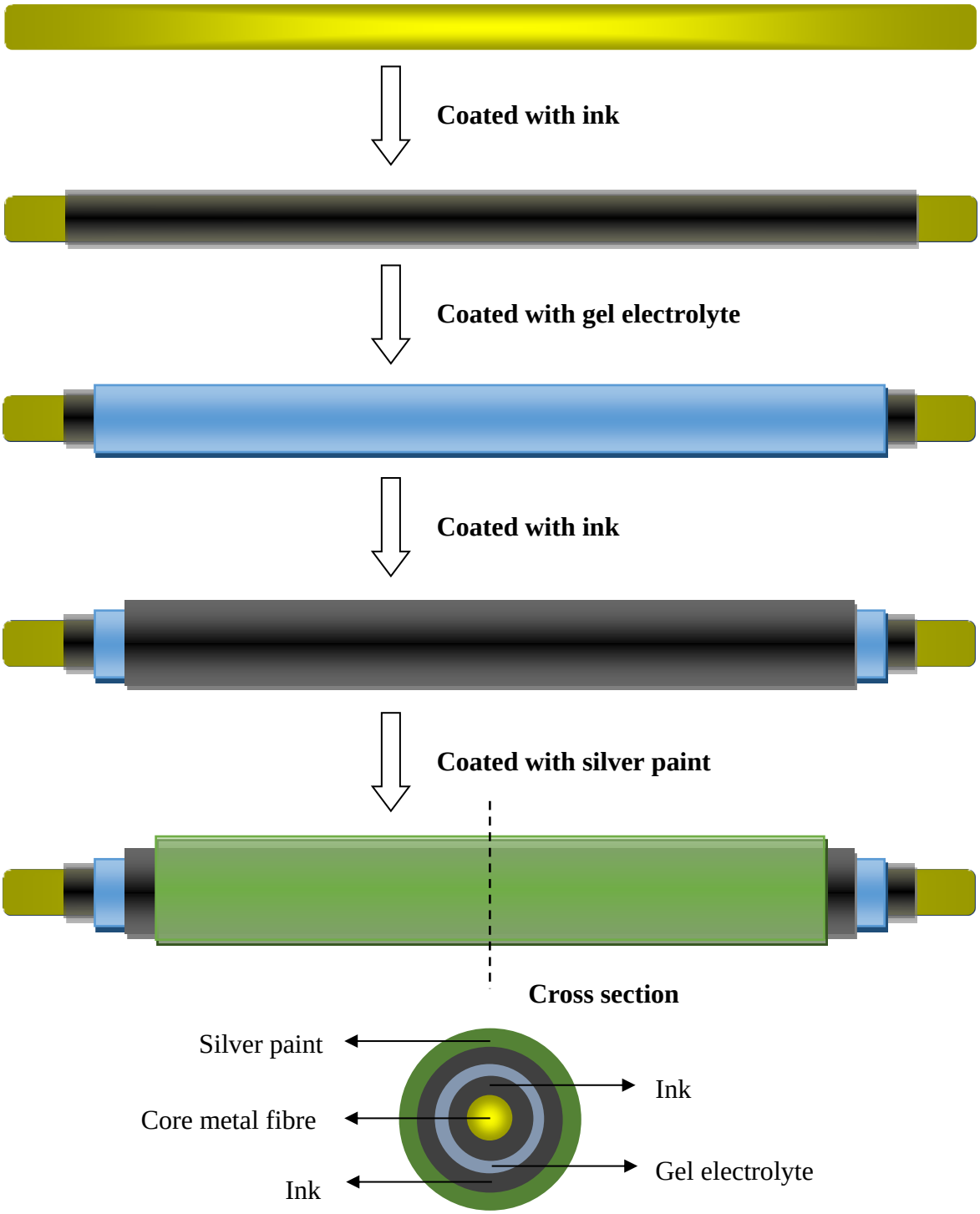


Figure 6.2 Schematic of dip-coating method used for manufacturing fibre supercapacitors.

### 6.2.4.2. Dip-coating device

Figure 6.3 schematically shows two experimental setups for coating the energy storage fibre. The schematic of a manual control dip-coating device is shown in Figure 6.3a. A reel of metal wire was put on a rod with a step as an axle though a crude bearing fixed horizontally onto a plate. A weight was clamped to the bottom end of the core wire to keep the wire straight and in alignment with the coating vessel, which was made by cutting a commercial plastic pipette. A turning handle was used to control the coating speed. When the coating process is carried out, coating liquid is filled in the coating vessel. During the movement of the core metal wire through the hole in the bottom of the coating vessel, the wire drags some of the coating liquid with it, then is dried by hair drier, the solvent is evaporated and the coating materials deposit on the wire. In order to control the coating speed, the dip-coating device was redesigned and improved. Figure 6.3b shows the automatic dip-coating device which was controlled by a RE 540/1 motor with a gearbox. The manual handle was replaced by a motor driving the axle with two-direction controller in the new experimental setup. This motor with two-direction controller can drive the fibre up and down to increase the coating times which will increase the thickness of a coating layer. Different vessels with the holes of 150 µm, 230 µm, 330 µm and 430 µm for diameter were used to coat the first ink layer, the gel electrolyte layer, the second ink layer and the silver paint layer, respectively. Two pulleys were also fixed horizontally on the plate to control the position of the core fibre.

a

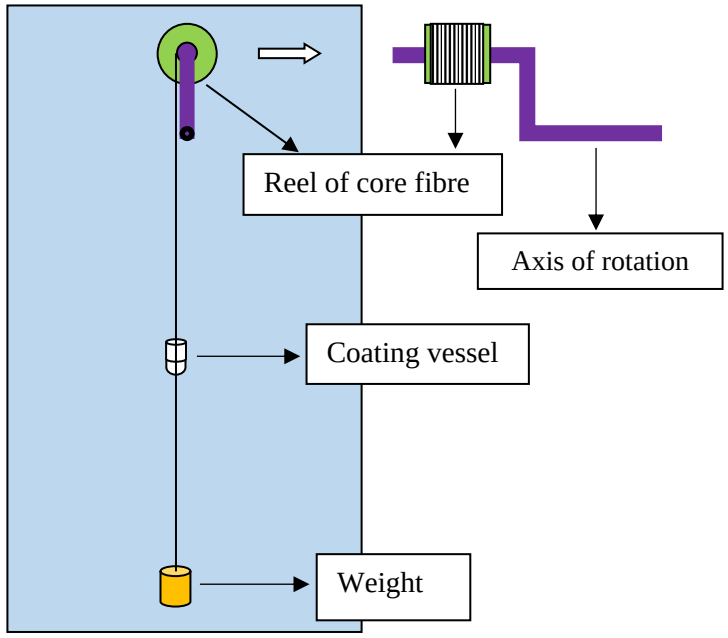

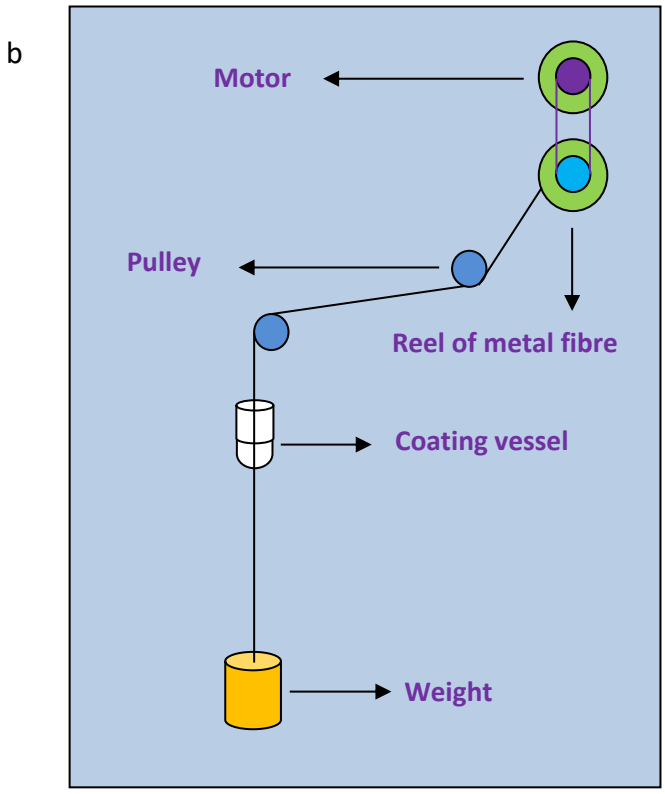


Figure 6.3 Schematic of manual control dip-coating device (a) and the automatic dip-coating device (b).

### 6.2.5. Characterisation method of fibre supercapacitors structure

The five-layer structure of a cross-section of the fibre supercapacitor was observed by optical microscopy and SEM, and their elements were analysed by the energy dispersive spectroscopy (EDS). And SEM samples mounted some fibre supercapacitors were produced by resin method: these fibre supercapacitors were set up by a tweezer in a rubber mould first and then some liquid resin were poured into this mould to maintain this vertical state until removing the tweezer. After about 6 h, this liquid resin was solidified. By polishing, a SEM sample mounted some fibre supercapacitors could be prepared for the cross-section observation.

### 6.2.6. Characterisation of the electrochemical properties of fibre supercapacitors

The electrochemical performance of the energy storage fibres developed was studied by CV, GCD and EIS using a VersaSTAT 3 electrochemical workstation. The details of the characterisation methods and capacitance measurement methods are described in Section 3.3 of Chapter 3.

Here, an equation was added to calculate the specific capacitance per unit length:

$$C_L = C/L \tag{6.1}$$

$C$ is the capacitance, and $C_L$ is the specific capacitance per unit length. $L$ is the length of the fibre supercapacitors.

EIS is a very effective method to study in-depth the electrochemical performance of supercapacitors. Figure 6.4 shows a typical Nyquist plot of a fibre supercapacitor at high frequencies from 100 kHz down to 0.01 Hz using AC 4 mV potential modulation. Compared with the Nyquist plot of a strip supercapacitor, there is no semicircle shape in high frequency range. This is probably because of the interface processes of the active layers and current collector. Similar results were reported in the references [203] and [204]. The semicircle in Nyquist plot at high frequency disappears when the contact between electrodes and current collector was improved. At high frequency, the ESR value of the fibre supercapacitor was obtained from the intercept of the Nyquist plots with the real axis. ESR value is mainly determined by the electrolyte resistance and contact resistance of the active material/current collector interface. In this Figure, the ESR is about 54 Ω. At the intermediate frequency, the inclined line suggests some ion diffusion behaviour of the electrolyte inside the composite electrode. At lower frequency, the capacitor with aqueous acid electrolyte exhibits larger dependence on frequency of the real impedance, which is likely dependent on a greater distributed resistance in deeper carbon pores [183].

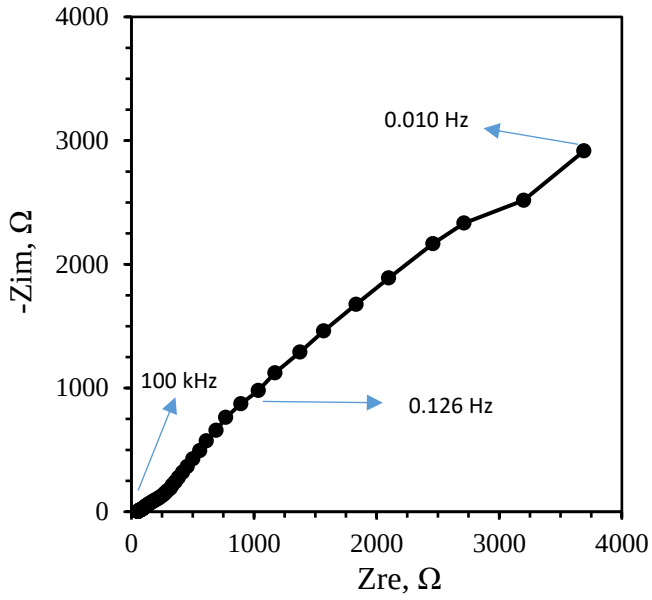


Figure 6.4 A typical Nyquist impedance plot of a fibre supercapacitor.

## 6.3. Results and discussion

### 6.3.1. Fabrication and characterisation of the initial fibre supercapacitors

#### 6.3.1.1. GCD test for the fibre supercapacitors

An initial fibre supercapacitor with the length of 5 cm was made by a dip coating method following the coating process as shown in Figure 6.2, and was tested by electrochemical workstation. The typical GCD curve (first five cycles at a charge current of 0.5 mA) is shown in Figure 6.5a. All the charge-discharge curves showed that the IR drop happened at the early stage, and the size of the iR drop is similar in each charge-discharge curve. This suggests that the performance of this short fibre supercapacitor is stable. Figure 6.5b shows the GCD curves run on this fibre supercapacitor at different currents. It can be seen that the charge and discharge time decreases as the charge current increases, and the iR drop increases as the charging current increases as one would expect. The capacitance can be calculated using Equation (3.4). When the charging current increased from 0.5 to 1.5 mA, the capacitance decreased from 1.32 to 1.04 mF; the specific capacitance per length unit decreased from 0.26 to 0.21 mF/cm (Figure 6.5c). This may be caused by the slow diffusion of electrolyte ions through the double layer on the electrode surface or the

permeation of ions through the pores in the carbon particles. The capacitance at the charging current 1.5 mA was 79% of that measured at the charging current of 0.5 mA. This suggests that the Chinese ink used as activated materials has reasonably good electrical properties.

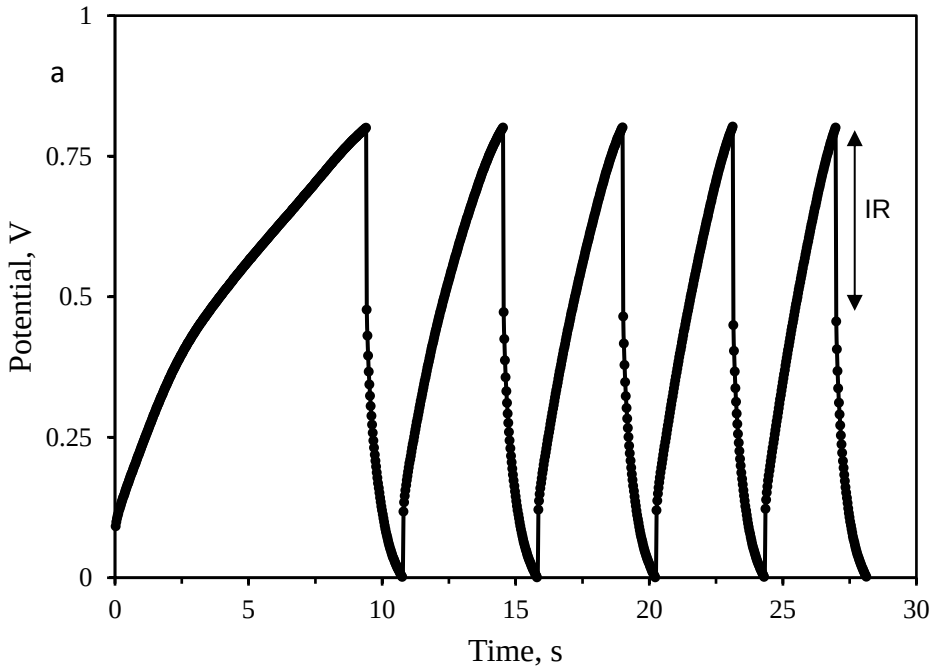


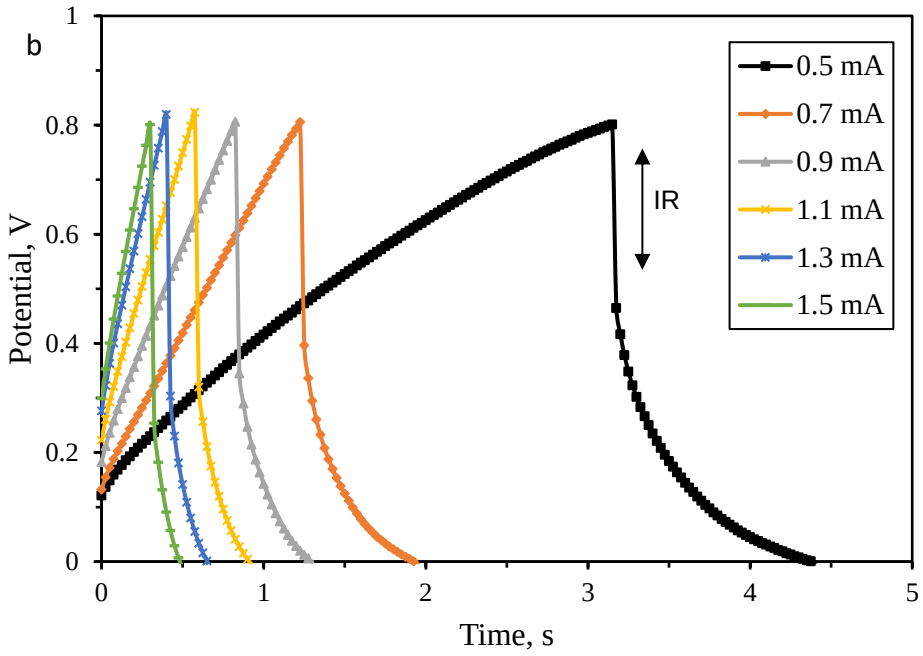

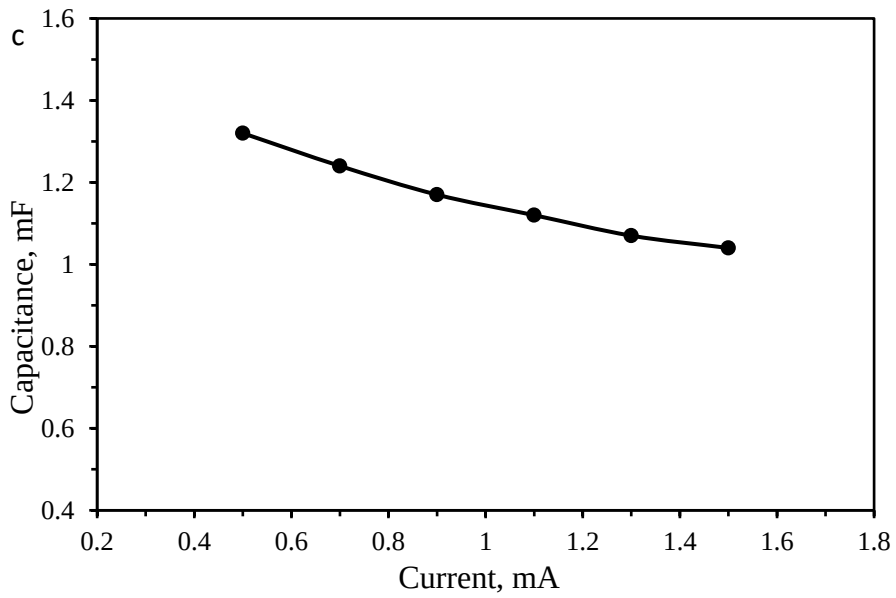


Figure 6.5 (a) GCD curves recorded at a charging current of 0.5 mA; (b) GCD curves at different charging currents (0.5, 0.7, 0.9, 1.1, 1.3 and 1.5 mA); (c) the relationship between the charging current and corresponding capacitances.

#### 6.3.1.2. CV test for the fibre supercapacitors

CV tests were conducted to characterise the electrochemical performance. All the CV curves were recorded using a two-electrode system with a voltage window from 0 to 0.8 V. Figure 6.6a reveals the CV curves of the supercapacitor at the scan rate from 0.02 V/s to 0.10 V/s. The capacitances were calculated by equation (6.1). As shown in Figure 6.6b, the capacitance decreased when the scan rate increased. When the scan rates increased to 0.04 V/s and 0.06 V/s, the capacitances dropped to 2.8 mF and 2.2 mF, respectively. They are almost equal to 76% and 60% of that measured at 0.02 V/s. When the scan rate increased to 0.08 V/s, the capacitance is still 1.8 mF, which is still 49% of that measured at 0.02 V/s. The capacitance decay at higher scan rates implies a good rate performance of the Chinese ink. The reason of capacitance reduction with the increased scan rate can be ascribed to the inefficient diffusion of ions at the higher scan rates.

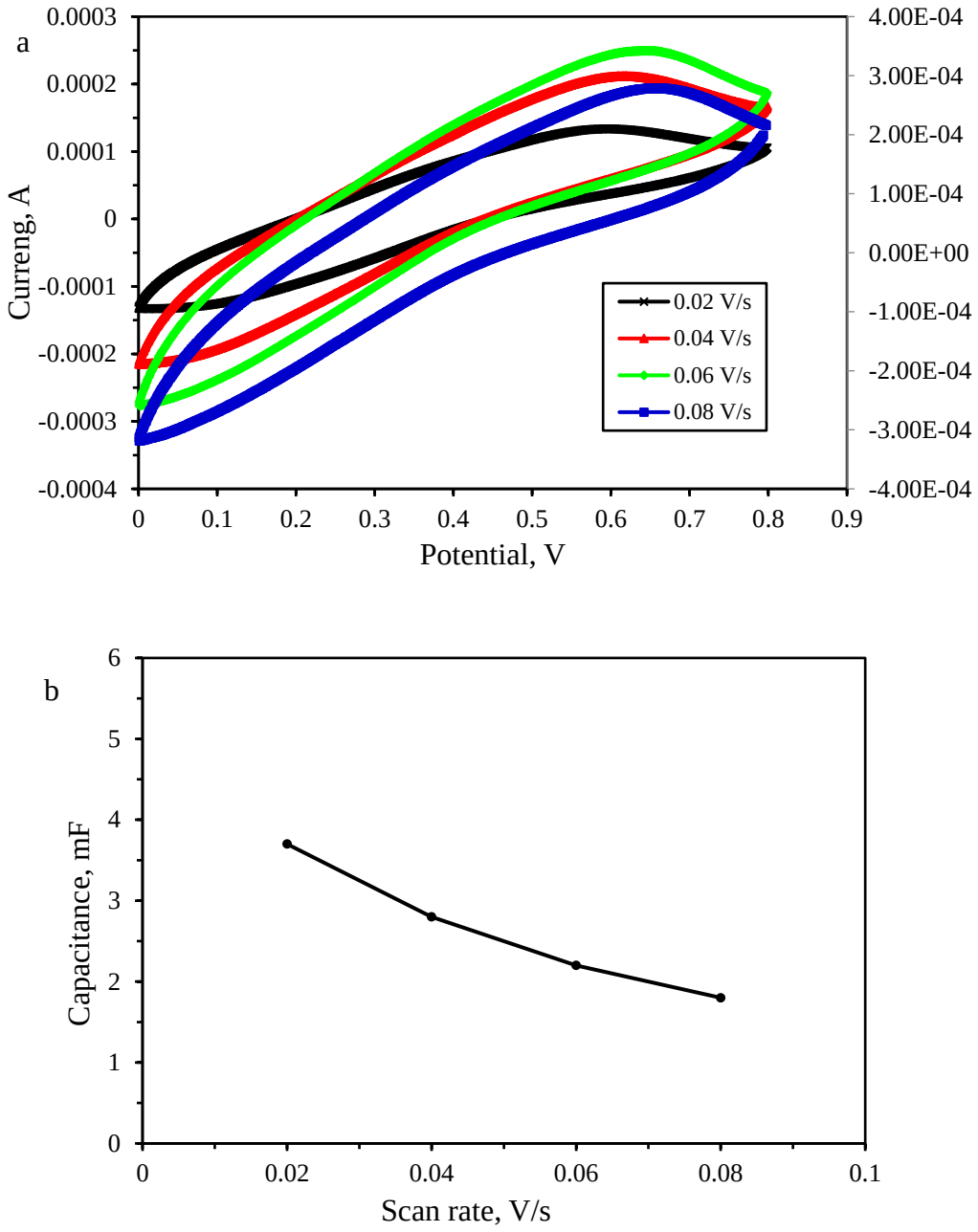


Figure 6.6 (a) CV curves recorded at different scan rates (0.02, 0.04, 0.06 and 0.08 V/s); (b) the relationship between the scan rate and the corresponding capacitances.

### 6.3.2. Fabrication and characterisation of a longer fibre supercapacitor

In order to make longer fibre supercapacitors, dip-coating devices were designed and manufactured using the apparatus shown in Figure 6.3. From Figure 6.3a and Figure 6.3b,

we can see that the manual dip-coating device was improved to a motor-drive dip-coating setup. The coating speed could be controlled by this two-direction motor. A longer energy storage fibre (35 cm for length) was made using the dip coating device as shown in Figure 6.3b. The active layer was coated 6 times to make sure this ink layer was complete. The CV curve of the fibre supercapacitor sample with the length of 35 cm is shown in Figure 6.7. The CV curve is closed and regular; therefore, the capacitance and specific capacitance can be evaluated using Equations (3.2) and (6.1). The capacitance and specific capacitance per unit length were 18 mF and 0.5 mF/cm, respectively. This shows that this kind of fibre supercapacitors is functional, although the capacitance is not as high as expected. This is probably because insufficient active material was coated on the fibre in the manufacturing process.

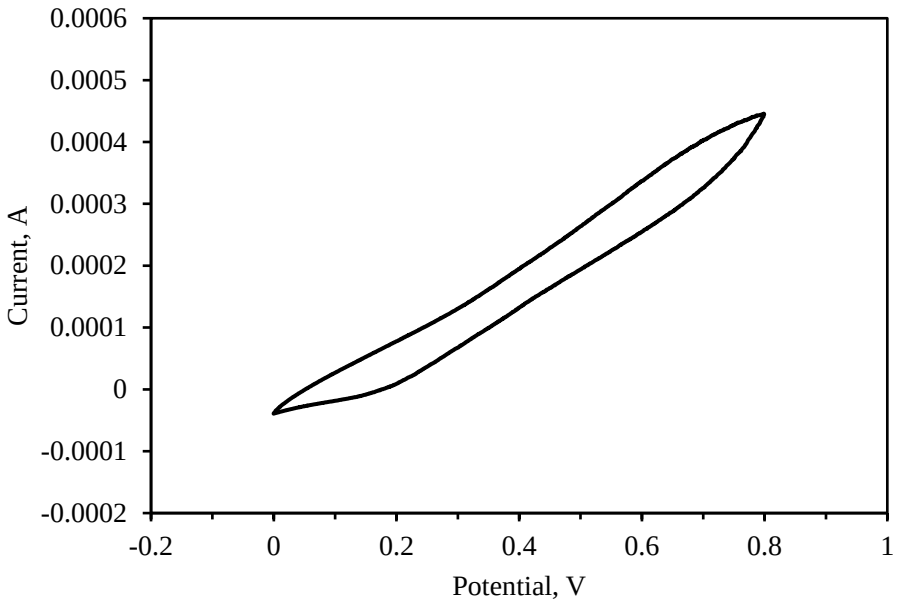


Figure 6.7 The CV curve of a 35 cm long fibre supercapacitor sample.

### 6.3.3. Characterisation of the five layers structure of fibre supercapacitors

A typical cross-section of a copper fibre supercapacitor is shown in Figure 6.8a. The five layer structure can be seen clearly. The copper fibre core is easy to see. The second layer of Chinese ink was not uniform. The gel electrolyte layer, the third layer, was complete but the thickness was not uniform. The fourth layer was also of Chinese ink and was

uneven. In order to further characterise the five layer structure of fibre supercapacitor, a longitudinal section sample was made and tested by SEM. As shown in Figure 6.8b, the core fibre could be found in the middle. The corresponding elemental profile plot further proved the core fibre is copper fibre. The outer layer is bright white and easy to be found. It is rich in Ag in this bright area as shown in the elemental profile. The copper core fibre and silver paint layer used as the two current collectors in this structure were found. Between these two current collectors, there should be two ink layers separated by a gel electrolyte layer. Although it is not easy to distinguish the ink layer from the gel electrolyte layer based on the colour of the area in Figure 6.8b, the element profile plot is beneficial to further distinguish the ink layer from gel electrolyte layer. It is seen that there is little carbon found in the core fibre area and silver paint layer area, the content of carbon in the area between the core fibre and silver paint area shows higher-lower-higher levels. It indicts that there are corresponding ink layer which is rich in carbon, gel electrolyte layer and another ink layer between the copper fibre and the silver paint layer. Phosphorus and oxygen could be found in the core fibre, because there could be some compounds produced by the slow reaction between the copper and $H_3PO_4$ solution, which are rich in phosphorus, oxygen and copper elements. It is also found that phosphorus and oxygen appear in all the areas chosen for testing. This proves the $H_3PO_4$ electrolyte diffuses well through the whole structure.

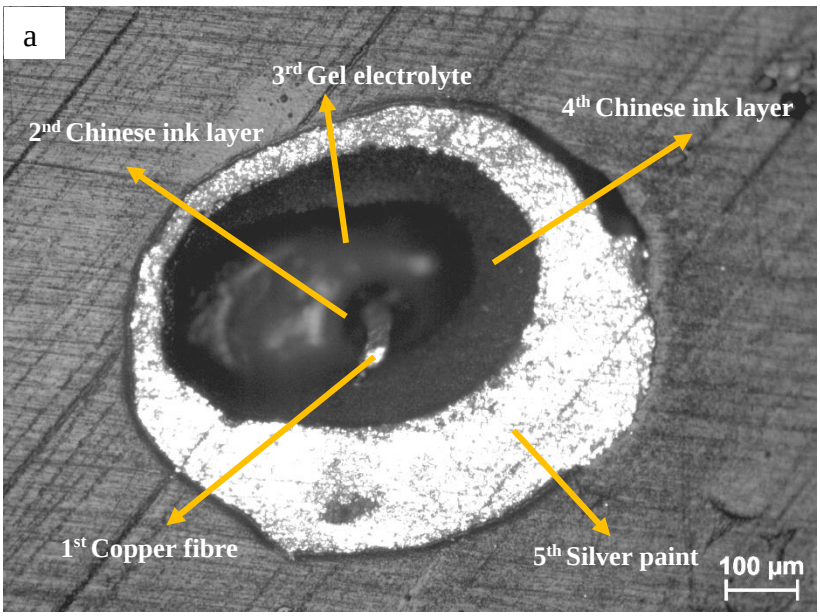

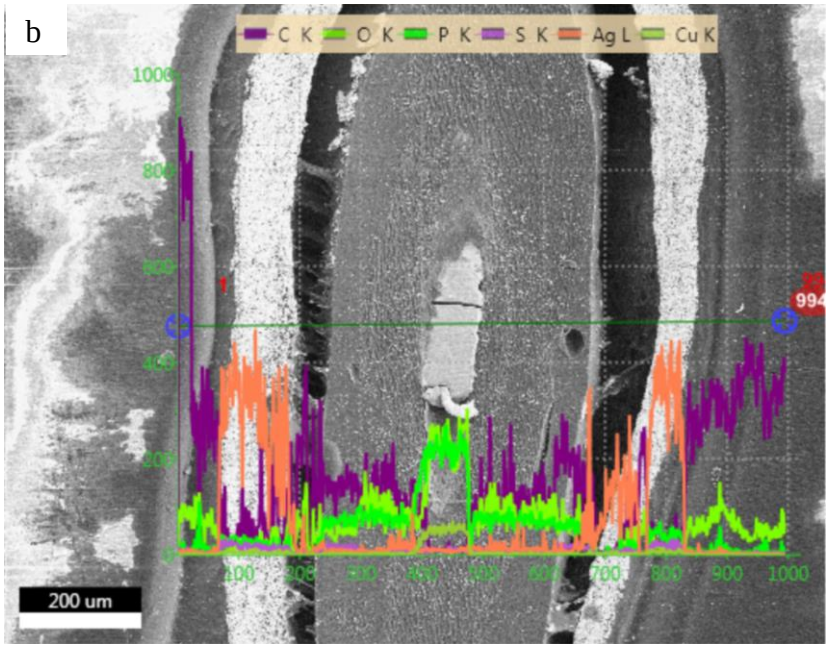


Figure 6.8 (a) Optical image of the cross-section of a fibre supercapacitor; (b) SEM micrograph and EDS line scanning of the longitudinal section of a fibre supercapacitor.

Figure 6.9a shows the typical porous structure of Chinese ink layer surface. The diameter of the holes is about 200 nm. This micro structure should allow a good electrolyte accessibility to the inner surface of the active layer. This porous structure should also provide a large surface area for electrical charge storage. This suggests that commercial ink has the potential to be used as the active material for the fibre supercapacitors designed in this work. The SEM photo of the gel electrolyte is shown in Figure 6.9b. It is obvious that the surface of this gel electrolyte layer is rough, which is considered to be beneficial for coating another ink layer on it. Some small holes are also found on the surface, which will help the $H_3PO_4$ acid solution diffuse though this layer. Also, there is no big defect in the SEM photo, which suggests this layer is complete. For this reason the PVA solution, in this gel electrolyte layer produced by mixing PVA and water, was considered as a separator and also as an electrolyte support in this structure. Furthermore, this layer also has a good flexibility, which is contributed by the PVA, which will enhance the overall flexibility of the energy storage fibre.

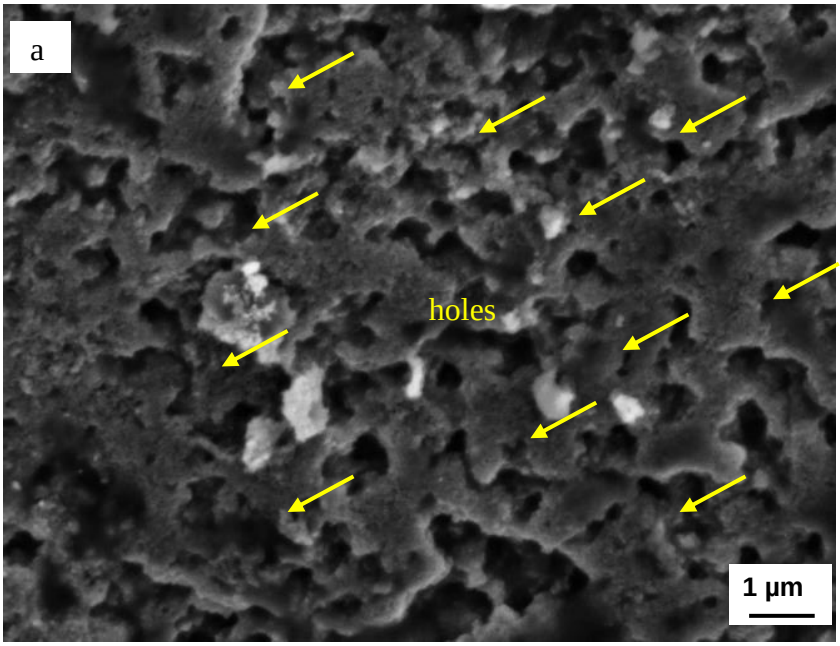


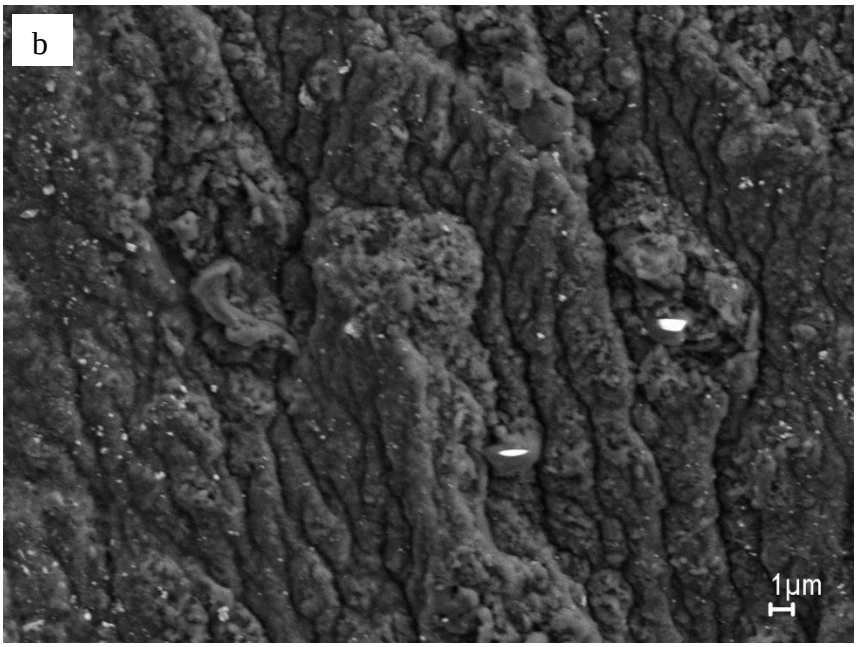


Figure 6.9 (a) SEM photo of the surface of the Chinese ink layer; (b) SEM photo of the surface of gel electrolyte layer.

### 6.3.4. The electrochemical stability of longer fibre supercapacitors

In order to test the electrochemical stability of the fibre supercapacitors with a five layer structure, long time cycling of CV testing was used. Figure 6.10a shows CV curves for

different cycles recorded at the scan rate of 0.8 V/s, and the corresponding capacitance calculated from the CV curves are shown in Figure 6.10b. It can be seen that the shape of the curves is uniform and close to the ideal rectangle shape, however the area of the CV curve became smaller as the cycling number increased. In Figure 6.10b, it can be seen that the capacitances, which are calculated from Figure 6.10a by equation (3.2), decrease gradually as the number of cycles increases in the range of 1-1000. If the capacitance calculated from the $10^{th}$ curve is taken as 100% and considered as the initial capacitance, when the cycling number increased from 10 to 100, the capacitance decreased to 79.2% of that calculated from the $10^{th}$ curve. Capacitance further drops dramatically to 58.3% of that initial capacitance as the cycling number increased to 300. It is seen in the first 300 curves, the capacitance decreases about 41.7% of initial capacitance calculated from $10^{th}$ curve. When the cycling number increased to 600, the capacitance is 50.0% of initial capacitance, so the capacitance decreases about 50% than that of the initial capacitance from the $10^{th}$ curve to the $600^{th}$ curve, and in the second 300 curves (from $300^{th}$ to $600^{th}$ curve), the capacitance decreased about 8.3% of the initial capacitance. Then from the $600^{th}$ curve to the $900^{th}$ curve, the capacitance decreases about 12.5% of the initial capacitance. The capacitance keeps the same (37.5% of the initial capacitance) when the cycling number is 900 or 1000. It seems that the capacitance decreases dramatically because 62.5% of the initial capacitance vanishes in the first 1000 cycling. The main reason is considered that during the long time cycling, the activity level of the ion diffusion in the electrolyte decreases due to the solvent in electrolyte (water) is evaporating. As shown in Figure 6.8, this fibre supercapacitor has a typical five layer structure. The outer layer is silver paint layer, which cannot prevent the water evaporating and is also fragile.

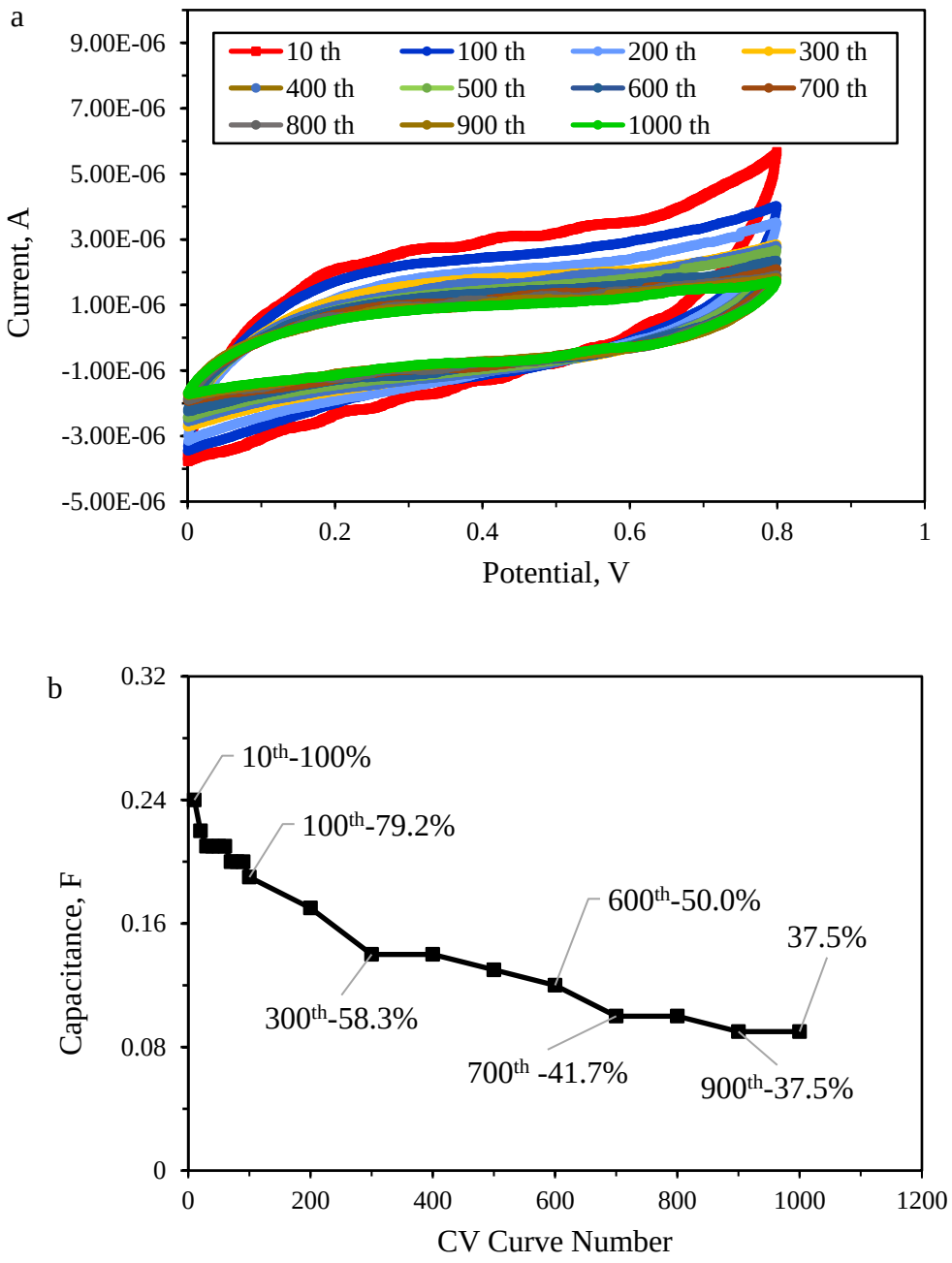


Figure 6.10 (a) Stability of CV test for a fibre supercapacitor with five layer structure; (b) the relationship between the capacitance calculated from the CV curve and the number of CV cycles.

### 6.3.5. Improvement of the stability of the electrochemical performance

Figure 6.11a shows a typical crack in the fibre supercapacitor with the silver paint layer as the outer layer. This phenomenon occurred because the water loss in this whole structure results in the coated layer became hard and fragile. The key to the problem may be to avoid the water evaporating. If this problem can be solved, the stability of the performance and the flexibility of this energy storage fibre will be improved, too. It is known, PVA has excellent film forming and adhesive properties. The gel electrolyte in the fibre supercapacitor was made by mixing the $H_3PO_4$, PVA and water, which is considered a good support for the whole structure of the fibre supercapacitor (Figure 6.9b). Therefore, a 10% PVA solution was considered as a coating on the silver paint layer to improve the fibre supercapacitors. As shown in Figure 6.11b, when the 10% PVA solution coated is dried, a PVA film layer appears to integrate with the silver paint layer, and thus covers the whole fibre.

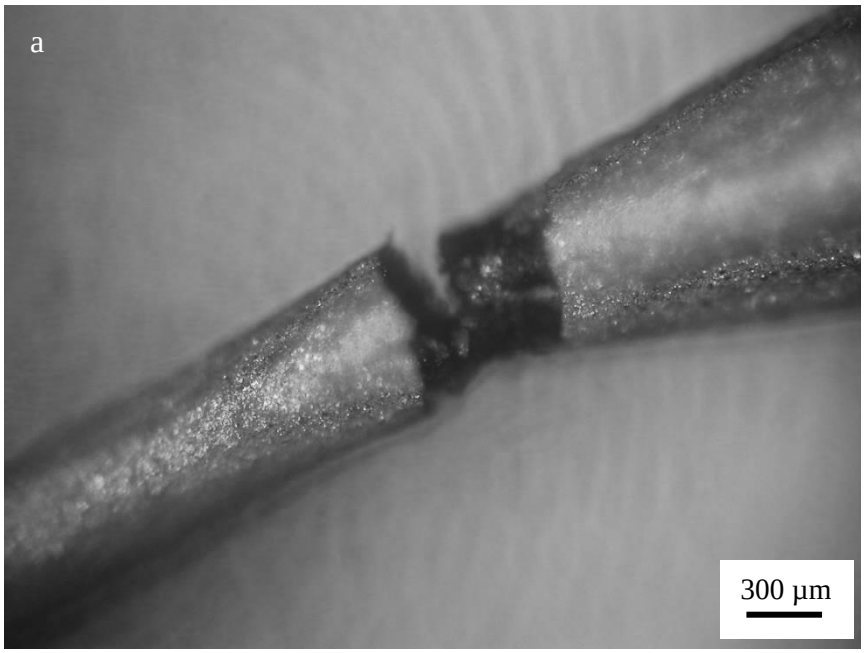

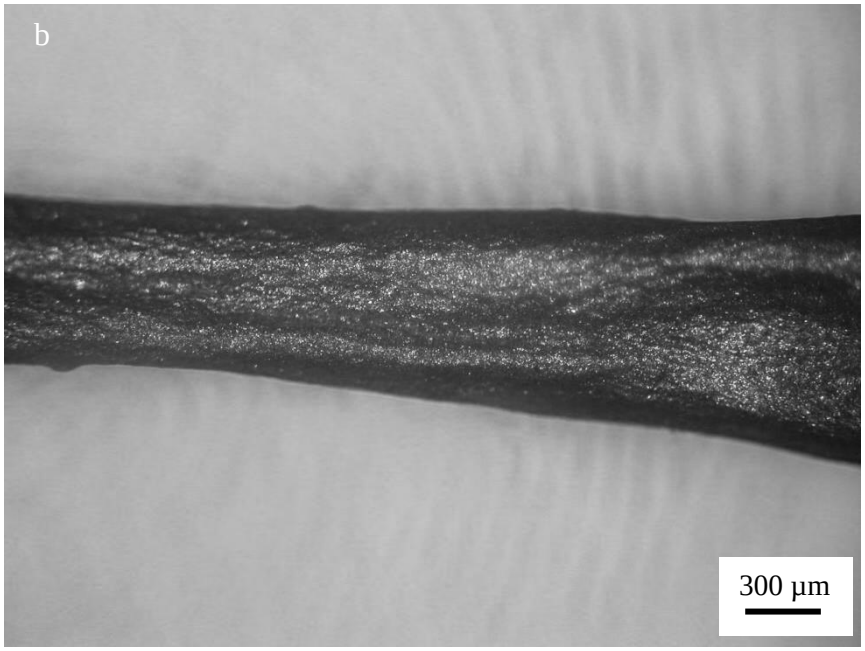


Figure 6.11 (a) Optical image of a part of a fibre supercapacitor with the silver paint as the outer layer; (b) Optical image of a part of a fibre supercapacitor with the 10% PVA solution as the outer layer.

As shown in Figure 6.12a, a copper fibre was connected to the silver paint layer in this fibre supercapacitor with PVA outer layer. This copper fibre was used to connect with workstation for testing or with the energy supply for charging/discharging. The PVA outer layer compacted tightly with the silver paint layer when it was dried, so it is difficult to exfoliate the PVA outer layer. In the process, it is easier to connect the copper conducting line with the silver layer before the outer layer is coated. Figure 6.12b shows the CV curves of a fibre supercapacitor with a PVA outer layer tested at different time. It is seen that the area of the CV curve change slightly over 7 days. The corresponding capacitances calculated based on these two curves are 0.72 mF and 0.66 mF, respectively. After 7 days, the capacitance is still 92% of the original capacitance for this sample. The reason is considered to be that the outer PVA layer obstructs the evaporation of the solvent of the electrolyte. As well, this outer layer can protect the whole structure of the fibre supercapacitors from abrasion.

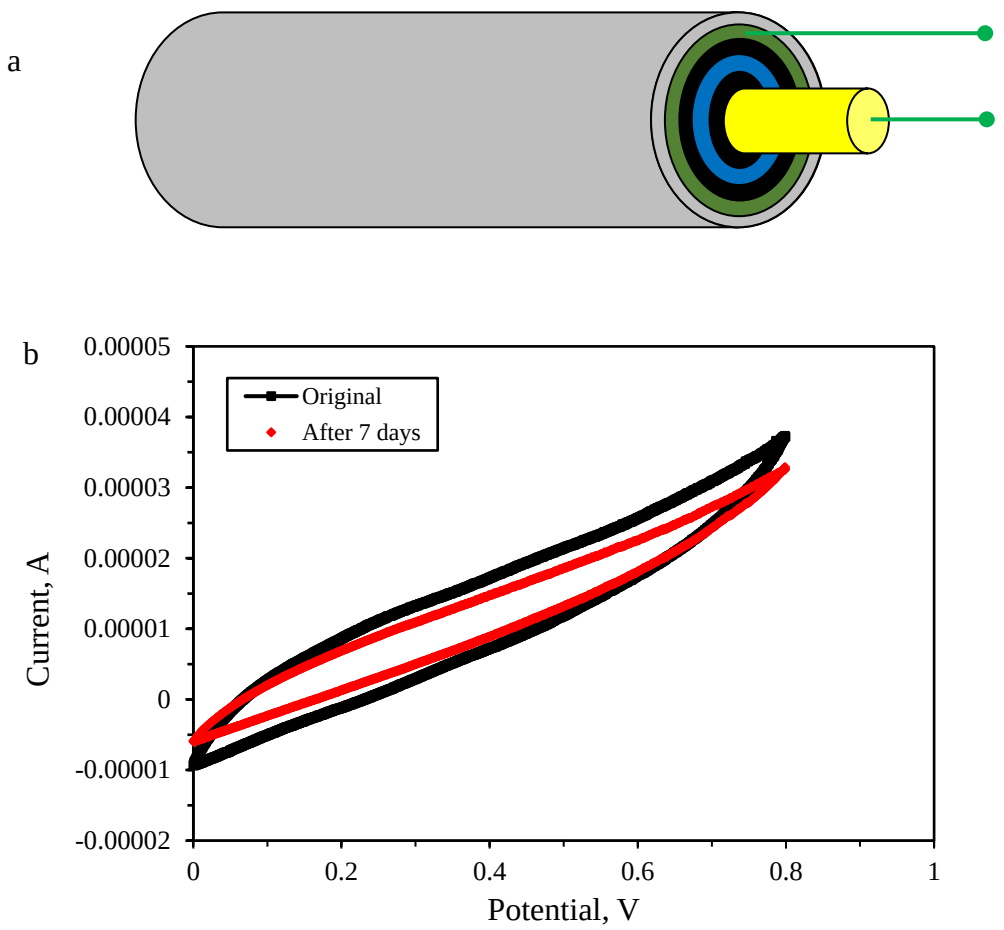


Figure 6.12 (a) The connection diagram of a fibre supercapacitor with PVA outer layer for testing; (b) CV curves of a fibre supercapacitor with PVA outer layer recorded at different time.

### 6.3.6. Testing the flexibility of fibre supercapacitors

A new fibre supercapacitor with a length of 41 cm was made based on the experience of many laboratory trials (Figure 6.13). The flexibility of the fibre supercapacitors was also studied. The specific capacitance of the 41 cm long supercapacitor was examined when the fibre was bent on glass rods of different curvatures. The diameters of the glass rods were 10.5, 3.0 and 1.5 cm. Figure 6.13 shows the CV curves of the fibre supercapacitor bent at different curvatures. And the compared capacitances calculated from Figure 6.13 are shown in Figure 6.14. It can be seen the CV curves were the same when the fibre supercapacitor was bent using the glass rods with the diameters of 1.5 and 3.0 cm. When

the fibre supercapacitor was bent on the glass rod with the diameter of 10.5 cm, the specific capacitance decreased slightly to 32.2 mF/cm, which was about 93% of the original straight sample. When the diameter of rods decreased to 3.0 and 1.5 cm, the specific capacitance changed to 26.2 mF/cm for both cases, which was 76% of the straight sample.

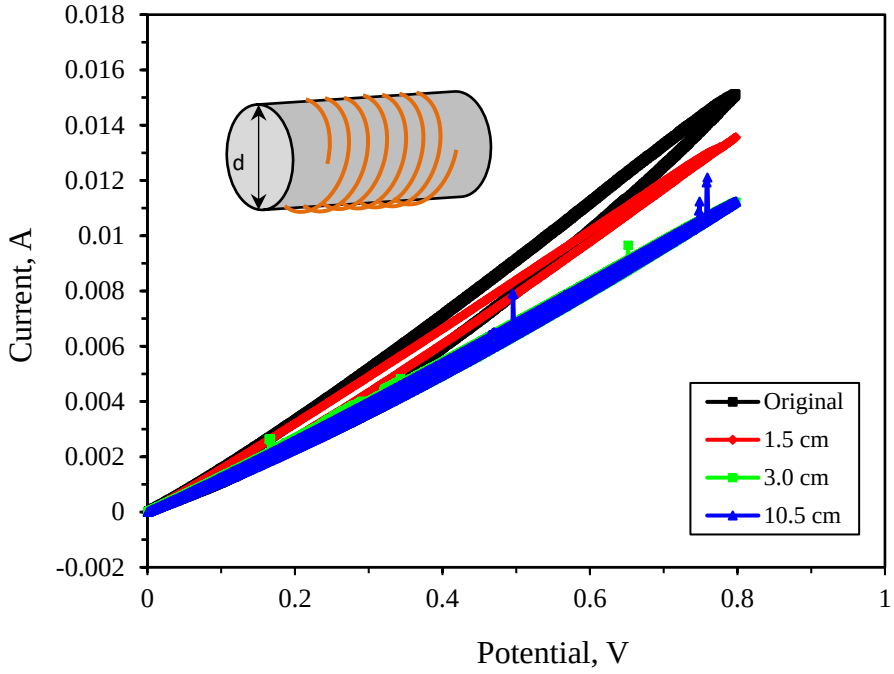


Figure 6.13 CV curves of the 41 cm long fibre supercapacitor at different testing conditions (straight and bent with different curvatures).

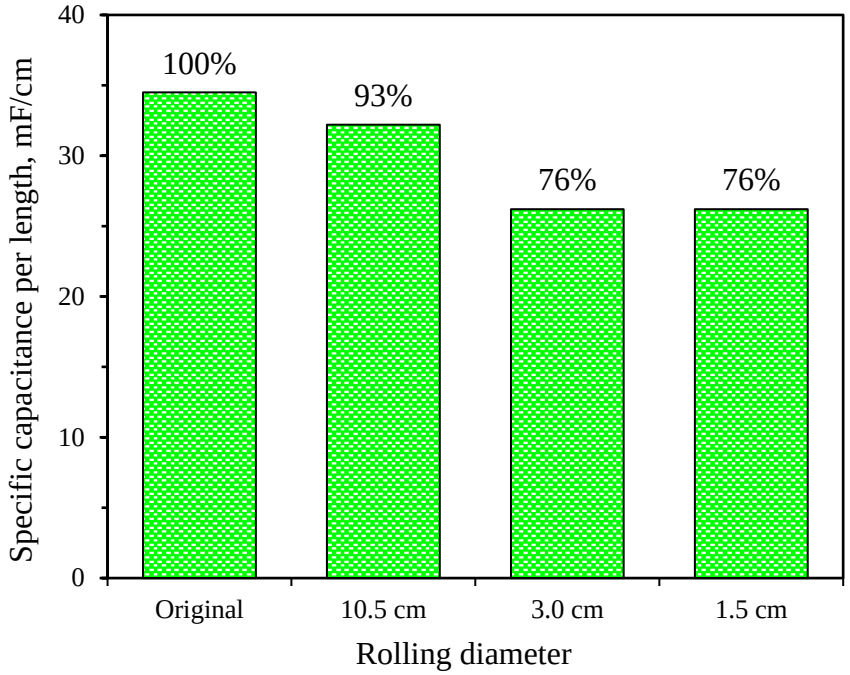


Figure 6.14 Comparison of the specific capacitance per length of the fibre supercapacitor being bent with different curvatures with the original straight sample.

### 6.3.7. Woven fibre supercapacitors

A 50 cm long fibre supercapacitor and cotton yarn were woven together to make an e-textile by using a mini loom kit (Item no. WG-164, Hawthorne direct Limited Liability Company) as shown in Figure 6.15. The fabric was designed with a 135 mm weaving width. There are 17 warp threads, and the energy storage fibre and cotton yarn were used as the weft.

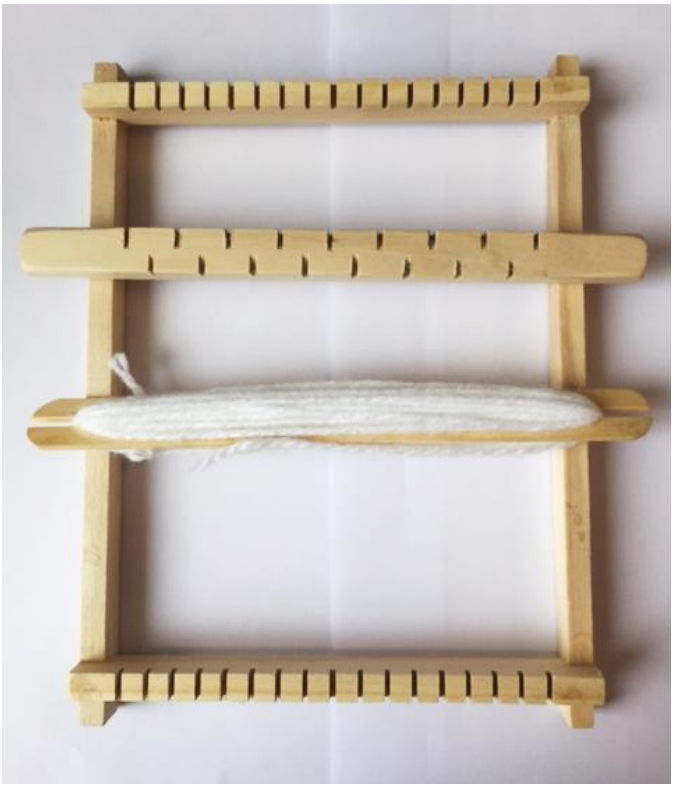

Figure 6.15 Photo of the mini loom kit (size: 22.0 cm ×16.5 cm) .

The specific capacitance of the fibre supercapacitor at different bending conditions of the original sample shown in Figure 6.14 indicates that the fibre supercapacitors are able to work whilst being severely bent. A 50 cm long fire supercapacitor was woven with cotton yarn to produce fabric using a simple mini loom as shown in Figure 6.15. Figure 6.16a and b show a photo and the structure diagram of the woven supercapacitor fabric. There are sharp bends along the two sides of the fabric. The CV was employed to test the effects of weaving a fibre supercapacitor. Figure 6.17 shows the CV curves recorded at 30 mV/s of this fibre supercapacitor before and after being woven into the fabric. It demonstrates that even with a few sharp bends, the woven fibre supercapacitor can still work and its flexibility is more than sufficient for this use. These two CV curves were asymmetric, the reason is that the area of two active layers is not equal for a coaxial fibre supercapacitor. There are differences between the features of these two CV curves. The CV curve of the fibre supercapacitor woven into the fabric showed a better shape which is closer to the ideal rectangle shape. The reason is believed that the coated layers of the supercapacitor contacted in a better condition with each other while the fibre supercapacitor was being

stretched in the weaving process. The capacitance of this woven supercapacitor calculated using Equation (6.1) is 16.9 mF, which was the same as the capacitance of the free fibre supercapacitor. This demonstrates that the fibre supercapacitors are suitable to be woven into fabrics and their electrochemical performance will not be significantly affected by the weaving process.

a

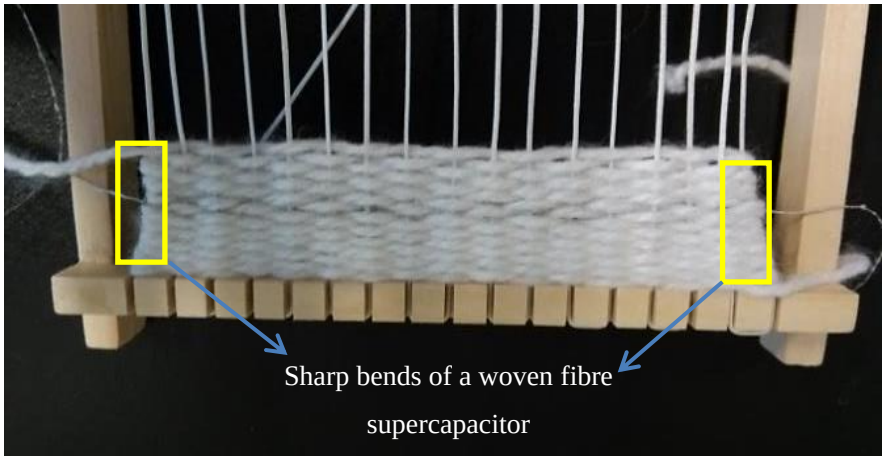


b

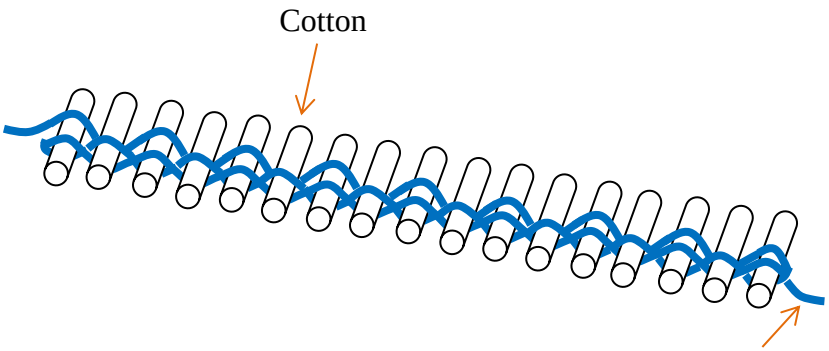


Figure 6.16 (a) The photo of the fibre supercapacitor woven into a fabric; (b) the schematic of the fibre supercapacitor in the fabric.

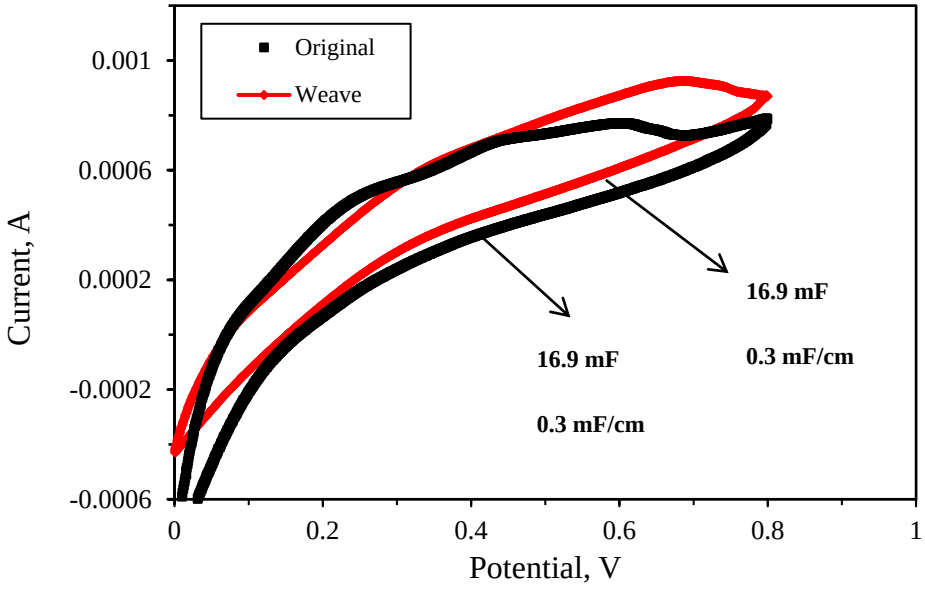


Figure 6.17 CV curves of the free fibre supercapacitor and that woven into fabric.

### 6.3.8. Testing the combination of two fibre supercapacitors

For a single fibre supercapacitor, the energy storage ability and operating potential is limited by the decomposing potential of water or phosphoric acid. In order to meet the requirements for use at a higher potential, the performance of combination circuits of the fibre supercapacitors in parallel and in series has been studied.

Figure 6.18 shows the schematic structure of two single fibre supercapacitors (Samples **a** and **b**) and their series and parallel combination circuits. In order to protect the fine fibre supercapacitor, a PVA gel was coated as the outer support layer as before. The copper core fibre and the silver paint layer were the current collectors, so another copper wire used as a conductor was glued with the silver paint layer to make an external connection. As shown in Figure 6.19, the working potential of the two fibre supercapacitors in parallel is the same as the working potential of the individual single samples, and half of that of samples in series (1.6 V). The areas of CV curve of the parallel circuits is close to the sum of the areas of the two Sample **a** and Sample **b**. The area of CV curve of the series circuits would be half of the total area of these two samples. The capacitances calculated by equation (6.1) from the CV curves are shown in Table 1. The capacitance of the parallel

circuit is 12.0 mF, which is almost the same as the sum of the capacitances (12.5 mF) of the two single samples. The capacitance of series circuit is 3.4 mF, which is higher than the theoretically expected series capacitance of 2.3 mF. As shown in Table 6.1, there is a considerable difference between the ESRs and capacitances of Sample **a** and Sample **b** because they are of different length. Therefore the voltage is not equal across both capacitors which might account for the difference between the experimental and theoretical capacitance for the series case. These results illustrate that the electrical properties of the parallel combinations of the fibre supercapacitors showed a reasonable agreement with the theoretical models of series circuit combinations.

Figure 6.20 shows the GCD curves at the charge current of 0.2 mA for the two single supercapacitors and the series circuit, and of 0.4 mA for the parallel circuit. The potential window of parallel circuit is set at 0.8 V, the same as the two single fibre supercapacitors, and half of the series circuit. As shown in the Table 6.1, the capacitances of the different cases calculated by equation (3.4) from the charge-discharge curve are generally following the trend which is in agreement with the theoretical models. Nyquist plots of the two single samples and the combinations in series or in parallel are shown in Figure 6.21. It can be seen that the shapes of electrochemical impedance curves for the combination circuits were similar to those of the single fibre supercapacitors. This indicates that the ion diffusion processes for all samples are similar. The high intercept on the real axis is the ESR, which is shown in Table 6.1. For the case of the series circuit, the ESR is 75.2 Ω. This is very close to the sum of the ESR of the two Samples **a** and **b**; the ESR of the parallel circuit is about 15.1 Ω, which is slightly less than the expected ESR of the parallel circuits of sample a and b. These results have a reasonable agreement with the theoretical models.

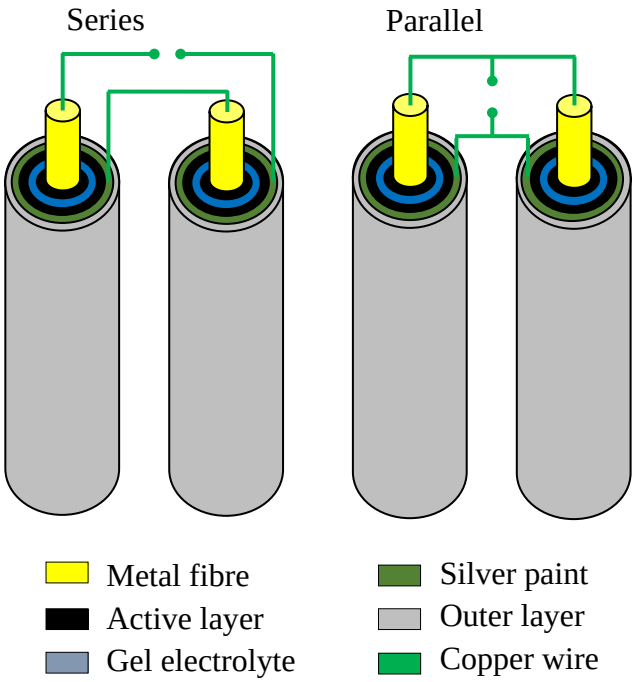


Figure 6.18 Schematic of two fibre supercapacitors combined in series or in parallel circuits.

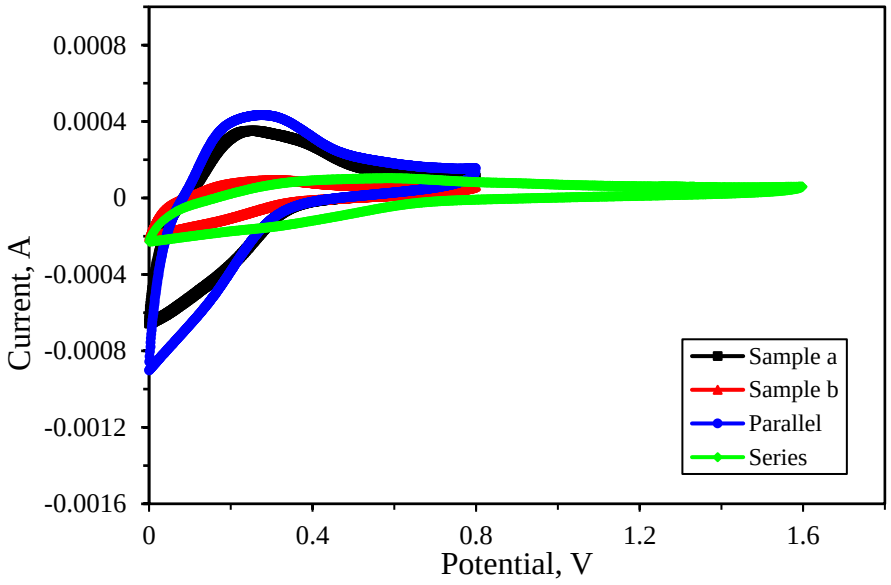


Figure 6.19 CV curves recorded at 20 mV $s^{-1}$ for two single fibre supercapacitors and their electrical combinations in series and parallel.

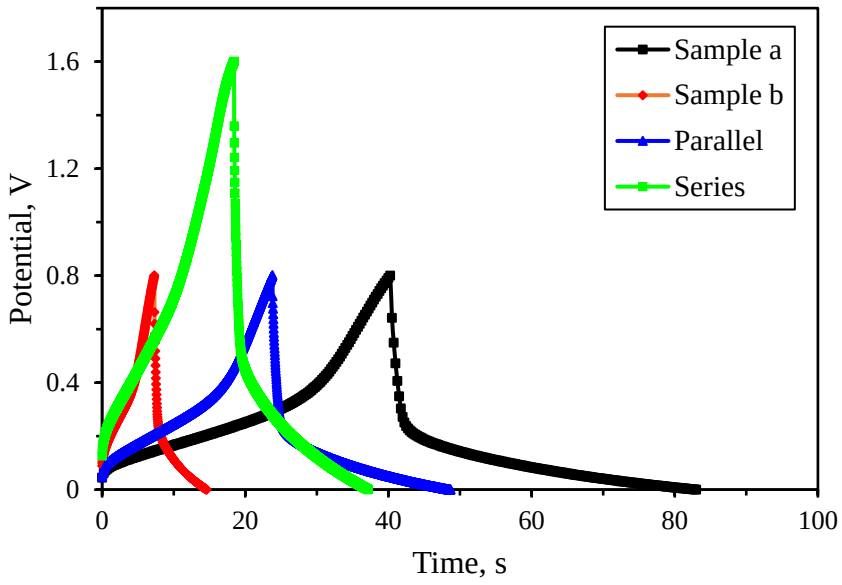


Figure 6.20 GCD curves of the 4th cycles of each case, for single and series circuit 0.2 mA was used, and 0.4 mA for the parallel circuit.

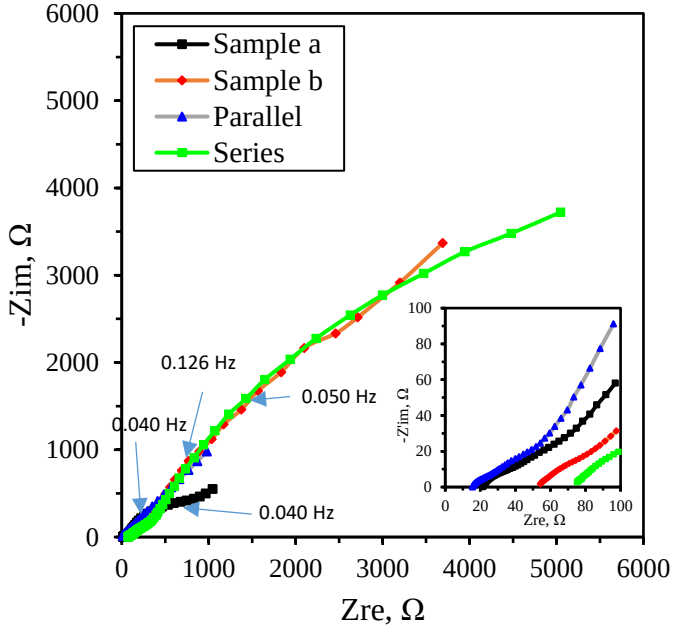


Figure 6.21 Electrochemical performances of two single fibre supercapacitors and their electrical combinations in series and parallel using a 4 mV AC modulation for a frequency range of 100 kHz to 0.01 Hz (insert shows an enlarged curve at a high-frequency region).

Table 6.1 Summary of ESRs from Nyquist plots and the capacitances from CV curves and GCD curves with those calculated using theory for series and parallel circuits.

| | Capacitance, mF (CV) | | Capacitance, mF (GCD) | | ESR, Ω | |
|---|---|---|---|---|---|---|
| | exp. | theory | exp. | theory | Exp. | theory |
| Sample a | 9.4 | | 13.2 | | 21.2 | |
| Sample b | 3.1 | | 2.2 | | 54.3 | |
| Series connection | 3.4 | 2.3 | 2.8 | 1.9 | 75.2 | 75.5 |
| Parallel connection | 12.0 | 12.5 | 13.8 | 15.4 | 15.1 | 15.2 |

## 6.4. Conclusions

Coaxial single fibre supercapacitors were successfully manufactured and characterised in this study. Chinese ink was used as the electrode material. A hand-made short sample proved that the fibre supercapacitor designed was functional. A dip coating setup was designed to produce longer fibre supercapacitors. When the coating number of carbon ink in each electrode layer increased substantially, the amount of active material deposited on the electrodes increased dramatically. This improved the electrical storage of the fibre supercapacitor tens of times. The specific capacitance of the supercapacitors at various bending conditions was examined. The results showed that the supercapacitors manufactured using the present method kept a good electrochemical performance under severe bending conditions. The fibre supercapacitor kept the same capacitance as the original capacitance of the original free fibre when it was woven into a fabric. This indicated that the supercapacitors designed and made in this study have very good flexibility. The electrical performance of a combination of two fibre supercapacitors in series or parallel has been studied. The current and potential range can be improved by connecting multiple fibre supercapacitors in parallel or in series to meet the power and energy requirements. This shows that these kinds of flexible energy storage fibres can be woven into other fabrics and connected into series or parallel to make smart textile materials with appropriate electrical performance for a desired use. Based on these results, next step, the mechanical properties will be tested and a new ink will be used to optimise

the energy storage performance. This could be used as a flexible energy storage and woven or perhaps embroidered into other fabrics to make smart textile materials.

# Chapter 7. Optimisation of the Performance of Flexible Fibre Supercapacitors

## 7.1. Introduction

Carbon in various forms is the main active material used as the electrode material in EDLCs. In particular, AC was used widely as electrode material over the last decade due to its high surface area, low cost, as well as having stable physical and chemical properties [1][205][54][206][207]. In an EDLC, energy is stored in the double-layer formed at the interface between the electrode material surface and the electrolyte. Thus, the purpose of the AC used is to increase the surface area of the electrode to allow more sites for charge storage. Recently, it has been proved that electrode properties of AC play important roles on the performance of the EDLCs, properties such as specific surface area and particle pore size distribution [26][32][33][208][209]. Gamby et al. [32] tested various activated carbons from the PICA Company. The results showed that higher surface area with a higher mesoporous volume could lead to a higher specific capacitance. Furthermore, Qu [26] studied the effect of the structure and the surface condition of the activated materials on the performance of a supercapacitor. It was found that the specific capacitance of an activated carbon device also relied on the crystal orientation and surface functional groups. Furthermore, Zhang et al. [210] made a series of AC with different particle sizes by ball milling. The results showed the effect of ball-milling time on particle size, pore structure and wettability of the AC. These properties changed with the ball-milling time which affected the resistance and the capacitance of the supercapacitors that used milled AC as the electrode material.

Ball milling is regularly applied to carbon materials. Kim et al. [211] studied the ball milling effect on the morphology of cup-stacked carbon nanotubes. The results are the shortening of the nanotubes and the formation of nano-barrels exhibiting an increased number of accessible active sites and anisotropic properties at both ends. Furthermore, it is reported in reference [212] that the ball-milling treatment can be used to decrease the SWNTs length and to increase their specific surface area. However, SWNTs do not resist

very long milling times. The optimum time of ball milling treatment to cut SWNTs is 2 h to keep the tubular structure and to maximise their specific surface area. In chapter 5, an experimental design method was used to optimise the electrical performance of the strip supercapacitor by determining the effect of the key practical factors. In this chapter, in order to optimise the performance of the electrode material, a ball-milling method was used to produce a series of ACs with different particle sizes, at the same time, the relationship between the particle sizes, specific surface area as well as pore distribution and ball-milling time was further studied. Furthermore, the milled AC with an optimum specific capacitance was used as the active material for the energy storage fibre to improve the performance.

## 7.2. Experimental methods

### 7.2.1. Ball-milling process

Mechanical milling was performed at room temperature using a ball-milling apparatus (Planetary Mono Mill Pulverisette 6 Fritch), which is composed of a cylindrical stainless steel container and stainless steel balls with 100 mm and 7 mm in diameter, respectively. AC powder (5 g) with a process control agent of 50 mL of deionized water was added to the container. Ball-milling speed was constant and set at 300 revolution/min. Milling was conducted from 0 to 48 h in air. Ball-milled AC samples were labelled as ACx, in which, x stands for the ball-milling time. For example, AC4 indicated that the original AC was milled for 4 h under the conditions mentioned above. In the same way, original AC was labelled as AC0.

### 7.2.2. Manufacturing of the strip supercapacitors using milled AC

The milled AC slurries with CMC binder were made as follows: 0.05 g CMC was added into deionized water/ethanol (1:1) solvent at room temperature with magnetic stirring until it was transparent. Then 0.4 g of the milled AC was added into the CMC binder solution with magnetic stirring for 8 h to get a homogeneous slurry. Then the slurry is coated on the exposed surface of the stainless steel strip (10 mm × 20 mm) using a sharp blade. The electrodes are dried after being coated with the slurry at room temperature

overnight, then at 100 °C for 2 h.

The organic electrolyte (1 mol/L tetrabutylammonium tetrafluoroborate in propylene carbonate) was dropped on the surface of the coated active materials on the 316 stainless steel strip. These electrodes with the electrolyte imbibed were put in a vacuum desiccator at room temperature for 0.5 h to allow the electrolyte to fully access the porous structures of the milled AC material. Meanwhile, a filter paper as a separator was also fully wetted with the electrolyte. Then, two electrodes separated by the separator were pressed together to make a supercapacitor with a sandwich structure as shown in Figure 7.1. Finally, this supercapacitor was sealed using a laminator to avoid the loss of electrolyte, using heat cured adhesive laminating film.

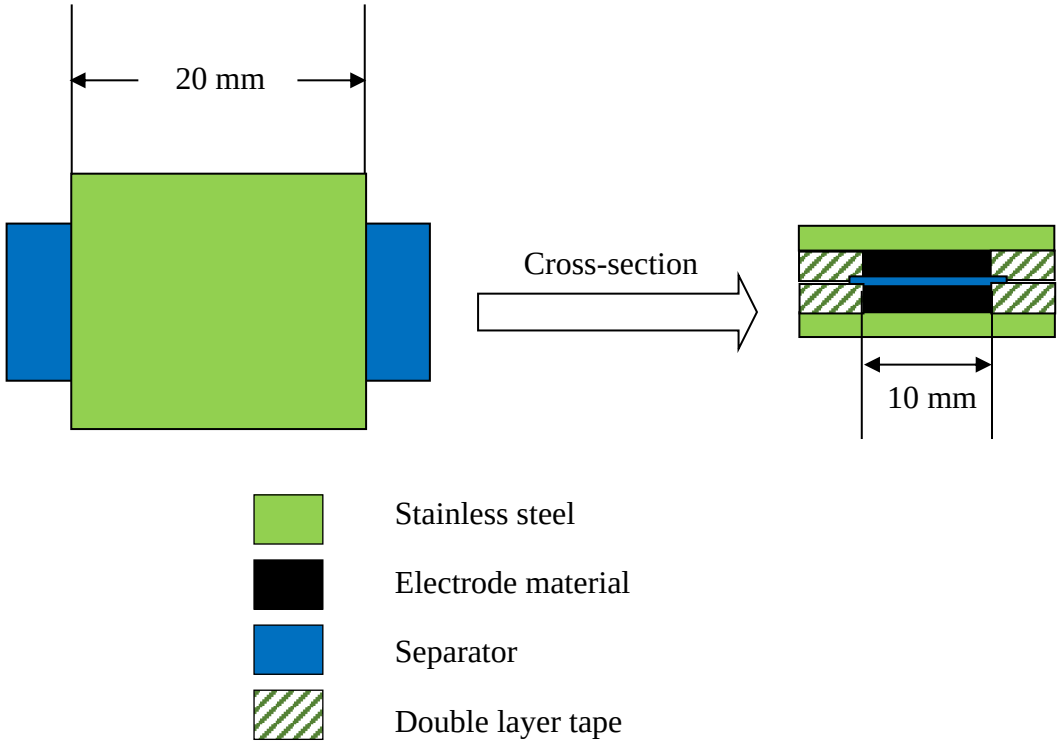


Figure 7.1 Schematic of a strip supercapacitor made in this chapter.

### 7.2.3. Manufacturing of the fibre supercapacitors using ball milled AC

In this experiment, the milled AC with an optimum electrochemical performance will be added to the commercial Chinese ink to produce a new mixed ink. The amount of the milled AC added is 5% of the total mass of ink. Then the inks mixed with milled AC are stirred for 6 h to produce a uniform ink. The new ink was used as the active layer material to fabricate the fibre supercapacitor following the manufacturing process shown in section 6.2.4.

### 7.2.4. Analysis and characterization of ACx

The ACs were tested on a Zeiss Supera 35 scanning electron microscopy. Based on the SEM photos, the particle size distribution of AC was analysed by software Nano Measurer.

### 7.2.5. Test and characterisation the electrochemical properties

The electrochemical performance of the EDLCs developed was studied by CV, GCD and EIS testing, using a VersaSTAT 3 electrochemical workstation.

The details of the characterisation methods and capacitance measurement methods are described in Section 3.3 of Chapter 3. And, the specific capacitance per unit length of a fibre supercapacitor (F $cm^{-1}$) is calculated by equation 6.1 in Section 6.2.6.

## 7.3. Results and discussion

Original AC material was milled by ball-milling apparatus to get ACs with different particle sizes. There are 8 kinds of ACs: AC0, AC4, AC8, AC12, AC16, AC20, AC24 and AC48. From SEM observations, it was possible to measure ACs particle size and distribution. The average AC particle size as a function of the ball milling time was determined.

### 7.3.1. Effect of ball-milling time on particle size

Figure 7.2 shows pictures of the suspensions of the ACs kept in vials. The suspension was made by mixing a small amount of milled AC powders with a mixture of water and

ethanol (1:1). In order to let the milled AC particles disperse well, an ultrasonic bath was used for the same time to all the suspensions. As shown in Figure 7.2a and b, the colour of all the suspensions are similar. That indicates that the milled AC particles were dispersed well in the solvent after the ultrasonic bath. Figure 7.2c and d show the suspensions of all the milled ACs after setting on a table at room temperature for 15 min. It is clear that there is a big difference between the samples. The colour of upper portion of the suspensions of AC0 turns grey from the black, and it is found some AC0 particles disperse there. The reason is that some of the big AC particles precipitated because of their density and size, and are found at the bottom of the bottle. Some small AC0 particles are still suspended resulting in the light black colour of the upper portion of the suspension. This suggested that the particle sizes of the AC0 are different. As shown in Figure 7.2a and c, the colours of the suspensions of AC4 changes slightly compared with the colour of this sample after 15 min. The same phenomenon can be found in the suspensions of AC8, AC12 and AC16, respectively. It suggests that the particles size decreased most likely after ball-milling compared with the original AC particle size. The details of the particle size change was tested by SEM and analysed further. It is seen that the colour of the AC20 suspension also turns to light black after setting on the table for 15 min. A similar phenomenon occurred in suspension of AC24. There is a small difference in this phenomenon and that of the phenomenon seen in AC0 suspension: it is found that the particle dispersed in the upper portion of AC0 suspension is bigger than that dispersed in the upper portion of the AC20 or AC24. Compared with other samples, there is an interesting phenomenon occurred in suspension of AC48: the supernatant turns clear. It is quite obvious to find the visible precipitate of the AC particles at the bottom of the bottle. The main trend of the precipitate phenomenon decreased firstly, then maintained, increased at the end. Because the density of the big particles in AC0 suspension resulting in precipitation. When the ball-milling time prolonged from 4 to 16 h, the particle size decreased, these small particles are easy to disperse in the solvent than the big ones. When the ball-milling time was further prolonged to 20 h, although the particles size became smaller, the agglomeration of the small particles occurred which resulted in precipitation [213][214]. Furthermore, the agglomeration increased when the ball-milling time prolonged from 20 to 48 h. It suggests that the particle size of the ACs decreased with prolonged ball-milling time.

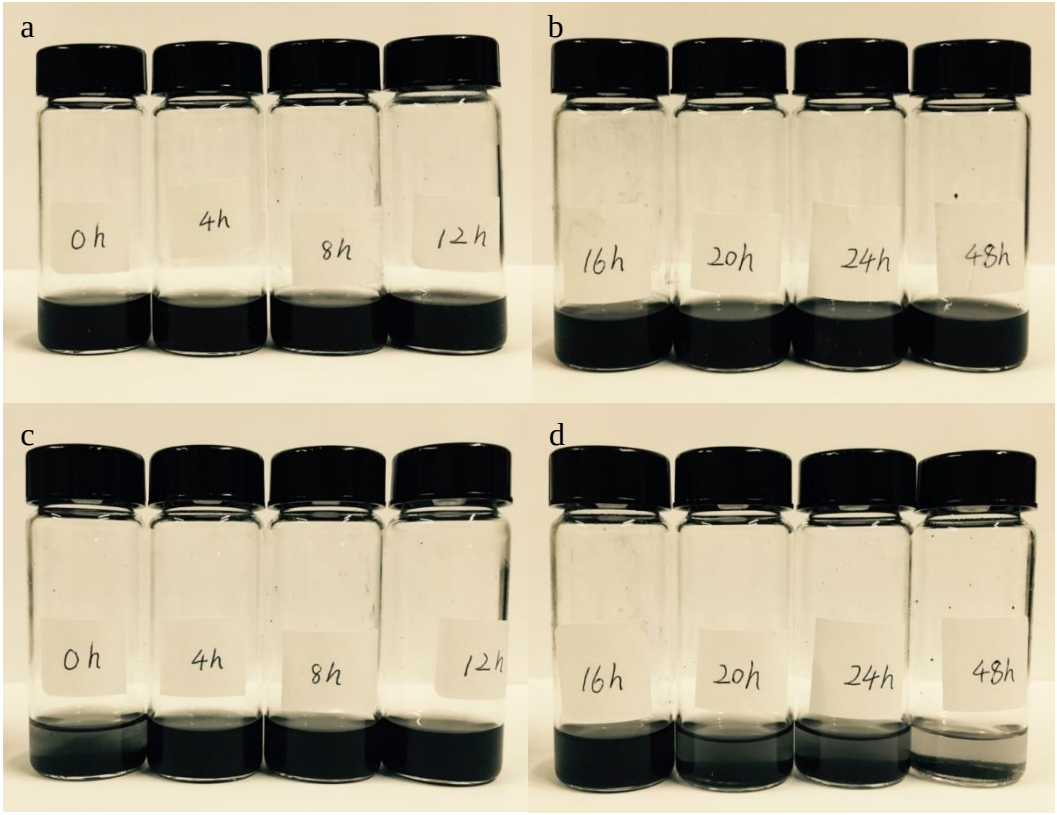


Figure 7.2 The suspension of ACx before (a and b) and after setting still for 15 mins (c and d).

Figure 7.3a shows the SEM image of AC0 particles. It can be seen that the size of the AC particles is not equal. The AC particles are polydisperse and range from hundreds of nanometres to tens of microns. Compared with the original AC0 particles, the particle size of milled AC4 decreased dramatically and become more uniform than the original AC0. However, some big particles with the size of tens of microns still can be found in Figure 7.3b. When the ball-milling time prolonged to 24 h, the particle size seemed much more uniform and became smaller than AC0 and AC4. There are a few long big particles in the sample. The agglomeration is seen in Figure 7.3c. When the ball-milling time further prolonged form 24 to 48 h, the particles became smaller. The big particles with the size of tens of microns almost were not found in Figure 7.3d. Furthermore, the agglomeration increased. This observation is in good agreement with that seen in the suspensions of ACx after setting still on a table for 15 mins. The milled AC with a longer

ball-milling time has a smaller particle size, these smaller particles agglomerate more easily than the big particles. The reason is that the particles with smaller size have higher surface energy, which results in the agglomerate as agglomeration can diminish this energy [213][214].

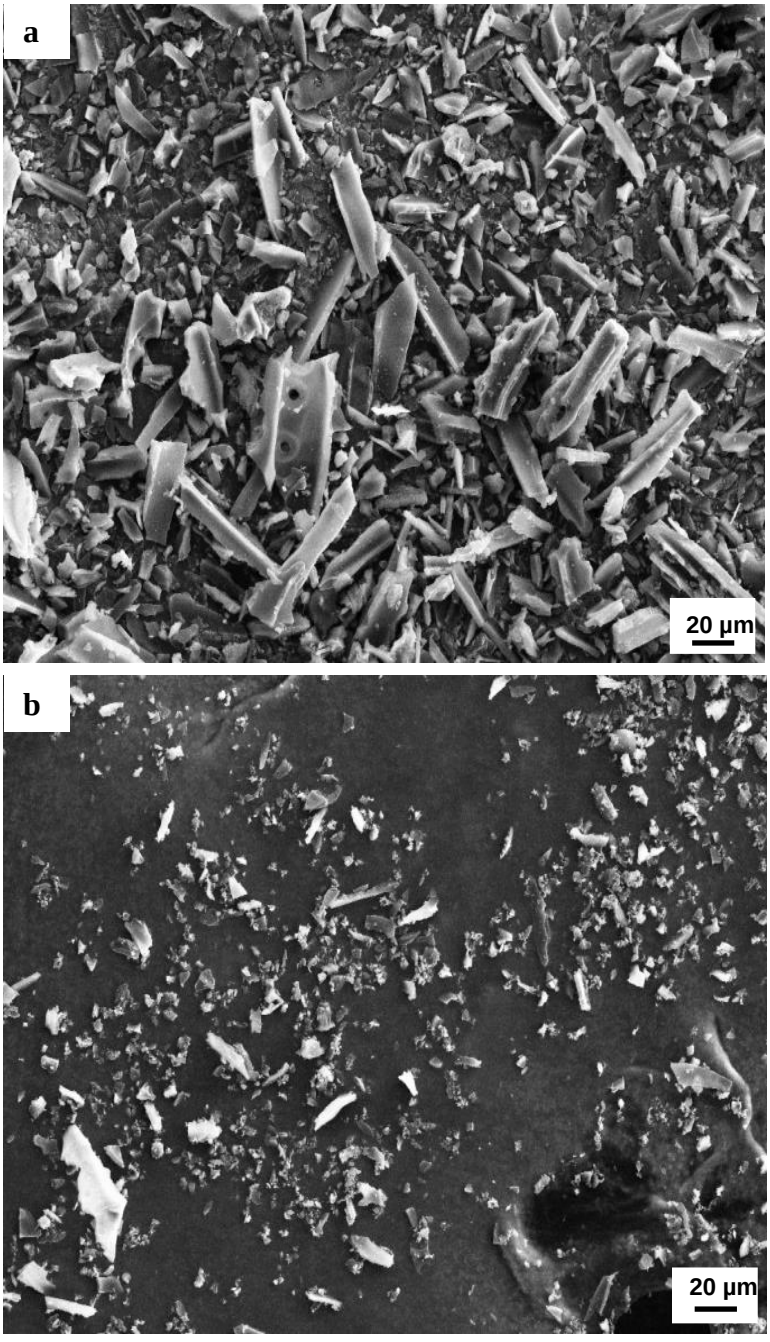

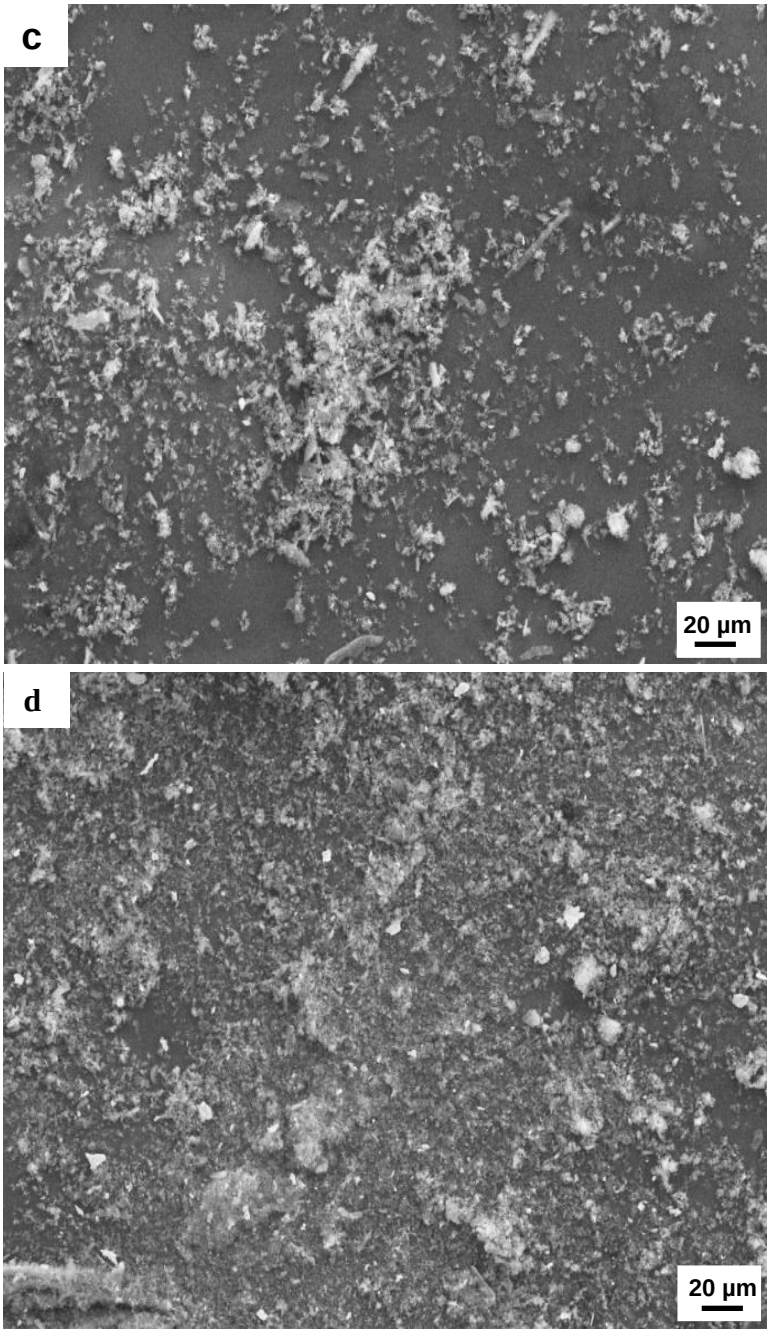


Figure 7.3 SEM photos of AC0 (a), AC4 (b), AC24 (c) and AC48 (d).

Using the SEM photos, image analysis software, Nano Measurer, is used to measure the size of AC particles. After the analysis of the data, the size distribution of the AC particles was obtained and shown in Figure 7.4. And the average particle size of the milled AC with different ball-milling time is shown in Figure 7.5.

Figure 7.4 showed the particle size dispersion of the original AC and ACx prepared using ball-milling method. As shown in Figure 7.4a, it is seen that the size of the original AC (AC0) particles has a big range. The approximate range of the AC0 particles size is from 0 to 150 μm. It indicates that the particles of original AC are not uniform. The average size of the AC0 particles is about 39.264 μm as shown in Figure 7.5. It is obvious that the particle size decreased dramatically when the original AC was milled for 4 h as shown in Figure 7.4a. The main range of the AC4 particle size is from 0 to 40 μm. The range becomes narrower than the original AC particle size range. And its average particle size decrease about 76.2% from 39.264 to 9.354 μm because of high number of 'crushing' events during the ball-milling process. When the ball-milling time further extended to 8 h and 12 h, the particle size distributions are 0-15 μm and 0-10 μm, respectively. The corresponding average particle sizes are about 5.664 and 3.399 μm, respectively (Figure 7.5). As shown in Figure 7.4b, the particle size distribution also becomes narrow when the ball-milling time further prolonged to 24 h, and the average particle size further decreased to a few microns from tens of microns. It is obvious that the pace of the change for the size distribution and the average particle size becomes slow. When the milling time further increased to 48 h, the range of the particle size dispersion is from 0 to 0.4 μm, which similar to that of the AC24 (0-0.4 μm). And its average particle size is 149 nm, which is very close to that of the AC24 (160 nm). It has been reported that there is no further size reduction after some h of grinding of some materials in laboratory ball mills [215]. The above results are probably caused by the mechanical strength of AC particles and the cushion strength among AC particles increases with the particle size decreasing. The other reason is that the AC48 nanoparticles are easy to agglomerate as shown in Figures 7.3c and d. As shown in Figure 7.5, the AC nanoparticles can be produced by a ball-milling treatment.

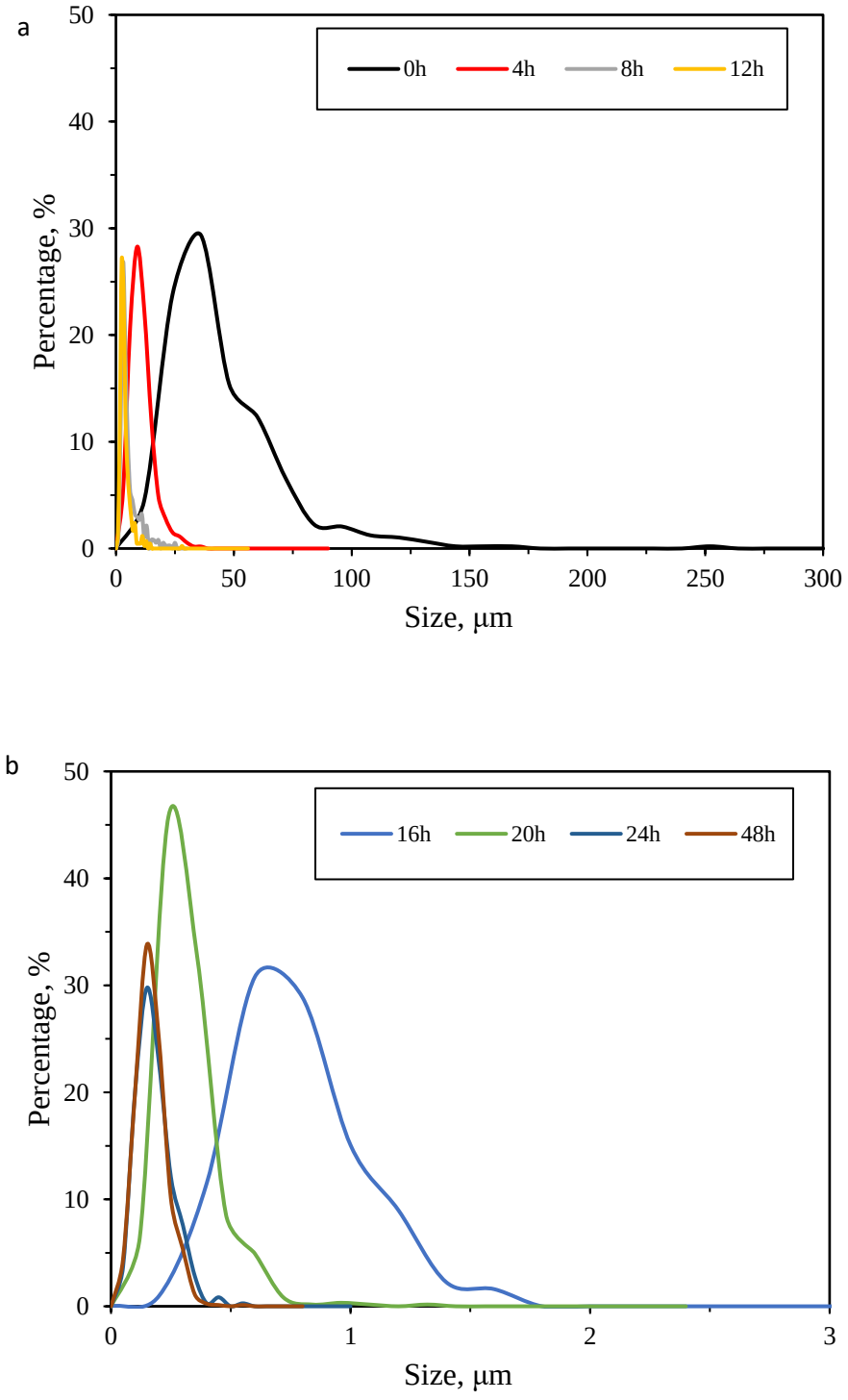


Figure 7.4 Particle size dispersions of AC0, AC4, AC8 and AC12 (a), AC16, AC20, AC24 and AC48 (b).

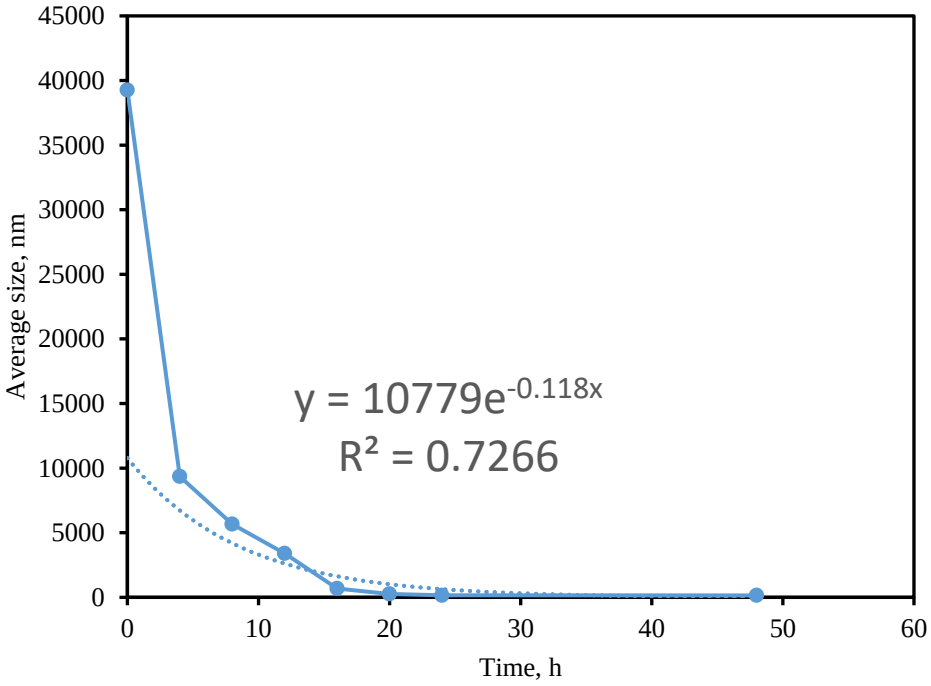


Figure 7.5 Effect of the ball-milling time on the average particle size.

### 7.3.2. Effect of ball-milling time on X-ray diffraction performance

Figure 7.6 shows comparison of XRD patterns for ACs milled from 0 to 48 h. It can be seen there are two features appearing on the patterns of AC0. The first broad peak, which is located at around 22-23°, corresponds the (002) reflection of carbon [26][216]. This wide peak showed the AC0 sample has no significant crystalline structure [217]. Compared with the first peak, the second one, which located around 43-44°, becomes narrow and less intense. This peak corresponds the (100) reflection. When the milling time prolonging from 0 to 20 h, the broad peaks which corresponds the (002) reflection became less intense. When the milling time further prolonged to 24 and 48 h, the peaks (002) almost disappeared. It is also found that there were some new peaks appearing when the milling time was prolonged. For both forms of carbon, a peak around 36° and 46°, which was due to iron–carbon phases ($Fe_xC$) which was probably formed during the milling of iron and carbon together, as it emerged with increasing milling time. Other new peaks around 45°, 57° and 63° emerged with prolonging milling time were attributed to $Fe_2O_3$ which may be formed during the milling of iron in the air. Iron was abraded from

stainless steel balls and container used in the milling process. And the intense of the $Fe_xC$ or $Fe_2O_3$ became bigger when the milling time increasing, the same phenomenon was also presented in these references [217][218][219]. Furthermore, Janol et al. [219] have proved the iron compound introduced during ball-milling process can contribute to the electrochemical performance of the powders.

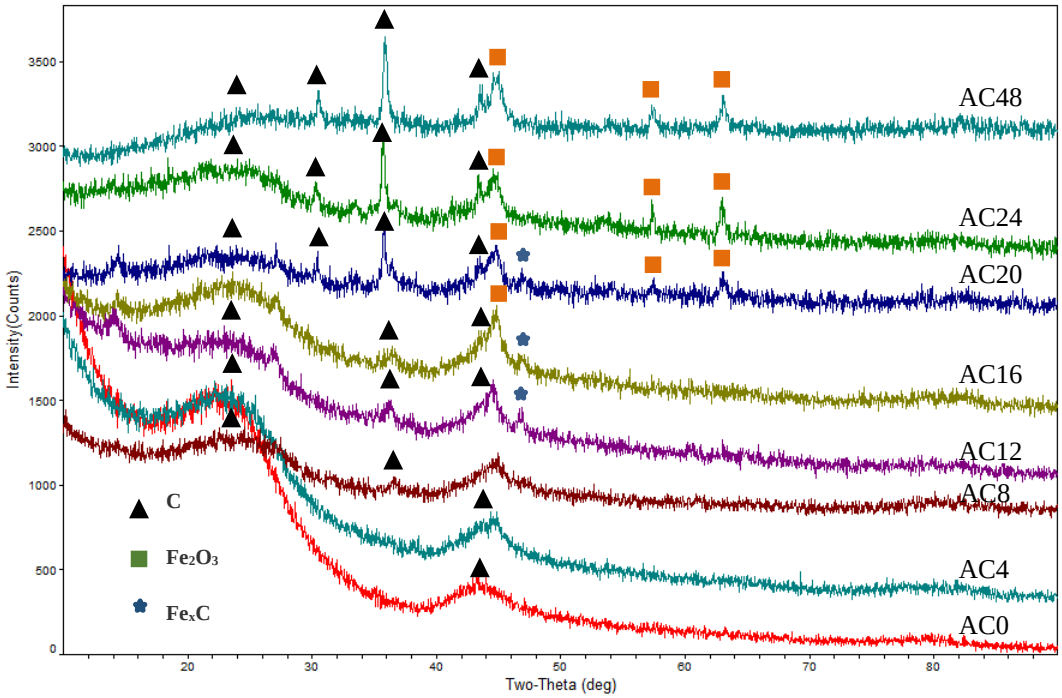


Figure 7.6 Normalised XRD traces for AC milled for 0, 4, 8, 12, 16, 20, 24 and 48 h.

### 7.3.3. Effect of the ball-milling time on the specific capacitance of ACx

As shown in Table 7.1 and Figure 7.7, the specific capacitance of the ACx electrodes increased when the ball-milling time was prolonged. For example, the AC4 is produced by milling the original AC0 for 4 h, its specific capacitance is about 33.1 F/g, which increased by 65.5% more than the specific capacitance of the original AC0 (20 F/g). When the milling prolonged to 8 h, the specific capacitance of AC8 (34.7 F/g) increased about 73.5% more the specific capacitance of AC0. As shown in Figure 7.7, when the ball-milling time prolonged to 4 and 8 h, the average particle size decreased form about 39.264 μm for AC0 to 9.354 μm for AC4 and 5.664 μm, respectively. It is found that the average particle size decreased dramatically (decreased about 76.2% than average particle

size for AC0) when the original AC0 was milled in first four h, while the specific capacitance increased dramatically (65.5% than that of AC0). Then when the ball-milling time was further extended to 8 h, the average particle size decreased 85.6% than original average particle size of AC0, that means the average particle size decreased 9.4% based on the original particle size when the AC0 was milled in the second 4 h, meanwhile, the specific capacitance increased by about 8% based on the original specific capacitance of AC0. That suggested that as the particle size decreased the specific surface area increased which is the main reason that results in higher specific capacitance. However, when the ball-milling time prolonged from 8 h to 12 h, the specific capacitance for AC12 (33.3 F/g) does not increase compared to that of AC8 (34.7 F/g), although the average particle size still decreased. It is considered that because the agglomeration occurred when the particle size becomes smaller, this has a negative effect on the specific surface area. This may be the reason that when ball-milling time prolonged to 16 and 20 h, the specific capacitance shows a slow growth. On one hand, the particle size decreases generally has a positive effect on the specific surface area during ball-milling; on the other hand, if the particle size becomes too small, it will enhance agglomeration resulting in a specific surface area decrease. Therefore, the variation of specific capacitance for milled carbons is the combined result of these two opposing effects. When the ball-milling time is prolonged from 20 h to 24 h, the specific capacitance increased dramatically into 44.7 F/g from 36.7 F/g. That suggests the positive effect of the particle size decrease plays a more important role. Moreover, the average particle size decreased from 160 nm to 149 nm when the ball-milling time extended from 24 h to 48 h, and the specific capacitance for AC48 (45.3 F/g) increased slightly compared to that of AC24 (44.7 F/g), because the negative effect of the agglomeration plays the determinative role during this process. The results above show that there is an optimum ball-milling time to produce the milled AC with a good electrochemical performance.

Table 7.1 Composition of the electrode activated material.

| Sample | Ball-milling time, h | Particle size dispersion, μm | Average particle size, μm | Specific capacitance, F/g |
|---|---|---|---|---|
| AC0 | 0 | 0-150 | 39.264 | 20.0 |
| AC4 | 4 | 0-40 | 9.354 | 33.1 |
| AC8 | 8 | 0-15 | 5.664 | 34.7 |
| AC12 | 12 | 0-10 | 3.399 | 33.3 |
| AC16 | 16 | 0-1.75 | 0.687 | 36.0 |
| AC20 | 20 | 0-0.75 | 0.265 | 36.7 |
| AC24 | 24 | 0-0.4 | 0.160 | 44.7 |
| AC48 | 48 | 0-0.4 | 0.149 | 45.3 |

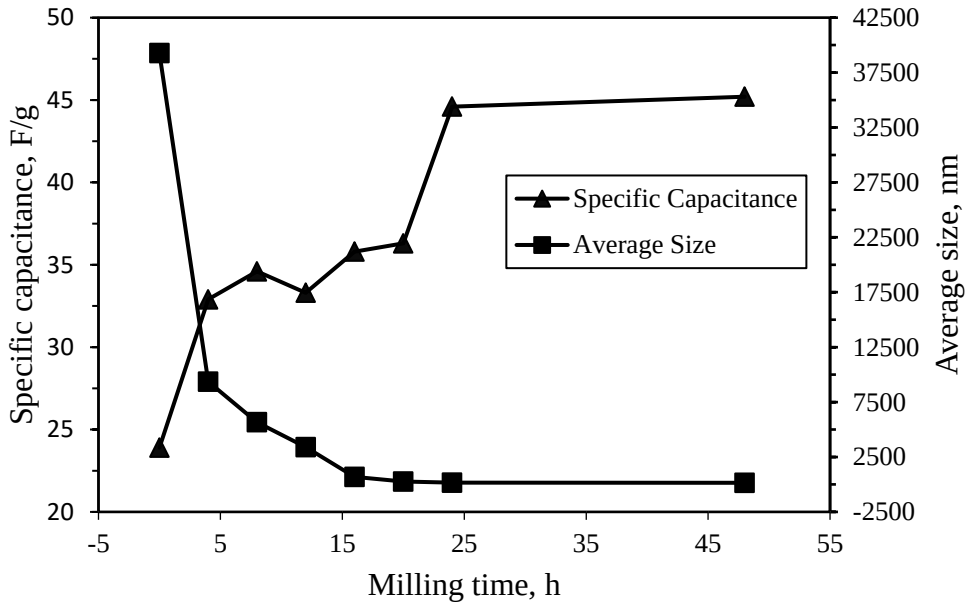


Figure 7.7 The relationship between the ball-milling time, the average particle size and the specific capacitance.

### 7.3.4. Optimisation of the capacitance of fibre supercapacitors using the new carbon ink

In order to improve the performance of fibre supercapacitors, the active layer coating ink was prepared by mixing the original Chinese ink with the milled AC. Above results suggests the optimum ball-milling time is 24 h, thus, AC24 was chosen as the active material added into the ink.

#### 7.3.4.1. Surface of the first active layer of fibres coated with different active inks

Figure 7.8 shows the SEM photos of coating copper fibres with the ink, the ink mixed with the AC0 and ink mixing with AC24. In Figure 7.8a, the surface of the ink layer coated on the copper fibre is quite smooth and complete. As shown in Figure 7.8b, when the ink mixed with AC0 was used as the active layer material, the coated layer surface became rough because of the AC0 particles added are bigger than the original ink particles, but this layer is still complete. It can also be seen that the particle size of AC0 is uneven. These particles are range from hundreds of nanometres to tens of microns in size. The details of the particle size dispersion and the average particle size have been shown in Figure 4a and Figure 5. The average particle size of the AC0 is about 39 μm. Figure 7.8c shows the SEM photo of the coated layer surface using ink mixing with AC24 as the slurry. It is seen that the coated layer is complete, and the surface is smoother than that of ink mixing with the AC0 because the particle size range (0-0.4 μm) of AC24 became much narrower than that of the AC0 (0-150 μm). The three samples are made by coating active material ink 10 times. After analysis, it is found that the average diameter of three samples are 105 μm for fibre coated with ink, 109 μm for fibre coated with ink mixing with AC0, and 108 μm for fibre coated with ink mixing with AC24, respectively. The reason is that the total content of the carbon increased when AC0 or AC24 were added into the commercial ink.

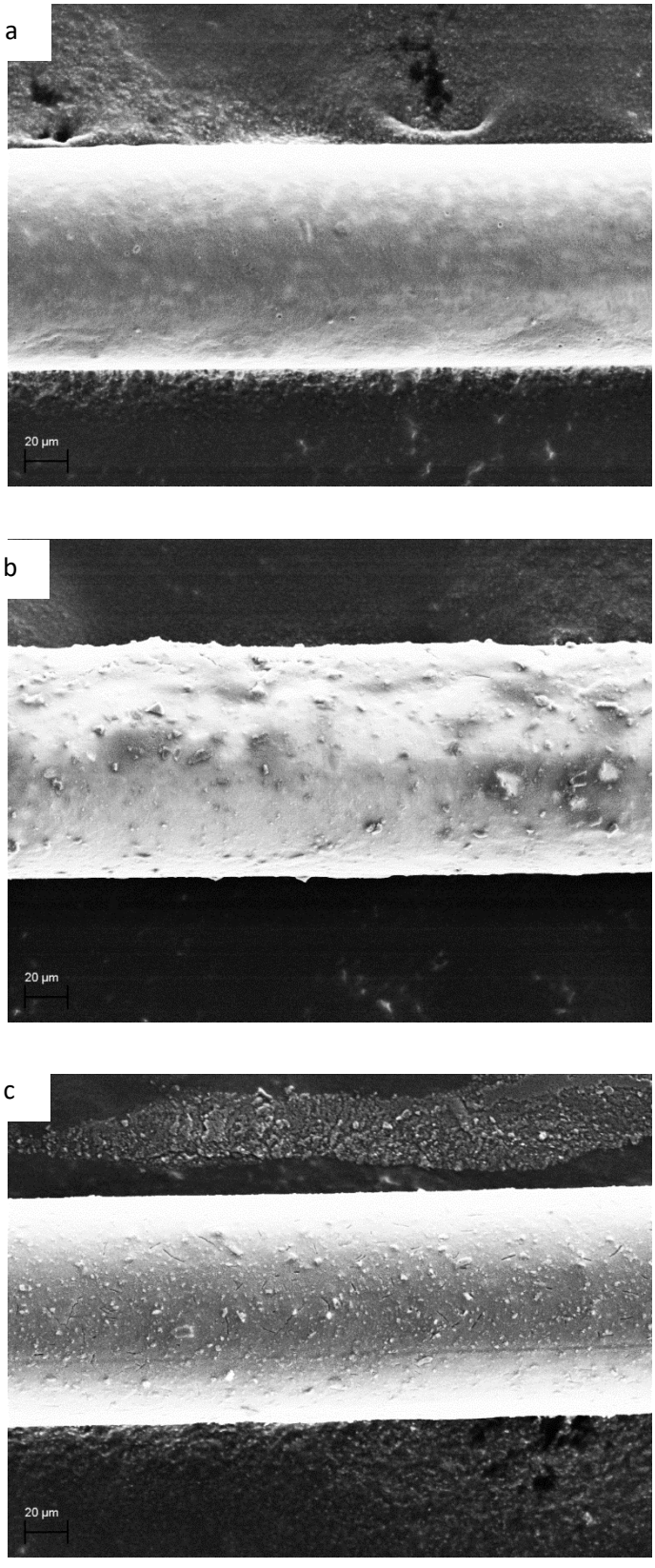


Figure 7.8 SEM photos of the three fibre samples coated with different active materials: commercial ink (a), ink mixing with AC0 (b) and ink mixing with AC24 (c).

### 7.3.4.2. Effect of different active materials on the performance of the fibre supercapacitors

As shown in Figure 7.9, CV curves of fibre supercapacitors using ink or ink mixed with AC0 as the active layer material were recorded at the scan rate of 0.010 V/s. It is found that when the AC0 was added into the active layer, the area of the CV curve increased. The fibre supercapacitor using ink mixed with AC0 shows a higher capacitance than the fibre supercapacitor using the commercial ink. Figure 7.10 shows the CV curves of the fibre supercapacitor using ink, ink mixed with AC0 and ink mixed with AC24 as the active layer material, respectively. The scan rate was also fixed at 0.010 V/s. It is seen that the area of the fibre supercapacitor using ink mixed with AC24 is greatest among all the three curves of fibre supercapacitors. It shows the capacitance for the sample using ink mixing with AC24 is bigger than other two samples.

All the capacitances and specific capacitances calculated based on the CV curves are shown in Table 7.2. The capacitance of S1 using just ink as the active layer material is 0.029 F. The length of S1 is 21 cm, so the corresponding specific capacitance is 0.9 mF/cm. And the capacitances of S2 using ink mixed with AC0 and S3 using ink mixed with AC24 as the active layer material is 0.119 F and 0.811 F, respectively. The length of S2 is 18 cm, and the length of S3 is 35 cm, the corresponding specific capacitances are 4.0 mF/cm for S2 and 14.5 mF/cm for S3, respectively. The specific capacitance of S2 increases about 4 times than that of S1, and specific capacitance of S3 is about 16 times more than that of S1. The reason is that the AC0 or AC24 added provides more surface area for energy storage. It is seen specific capacitance of S3 is also bigger than that of S2, the reason is further discussed in the following sections.

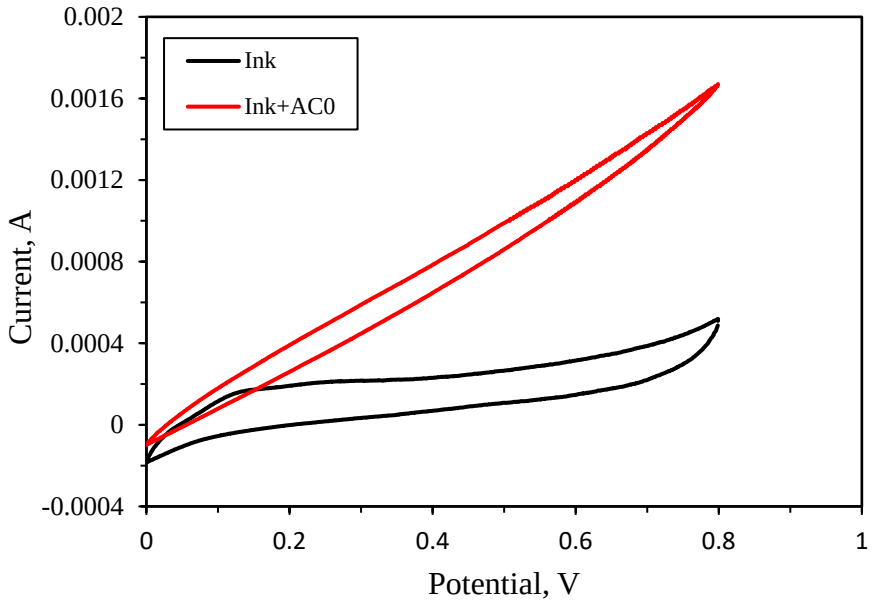


Figure 7.9 CV curves of fibre supercapacitors using ink or ink mixing with AC0 as the active layer material at the scan rate of 0.010 V/s.

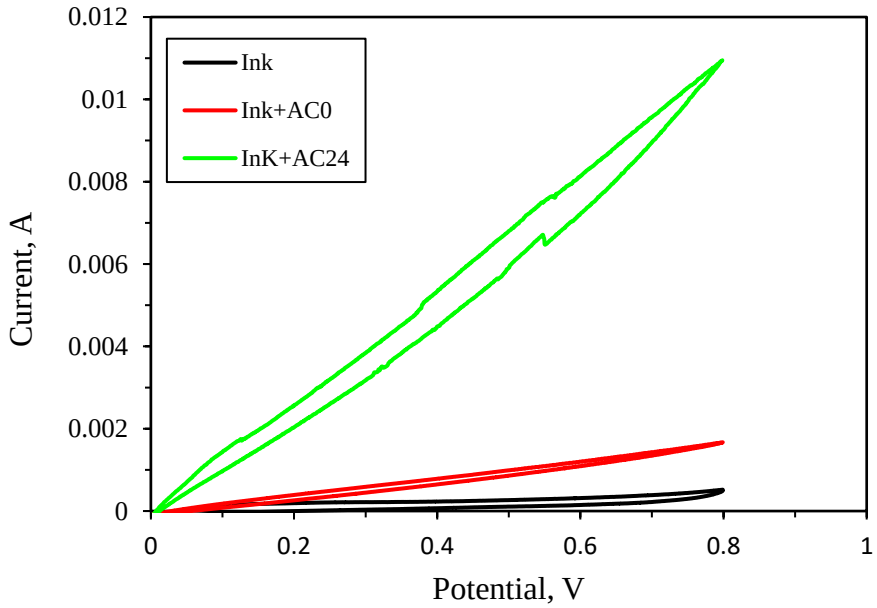


Figure 7.10 CV curves of fibre supercapacitors (at the scan rate of 0.010 V/s) using ink, ink mixing with AC0 and ink mixing with AC24 as the active layer material, respectively.

Table 7.2 Capacitances and specific capacitances of the fibre supercapacitors using different active materials.

| slurry | AC amount | Capacitance, F | Length, cm | $C_L$, mF/cm |
|---|---|---|---|---|
| S1-Ink | | 0.029 | 21 | 0.9 |
| S2-Ink+AC0 | 5% | 0.119 | 18 | 4.0 |
| S3-Ink+AC24 | 5% | 0.811 | 35 | 14.5 |

### 7.3.4.3. The reason of a specific capacitance increase of fibre supercapacitors using the ink mixing milled AC

In order to further discuss the reason for the capacitance increase of the fibre supercapacitor using ink mixing with milled AC, the thickness and the mass of first active carbon layer using different inks was studied. Four samples were made with the same length of 60 cm. Sample a is only copper fibre, Sample b, c and d are the copper fibres coated with the ink, ink mixing AC0 and ink mixing with AC24. As shown in Table 7.3, the thicknesses of the active layer was about 4 μm for sample b, 7 μm for sample c and 6 μm for sample d, respectively. The thickness for active layer in sample c is very close to that in sample d. They are all more than the thickness of active layer in sample a. The mass of the first active layer was measured using a balance with the readability of 0.00001 g. It is found that the mass for the active layer in sample b, c and d are 0.58, 1.38 and 1.33 mg, respectively. The corresponding values of specific mass per length are 0.01, 0.02 and 0.02 mg/cm, respectively. It is obvious that the mass of active layer in sample c is very close to that in sample d, and they are all bigger than that in sample b. The specific mass shows the same trend. As shown in Figure 7.11, the thickness of active layer increases, so the volume of the active layer increases resulting in the corresponding mass increase. As the amount of the AC0 and AC24 added are about the same, the content of the carbon is equal in the ink mixed with AC0 and ink mixed with AC24. This leads to a similar thickness and mass for sample c and d. Figure 7.12 shows the specific capacitance of fibre supercapacitors using different active layer materials. As the mass of the active layer in sample c and d increased, the active layer can provide more surface area for energy storage which results in the capacitance increase for the fibre supercapacitors using mixed ink. The mass increase is about 2 times more than that in sample b, and the

capacitance increases more than twice. This suggests the AC shows a better electrochemical performance when mixing carbon materials with the commercial ink. Although the mass increase for fibre supercapacitor using ink mixing AC0 is as the same as that using ink mixing with AC24, the capacitance for former sample is smaller than latter one. The reason is that the specific capacitance for AC24 is more than AC0 has been shown in Figure 7.7.

Table 7.3 Thickness and mass as well as specific mass of the first active layer in fibre supercapacitors using different active materials.

| sample | Length, cm | Mass, mg | Mass of active material layer, mg | Mass of active material layer per length unit, mg/cm | Thickness of active layer, μm |
|---|---|---|---|---|---|
| Sample a: Copper fibre | 60 | 41.09 | -- | -- | -- |
| Sample b: Copper fibre with ink | 60 | 41.67 | 0.58 | 0.01 | 4 |
| Sample c: Copper fibre with ink mixing AC0 | 60 | 42.47 | 1.38 | 0.02 | 7 |
| Sample d: Copper fibre with ink mixing AC24 | 60 | 42.42 | 1.33 | 0.02 | 6 |

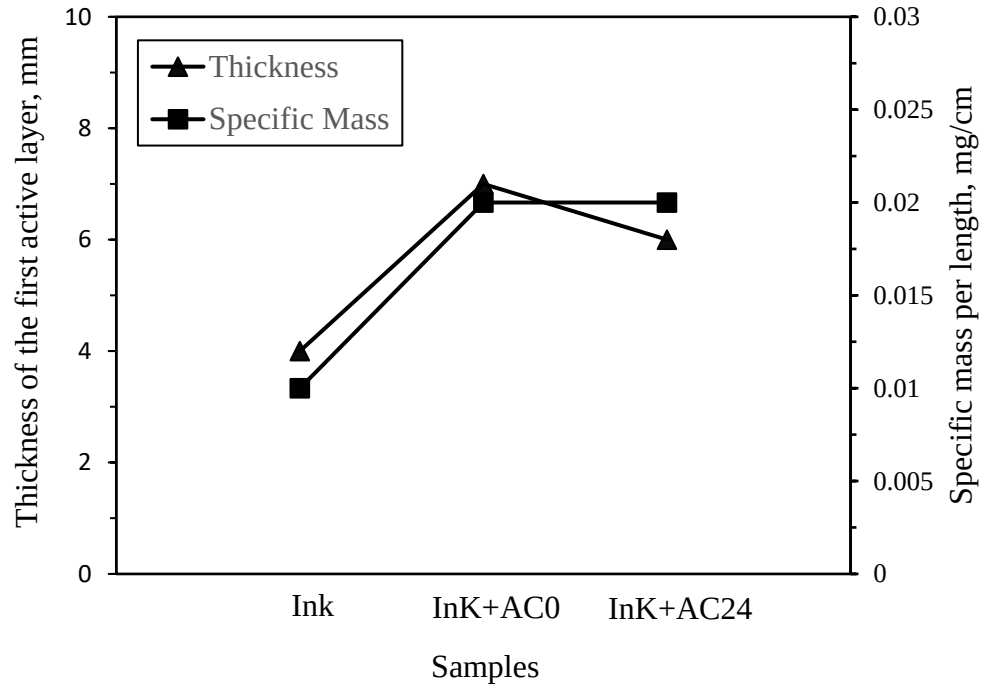


Figure 7.11 Specific mass and thickness of active layer in different samples using different active layer materials.

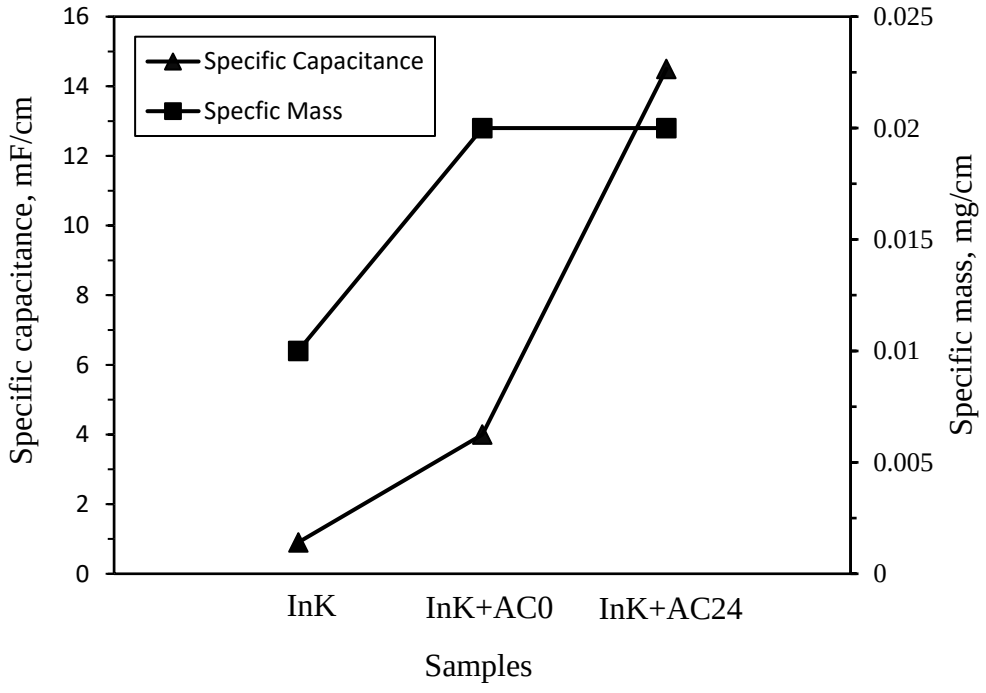


Figure 7.12 Specific capacitances of fibre supercapacitors using different active layer materials.

## 7.4. Conclusion

In this chapter, different kinds of AC materials were prepared by ball-milling. It was found that the particle size distributions become narrow, and the average particle size decreased into tens of nanometres from tens of microns when the ball-milling time was prolonged. When the milling time increased from 24 h to 48 h, the range of the particle size dispersion and average particle size changed little because of the agglomeration of small AC particles. XRD results indicated that $Fe_xC$ or $Fe_2O_3$ generated when the ball-milling time increased. The particle size decrease, specific surface area increase and $Fe_xC$ or $Fe_2O_3$ introduced in the ball-milling process are considered as the reasons for the specific capacitance of milled ACs increasing compared with that of original AC. Because agglomeration occurred when the particle size becomes smaller and smaller, this has a negative effect on the specific surface area. The specific capacitance grew slowly when the ball-milling time prolonged from 24 h to 48 h. The results above show that 24 h is an optimum ball-milling time to produce the milled AC with a good electrochemical performance. When a small amount of 24-h ball-milling AC was added into commercial ink to prepare a new active material for fibre supercapacitors, the specific capacitance is 16 times more than that of a fibre supercapacitor using commercial ink alone as the active layer material, and 4 times than that of fibre supercapacitor using ink mixed with original unmilled AC.

# Chapter 8. Conclusions

From this work, the following points summarise the main contributions to knowledge made in this thesis:

1. The mechanical testing method was combined with the electrochemical testing method to further test the flexibility and the performance of the flexible supercapacitors under the static and dynamic mechanical testing conditions.
    - The strip supercapacitor developed in our work was functional under bending conditions between the bending angles of 30° to 150°. The capacitance of the sample was still about 70% of the original capacitance at different bending angles. The correlation between the capacitance and the ESR/CTR was established and it was found that the increases of the ESR and CTR were the main reason of the capacitance decrease when the strip supercapacitor was bent.
    - The strip supercapacitors under static and dynamic mechanical tensile process work well: the capacitance and specific capacitance for this supercapacitor sample with the static load of 100 N or 200 N was bigger than that of this sample without any loading, with an increase of 22% and 9%, respectively. Furthermore, it was found that the capacitance increased when the sample was in the mechanical tensile stress test and press conditions. The reason might be that the mechanical loading was beneficial to the contact of each part in the strip supercapacitor resulting in a low charge transfer resistance.

2. In this work, the effect of the main operation factors on the performance of flexible supercapacitors was investigated by an experimental design method. This provides a novel way to optimise the performance of supercapacitors by controlling the practical parameters.
    - The relationships between the performance and the key factors of the strip EDLCs including the CMC binder concentration, the electrolyte concentration and the thickness of active material layer were presented. The results showed that in the range of 0.5-1.5 mol/L, the electrolyte concentration had little effect on the capacitance; when the thickness of AC electrode layer increased from 125 μm to

625 µm, the capacitance increased; and the capacitance decreased when the binder concentration increased from 1% to 8%.

3. The specific performance of the AC was optimised using ball-milling method. The effect of the ball-milling time on the performance of AC was further studied. 24-h ball-milled AC with the optimum specific capacitance was added into commercial ink to prepare a new active material for fibre supercapacitors. The specific capacitance of the fibre supercapacitors was improved dramatically by using this new active material.
    - The size distributions of the AC particles become narrow, and the average particle size decreased into tens of nanometres from tens of microns when the ball-milling time was prolonged. When the milling time increased from 24 h to 48 h, the range of the particle size dispersion and average particle size had not basically changed because of the agglomeration of small AC particles.
    - The specific capacitance of the milled AC increased when the ball-milled carbon prolonged. The particle size decrease, specific surface area increase and $Fe_xC$ or $Fe_2O_3$ introduced in the ball-milling process are considered as the reasons for the specific capacitance of milled ACs increasing compared with that of original AC. The specific capacitance grew slowly when the ball-milling time prolonged from 24 h to 48 h, because agglomeration occurred when the particle size became smaller and smaller, this had a negative effect on the specific surface area. The results above show 24 h may be an optimum ball-milling time to produce milled AC with a good electrochemical performance.
    - When a small amount of 24-h ball-milled AC was added into commercial ink to prepare a new active material for fibre supercapacitors, the specific capacitance was 16 times more than that of a fibre supercapacitor using commercial ink alone as the active layer material, and 4 times than that of fibre supercapacitor using ink mixed with original AC.

In addition, the following conclusions in this thesis are drawn:

4. Strip supercapacitors were successfully designed and fabricated using AC material as the electrode active material by blade coating. This AC showed a good electrochemical scan rate performance and an excellent electrochemical performance under different charging/discharging currents. At the same time, the preparation process of EDLCs

showed a good reproducibility.

5. Coaxial single fibre supercapacitors were successfully designed and manufactured using commercial ink as the active layer material by dip-coating method. The fibre supercapacitor showed a good flexibility: the fibre supercapacitors kept a good electrochemical performance under severe bending conditions, and the capacitance of the fibre supercapacitor woven into the fabric was the same as the original capacitance of the free standing sample.
6. The current and potential ranges were improved by connecting multiple fibre supercapacitors or strip supercapacitors in parallel or in series to meet the power and energy requirements. The electrical properties of the series and parallel combinations of two strip supercapacitors showed a good agreement with the theoretical models of series and parallel circuit combinations, as well as two fibre supercapacitors.

# Chapter 9. Suggestions for Further Work

In this thesis, flexible strip supercapacitors and fibre supercapacitors were designed and manufactured using low-cost materials and a simple method. The performance of the strip supercapacitors under mechanical bending, tensile and pressure was studied, as well as the performance of fibre supercapacitors under bending and woven into fabric. All of these kinds of supercapacitors showed good flexibility. For the strip supercapacitors, the effect of key practical factors including the binder content, the thickness of the active layer and the concentration of the electrolyte on the performance of strip supercapacitors were studied to allow the optimisation of the electrical performance. Another way to improve the performance using milled AC replacing the original AC was investigated. When this milled AC with the optimum specific capacitance was added into the ink to produce the new ink used as the active layer material for fibre supercapacitors, the specific capacitance of fibre supercapacitors improved dramatically. These results could be very important for flexible supercapacitors design and optimisation of the performance. However, some further study based on this thesis can be carried on for further work.

**Design and manufacture of composite supercapacitors**: it was proved that the electrical properties of the series and parallel combinations of two strip supercapacitors or fibre supercapacitors showed a good agreement with the theoretical model of series and parallel circuit combinations. If composite supercapacitors with multilayers of functional parts, such as electrodes, separators and current collectors, were fabricated, then different parts which can serve as different supercapacitors were connected in a parallel or series way, the desired operating voltage and energy can be obtained.

**Preparation of the new carbon slurry for fibre supercapacitors**: the commercial ink is stable and shows a good electrochemical performance. When the milled AC was added into the commercial ink, the electrochemical performance increased dramatically. It provides a potential way to prepare the new slurry for the fibre supercapacitors: the optimum milled AC can be used as the main active layer material mixed with the proper binder to produce stable slurry.

**Redesign of the dip-coating devices:** in this thesis, the dip-coating device designed and manufactured works well, and the flexible supercapacitors can be produced with lengths of tens of centimetres using this device. Based on this dip-coating device, the coating vessel and other parts can be redesigned to make longer fibre supercapacitors.

**Core fibre material**: the core fibre supercapacitor used in this thesis is copper fibre and the diameter is only 100 microns. The fibre supercapacitor using this copper fibre shows a good flexibility, however the mechanical loading properties of the thin copper fibre are not good. The polymer or carbon fibre with a good mechanical properties and conductivity is another choice for the core material.

**Developing of the new electrolyte**: the gel electrolyte used in this thesis is $H_3PO_4$/PVA, so the range of working potential is narrow. As is known, the working potential plays an important role on the total energy storage in supercapacitors. Developing a new electrolyte is quite important for the flexible supercapacitors.

# References


[1] R. Kötz, M. Carlen, Principles and applications of electrochemical capacitors, Electrochim. Acta. 45 (2000) 2483–2498.

[2] A. Burke, Ultracapacitors: why, how, and where is the technology, J. Power Sources. 91 (2000) 37–50.

[3] J.R. Miller, P. Simon, Materials science. Electrochemical capacitors for energy management., Science. 321 (2008) 651–652.

[4] D.P. Dubal, J.G. Kim, Y. Kim, R. Holze, C.D. Lokhande, W.B. Kim, Supercapacitors based on flexible substrates: An Overview, Energy Technol. 2 (2014) 325–341.

[5] P. Yang, W. Mai, Flexible solid-state electrochemical supercapacitors, Nano Energy. 8 (2014) 274–290.

[6] H. Becker, Low voltage electrolytic capacitor, 1957.

[7] R.A. Rightmire, Electrical energy storage apparatus, US Pat. 3288641. (1966).

[8] D.L. Boos, Electrolytic capacitor having carbon paste electrodes, US Pat. 3536963. (1970).

[9] Wikipedia, Double-layer capacitor, https://en.wikipedia.org/wiki/Electric_double-layer_capacitor.

[10] B.E. Conway, Transition from “supercapacitor” to “battery” Behavior in electrochemical energy storage, J. Electrochem. Soc. 138 (1991) 1539–1548.

[11] B.E. Conway, Electrochemical supercapacitors: scientific principles and technological application, Plenum, New York, 1999.

[12] P. Sharma, T.S. Bhatti, A review on electrochemical double-layer capacitors, Energy Convers. Manag. 51 (2010) 2901–2912.

[13] A. Schneuwly, R. Gallay, Properties and applications of supercapacitors From the state-of-the-art to future trends, in: Proceeding PCIM2000, 2000: pp. 1–10.

[14] M. Halper, J. Ellenbogen, Supercapacitors: A brief overview, 2006.

[15] B.E. Conway, Electrochemical supercapacitor: scientific fundamentals and technological applications, NewYork, 1999.

[16] A. Chu, P. Braatz, Comparison of commercial supercapacitors and high-power lithium-ion batteries for power-assist applications in hybrid electric vehicles: I. Initial characterization, J. Power Sources. 112 (2002) 236–246.

[17] S.M. Chen, R. Ramachandran, V. Mani, R. Saraswathi, Recent advancements in electrode materials for the high-performance electrochemical supercapacitors: a review, Int. J. Electrochem. Sci. 9 (2014) 4072–4085.

[18] Y. Zhang, H. Feng, X. Wu, L. Wang, A. Zhang, T. Xia, H. Dong, X. Li, L. Zhang, Progress of electrochemical capacitor electrode materials: A review, Int. J. Hydrogen Energy. 34 (2009) 4889–4899.

[19] J. Jiang, A. Kucernak, Electrochemical supercapacitor material based on manganese oxide: preparation and characterization, Electrochim. Acta. 47 (2002) 2381–2386.

[20] X. Lang, A. Hirata, T. Fujita, M. Chen, Nanoporous metal/oxide hybrid electrodes for electrochemical supercapacitors., Nat. Nanotechnol. 6 (2011) 232–236.

[21] H. Gómez, M.K. Ram, F. Alvi, P. Villalba, E. Stefanakos, A. Kumar, Graphene-conducting polymer nanocomposite as novel electrode for supercapacitors, J. Power Sources. 196 (2011) 4102–4108.

[22] E. Frackowiak, Q. Abbas, F. Béguin, Carbon/carbon supercapacitors, J. Energy Chem. 22 (2013) 226–240.

[23] M. Nasibi, M.A. Golozar, G. Rashed, Nanoporous carbon black particles as an electrode material for electrochemical double layer capacitors, Mater. Lett. 91 (2013) 323–325.

[24] L. Yang, L.R. Hou, Y.W. Zhang, C.Z. Yuan, Facile synthesis of mesoporous carbon nanofibres towards high-performance electrochemical capacitors, Mater. Lett. 97 (2013) 97–99.

[25] J.P. Zheng, P.C. Goonetilleke, C.M. Pettit, D. Roy, Probing the electrochemical double layer of an ionic liquid using voltammetry and impedance spectroscopy: A comparative study of carbon nanotube and glassy carbon electrodes in [EMIM]+[$EtSO_4$]-, Talanta. 81 (2010) 1045–1055.

[26] D. Qu, Studies of the activated carbons used in double-layer supercapacitors, J. Power Sources. 109 (2002) 403–411.

[27] H. Shen, E. Liu, X. Xiang, Z. Huang, Y. Tian, Y. Wu, Z. Wu, H. Xie, A novel activated carbon for supercapacitors, Mater. Res. Bull. 47 (2012) 662–666.

[28] P. Simon, Y. Gogotsi, Materials for electrochemical capacitors, Nat. Mater. 7 (2008) 845–854.

[29] C.S. Yang, Y.S. Jang, H.K. Jeong, Bamboo-based activated carbon for supercapacitor applications, Curr. Appl. Phys. 14 (2014) 1616–1620.

[30] K. Sing, D. Everett, R. Hual, L. Moscou, Physical and biophysical chemistry division commission on colloid and surface chemistry including catalysis, Pure Appl. Chem. 57 (1985) 603–619.

[31] G. Lota, T.A. Centeno, E. Frackowiak, F. Stoeckli, Improvement of the structural and chemical properties of a commercial activated carbon for its application in electrochemical capacitors, Electrochim. Acta. 53 (2008) 2210–2216.

[32] J. Gamby, P.L. Taberna, P. Simon, J.F. Fauvarque, M. Chesneau, Studies and characterisations of various activated carbons used for carbon/carbon supercapacitors, J. Power Sources. 101 (2001) 109–116.

[33] H. Shi, Activated carbons and double layer capacitance, Electrochim. Acta. 41 (1996) 1633–1639.

[34] D. Qu, H. Shi, Studies of activated carbons used in double-layer capacitors, J. Power Sources. 74 (1998) 99–107.

[35] G. Gryglewicz, J. Machnikowski, E. Lorenc-Grabowska, G. Lota, E. Frackowiak, Effect of pore size distribution of coal-based activated carbons on double layer capacitance, Electrochim. Acta. 50 (2005) 1197–1206.

[36] C.T. Hsieh, H. Teng, Influence of oxygen treatment on electric double-layer capacitance of activated carbon fabrics, Carbon. 40 (2002) 667–674.

[37] Y. Nian, H. Teng, Nitric acid modification of activated carbon electrodes for improvement of electrochemical capacitance, J. Electrochem. Soc. 149 (2002) 1008–1014.

[38] R.W. Pekala, Organic aerogels from the polycondensation of resorcinol with formaldehyde, J. Mater. Sci. 24 (1989) 3221–3227.

[39] X. Lu, R. Caps, J. Fricke, C.T. Alviso, R.W. Pekala, Correlation between structure and thermal conductivity of organic aerogels, J. Non. Cryst. Solids. 188 (1995) 226–234.

[40] Y.J. Lee, J.C. Jung, S. Park, J.G. Seo, S.H. Baeck, J.R. Yoon, J. Yi, I.K. Song, Preparation and characterization of metal-doped carbon aerogel for supercapacitor, Curr. Appl. Phys. 10 (2010) 947–951.

[41] U. Fischer, R. Saliger, V. Bock, R. Petricevic, J. Fricke, Carbon aerogels as electrode material in supercapacitors, J. Porous Mater. 17 (1997) 281–285.

[42] R.W. Pekala, J.C. Farmer, C.T. Alviso, T.D. Tran, S.T. Mayer, J.M. Miller, B. Dunn, Carbon aerogels for electrochemical applications, J. Non. Cryst. Solids. 225 (1998) 74–80.

[43] X. Yang, C. Cheng, Y. Wang, L. Qiu, D. Li, Liquid-mediated dense integration of graphene materials for compact capacitive energy storage, Science. 341 (2013) 534–537.

[44] E. Frackowiak, F. Béguin, Carbon materials for the electrochemical storage of energy in capacitors, Carbon. 39 (2001) 937–950.

[45] S.T. Mayer, R.W. Pekala, J.L. Kaschmitter, The aerocapacitor: an electrochemical double−layer energy−storage device, J. Electrochem. Soc. 140 (1993) 446–451.

[46] C. Lin, J.A. Ritter, Effect of synthesis pH on the structure of carbon xerogels, Carbon N. Y. 35 (1997) 1271–1278.

[47] B. Fang, Y.Z. Wei, K. Maruyama, M. Kumagai, High capacity supercapacitors based on modified activated carbon aerogel, J. Appl. Electrochem. 35 (2005) 229–233.

[48] L. Chang, Z. Fu, M. Liu, L. Yuan, J. Wei, Y.W. He, X. Liu, C. Wang, Optimal electrochemical performances of $CO_2$ activated carbon aerogels for supercapacitors, J. Wuhan Univ. Technol. Mater. Sci. Ed. 29 (2014) 213–218.

[49] L. Zubizarreta, A. Arenillas, A. Domínguez, J.A. Menéndez, J.J. Pis, Development of microporous carbon xerogels by controlling synthesis conditions, J. Non. Cryst. Solids. 354 (2008) 817–825.

[50] R.H. Baughman, A.A. Zakhidov, W.A. De Heer, Carbon nanotubes--the route toward applications, Science. 297 (2002) 787–793.

[51] R.G. Ding, G.Q. Lu, Z.F. Yan, M.A. Wilson, Recent advances in the preparation and utilization of carbon nanotubes for hydrogen storage, J. Nanosci. Nanotechnol. 1 (2001) 7–29.

[52] J.H. Chen, W.Z. Li, D.Z. Wang, S.X. Yang, J.G. Wen, Z.F. Ren, Electrochemical characterization of carbon nanotubes as electrode in electrochemical double-layer capacitors, Carbon. 40 (2002) 1193–1197.

[53] B. Xu, F. Wu, Y. Su, G. Cao, S. Chen, Z. Zhou, Y. Yang, Competitive effect of KOH activation on the electrochemical performances of carbon nanotubes for EDLC: balance between porosity and conductivity, Electrochim. Acta. 53 (2008) 7730–7735.

[54] A.G. Pandolfo, A.F. Hollenkamp, Carbon properties and their role in supercapacitors, J. Power Sources. 157 (2006) 11–27.

[55] S. Ban, K. Malek, C. Huang, Z. Liu, A molecular model for carbon black primary particles with internal nanoporosity, Carbon. 49 (2011) 3362–3370.

[56] L.L. Zhang, R. Zhou, X.S. Zhao, Graphene-based materials as supercapacitor electrodes, J. Mater. Chem. 20 (2010) 5983–5992.

[57] H.J. Choi, S.M. Jung, J.M. Seo, D.W. Chang, L. Dai, J.B. Baek, Graphene for energy conversion and storage in fuel cells and supercapacitors, Nano Energy. 1 (2012) 534–551.

[58] K.S. Novoselov, A.K. Geim, S.V. Morozov, D. Jiang, Y. Zhang, S.V. Dubonos, I.V. Grigorieva, A.A. Firsov, Electric field effect in atomically thin carbon films, Science. 306 (2004) 666–669.

[59] V.C. Tung, M.J. Allen, Y. Yang, R.B. Kaner, High-throughput solution processing of large-scale graphene, Nat. Nanotechnol. 4 (2009) 25–29.

[60] D.V. Kosynkin, A.L. Higginbotham, A. Sinitskii, J.R. Lomeda, Longitudinal unzipping of carbon nanotubes to form graphene nanoribbons, Nature. 458 (2009) 872–876.

[61] K.V. Emtsev, A. Bostwick, K. Horn, J. Jobst, G.L. Kellogg, Towards wafer-size graphene layers by atmospheric pressure graphitization of silicon carbide, Nat. Mater. 8 (2009) 203–207.

[62] K.S. Kim, Y. Zhao, H. Jang, S.Y. Lee, J.M. Kim, J.H. Ahn, P. Kim, J.Y. Choi, B.H. Hong, Large-scale pattern growth of graphene films for stretchable transparent electrodes., Nature. 457 (2009) 706–710.

[63] W.S. Hummers, R.E. Offeman, Preparation of graphitic oxide, J. Am. Chem. Soc. 80 (1958) 1339–1339.

[64] N.I. Kovtyuhova, P.J. Ollivier, B.R. Martin, T.E. Moallouk, S.A. Chizhik, E.V. Buzaneva, A.D. Gorchinskiy, Layer-by-layer assembly of ultrathin composite films from micron-sized graphite oxide sheets and polycations, Chem. Mater. 11 (1999) 771–778.

[65] S. Park, R.S. Ruoff, Chemical methods for the production of graphenes, Nat. Nanotechnol. 4 (2009) 45–47.

[66] W. Gao, L.B. Alemany, L. Ci, P.M. Ajayan, New insights into the structure and reduction of graphite oxide., Nat. Chem. 1 (2009) 403–408.

[67] S.R.C. Vivekachand, C.S. Rout, K.S. Subrahmanyam, A. Govindaraj, C.N.R. Rao, Graphene-based electrochemical supercapacitors, J. Chem. Sci. 120 (2008) 9–13.

[68] M.D. Stoller, S. Park, Y. Zhu, J. An, R.S. Ruoff, Graphene-based ultracapacitors., Nano Lett. 8 (2008) 3498–3502.

[69] Y. Sun, Q. Wu, G. Shi, Graphene based new energy materials, Energy Environ. Sci. 4 (2011) 1113–1132.

[70] B. Xu, S. Yue, Z. Sui, X. Zhang, S. Hou, G. Cao, Y. Yang, What is the choice for supercapacitors: graphene or graphene oxide?, Energy Environ. Sci. 4 (2011) 2826–2830.

[71] M. Jayalakshmi, K. Balasubramanian, Simple capacitors to supercapacitors-an overview, Int. J. Electrochem. Sci. 3 (2008) 1196–1217.

[72] A. Rudge, J. Davey, I. Raistrick, S. Gottesfeld, J.P. Ferraris, Conducting polymers as active materials in electrochemical capacitors, J. Power Sources. 47 (1994) 89–107.

[73] J.P. Zheng, T.R. Jow, A New Charge Storage Mechanism for electrochemical capacitors, J. Electrochem. Soc. 142 (1995) 6–8.

[74] I.H. Kim, K.B. Kim, Ruthenium Oxide Thin film electrodes for supercapacitors, Electrochem. Solid-State Lett. 4 (2001) 62–64.

[75] P. Simon, Y. Gogotsi, Materials for electrochemical capacitors., Nat. Mater. 7 (2008) 845–854.

[76] B.O. Park, C.D. Lokhande, H.S. Park, W.D. Jung, O.S. Joo, Electrodeposited ruthenium oxide ($RuO_2$) films for electrochemical supercapacitors, J. Mater. Sci. 39 (2004) 4313–4317.

[77] J.P. Zheng, T.R. Jow, High energy and high power density electrochemical capacitors, J. Power Sources. 62 (1996) 155–159.

[78] C.C. Hu, K.H. Chang, M.C. Lin, Y.T. Wu, Design and tailoring of the nanotubular arrayed architecture of hydrous $RuO_2$ for next generation supercapacitors, Nano Lett. 6 (2006) 2690–2695.

[79] L.L. Zhang, T. Wei, W. Wang, X.S. Zhao, Manganese oxide-carbon composite as supercapacitor electrode materials, Microporous Mesoporous Mater. 123 (2009) 260–267.

[80] N.L. Wu, Nanocrystalline oxide supercapacitors, Mater. Chem. Phys. 75 (2002) 6–11.

[81] X. Zhou, H. Chen, D. Shu, C. He, J. Nan, Study on the electrochemical behavior of vanadium nitride as a promising supercapacitor material, J. Phys. Chem. Solids. 70 (2009) 495–500.

[82] T. Cottineau, M. Toupin, T. Delahaye, T. Brousse, D. Bélanger, Nanostructured transition metal oxides for aqueous hybrid electrochemical supercapacitors, Appl. Phys. A. 82 (2006) 599–606.

[83] A. Davies, A. Yu, Material advancements in supercapacitors: from activated carbon to carbon nanotube and graphene, Can. J. Chem. Eng. 89 (2011) 1342–1357.

[84] C. Xu, F. Kang, B. Li, H. Du, Recent progress on manganese dioxide based supercapacitors, J. Mater. Res. 25 (2010) 1421–1432.

[85] H.Y. Lee, J.B. Goodenough, Supercapacitor behavior with KCl electrolyte, J. Solid State Chem. 144 (1999) 220–223.

[86] M.S. Hong, S.H. Lee, S.W. Kim, Use of KCl aqueous electrolyte for 2V manganese oxide/activated carbon hybrid capacitor, Electrochem. Solid-State Lett. 5 (2002) 227–230.

[87] S. Devaraj, N. Munichandraiah, Electrochemical supercapacitor studies of nanostructured α-$MnO_2$ synthesized by microemulsion method and the effect of annealing, J. Electrochem. Soc. 154 (2007) 80–88.

[88] S. Devaraj, G.S. Gabriel, S.R. Gajjela, P. Balaya, Mesoporous $MnO_2$ and its capacitive behavior, Electrochem. Solid-State Lett. 15 (2012) 57–59.

[89] G.A. Snook, P. Kao, A.S. Best, Conducting-polymer-based supercapacitor devices and electrodes, J. Power Sources. 196 (2011) 1–12.

[90] A.D. Pasquier, A. Laforgue, P. Simon, G.G. Amatucci, J.F. Fauvarque, A nonaqueous asymmetric hybrid $Li_4Ti_5O_{12}$/poly(fluorophenylthiophene) energy storage device, J. Electrochem. Soc. 149 (2002) 302–306.

[91] S.R. Sivakkumar, R. Saraswathi, Performance evaluation of poly(N-methylaniline) and polyisothianaphthene in charge-storage devices, J. Power Sources. 137 (2004) 322–328.

[92] K. Wang, H. Wu, Y. Meng, Z. Wei, Conducting polymer nanowire arrays for high performance supercapacitors, Small. 10 (2014) 14–31.

[93] H. Talbi, P.E. Just, L.H. Dao, Electropolymerization of aniline on carbonized polyacrylonitrile aerogel electrodes: Applications for supercapacitors, J. Appl. Electrochem. 33 (2003) 465–473.

[94] C. Arbizzani, M. Mastragostino, F. Soavi, New trends in electrochemical supercapacitors.pdf, J. Power Sources. 100 (2001) 164–170.

[95] M. Mastragostino, C. Arbizzani, F. Soavi, Conducting polymers as electrode materials in supercapacitors, Solid State Ionics. 148 (2002) 493–498.

[96] A. Laforgue, P. Simon, J.F. Fauvarque, M. Mastragostino, F. Soavi, J.F. Sarrau, P. Lailler, M. Conte, E. Rossi, S. Saguatti, Activated carbon/conducting polymer hybrid supercapacitors, J. Electrochem. Soc. 150 (2003) 645–651.

[97] C. Peng, S. Zhang, D. Jewell, G.Z. Chen, Carbon nanotube and conducting polymer composites for supercapacitors, Prog. Nat. Sci. 18 (2008) 777–788.

[98] W.G. Pell, B.E. Conway, Peculiarities and requirements of asymmetric capacitor devices based on combination of capacitor and battery-type electrodes, J. Power Sources. 136 (2004) 334–345.

[99] H. Li, L. Cheng, Y. Xia, A hybrid electrochemical supercapacitor based on a 5V Li-ion battery cathode and active carbon, Electrochem. Solid-State Lett. 8 (2005) A433-A436.

[100] X. Wang, J.P. Zheng, The optimal energy density of electrochemical capacitors using two different electrodes, J. Electrochem. Soc. 151 (2004) 1683–1689.

[101] K. Naoi, P. Simon, New materials and new configurations for advanced electrochemical capacitors, J. Am. Chem. Soc. 17 (2008) 34–37.

[102] J.P. Zheng, P.J. Cygan, T.R. Jow, Hydrous ruthenium oxide as an electrode material for electrochemical capacitors, J. Electrochem. Soc. 142 (1995) 2669–2703.

[103] D.A. McKeown, P.L. Hagans, L.P.L. Carette, A.E. Russell, K.E. Swider, D.R. Rolison, Structure of hydrous ruthenium oxides : implications for charge storage, J. Phys. Chem. B. 103 (1999) 4825–4832.

[104] C.C. Hu, W.C. Chen, K.H. Chang, How to achieve maximum utilization of hydrous ruthenium oxide for supercapacitors, J. Electrochem. Soc. 151 (2004) 281–290.

[105] J.H. Park, J.M. Ko, O.O. Park, Carbon nanotube/$RuO_2$ nanocomposite electrodes for supercapacitors, J. Electrochem. Soc. 150 (2003) 864–867.

[106] H. Kim, B.N. Popov, Characterization of hydrous ruthenium oxide/carbon nanocomposite supercapacitors prepared by a colloidal method, J. Power Sources. 104 (2002) 52–61.

[107] L. Wang, T. Morishita, M. Toyoda, M. Inagaki, Asymmetric electric double layer capacitors using carbon electrodes with different pore size distributions, Electrochim. Acta. 53 (2007) 882–886.

[108] L. Nyholm, G. Nyström, A. Mihranyan, M. Strømme, Toward flexible polymer and paper-based energy storage devices, Adv. Mater. 23 (2011) 3751–3769.

[109] V.L. Pushparaj, M.M. Shaijumon, A. Kumar, S. Murugesan, L. Ci, R. Vajtai, R.J. Linhardt, O. Nalamasu, P.M. Ajayan, Flexible energy storage devices based on nanocomposite paper, Proc. Natl. Acad. Sci. U. S. A. 104 (2007) 13574–13577.

[110] D. Wei, S.J. Wakeham, T.W. Ng, M.J. Thwaites, H. Brown, P. Beecher, Transparent, flexible and solid-state supercapacitors based on room temperature ionic liquid gel, Electrochem. Commun. 11 (2009) 2285–2287.

[111] K. Jost, C.R. Perez, J.K. McDonough, V. Presser, M. Heon, G. Dion, Y. Gogotsi, Carbon coated textiles for flexible energy storage, Energy Environ. Sci. 4 (2011) 5060–5067.

[112] K. Cherenack, C. Zysset, T. Kinkeldei, N. Münzenrieder, G. Tröster, Woven electronic fibers with sensing and display functions for smart textiles, Adv. Mater. 22 (2010) 5178–5182.

[113] V.T. Le, H. Kim, A. Ghosh, J. Kim, J. Chang, Q.A. Vu, D.T. Pham, J.H. Lee, S.W. Kim, Y.H. Lee, Coaxial fiber supercapacitor using all-carbon material electrodes, ACS Nano. 7 (2013) 5940–5947.

[114] Y. Fu, X. Cai, H. Wu, Z. Lv, S. Hou, M. Peng, X. Yu, D. Zou, Fiber supercapacitors utilizing pen ink for flexible/wearable energy storage, Adv. Mater. 24 (2012) 5713–5718.

[115] D. Harrison, F. Qiu, J. Fyson, Y. Xu, P. Evans, D. Southee, A coaxial single fibre supercapacitor for energy storage, Phys. Chem. Chem. Phys. 15 (2013) 12215–12219.

[116] C. Xu, C. Wei, B. Li, F. Kang, Z. Guan, Charge storage mechanism of manganese dioxide for capacitor application: Effect of the mild electrolytes containing alkaline and alkaline-earth metal cations, J. Power Sources. 196 (2011) 7854–7859.

[117] S. Shi, C. Xu, C. Yang, J. Li, H. Du, B. Li, F. Kang, Flexible supercapacitors, Particuology. 11 (2013) 371–377.

[118] L. Wei, N. Nitta, G. Yushin, M. Science, U. States, Lithographically patterned thin activated carbon films as a new technology platform for on-chip, ACS Nano. (2013) 6498–6506.

[119] Z. Yang, J. Deng, X. Chen, J. Ren, H. Peng, A highly stretchable, fiber-shaped supercapacitor, Angew. Chemie Int. Ed. 52 (2013) 13453–13457.

[120] Q. Wang, L. Jiao, H. Du, Y. Wang, H. Yuan, Biomass-derived sponge-like carbonaceous hydrogels and aerogels for supercapacitors, ACS Nano. 7 (2013) 3589–3597.

[121] Z. Wu, Y. Sun, Y. Tan, S. Yang, Three-dimensional graphene-based macro-and meso-porous frameworks for high performance electrochemical capacitive energy storage-supporting information, J. Am. Chem. Soc. 134 (2012) 19532–19535.

[122] Y.J. Kang, H. Chung, C.-H. Han, W. Kim, All-solid-state flexible supercapacitors based on papers coated with carbon nanotubes and ionic-liquid-based gel electrolytes, Nanotechnology. 23 (2012) 065401.

[123] M. Kaempgen, C.K. Chan, J. Ma, Y. Cui, G. Gruner, Printable thin film supercapacitors using single-walled carbon nanotubes, Nano Lett. 9 (2009) 1872–1876.

[124] Y. Zhu, S. Murali, M.D. Stoller, K.J. Ganesh, W. Cai, P.J. Ferreira, A. Pirkle, R.M. Wallace, K.A. Cychosz, M. Thommes, D. Su, E.A. Stach, R.S. Ruoff, Carbon-based supercapacitors produced by activation of graphene, Science. 332 (2011) 1537–1541.

[125] Z. Niu, L. Zhang, L. Liu, B. Zhu, H. Dong, X. Chen, All-solid-state flexible ultrathin micro-supercapacitors based on graphene, Adv. Mater. 25 (2013) 4035–4042.

[126] M.F. El-Kady, V. Strong, S. Dubin, R.B. Kaner, Laser scribing of high-performance and flexible graphene-based electrochemical capacitors, Science. 335 (2012) 1326–1330.

[127] W. Liu, X. Yan, J. Lang, C. Peng, Q. Xue, Flexible and conductive nanocomposite electrode based on graphene sheets and cotton cloth for supercapacitor, J. Mater. Chem. 22 (2012) 17245–17253.

[128] Z.S. Wu, A. Winter, L. Chen, Y. Sun, A. Turchanin, X. Feng, K. Müllen, Three-dimensional nitrogen and boron co-doped graphene for high-performance all-solid-state supercapacitors, Adv. Mater. 24 (2012) 5130–5135.

[129] S. Wang, B. Pei, X. Zhao, R. a W. Dryfe, Highly porous graphene on carbon cloth as advanced electrodes for flexible all-solid-state supercapacitors, Nano Energy. 2 (2013) 530–536.

[130] M.B. Sassin, C.N. Chervin, D.R. Rolison, J.W. Long, Redox deposition of nanoscale metal oxides on carbon for next-generation electrochemical capacitors, Acc. Chem. Res. 46 (2013) 1062–1074.

[131] D.P. Dubal, G.S. Gund, R. Holze, H.S. Jadhav, C.D. Lokhande, C.J. Park, Solution-based binder-free synthetic approach of RuO2 thin films for all solid state supercapacitors, Electrochim. Acta. 103 (2013) 103–109.

[132] W. Wei, X. Cui, W. Chen, D.G. Ivey, Manganese oxide-based materials as electrochemical supercapacitor electrodes, Chem. Soc. Rev. 40 (2011) 1697–1721.

[133] M. Toupin, T. Brousse, D. Bélanger, Charge storage mechanism of $MnO_2$ electrode used in aqueous electrochemical capacitor, Chem. Mater. 16 (2004) 3184–3190.

[134] P. Yang, Y. Li, Z. Lin, Y. Ding, S. Yue, C.P. Wong, X. Cai, S. Tan, W. Mai, Worm-like amorphous $MnO_2$ nanowires grown on textiles for high-performance flexible supercapacitors, J. Mater. Chem. A. 2 (2014) 595.

[135] D.P. Dubal, R. Holze, All-solid-state flexible thin film supercapacitor based on $Mn_3O_4$ stacked nanosheets with gel electrolyte, Energy. 51 (2013) 407–412.

[136] L. Yuan, X. Xiao, T. Ding, J. Zhong, X. Zhang, Y. Shen, B. Hu, Y. Huang, J. Zhou, Z.L. Wang, Paper-based supercapacitors for self-powered nanosystems, Angew. Chemie - Int. Ed. 51 (2012) 4934–4938.

[137] Z.. Wang, R. Guo, G.R. Li, H.L. Lu, Z.Q. Liu, F.M. Xiao, Y.X. Tong, Polyaniline nanotube arrays as high-performance flexible electrodes for electrochemical energy storage devices, J. Mater. Chem. 22 (2012) 2401–2404.

[138] F. Meng, Y. Ding, Sub-micrometer-thick all-solid-state supercapacitors with high power and energy densities, Adv. Mater. 23 (2011) 4098–4102.

[139] B. Yao, B. Hu, W. Chen, Polypyrrole-coated paper for flexible solid- state energy storage Energy &, Energy Environ. Sci. 6 (2013) 470–476.

[140] J.M. Jeong, B.G. Choi, S.C. Lee, K.G. Lee, S.J. Chanhg, Y.K. Han, Y.B. Lee, H.U. Lee, S. Kwon, G. Lee, C.S. Lee, Y.S. Huh, Hierarchical Hollow Spheres of $Fe_2O_3$ @ Polyaniline for Lithium Ion Battery Anodes, Adv. Mater. 25 (2013) 6250–6255.

[141] R.I. Jafri, A.K. Mishra, S. Ramaprabhu, Polyaniline-$MnO_2$ nanotube hybrid nanocomposite as supercapacitor electrode material in acidic electrolyte, J. Mater. Chem. 21 (2011) 17601–17605.

[142] Z. Wang, X. He, S. Ye, Y. Tong, G. Li, Design of polypyrrole/polyaniline double-walled nanotube arrays for electrochemical energy storage design of polypyrrole/polyaniline double-walled nanotube arrays for electrochemical energy storage, Appl. Mater. Interfaces. 6 (2014) 642–647.

[143] L. Yuan, X.H. Lu, X. Xiao, T. Zhai, J. Dai, F. Zhang, B. Hu, X. Wang, L. Gong, J. Chen, C. Hu, Y. Tong, J. Zhou, Z.L. Wang, Flexible solid-state supercapacitors based on carbon nanoparticles/$MnO_2$ nanorods hybrid structure, ACS Nano. 6 (2012) 656–661.

[144] L. Bao, X. Li, Towards textile energy storage from cotton T-shirts, Adv. Mater. (2012) 3246–3252.

[145] Y.C. Chen, Y.K. Hsu, Y.G. Lin, Y.K. Lin, Y.Y. Horng, L.C. Chen, K.H. Chen, Highly flexible supercapacitors with manganese oxide nanosheet/carbon cloth electrode, Electrochim. Acta. 56 (2011) 7124–7130.

[146] L. Yang, S. Cheng, Y. Ding, X. Zhu, Z.L. Wang, M. Liu, Hierarchical network architectures of carbon fiber paper supported cobalt oxide nanonet for high-capacity pseudocapacitors, Nano Lett. 12 (2012) 321–325.

[147] L. Bao, J. Zang, X. Li, Flexible $Zn_2SnO_4$/$MnO_2$ core/shell nanocable-carbon microfiber hybrid composites for high-performance supercapacitor electrodes, Nano Lett. 11 (2011) 1215–1220.

[148] Z. Lei, F. Shi, L. Lu, Incorporation of $MnO_2$-coated carbon nanotubes between graphene sheets as supercapacitor electrode., ACS Appl. Mater. Interfaces. 4 (2012) 1058–1064.

[149] Z. Chen, I.R. Gentle, D. Wang, F. Li, J. Zhao, W. Ren, Z. Chen, J. Tan, Z. Wu, Fabrication of graphene/polyaniline composite paper via in situ anodic electropolymerization for high-performance flexible electrode, ACS Nano. (2009) 1745–1752.

[150] J. Ge, G. Cheng, L. Chen, Transparent and flexible electrodes and supercapacitors using polyaniline/single-walled carbon nanotube composite thin films, Nanoscale. (2011) 3084–3088.

[151] Y. Horng, Y. Lu, Y. Hsu, C. Chen, L. Chen, K. Chen, Flexible supercapacitor based on polyaniline nanowires/carbon cloth with both high gravimetric and area-normalized capacitance, J. Power Sources. 195 (2010) 4418–4422.

[152] C. Meng, C. Liu, L. Chen, C. Hu, S. Fan, Highly flexible and all-solid-state paper like polymer supercapacitors, Nano Lett. 10 (2010) 4025–4031.

[153] C. Meng, C. Liu, S. Fan, Flexible carbon nanotube/polyaniline paper-like films and their enhanced electrochemical properties, Electrochem. Commun. 11 (2009) 186–189.

[154] X. Li, F. Gittleson, M. Carmo, R.C. Sekol, A.D. Taylor, Scalable fabrication of multifunctional freestanding carbon nanotube/polymer composite thin films for energy conversion, ACS Nano. 6 (2012) 1347–1356.

[155] B. Yao, L. Yuan, X. Xiao, J. Zhang, Y. Qi, Paper-based solid-state supercapacitors with pencil-drawing graphite/polyaniline networks hybrid electrodes, Nano Energy. 2 (2013) 1071–1078.

[156] P.C. Chen, G. Shen, Y. Shi, H. Chen, C. Zhou, Preparation and characterization of flexible asymmetric supercapacitors based on transition-metal-oxide nanowire/single-walled carbon nanotube hybrid thin-film electrodes, ACS Nano. 4 (2010) 4403–4411.

[157] L. Hu, J.W. Choi, Y. Yang, S. Jeong, F.L. Mantia, L.F. Cui, Y. Cui, Highly conductive paper for energy-storage devices, Proc. Natl. Acad. Sci. U. S. A. 106 (2009) 21490–21494.

[158] C. Yu, C. Masarapu, J. Rong, B. Wei, H. Jiang, Stretchable supercapacitors based on buckled single-walled carbon-nanotube macrofilms, Adv. Mater. 21 (2009) 4793–4797.

[159] S. Shi, C. Xu, C. Yang, J. Li, H. Du, B. Li, F. Kang, Flexible supercapacitors, Particuology. 11 (2013) 371–377.

[160] Q. Wang, X. Wang, J. Xu, X. Ouyang, X. Hou, D. Chen, R. Wang, G. Shen, Flexible coaxial-type fiber supercapacitor based on $NiCo_2O_4$ nanosheets electrodes, Nano Energy. 8 (2014) 44–51.

[161] C.C. Ho, D.S. Steingart, J. Evans, P. Wright, Tailoring electrochemical capacitor energy storage using direct write dispenser printing, ECS Trans. 16 (2008) 35–47.

[162] S. Shi, C. Xu, C. Yang, Y. Chen, J. Liu, F. Kang, Flexible asymmetric supercapacitors based on ultrathin two-dimensional nanosheets with outstanding electrochemical performance and aesthetic property., Sci. Rep. 3 (2013) 2598.

[163] H. Yu, J. Wu, L. Fan, K. Xu, X. Zhong, Y. Lin, J. Lin, Improvement of the performance for quasi-solid-state supercapacitor by using PVA–KOH–KI polymer gel electrolyte, Electrochim. Acta. 56 (2011) 6881–6886.

[164] B.G. Choi, J. Hong, W.H. Hong, P.T. Hammond, H. Park, Facilitated ion transport in all-solid-state flexible supercapacitors, ACS Nano. 5 (2011) 7205–7213.

[165] Y. Matsuda, M. Morita, M. Ishikawa, M. Ihara, New electric double-layer capacitors using polymer solid electrolytes containing tetraalkylammonium salts, J. Electrochem. Soc. 140 (1993) 109–110.

[166] M. Yamagata, K. Soeda, S. Yamazaki, M. Ishikawa, Alginate gel containing an ionic liquid and its application to non-aqueous electric double layer capacitors, Electrochem. Solid-State Lett. 14 (2011) 165–169.

[167] D.R. MacFarlane, N. Tachikawa, M. Forsyth, J.M. Pringle, P.C. Howlett, G.D. Elliott, J.H. Davis, M. Watanabe, P. Simon, C.A. Angell, Energy applications of ionic liquids, Energy Environ. Sci. 7 (2014) 232–250.

[168] N. Liu, W. Ma, J. Tao, X. Zhang, J. Su, L. Li, C. Yang, Y. Gao, D. Golberg, Y. Bando, Cable-type supercapacitors of three-dimensional cotton thread based multi-grade nanostructures for wearable energy storage, Adv. Mater. 25 (2013) 4925–4931.

[169] T. Chen, R. Hao, H. Peng, L. Dai, High-performance, stretchable, wire-shaped supercapacitors, Angew. Chemie -Int. Ed. 54 (2015) 618–622.

[170] L. Liu, Y. Yu, C. Yan, K. Li, Z. Zheng, Wearable energy-dense and power-dense supercapacitor yarns enabled by scalable graphene–metallic textile composite electrodes, Nat. Commun. 6 (2015) 7260.

[171] C. Choi, S.H. Kim, H.J. Sim, J.A. Lee, A.Y. Choi, Y.T. Kim, X. Lepro, G.M. Spinks, R.H. Baughman, S.J. Kim, Stretchable, weavable coiled carbon nanotube/$MnO_2$/polymer fiber solid-state supercapacitors, Sci. Rep. 5 (2015) 09387.

[172] X. Zhao, B. Zheng, T. Huang, C. Gao, Graphene-based single fiber supercapacitor with a coaxial structure, Nonoscale. 7 (2015) 9399–9404.

[173] J. Smithyman, R. Liang, Flexible supercapacitor yarns with coaxial carbon nanotube network electrodes, Mater. Sci. Eng. B. 184 (2014) 34–43.

[174] S.L. Chou, J.Z. Wang, S.Y. Chew, H.K. Liu, S.X. Dou, Electrodeposition of $MnO_2$ nanowires on carbon nanotube paper as free-standing, flexible electrode for supercapacitors, Electrochem. Commun. 10 (2008) 1724–1727.

[175] P. Yang, Y. Ding, Z. Lin, Y. Li, P. Qiang, Low-cost high-performance solid-state asymmetric aupercapacitors based on $MnO_2$ nanowires and $Fe_2O_3$ nanotubes, Nano Lett. 14 (2014) 731–736.

[176] P. Yang, X. Xiao, Y. Li, Y. Ding, P. Qiang, X. Tan, W. Mai, Z. Lin, Hydrogenated ZnO core-shell nanocables for flexible supercapacitors, ACS Nano. (2013) 2617–2626.

[177] I. Shakir, High energy density based flexible electrochemical supercapacitors from layer-by-layer assembled multiwall carbon nanotubes and graphene, Electrochim. Acta. 129 (2014) 396–400.

[178] K. Wang, P. Zhao, X. Zhou, H. Wu, Z. Wei, Flexible supercapacitors based on cloth-supported electrodes of conducting polymer nanowire array/SWCNT composites, J. Mater. Chem. 21 (2011) 16373–16378.

[179] C. Shi, Q. Zhao, H. Li, Z. Liao, D. Yu, Low cost and flexible mesh-based supercapacitors for promising large-area flexible/wearable energy storage, Nano Energy. 6 (2014) 82–91.

[180] R. Kötz, M. Hahn, R. Gallay, Temperature behavior and impedance fundamentals of supercapacitors, J. Power Sources. 154 (2006) 550–555.

[181] V. Khomenko, E. Frackowiak, F. Béguin, Determination of the specific capacitance of conducting polymer/nanotubes composite electrodes using different cell configurations, Electrochim. Acta. 50 (2005) 2499–2506.

[182] A. Lewandowski, A. Olejniczak, M. Galinski, I. Stepniak, Performance of carbon-carbon supercapacitors based on organic, aqueous and ionic liquid electrolytes, J. Power Sources. 195 (2010) 5814–5819.

[183] F. Lufrano, P. Staiti, Performance improvement of Nafion based solid state electrochemical supercapacitor, Electrochim. Acta. 49 (2004) 2683–2689.

[184] H.T. Jeong, Fabrication of stretchable and flexible supercapacitor using nanocarbon based materials, University of Wollongong, 2015.

[185] Z. Niu, J. Du, X. Cao, Y. Sun, W. Zhou, H.H. Hng, J. Ma, X. Chen, S. Xie, Electrophoretic build-up of alternately multilayered films and micropatterns based on graphene sheets and nanoparticles and their applications in flexible supercapacitors, Small. 8 (2012) 3201–3208.

[186] Z. Li, J. Wang, X. Liu, S. Liu, J. Ou, S. Yang, Electrostatic layer-by-layer self-assembly multilayer films based on graphene and manganese dioxide sheets as novel electrode materials for supercapacitors, J. Mater. Chem. 21 (2011) 3397–3403.

[187] S. Mohammad, R. Niya, M. Hoorfar, On a possible physical origin of the constant phase element, Electrochim. Acta. 188 (2016) 98–102.

[188] W. Cai, T. Lai, W. Dai, J. Ye, A facile approach to fabricate flexible all-solid-state supercapacitors based on $MnFe_2O_4$/graphene hybrids, J. Power Sources. 255 (2014) 170–178.

[189] R. Richner, S. Müller, M. Bärtschi, R. Kötz, A. Wokaun, Physically and chemically bonded carbonaceous material for double-layer capacitor applications, J. New Mater. Electrochem. Syst. 5 (2002) 297–303.

[190] Z.R. Lazic, Design of experiments in chemical engineering: a practical guide, 2004.

[191] R.L. Mason, R.F. Gunst, J.L. Hess, Statistical design and analysis of experiments: with applications to engineering and Science, John Wiley, New York, 2003.

[192] W.G. Cochran, G.M. Cox, Experimental designs, Wiley, New York, 1957.

[193] E.A. Diler, R. Ipek, An experimental and statistical study of interaction effects of matrix particle size, reinforcement particle size and volume fraction on the flexural strength of Al–$SiC_p$ composites by P/M using central composite design, Mater. Sci. Eng. A. 548 (2012) 43–55.

[194] G.E.P. Box, J.S. Hunter, Mujlti-factor response surfaces, Ann. Math. Stat. 28 (1957) 195–241.

[195] J.P. Zhang, T.R. Jow, The effect of salt concentration in electrolytes on the maximum energy storage for double layer capacitors, J. Electrochem. Soc. 144 (1997) 2417–2420.

[196] S. Kumagai, K. Mukaiyachi, D. Tashima, Rate and cycle performances of supercapacitors with different electrode thickness using non-aqueous electrolyte, J. Energy Storage. 3 (2015) 10–17.

[197] K.C. Tsay, L. Zhang, J. Zhang, Effects of electrode layer composition/thickness and electrolyte concentration on both specific capacitance and energy density of supercapacitor, Electrochim. Acta. 60 (2012) 428–436.

[198] Q. Abbas, D. Pajak, E. Frąckowiak, F. Béguin, Effect of binder on the performance of carbon/carbon symmetric capacitors in salt aqueous electrolyte, Electrochim. Acta. 140 (2014) 132–138.

[199] B. Yi, X. Chen, K. Guo, L. Xu, C. Chen, H. Yan, J. Chen, High-performance carbon nanotube-implanted mesoporous carbon spheres for supercapacitors with low series resistance, Mater. Res. Bull. 46 (2011) 2168–2172.

[200] F. Qiu, D. Harrison, J. Fyson, D. Southee, Fabrication and characterisation of flexible coaxial thin thread supercapacitors, Smart Sci. 2 (2014) 107–115.

[201] R. Zhang, Y. Xu, D. Harrison, J. Fyson, D. Southee, A. Tanwilaisiri, Fabrication and characterisation of energy storage fibres, Proceeding 20th Int. Conf. Autom. Comput., 2014: pp. 12–13.

[202] H.S. Technologies, M. Heights, Dip coating, Met. Finish. 108 (2010) 130–132.

[203] Y.C. Choi, S.M. Lee, D.C. Chung, Supercapacitors using single-walled carbon, Adv Mater. 13 (2001) 497–500.

[204] X. Liu, All-solid-state electric double-layer capacitor with isotropic high-density graphite electrode and polyethylene oxide/$LiClO_4$ polymer electrolyte, J. Electrochem. Soc. 143 (1996) 3982–3986.

[205] T.A. Centeno, F. Stoeckli, The role of textural characteristics and oxygen-containing surface groups in the supercapacitor performances of activated carbons, Electrochim. Acta. 52 (2006) 560–566.

[206] P. Liu, M. Verbrugge, S. Soukiazian, Influence of temperature and electrolyte on the performance of activated-carbon supercapacitors, J. Power Sources. 156 (2006) 712–718.

[207] A. Jänes, H. Kurig, E. Lust, Characterisation of activated nanoporous carbon for supercapacitor electrode materials, Carbon. 45 (2007) 1226–1233.

[208] O. Barbieri, M. Hahn, A. Herzog, R. Kotz, Capacitance limits of high surface area activated carbons for double layer capacitors, Carbon. 43 (2005) 1303–1310.

[209] J.H. Kim, Y.S. Lee, A.K. Sharma, C.G. Liu, Polypyrrole/carbon composite electrode for high-power electrochemical capacitors, Electrochim. Acta. 52 (2006) 1727–1732.

[210] L.M. Zhang, R. Zhang, L. Zhan, W.M. Qiao, X.Y. Liang, L.C. Ling, Effect of ball-milling technology on pore structure and electrochemical properties of activated carbon, J. Shanghai Univ. (English Ed). 12 (2008) 372–376.

[211] Y.A. Kim, T. Hayashi, Y. Fukai, M. Endo, M.S. Dresselhaus, Effect of ball milling on morphology of cup-stacked carbon nanotubes, Chem. Phys. Lett. 355 (2002) 279–284.

[212] N. Pierard, A. Fonseca, J.F. Colomer, C. Bossuot, J.M. Benoit, G.V. Tendeloo, J.P. Pirard, J.B. Nagy, Ball milling effect on the structure of single-wall carbon nanotubes, Carbon. 42 (2004) 1691–1697.

[213] A.M. Brasil, T.L. Farias, M.G. Carvalho, A recipe for image characterization of fractal-like aggergates, J. Aerosol Sci. 30 (1999) 1379–1389.

[214] Y. Chen, J.F. Gerald, L.T. Chadderton, L. Chaffron, Nanoporous carbon produced by ball milling Nanoporous carbon produced by ball milling, Appl. Phys. Lett. 74 (1999) 2782.

[215] R. Hukki, I. Reddy, Size reduction, 1967.

[216] W. Bratek, A. Świątkowski, M. Pakuła, S. Biniak, M. Bystrzejewski, R. Szmigielski, Characteristics of activated carbon prepared from waste PET by carbon dioxide activation, J. Anal. Appl. Pyrolysis. 100 (2013) 192–198.

[217] N.J. Welham, J.S. Williams, Extended milling of graphite and activated carbon, Carbon. 36 (1998) 1309–1315.

[218] E. Gomibuchi, T. Ichikawa, K. Kimura, S. Isobe, K. Nabeta, H. Fujii, Electrode properties of a double layer capacitor of nano-structured graphite produced by ball milling under a hydrogen atmosphere, Carbon. 44 (2006) 983–988.

[219] R. Janot, D. Guérard, Ball-milling : the behavior of graphite as a function of the dispersal media, Carbon. 40 (2002) 2887–2896.